2019

Growth, characterization and study of critical rare-earth poor/free magnetic materials

Tej Nath Lamichhane
Iowa State University

Growth, characterization and study of critical rare-earth poor/free magnetic materials

by

Tej Nath Lamichhane

A dissertation submitted to the graduate faculty

in partial fulfillment of the requirements for the degree of

DOCTOR OF PHILOSOPHY

Major: Condensed Matter Physics

Program of Study Committee:
Paul C. Canfield, Major Professor
Sergey L. Bud'ko
Ruslan Prozorov
Rebecca Flint
John Lajoie
Ralph Napolitano

The student author, whose presentation of the scholarship herein was approved by the program of study committee, is solely responsible for the content of this dissertation. The Graduate College will ensure this dissertation is globally accessible and will not permit alterations after a degree is conferred.

Iowa State University

Ames, Iowa

2019

DEDICATION

I would like to dedicate this work to my wife Sarita Adhikari, my daughter Safala Lamichhane, and all my family members. Sarita witnessed all the ups and downs during my PhD and supported me in every difficult situation. She always helped me to focus on my study by managing all household chores and taking care of our daughter. I am highly indebted to her for prioritizing my study more than her. She comforted me while I was exhausted and encouraged me when I was skeptical. Despite her very young age, my daughter Safala has been a great source of inspiration and entertainment. I would like to thank my parents who always encouraged and motivated me to achieve my PhD. Without help and support from all of my six siblings, I would not have been able to accomplish my goal. I would like to thank them all for their help, support, and care in every step of my life.

TABLE OF CONTENTS

Page

LIST OF TABLES

LIST OF FIGURES

ACKNOWLEDGMENTS

I sincerely thank all the helping hands and well wishers to complete my PhD. For the foremost, I would like to thank my PhD advisor Dr. Paul C. Canfield for giving me an opportunity to pursue my PhD in his research group "Novel Materials and Ground States" at Iowa State University. I express my heartfelt indebtedness to my advisor for his constant support, guidance and encouragement throughout my PhD. I take him as my role model because of his fascinating teaching strategies. I also would like to thank Dr. Sergey L. Bud'ko for his constant guidance in instrument operations, troubleshooting and safe handling. Moreover, I would like to thank him for his invaluable scientific feedback in my research manuscripts.

Likewise, I would like to thank all my committee members Dr. Ruslan Prozorov, Dr. Rebecca Flint, Dr. John Lajoie, and Dr. Ralph Napolitano for their support, guidance and valuable comments during my PhD.

I want to offer my sincere gratitude to all members of Canfield's army throughout my PhD period for their help and support. Especially, I would like to remember Drs. Tai Kong and Udhara Kaluarachchi for their help in learning single crystal growth, physical properties measurement and data analysis methods. I would like to thank Dr. Valentin Taufour for his assistance in understanding and analysis of anisotropic magnetic data. I would like to thank Dr. Andriy Palasyuk for introducing me to heat treatment strategies to develop microstructures in magnets for pinning. Although it is difficult to remember in issue by issue, I want to thank Dr. Anton Jesche, Dr. Eundeouk Mun, Dr. Hyunsoo Kim, Dr. Xiaoming Ma, Dr. Anna Bohmer, Dr. Gil Drachuck, Dr. Soham Manni, Dr. Guijiang Li, Dr. William R. Meier, Dr. Na Hyun, Dr. Elena Gati, Jo, Dr. Raquel A. Ribeiro, Dr. Dominic Ryan, Li Xiang, Mingyu Xu, Brinda Kuthanazhi, Seth Heerschap, Scott Saunders, Michael Onyszczak, Morgan M. Masters, Olena Palasyuk, Kathryn Neilson, Savannah Downing, Connor Schmidt and Joshua Slagle for valuable discussions and their

help in laboratory work. Similarly, I want to acknowledge the support from my collaborators namely Dr. Yuji Furukawa, Dr. Qisheng Lin, Dr. David Parker, Dr. Tribhuwan Pandey, Dr. Srinivasa Thimmaiah, Dr. Liqin Ke and Dr. Ikenna C. Nlebedim. I would like to acknowledge Dr. Warren Straszheim for doing SEM and WDS on various samples. I would also like to thank Dr. Peter Orth for his valuable help during my thesis revision. Finally, I would like to acknowledge the support from staff of Ames Lab Materials Preparation Center, machine shop, Ames Lab store and ESH&A.

Finally, I would like to remember all my Nepalese friends here in Ames and around the globe who always encouraged me to do my best. This work was supported by the Critical Materials Institute, an Energy Innovation Hub funded by the U.S. Department of Energy, Office of Energy Efficiency and Renewable Energy, Advanced Manufacturing Office. This work was also supported by the US Department of Energy, Office of Basic Energy Sciences, Division of Materials Sciences and Engineering. Ames Laboratory is operated for the US Department of Energy by the Iowa State University under Contract No.DE-AC02-07CH11358.

ABSTRACT

Permanent magnets are very essential in numerous applications such as automobiles, wind turbines, computers, electrical motors and many more. The demand for the high-flux permanent magnet is increasing day by day and doubles roughly in every ten years. Surging demand for portable mechanical and digital devices need miniaturization of energy storage devices such as permanent magnets and batteries. Current rare-earth-based high flux permanent magnets such as $Nd_2Fe_{14}B$ magnets are "critical" and Sm based magnets ($SmCo_5$ and Sm_2Co_{17}) are "likely to be critical", meaning that the raw materials' supply security is not guaranteed despite their great importance in clean energy technologies. Additionally, the mining and the purification of these critical materials create large ecological destruction and generate huge amount of acidic hazardous waste and tons of greenhouse and toxic gases.

Moreover, there is a gap in maximum energy product $(BH)_{max}$ between the existing transition metal-based magnets (e.g. Alnico and ferrites) and the above-mentioned rare-earth-based magnets. If new permanent magnets, performing at the higher end of this gap were to be discovered, the dependency of the magnet industries on the critical rare earth elements could be greatly reduced.

This thesis is a summary of results obtained in a search of relatively more abundant, environment friendly and cheaper transition-metal-based, or Ce-based, ferromagnets for permanent magnets applications. In this work, transition-metal-based ferromagnets (i.e. Fe_5B_2P, HfMnP, ZrMnP and $AlFe_2B_2$), antiferromagnetic $AlMn_2B_2$ and Ce-based ferromagnets ($Ce_{3-x}Mg_xCo_9$ and $Ce(Co_{1-x-y}Cu_xFe_y)_5$) are synthesized in single-crystalline forms and anisotropic magnetic properties were studied.

Fe_5B_2P is a tetragonal transition metal ferromagnetic compound with a Curie temperature of 655±2 K and a room temperature magnetocrystalline anisotropy energy density, $\sim$ 0.35 MJ/m^3, comparable to hexaferrites. For comparison with a high-flux system, $Nd_2Fe_{14}B$ has a room tem-

perature magnetocrystalline anisotropy of $\sim$ 5 MJ/m^3. HfMnP and ZrMnP are two additional phosphorous based compounds that were identified as orthorhombic ferromagnetic materials with Curie temperatures of 320 K and 371 K respectively. They also exhibit hard axis high anisotropy fields of 4.5 T and 10.5 T respectively at 50 K. $AlFe_2B_2$ is an itinerant, rare-earth free, anisotropic, magnetocaloric material with a Curie temperature of 274 K. Similarly, $AlMn_2B_2$ is an antiferromagnetic material with a Néel temperature of $T_N = 313\pm2$ K with low dimensional magnetic properties inferred via smaller critical exponent $\beta = 0.21 \pm 0.02$.

Although Ce is the most abundant and easiest to purify rare-earth element, Ce based permanent magnets have been overlooked in the past due to their low anisotropy and rapid decline of the magnetic properties with temperature. These properties were assumed to be associated with the ambivalent and itinerant nature of Ce in intermetallic compounds. An appropriate chemical substitution also known as rehabilitation can be an effective way to improve the ferromagnetic properties and to decrease the content of the critical element in a permanent magnet. The rehabilitation is the process of development of four major intrinsic properties namely uniaxial anisotropy, high saturation magnetization, high Curie temperature and magnetocrystalline anisotropy by the method of noncritical elements alloying such as Mg or Fe.

Mg, a non-magnetic element, alloying in $CeCo_3$ induced a quantum phase transition of Pauli paramagnetic $CeCo_3$ to isostructural, ferromagnetic, solid solution $Ce_{3-x}Mg_xCo_9$ at as low as $0.35 \leq x \leq 0.40$ along with a significant magnetic anisotropy energy density, useful for a gap magnet with $x \sim 1.40$. In this study, the Curie temperature increases linearly with the Mg content in the solid solution and reaches as high as 450 K for the highest Mg content ($x\sim1.4$). As an additional benefit of Mg, we discovered a Mg-flux growth method of high-flux ferromagnetic compound Sm_2Co_{17}. Then the low-temperature anisotropy field and Curie temperature were determined. Similarly, the optimum amount of Fe and Cu addition to $CeCo_5$ phase adjusts anisotropy and Curie temperature of the system along with the development of 13 Mega-Gauss-Oersted (MG Oe) (103.45 kJ/m^3: See conversion table in the Appendix B.1) energy-product in single-crystalline permanent magnets after appropriate heat treatment.

In summary, exploratory synthesis (including mostly single and sometime polycrystalline samples) of various magnetic systems were performed using flux-growth methods on Fe-, Mn- and Co-rich compounds to identify potential noncritical, ferromagnets for permanent magnet applications. In addition to identifying new ferromagnetic systems (HfMnP, ZrMnP and $Ce_{3-x}Mg_xCo_9$) the anisotropic magnetic properties were characterized for the materials under study. $Ce_{3-x}Mg_xCo_9$ system shows promising properties to be useful ferromagnetic material. A 13 MG Oe energy product was developed in Cu, Fe and Ta substituted single-crystalline $CeCo_5$ permanent magnets. These results can serve as proof of the principle of our research goal of discovery and characterization of non-critical, ferromagnetic materials for gap-magnets applications.

CHAPTER 1. CRITICAL MAGNETIC MATERIALS

1.1 Introduction

1.1.1 Criticality

In the 21^{st} century, ultra-modernization of industrial and information technologies have generated an unprecedented pressure on natural resources. Among such resources, rare-earth elements are becoming increasingly scarce and are considered crucial in clean energy technologies including permanent magnets, magnetic refrigeration, electrolytic cells, and lighting phosphors. The demand of high-flux permanent magnets is ever-increasing with an approximate double digit growth rate [1]. The rare-earth elements' demand-supply analysis has already triggered an alarm in the material science communities. The scale of scarcity is predicted to be so severe that the traditional ore mining, purifying and recycling will be insufficient to sustain the projected supply-chain demands for these materials. As an alternative, scientists are discussing the possibility of harvesting the rare-earth deposits from the Pacific Ocean sea-bed [2] as well as from extra-terrestrial resources like meteors, moon and neighboring planets [3]. Even though these ideas sound amazing, discussing the feasibility of them is irrelevant at the current stage of development of underwater diving technologies and interstellar aviation capabilities. In addition to supply security, the mining and the purification of these critical materials produce large ecological destruction and generate tons of very harmful chemical wastes such as acids and toxic gases. To solve these two big problems, discoveries of noncritical functional materials to replace the scarce rare-earth elements, and substituting less critical rare-earth elements for more critical rare-earth elements are more practical ways to address this growing materials crisis.

Starting in early 2010, there was an unexpected rise in rare-earth ores prices. In 2010 United States Department of Energy published a report named "Critical material strategies" [4] that was updated twice: in 2011 and 2017. According to this report, criticality is defined as the importance

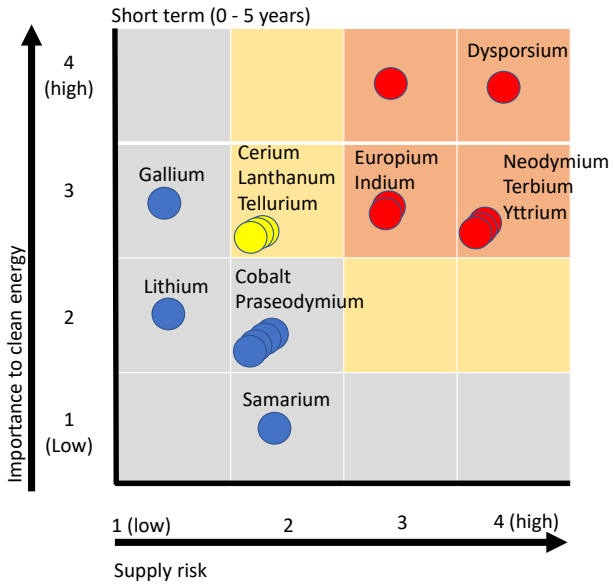

Figure 1.1 Short term criticality as of 2010 clean energy elements reconstructed from the information in reference [4]. The horizontal axis is depicting the supply risk and vertical axis is depicting the importance to the clean energy technologies. The blue colored elements are noncritical, yellow colored elements are near-critical and red colored elements are critical.

of a raw material in clean energy technologies and associated supply risk. In this report, magnetic materials (Nd and Dy), light emitting phosphors and solar cells elements (Y, Eu and Tb, Ga, In and Te) and battery materials mainly Li and Co are listed as critical materials. The short term and medium term criticality of different materials are shown in Fig. 1.1 and Fig. 1.2. Although the time line for the short term criticality is already passed, the reports are still relevant. According to the long term criticality chart, excess Ce is supposed to accumulate as time progress and will be even less critical than in the short term criticality period. In the critical materials strategies report, there are some possible strategies to address these criticalities. Some of them being diversification of the supplies, developing substitutes and recycling of critical materials. The objective of this thesis was to search for rare-earth poor (or free) alternatives to current commercial permanent magnets.

The requirements of a new ferromagnetic material to qualify for permanent magnets application are (i) high Curie temperature ($T_C \geq 550$ K) (ii) high magnetization and (iii) high uniaxial

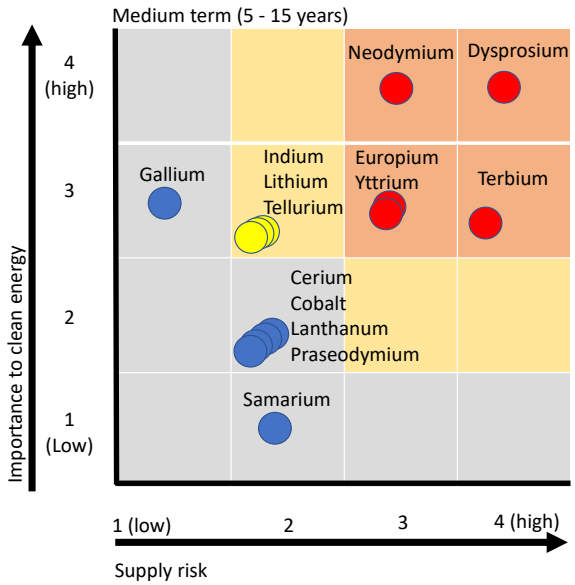

Figure 1.2 Medium term criticality as of 2010 clean energy elements reconstructed from the information in reference [4]. The horizontal axis is depicting the supply risk and vertical axis is depicting the importance to the clean energy technologies. The blue colored elements are noncritical, yellow colored elements are near-critical and red colored elements are critical.

anisotropy [5]. Current rare-earth element based, strong, commercial magnetic materials that satisfies these criteria are $Nd_2Fe_{14}B$, $SmCo_5$ and Sm_2Co_{17}. In these materials, the high magnetization comes from the magnetic transition metals like Fe and Co. The high magnetic anistropy comes from the unpaired localized $4f$ magnetic moments of rare-earth elements. The $4f$ electronic orbitals are screened by $5p$ and $6s$ orbitals [6] and less affected by crystal electric potentials. The most abundant and easiest to purify rare-earth element, Ce, was one of the key constituent of the research projects in this thesis.

To accomplish the objective of finding potentially applicable new ferromagnetic materials, the research projects were focused on exploratory search of new or poorly studied critical element-free ferromagnetic materials and their characterization. The transition metals Fe and Co were used as a source of high magnetization in these systems. Ce was chosen as a cheap source of magnetic anisotropy as well as moderate magnetization in the Ce^{3+} state. In addition to transition metals and

Ce, research projects included a volatile and high vapour pressure element such as P and Mg as a third constituent of a ternary phase diagram to increase the possibility of finding new ferromagnetic materials. The following tree diagram illustrates the strategies adopted in this thesis.

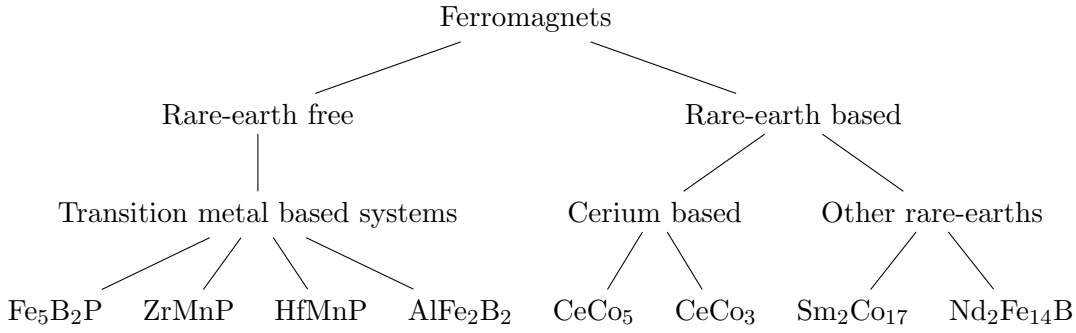

Three phosphorous based ferromagnetic compounds were studied in this thesis. Phosphorous is highly volatile, has a high vapor pressure and is a challenging element to handle safely. So, phosphorous containing phase diagrams are often inaccurate and incomplete. The re-investigation of phosphorous based ternary phase diagrams provides a higher possibility of identifying new, potentially useful, ferromagnetic materials as well as better quantifying the magnetic properties of poorly characterized magnetic materials. We focused on the Fe, Co and Mn rich, transition metal-phosphorous eutectic and introduced small amounts of B, Zr and Hf. In the Fe-P-B phase diagram, we characterized anisotropic magnetic properties of Fe_5B_2P. In the case of known rare-earth free permanent magnetic materials (e.g. FePt, CoPt, and MnBi), the presence of a relatively high atomic number element which exhibits large spin orbit interaction to achieve high anisotropy and coercivity is required in the absence of rare-earth element. Pt is much more critical than any of the rare-earth elements. So, we chose heavy 5d transition metals, Hf and Zr, for the exploratory search of phosphorous based ferromagnets and introduced them in T-P (T = Fe, Mn) eutectics. Ultimately we identified two new ferromagnets ZrMnP and HfMnP.

Ce is the most abundant rare-earth element with moderate anisotropy but is generally overlooked as its ambivalent character leads to a rapid degradation of magnetic properties [7]. Currently, Ce is a byproduct of rare-earth mining and is underutilized [8]. We focused on some poorly studied or overlooked Ce compounds namely $CeCo_n$ (n = 3, 5) and try to rehabilitate [9] the Ce based

Pauli paramagnetic or relatively weak magnetic materials into hard ferromagnets by alloying them with noncritical elements. Pauli paramagnetic $CeCo_3$ was rehabilitated into a hard ferromagnet by Mg alloying. Similarly, phase stability and the rapid degradation of magnetic properties of $CeCo_5$ with temperature was overcome by substituting Co with Fe and Cu. The Fe and Co substituted as-grown single crystalline samples exhibit as high as 1.5 kOe coercivity and 3 MG Oe energy product comparable to Alnico. The single crystalline samples were heat treated to develop the necessary microstructures to generate the domain pinning. Part of this thesis is the summary of the efforts to find rare-earth free or Ce-based ferromagnets for gap magnet production.

The major task of these thesis projects was to synthesize, characterize structural and magnetic properties and measure the anisotropic magnetic properties of single crystalline samples so as to check for the potential of ferromagnetic materials for permanent magnets applications. To complete these tasks basic ideas of planing the exploratory synthesis of magnetic materials and characterizing anisotropic magnetic properties require the understanding of the key theoretical concepts of magnetism. In the following sections of this chapter and the next chapter, a quick survey of associated theoretical and experimental concepts that are used in various chapters in this thesis are discussed.

1.2 Magnetic materials

1.2.1 Origin of magnetism

Magnetism originates from the orbital and spin angular momentum of electrons. Classically, magnetism is associated with a current loop [10]. An electron around a nucleus mimics a current loop and magnetism is inherent to every material via orbital angular momentum. Quantum mechanically, magnetism is also associated with intrinsic electronic spin angular momentum [11]. The magnetic moments of materials are explained on the basis of these two types of angular momenta of electrons. The electrons are filled in the available atomic orbitals following the Aufbau principle in compliance with Pauli exclusion principle. The magnetic moments of ions/atoms depend on number of unpaired electrons in a valence shell.

The completely filled valence shells have no magnetic moments and they contribute to diamagnetism via Lenz's law [12] which is also called core diamagnetism. The unpaired bound electrons in a partially filled valence orbit are responsible for magnetic moments of an ion/atom. The atomic magnetic ground states, which are explained with Hund's rules (see section 1.2.3), are degenerate. The degeneracy is lifted, at least partially, by Coulomb interaction, spin-orbit interaction, crystal electric field and Zeeman interaction in an external magnetic field [13, 14]. Magnetic ground states can be stabilized with the resultant effect of several factors such as exchange interaction, spin orbit interaction, and crystal electric field effect [12, 14, 15].

So, to understand how a magnetic ion acquires its magnetic moment and develops exchange interaction with its neighbours via electronic wave function overlap, lets start from the magnetism of single electron orbit. The orbital angular momentum of an electron around an orbit is given as $l = m_e v r$ and corresponding orbital magnetic moment is [12]

$$\mu_l = -\frac{e}{2m_e\hbar}|\mathbf{l}| = -\frac{e\hbar}{2m_e}\sqrt{l(l+1)} \tag{1.1}$$

where $|\mathbf{l}| = \hbar\sqrt{l(l+1)}$ are the eigenvalues of orbital angular momentum $\mathbf{l}$.

Similarly, in a quantum mechanical picture, the magnetic moment is also associated with the spin of the electron which is given as [16]

$$\mu_s = -g\frac{e}{2m_e}|\mathbf{s}| = -g\frac{e\hbar}{2m_e}\sqrt{s(s+1)} \tag{1.2}$$

where $|\mathbf{s}| = \hbar\sqrt{s(s+1)}$ are the eigenvalues of spin angular momentum $\mathbf{s}$ and g is the Landé g-factor.

The total angular momentum of an electron is given as a vector sum of orbital and spin angular momenta as $|\mathbf{j}| = |\mathbf{l} + g\mathbf{s}|$ and corresponding magnetic moment is given as

$$\mu_j = -g|\mathbf{j}|\frac{e}{2m_e} = -g\frac{e\hbar}{2m_e}\sqrt{j(j+1)} \tag{1.3}$$

For a multiple number of unpaired valence electrons (pairing up of electrons in a state forms a spin singlet state which does not contribute in magnetic moment) in an atom, total magnetic

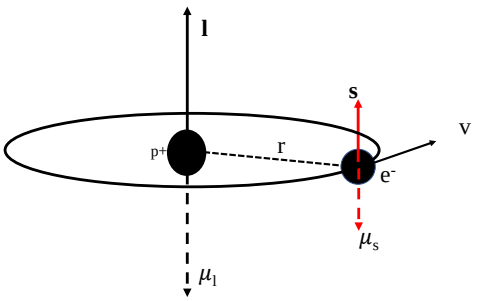

Figure 1.3 The orbital (l, μ_l) and spin (s, μ_s) angular momenta and corresponding magnetic moments of an electronic orbit around a nucleus when both moments are considered to be parallel. The solid arrows represent the directions of angular momenta pointing upward. The dotted arrows represent the directions of magnetic moments pointing downward.

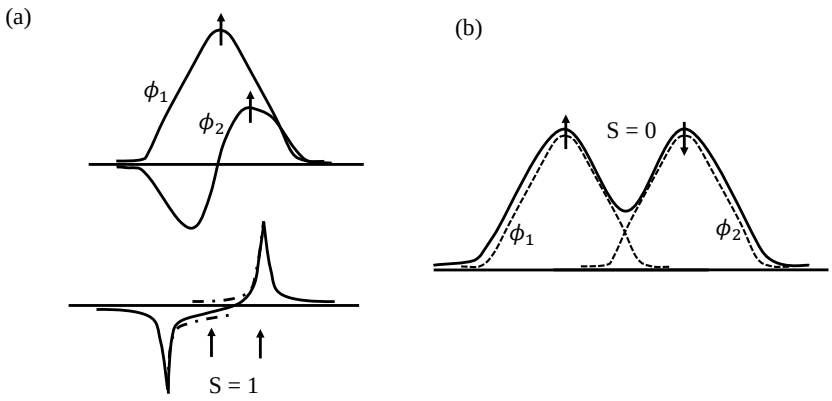

Figure 1.4 Mechanism of direct exchange interaction between two magnetic sites to form (a) a ferromagnetic antisymmetric (anti bonding) wave function and (b) antiferromagnet symmetric (bonding) spin wave function [17, 11]

moment is given as [18]

$$\mu = - < \sum_i (l_i + g s_i)\mu_B >= -gJ\mu_B \tag{1.4}$$

which is called the net-magnetization of a ion summed over all unpaired valance electrons using the index i. Here J value is detected by Hund's rule [14, 12] which will be discussed later in section 1.2.3.

If the wave functions of these magnetic moment bearing ions are not overlapped and noninteracting, then the material will be of a paramagnetic nature [14]. To form a spin ordered magnetic structures, there should exist appreciable Coulomb repulsion between electrons whether they are localized or delocalized. In the localized electronic wave functions, the spin interaction happens through wave function overlapping and hybridization [12]. If the two orthogonal electronic wave functions ϕ_1 and ϕ_2 significantly overlap as shown in Fig. 1.4(a), then the compound forms a ferromagnetic antisymmetric spin state also known as antibonding state [11, 17]. In such alignment, Coulomb interaction energy of the ferromagnetic system is reduced. On the other hand, if the electronic orbitals are nonorthogonal and nonoverlapping but are close enough to form hybridized states, then the compound forms a symmetric antiferromagnetic spin state as shown in Fig. 1.4(b). In this condition, an electron can hop from one ion to another reducing its kinetic energy to form a singlet state within a hybridized state also known as bonding state [11, 17]. If the spin wave function is symmetric, the spatial wave function need to be antisymmetric to maintain the requirement of total antisymmetric wave function for a fermionic state [11].

The exchange interaction is expressed as $\hat{H}_{exchange} = -\sum_{ij} J_{ij} \overrightarrow{S}_i \cdot \overrightarrow{S}_j$, where J_{ij} is called exchange integral between electronic wave functions $\phi_i(r_i)$ and $\phi_j(r_j)$ with spin angular momentum $\overrightarrow{S}_i$ and $\overrightarrow{S}_j$ respectively [19, 12]. The above discussion for ferromagnetism and antiferromagnetism relates to the exchange interaction. Antiferromagnetism is also explained by indirect exchange interaction also known as superexchange [12]. A simple example of superexchange is exchange interaction between Mn ions via O wave functions in antiferromagnetic MnO [20]. Additional discussion about the origin and the types of exchange interactions are discussed in section 1.2.8.

In paramagnetic metals such as alkali and alkaline group the electrons are delocalized within the whole volume of the material and form energy bands for conduction electrons. The electrons bands are degenerated for $\pm\frac{1}{2}$ spins. Only in presence of the external magnetic field, the conduction electrons bands (usually wide) splits in to two separate bands of spin $\frac{1}{2}$ and $-\frac{1}{2}$ and small temperature independent paramagnetic susceptibility is developed since only a small number of electrons that lie within k_BT of the Fermi level can be excited with external field. The details of the metallic paramagnetism with wide electrons band such as $4s$ orbital is discussed in sections 1.2.12.

If the electrons are delocalized in a sufficiently narrow energy band in a ferromagnetic metal can form. The sufficiently narrow bands, such as in $3d$ transition metals, have large electronic density of states ($g(E_F) \propto \frac{1}{\text{band width}}$) and Coulomb repulsion U becomes large enough so that Stoner's criterion ($Ug(E_F) > 1$) is met [11]. Physically, the Stoner's criterion is the condition for evolution of spontaneous magnetization in metals via spontaneous splitting of conduction electron spins bands. The details of the metallic ferromagnetism magnetism is discussed in section 1.2.13.

When the temperature becomes sufficiently high, then the thermal energy per magnetic ion k_BT becomes sufficiently higher than exchange interaction J i.e., $k_BT > J$, phase transition occurs. Above the phase transition, a magnetic (e.g., Ferromagnetic, antiferromagnetic or ferrimagnetic) material becomes paramagnetic.

1.2.2 Classification of magnetic materials

Magnetic materials are categorized depending upon the nature of alignment of magnetic moments, interaction among them and their response in an external magnetic field. The major types of magnetic materials are as follows:

(1) Diamagnetic materials: In diamagnetic materials, there is no unpaired electron which can contribute in magnetism. Most diamagnetic materials are weakly repealed by an applied magnetic field (Superconductors are strongly diamagnetic, but outside the scope of this review.). In classical

theory, when a magnetic field H is applied, an electron either accelerates or retards in its orbit according to the Lenz's law [12].

The net change in magnetic moment of an electronic orbit is found to be [10]

$$\Delta\mu_l = -\frac{e^2r^2}{4m_e}H \tag{1.5}$$

This phenomenon of induction of opposite magnetization proportional to magnetic field H is called diamagnetism.

The diamagnetic susceptibility of the orbit is defined as

$$\chi = \frac{\partial\Delta\mu_l}{\partial H} = -\frac{e^2r^2}{4m_e} = -\frac{e^2 < r^2 >}{6m_e} \tag{1.6}$$

where $< r^2 >= \frac{3}{2}r^2$ [11].

(2) Paramagnetic materials: Paramagnetism is associated with both unpaired bound or delocalized electrons [11]. Paramagnetic materials are characterized with a positive susceptibility [11, 15]. They are generally weakly attracted by magnets. The origin of this weak attraction is the development of small positive magnetization in a magnetizing field [14]. These materials could not retain magnetization after the removal of the magnetizing field.

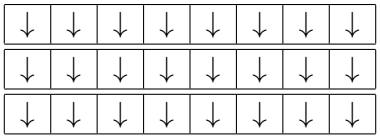

Figure 1.5 Ferromagnetic order

(3) Ferromagnetic materials: These materials contain net spontaneous magnetic moment [21] due to a unique directional alignment of atomic magnetic moments as shown in Fig. 1.5. Ferromagnetic materials are, generally, strongly attracted by magnets and they have large values of magnetization. The ferromagnetic materials undergo a phase transition to a spin disordered state called the paramagnetic state above a certain temperature called the Curie temperature.

(4) Antiferromagnetic materials: In antiferromagnetic materials, there exist a net zero spontaneous magnetic moment [15] with numerous types of spin arrangements such as Néel order, stripe order, spin vortex crystals etc. They develop small positive susceptibility with an external magnetizing field. A simple example of this order is displayed in a stripe type linear antiferromagnetic chain in which the neighboring spins are aligned up and down as shown in Fig. 1.6. An antiferromagnetic material transforms to the paramagnetic regime at temperature higher than the phase transition temperature called Néel temperature.

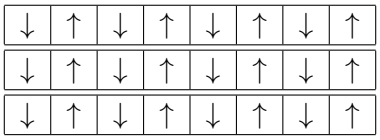

Figure 1.6 Antiferromagnetic order

(5) Ferrimagnetic materials: In ferrimagnets, magnetic moments are arranged similar to antiferromagnets but the magnitude of atomic moments are not equal in up and down directions as shown in Fig. 1.7. Since the net moment is not cancelled, the ferrimagnetic materials possess net spontaneous moments as ferromagnets do [15].

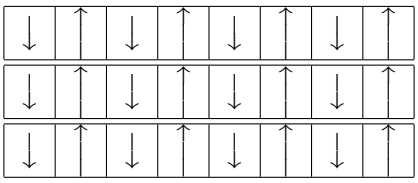

Figure 1.7 Ferrimagnetic order

1.2.3 Magnetic ground states of ions (local magnetic moments)

In atoms, magnetic ground states for bound electrons are determined using Hund's rules [12, 14, 15]. There are three empirical Hund's rules which provide the priority order for electronic sub-

shell filling and spin and orbital angular momentum calculations of bound electrons. The magnetic moments of these bound unpaired electrons are called local magnetic moments.

First rule: According to the first rule, valence electrons are arranged in the valence shell in such a way that the total spin S state is maximized. This requires the single filling of all available electronic states before doubly filling them in singlet spin configuration. The physical reason behind this is the minimization of Coulomb energy of the system in compliance with Pauli exclusion principle. The Pauli exclusion principle prevents the double occupancy of the electrons with same spin quantum number and minimizes the Coulomb energy [14].

Second rule: Given that first rule of highest spin S is fulfilled for the lowest energy state, the second rule dictates the electronic subshell filling order such that total orbital angular momentum L of the state should be maximized. The physical reasoning behind this rule is also to minimize the Coulomb energy of the system [12].

Third rule: In the third Hund's rule, total angular momentum of the state is determined. For the determined S and L from the first and second rules, the total angular momentum is determined [14] as

$$\begin{aligned} J &= |L - S| \text{ for n} \leq (2\text{l} + 1) \\ &= |L + S| \text{ for n} \geq (2\text{l} + 1) \end{aligned}$$

where n is the total number of the electrons in a valence orbital and $(2l+1)$ is the total orbital angular momentum multiplicity number. The third Hund's rule provides the condition for the minimization of spin-orbit interaction energy [12]. With the known L, S and J values, the ground state term symbols are given as ${}^{2S+1}X_J$ where $(2S+1)$ is the total spin multiplicity and J can take $(2J+1)$ values J, $(J\text{-}1)$, ..., -J. X symbols are designated for different total orbital angular momentum values as $(L{=}0){\rightarrow}S$, $(L{=}1){\rightarrow}P$, $(L{=}2){\rightarrow}D$, $(L{=}3){\rightarrow}F$, $(L{=}4){\rightarrow}G$ etc.

1.2.4 Quantum mechanical theory of diamagnetism

In the presence of a uniform external magnetic field H, the Hamiltonian of a magnetic system can be expressed as [12, 14]

$$\hat{H} = \hat{H}_0 + \mu_B(\mathbf{L} + g\mathbf{S}) \cdot \mathbf{H} + \frac{e^2}{8m_e}\sum_i (\mathbf{H} \times \mathbf{r}_i)^2$$
$$\hat{H} = \hat{H}_0 + \Delta\hat{H} \tag{1.7}$$

where $\hat{H}_0 = \sum_{i=1}^{Z}(\frac{p_i^2}{2m_e} + V_i)$ is the magnetic field independent Hamiltonian and $\Delta\hat{H}$ is the field dependent Hamiltonian which can be considered as a perturbative correction in the field independent Hamiltonian [14].

$$\Delta\hat{H} = \sum_{i=1}^{Z} \mu_B(\mathbf{L} + g\mathbf{S}) \cdot \mathbf{H} + \frac{e^2}{8m_e}\sum_i (\mathbf{H} \times \mathbf{r}_i)^2 \tag{1.8}$$

The first term in the perturbation Hamiltonian in equation 1.8 is called Zeeman interaction term and it is associated with unpaired bound electrons which contributes to the paramagnetic susceptibility and the second term is associated with completely filled electronic orbitals which contributes to the diamagnetic susceptibility.

Using the perturbation theory up to the second order, the influence of the magnetic field in the system energy is calculated using Dirac notation of electronic states $|n>$ as

$$< n|\Delta\hat{H}|n >= \mu_B < n|(\mathbf{L} + g\mathbf{S}) \cdot \mathbf{H}|n > + \sum_{n' \neq n} \frac{| < n|\mu_B(\mathbf{L} + g\mathbf{S}) \cdot \mathbf{H}|n' > |^2}{E_n - E_{n'}}$$
$$+ \frac{e^2H^2}{8m_e} < n|\sum_i (x_i^2 + y_i^2)|n > \tag{1.9}$$

where E_n and $E_{n'}$ are the energy eigenvalues for ground state $|n>$ and excited state $|n'>$ respectively.

In a completely filled valence shell, the contribution due to the first and second terms are zero ($< 0|\mu_B(\mathbf{L} + g\mathbf{S}).\mathbf{H})|0 > =0$) and only the third term contributes to diamagnetism as

$$< 0|\Delta\hat{H}|0 >= \Delta\hat{E}_0 = \frac{e^2H^2}{8m_e} < 0|\sum_i (x_i^2 + y_i^2)|0 >$$
$$\Delta\hat{E}_0 = \frac{e^2H^2}{12m_e} < 0|\sum_i r_i^2|0 > \quad (1.10)$$

where spherical symmetry was assumed $< x_i^2 >=< y_i^2 >= \frac{1}{3}r_i^2$ to obtain this relation. Then, the diamagnetic susceptibility is defined as

$$\chi = -\frac{N}{V}\frac{\partial^2\Delta E_0}{\partial H^2} = -\frac{e^2}{6m_e}\frac{N}{V} < 0|\sum_i r_i^2|0 > \quad (1.11)$$

Here the negative susceptibility in equation 1.11 is called Larmor diamagnetic susceptibility [14]. Assuming an average radius r for all electrons in an atom, the diamagnetic susceptibility can be expresses in terms of effective atomic number $Z_{eff} < r^2 >$ [12, 14] as

$$\chi = -\frac{e^2}{6m_e}\frac{NZ_{eff} < r^2 >}{V} \quad (1.12)$$

1.2.5 Quantum theory of paramagnetism

Unfilled valance orbital in an ion or an atom possess unpaired electrons which provide magnetic moments. There is an exception that unpaired electrons in one electron less than the half filled orbital can not provide ground state magnetic moment which I will discuss in Van Vleck paramagnetism. The magnetic ground state of the ion/atom is governed by the Hunds rule. For a given value of total angular momentum J for an ion/atom, there exist $(2J+1)$ degenerated levels at zero magnetic field [14]. When an weak external magnetic field H is applied (weak in a sense that $L-S$ coupling is still valid), the $(2J+1)$ degenerated levels split into equally spaced $(2J+1)$ states with the energy separation of $g\mu_B H$ [14]. If the energy separation between ground state and the first excited state is much larger than thermal energy and the field splitting between $(2J+1)$ states becomes much smaller compared to the thermal energy as $\Delta >> k_BT >> g\mu_BH$, then electrons excitation among (2J+1) field splitted states contribute to paramagnetic susceptibility which is

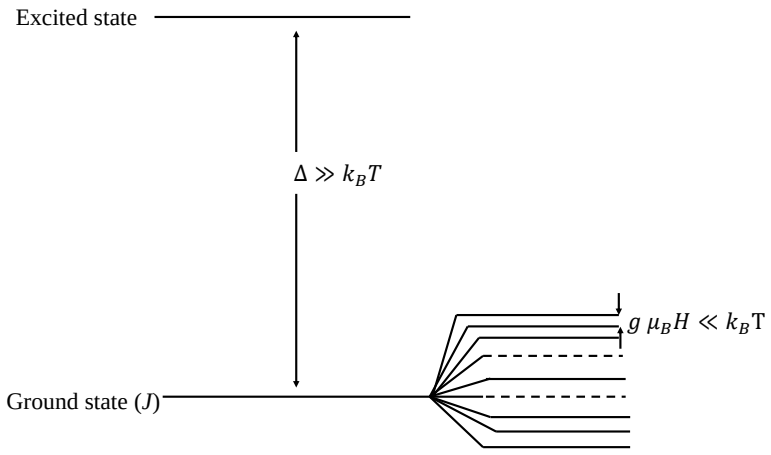

Figure 1.8 A schematic energy level splitting in a paramagnetic material in an external field with ground state total angular momentum J which splits into $(2J+1)$ levels with equal splitting $g\mu_B H$ [14].

calculated using the statistical partition function [14, 22]. A schematic of the energy splitting for paramagnetic system is shown in Fig. 1.8.

[14, 22]

The Zeeman term $\mu_B < n|(\mathbf{L}+g\mathbf{S})\cdot\mathbf{H}|n>$ is conveniently evaluated in diagonalized $|JLSJ_z>$ states using the Wigner-Eckart theorem as [14, 12, 15].

$$\Delta\hat{E}_Z = \mu_B < JLSJ_z|(\mathbf{L}+g\mathbf{S})\cdot\mathbf{H}|JLSJ_z'>= g\mu_B J_z H\delta_{J_z J_z'} \tag{1.13}$$

where $g = \frac{3}{2} + \frac{1}{2}[\frac{S(S+1)-L(L+1)}{J(J+1)}]$ is called Landé g-factor. If the quantum system is in thermal equilibrium at temperature T, then the magnetization density (contributed by N ions in a volume V) could be easily estimated as

$$M = -\frac{N}{V}\frac{\partial F}{\partial H} \tag{1.14}$$

Where $F = -k_B T ln Z$ is a statistical free energy of the system. The partition function Z given as

$$\begin{aligned} Z &= \sum_{J_z=-J}^{J} \exp(-\frac{\Delta \hat{E_Z}}{k_B T}) \\ &= \sum_{J_z=-J}^{J} \exp(-\frac{g\mu_B J_z H}{k_B T}), \quad x = \frac{g\mu_B H}{k_B T} \\ &= \frac{\sinh[(2J+1)\frac{x}{2}]}{\sinh[\frac{x}{2}]} \end{aligned} \tag{1.15}$$

Using equation 1.15 in equation 1.14 and substituting $y = Jx$, it takes the form

$$M = \frac{N}{V} g J \mu_B B_J(y) = M_0 B_J(y) \tag{1.16}$$

where $M_0 = \frac{N}{V} g J \mu_B = n g J \mu_B$ the base temperature ($T \to 0$ K) magnetization. Here $n = \frac{N}{V}$ is the number of magnetic ions per unit volume. Similarly,

$$B_J(y) = \frac{(2J+1)}{2J} \coth \frac{(2J+1)}{2J} y - \frac{1}{2J} \coth \frac{1}{2J} y \tag{1.17}$$

is called a Brillouin function [12].

Case I: Two level system $J = \frac{1}{2}$

Substituting $J = \frac{1}{2}$ in equation 1.17, the Brillouin function reduces to

$$B_{\frac{1}{2}}(y) = \tanh \frac{\mu_B H}{k_B T} \tag{1.18}$$

The two level magnetization is given as

$$M = M_0 \tanh \frac{\mu_B H}{k_B T} \tag{1.19}$$

Corresponding two level susceptibility is given as

$$\chi = \frac{\partial M}{\partial H} = \frac{N}{V} \frac{\mu_B^2}{k_B T} \mathrm{sech}^2 \frac{\mu_\mathrm{B} \mathrm{H}}{\mathrm{k_B T}} \tag{1.20}$$

In the low field and high temperature limit $y << 1$ for $k_B T >> \mu_B H$, the Brillouin function takes a form

$$B_{\frac{1}{2}}(y) = \tanh\frac{\mu_{\mathrm{B}}\mathrm{H}}{\mathrm{k_B T}} \approx \frac{\mu_B H}{k_B T} \tag{1.21}$$

Then the high temperature magnetization of the system is

$$M = \frac{N}{V}\frac{\mu_B^2 H}{k_B T} \tag{1.22}$$

which provides the paramagnetic susceptibility

$$\chi(T) = \frac{\partial M}{\partial H} = \frac{N}{V}\frac{\mu_B^2}{k_B T} = \frac{C}{T} \tag{1.23}$$

where $C = \frac{N}{V}\frac{\mu_B^2}{k_B}$ is called Curie constant for $J = \frac{1}{2}$.

Case II: Multilevel system $J = 1, \frac{3}{2}$ ....

In the high temperature and low field limit, the argument of the Brillouin function becomes small $y << 1$ (For example, if $J = 1$, $g = 2$, $\mu_B = 9.27 \times 10^{-21}$ erg/G, $k_B = 1.38 \times 10^{-16}$ erg/K and $H = 30000$ G then $y = \frac{gJ\mu_B H}{k_B T} \approx \frac{4}{T} = 0.04$ at 100 K) and it could be expanded as a Maculaurin series and only linear term is significant.

$$B_J(y) \approx \frac{J+1}{3J} y + O(y^3) \tag{1.24}$$

Then the high temperature magnetization of the system is

$$M = \frac{N}{V} g J \mu_B B_J(y) = \frac{N}{V}\frac{g^2\mu_B^2}{3}\frac{J(J+1)}{k_B T} H \tag{1.25}$$

which provides the paramagnetic susceptibility

$$\chi(T) = \frac{\partial M}{\partial H} = \frac{N}{V}\frac{g^2\mu_B^2}{3}\frac{J(J+1)}{k_B T} = \frac{C}{T} \tag{1.26}$$

where $C = \frac{N}{V}\frac{g^2\mu_B^2}{3}\frac{J(J+1)}{k_B}$ is called Curie constant.

The molar paramagnetic susceptibility is obtained as [14]

$$\chi_{molar}(T) = N_A \frac{g^2\mu_B^2}{3}\frac{J(J+1)}{k_B T} = \frac{C_{mol}}{T} \tag{1.27}$$

where N_A is Avogardo's constant. The order of magnitude of molar Curie constant for a typical ferromagnet (using $J = 1$) is estimated to be $C_{molar} = N_A \frac{g^2\mu_B^2}{3} \frac{J(J+1)}{k_B} = 6.023\times10^{23} \frac{2^2(9.27\times10^{-21})^2}{3} \frac{1(1+1)}{1.38\times10^{-16}} \approx$ 1 erg K/molG^2. For all other finite values of J, above formula can be easily applied.

Case III: Langevin theory (classical limit: $J \to \infty$)

In paramagnetic regime where dipole moments can rotate freely then the Brillouin function tends to classical Langevin function [12] as

$$B_\infty(y) = L(y) = \coth(y) - \frac{1}{y} \tag{1.28}$$

Using equation 1.16, the relative quantum mechanical magnetization can be expressed as

$$\frac{M}{M_0} = B_J(y) \tag{1.29}$$

Now using the Bohr correspondence principle, the classical relative magnetization can be obtained for infinite limit of J i.e.,

$$\frac{M}{M_0} = \lim_{J\to\infty} B_J(y) = B_\infty(y) = L(y) = \coth(y) - \frac{1}{y} \tag{1.30}$$

where $M_0 = n\mu_{eff}$, $n = \frac{N}{V}$, is the available magnetization per unit volume of a paramagnetic ions with measured effective moment $\mu_{eff} = g\mu_B\sqrt{J(J+1)} = \lim_{J\to\infty} \frac{M_0}{n} = gJ\mu_B$ [12]. Expanding $\coth(y)$ function for small value of $y = \frac{\mu_{eff}H}{k_BT} << 1$ the classical relative magnetization is obtained as

$$\begin{aligned} \frac{M}{M_0} = \coth(y) - \frac{1}{y} = \frac{1}{y} + \frac{y}{3} + ... - \frac{1}{y} = \frac{y}{3} \\ M = M_0\frac{y}{3} = \frac{n\mu_{eff}^2 H}{3k_BT} \end{aligned} \tag{1.31}$$

Then the Classical Langevin magnetic susceptibility is obtained as

$$\chi = \frac{\partial M}{\partial H} = \frac{n\mu_{eff}^2}{3k_BT} \tag{1.32}$$

1.2.6 Van Vleck paramagnetism

In the low temperature regime, certain magnetic ions can have zero effective moment thereby attaining the ground state with $< J >= 0$ [16]. This zero effective moment condition is found to be achieved in one electron less than half filled orbital ions such as Eu^{3+} and Sm^{2+} ions [16, 14]. A similar situation of zero effective J value ground state can occur in crystal field selected singlet ground state such as Pr ion in $PrOs_4Sb_{12}$ [23]. Then the Curie susceptibility effectively becomes zero since $\chi_{Curie} \propto J(J+1)$ below the characteristic temperature $T_{<J>=0}$. If the energy gap between singlet ground state and first excited state is very small such that $k_BT << \Delta = k_BT_{<J>=0}$ then the second order perturbation corrected susceptibility term becomes important which is related with electronic excitation between ground state and first excited state among the multiplets $< J \pm 1 > \neq 0$. The magnetic field induced excited state susceptibility which becomes temperature independent at low temperature regime is known as Van Vleck paramagnetism [14]. The actual energy scale for the Van Vleck paramagnetism is of the order of 1000 cm^{-1} (~ 0.124 eV) in Eu^{+3} excited states in $Cs_5Eu(N_3)_8$ compound [24].

A quick derivation of the second order perturbation susceptibility can be obtained from the from the second order correction in the Zeeman energy as developed in equation 1.9 as

$$< n|\Delta\hat{H}^{(2)}|n >= \sum_{n' \neq n} \frac{| < n|\mu_B(\mathbf{L} + g\mathbf{S}) \cdot \mathbf{H}|n' > |^2}{E_n - E_{n'}} \tag{1.33}$$

Evaluating this contribution using diagonalized states $|JLSJ_z >$ we get

$$< JLSJ_z|\Delta\hat{H}^{(2)}|J'LSJ_z >= \sum_{J' \neq J} \frac{| < JLSJ_z|\mu_B(\mathbf{L} + g\mathbf{S}) \cdot \mathbf{H}|J'LSJ_z > |^2}{E_J - E_{J'}} \tag{1.34}$$

Using the dipole selection rules $J' = J \pm 1$ among the matrix elements of field splitted multiplets, equation 1.34 takes the form

$$\Delta E^{(2)} = \mu_B^2 [\frac{|< JLSJ_z|(\mathbf{L}+g\mathbf{S})\cdot\mathbf{H}|J+1, LSJ_z>|^2}{E_J - E_{J+1}} + \frac{|< JLSJ_z|(\mathbf{L}+g\mathbf{S})\cdot\mathbf{H}|J-1, LSJ_z>|^2}{E_J - E_{J-1}}] \tag{1.35}$$

Then the susceptibility takes the form ($E_J < E_{(J\pm1)}$)

$$\chi = -\frac{N}{V}\frac{\partial^2 \Delta E^{(2)}}{\partial H^2} = \frac{N}{V}\mu_B^2 [\frac{|< JLSJ_z|(L_z+gS_z)|J+1, LSJ_z>|^2}{E_J - E_{J+1}} + \frac{|< JLSJ_z|(L_z+gS_z)|J-1, LSJ_z>|^2}{E_J - E_{J-1}}] \tag{1.36}$$

In a simplified form, above susceptibility can be expressed as

$$\chi \propto \frac{N\mu_B^2}{V\Delta} \tag{1.37}$$

Δ being the energy gap between singlet ground state and the first excited state such that $k_BT << \Delta$ even at very low temperature. As soon as the temperature becomes very low, the effective moment of the ground state vanishes and Curie susceptibility term vanishes then Van Vleck term becomes significant. In some of the Eu compounds, the Van Vleck susceptibility is predominantly flat up to 150 - 200 K [25]. As soon as the temperature is increased, the condition of zero effective moment is not valid, then Curie susceptibility becomes relevant [16]. The Van Vleck susceptibility could be an order of magnitude larger than Curie susceptibility such as in SmB_6 [19]. The Van Vleck susceptibility is also influenced by crystalline anisotropy as in Eu_2CuO_4 [26]. Moreover, Van vleck paramagnetism could occur along the hard axis of antiferromagnetic compound such as $KTb(WO_4)_2$ also known as Ising antiferromagnet [27].

1.2.7 Exchange interaction

Exchange interaction among the magnetic ions is the physical origin of spin ordered magnetic system such as ferromagnetism and antiferromagnetism [15, 12, 19]. Physically, the exchange

integral is the difference in electrostatic energy between triplet and singlet spin states of electrons between neighbouring sites. This difference is expressed as the exchange Hamiltonian. For a magnetic system it is expressed as:

$$\hat{H}_{exchange} = -\sum_{ij} J_{ij} \overrightarrow{S}_i \cdot \overrightarrow{S}_j \tag{1.38}$$

where $J_{ij} = \frac{\epsilon_s - \epsilon_T}{2}$ is called exchange integral and ϵ_s and ϵ_T are defined as follow [19]:

$$\begin{aligned} \epsilon_s &= \int \Psi_s^\star \hat{H} \Psi_s dr_1 dr_2 \\ \epsilon_T &= \int \Psi_T^\star \hat{H} \Psi_T dr_1 dr_2 \end{aligned} \tag{1.39}$$

Here Ψ_s and Ψ_T are singlet and triplet wave functions and H is the Hamiltonian of the magnetic system.

For J>0 the exchange interaction results in ferromagnetism and for J<0 it favours an antiferromagnetic arrangement. There are various types of exchange interactions that lead to a different types of magnetism.

(i) Direct exchange: In this scheme, an electron in an ion interacts with its surrounding via its own electronic wave function overlap. Generally, the direct overlap of wave function produces either the bonding (symmetric exchange) or anti-bonding (antisymmetric exchange) states [12, 11].

(ii) Indirect exchange in ionic solids : If the interactions among the magnetic ions is mediated via some nonmagnetic bridge ion, the exchange interaction is called indirect or superexchange. Indirect exchange occurs in insulators such as oxides and ionic solids [12, 11]. Magnetic interaction in an antiferromagnetic compound MnO with an internal bond structure Mn-O-Mn is an example [28].

(iii) Ruderman Kittel Kasuya Yosida (RKKY) interaction: The indirect exchange between magnetic ions in a metal via conduction electrons is called the RKKY interaction [12]. Such interaction occurs between localized inner shells (e.g., $4f$ orbit) magnetic moments mediated via conduction electrons [11]. The RKKY interaction is named after the scientists M. A. Ruderman, C. Kittel, T. Kasuya, and K. Yosida [29, 30, 31]. The interaction of a localized spin $\overrightarrow{S}_\alpha$ located at r = 0 interacts with other localized spin $\overrightarrow{S}_\beta$ at r via electron gas polarization. The RKKY interaction Hamiltonian is

$$H_{RKKY} \propto -\frac{J}{g^2\mu_B^2}\chi(r)\overrightarrow{S}_\alpha \cdot \overrightarrow{S}_\beta \tag{1.40}$$

The real space electron gas susceptibility $\chi(r)$ is calculated, assuming the delta like localized moment produces oscillating magnetization of all possible momenta in the conduction electron gas [12], as

$$\begin{aligned}\chi(r) &= \frac{1}{(2\pi)^3}\int d^3q\ \chi_q\ \exp(\text{iq.r}) \\ &= \frac{2k_F\chi_p}{\pi}F(2k_Fr)\end{aligned} \tag{1.41}$$

Here χ_q is the momentum space susceptibility of a paramagnetic electron gas [12] given as

$$\chi_q = \frac{\chi_p}{2}(1+\frac{4k_F^2-q^2}{4k_Fq}log|\frac{q+2k_F}{q-2k_F}|) \tag{1.42}$$

and

$$F(2k_Fr) = \frac{-2k_Fr\ \cos(2k_Fr)+\sin(2k_Fr)}{(2k_Fr)^4} \tag{1.43}$$

is an oscillatory function of the Fermi wave vector (k_F) and the distance between localized moments. The nature of the RKKY magnetism is an example of a conduction electron mediated, superexchange mechanism [32] and oscillates between ferromagnetism and antiferromagnetism with the range of interactions between two spins. An analogous oscillatory magnetic nature is observed in thin, multi-layered, giant magnetoresistance devices [33].

1.2.8 Mean field theory: Molecular field theory for interacting magnetic ions

In single domain ferromagnets and ferrimagnets, there exist a nonzero magnetization even at zero applied field. Such a nonzero magnetization in the absence of an applied magnetic field is called spontaneous magnetization [15]. Weiss introduced the concept of average (or mean) molecular magnetic field $\overrightarrow{H}_{mf} = \lambda\overrightarrow{M}$ acting on a particular spin due to all other spins in a ferromagnetic system to explain the observed spontaneous magnetization and the phase transition phenomena. Here λ is the molecular field parameter and M is the spontaneous magnetization. Theoretically,

the magnitude of molecular field can range up to 10^3 T in a ferromagnetic material [15]. Later Werner Heisenberg explained the necessity of larger molecular field $\lambda\overrightarrow{M}$ in ferromagnetic materials which is related to quantum mechanical exchange interaction. The physical origin of the exchange interaction among spins is the result of electronic wave functions overlap between ions, orbital hybridization and electrostatic repulsion between electrons.

The microscopic origin of the exchange constant λ could be understood simply by following the modification of Hamiltonian that contains exchange interaction and Zeeman energy terms. The Hamiltonian for exchange interaction, $\mathrm{J^{ex}}_{ij}$ being exchange integral and $\overrightarrow{J}_i$, $\overrightarrow{J}_j$ being spins at respective sites, is given as [12]

$$\begin{aligned}
\hat{H} &= -\sum_{ij} \mathrm{J}^{\mathrm{ex}}_{\mathrm{ij}} \overrightarrow{J}_i \cdot \overrightarrow{J}_j + g\mu_B \sum_j J_j \cdot \overrightarrow{H} \\
\hat{H} &= g\mu_B \sum_j \overrightarrow{J}_j \cdot (-\frac{1}{g\mu_B} \sum_i \mathrm{J}^{\mathrm{ex}}_{\mathrm{ij}} \overrightarrow{J}_i + \overrightarrow{H}) \\
\hat{H} &= g\mu_B \sum_j \overrightarrow{J}_j \cdot (\overrightarrow{H} + \overrightarrow{H}_{mf})
\end{aligned} \tag{1.44}$$

Here $\overrightarrow{H}_{mf} = -\frac{1}{g\mu_B} \sum_i \mathrm{J}^{\mathrm{ex}}_{\mathrm{ij}} \overrightarrow{J}_i$ is the Weiss mean field introduced to account the overall interaction of all other spins effect on a single spin. By doing so, he was able to treat the ferromagnetic interaction in a similar manner to paramagnetic spins placed in an enhanced external field $\overrightarrow{H}_{ext} = \overrightarrow{H} + \overrightarrow{H}_{mf}$.

The molecular field $\overrightarrow{H}_{mf}$ is an operator which has an influence on a particular spin on the basis of the detail configuration of all other spins. In a ferromagnet, every spin J_i has the same average moment which can be expressed in terms of magnetization density as

$$\begin{aligned}
\overrightarrow{M} &= -\frac{N}{V} g < \overrightarrow{J}_i > \mu_B \\
< \overrightarrow{J}_i > &= -\frac{V}{N} \frac{\overrightarrow{M}}{g\mu_B}
\end{aligned} \tag{1.45}$$

where M is magnetization (see equation 1.16 how base temperature magnetization is obtained) of a material with N ions within a volume V, g being Landé-g factor and μ_B is Bohr magneton [14] .

After factoring out the average value of $\overrightarrow{J}_i$, the average magnitude of the molecular field takes the form

$$\overrightarrow{H}_{mf} = - < J_i > \frac{1}{g\mu_B}\sum_i \mathrm{J_{ij}^{ex}} = (\frac{V}{N}\frac{\overrightarrow{M}}{g\mu_B})[\frac{1}{g\mu_B}\sum_i \mathrm{J_{ij}^{ex}}]$$
$$\overrightarrow{H}_{mf} = (\frac{V}{N}\frac{\overrightarrow{M}}{(g\mu_B)^2})[\sum_i \mathrm{J_{ij}^{ex}}] = \lambda\overrightarrow{M} \tag{1.46}$$

where $\lambda = \frac{V}{N}\frac{\mathrm{J_j^{ex}}}{(g\mu_B)^2}$ and $\mathrm{J_j^{ex}} = \sum_\mathrm{i} \mathrm{J_{ij}^{ex}}$.

Here λ is the mean field parameter which expresses the Weiss molecular field in terms of magnetization density [14, 15]. For a quick estimation, taking $\mathrm{J_j^{ex}} \approx 10$ mRy (taken of the order of α-Fe Heisenberg exchange integral value [34]), $\lambda = \frac{\mathrm{J_j^{ex}}}{n(g\mu_B)^2} \approx \frac{10\times10^{-3}\times13.6\times1.6\times10^{-12}}{10^{22}\times(2\times9.27\times10^{-21})^2} \approx 0.063\times10^6\ \frac{\mathrm{G}^2cm^3}{erg}$.

Again following the same steps for paramagnetic case, the total magnetization of N ions in volume V as in equation 1.16 takes the form

$$M = \frac{N}{V}gJ\mu_B B_J(y)$$
$$M = M_0 B_J(y) \tag{1.47}$$

where the modified y due to additional exchange field is given as

$$y = gJ\mu_B\frac{(H+\lambda M)}{k_B T} \tag{1.48}$$

As in equation 1.24, using the high temperature ($T > T_C$) and low field limit of the Brillouin function, we get

$$M = M_0\frac{(J+1)}{3J}gJ\mu_B\frac{(H+\lambda M)}{k_B T} = \frac{N}{V}\frac{g^2\mu_B^2 J(J+1)}{3k_B}\frac{(H+\lambda M)}{T} \tag{1.49}$$

In a simplified form, above relation can be expressed as

$$M = \frac{C}{T}(H+\lambda M)$$
$$M(T-\lambda C) = CH$$
$$\chi = \frac{\partial M}{\partial H} = \frac{C}{T-T_C} \tag{1.50}$$

This relation is called Curie-Weiss susceptibility for ferromagnetic materials where Curie temperature T_C is related to Curie constant C and mean field parameter λ as

$$T_C = \lambda C \tag{1.51}$$

A numerical estimate of exchange parameter λ from the Curie temperature is $\lambda = \frac{T_C}{C} = \frac{3k_B T_C}{ng^2\mu_B^2 J(J+1)} = 0.048 \times 10^6 \ \frac{G^2 cm^3}{egr}$ for $T_C = 300$ K and $J = \frac{1}{2}$ which agrees very well with microscopic estimation of λ using the exchange integral constant around 10 mRy unit as derived in equation 1.46.

In some cases at higher temperature, the temperature independent susceptibility χ_0 (e.g., Pauli paramagnetic, Landau or core diamagnetic terms) can be significant. Then the experimental susceptibility is expressed as

$$\chi = \chi_0 + \frac{C}{T - T_C} \tag{1.52}$$

In a ferrimagnetic compound, magnetic moments of two types of magnetic sub-lattices oppose each-other. Following the similar treatment for a ferromagnetic order for each sublattice, the ferrimagnetic susceptibility relation takes a form

$$\chi = \chi_0 + \frac{(C_A + C_B)T - 2\mu C_A C_B}{T^2 - T_C^2} \tag{1.53}$$

Where Curie temperature is related to mean-field parameter μ as $T_C = \mu(C_A C_B)^{\frac{1}{2}}$, C_A and C_B being the Curie constant for sub-lattices A and B respectively [15].

If opposing sublattices are identical i.e., $C_A = C_B$, the Curie-Weiss relation for an antiferromagnetic system becomes

$$\chi = \chi_0 + \frac{2C}{T + T_N} \tag{1.54}$$

where $T_N = \lambda C$.

The inverse magnetic susceptibilities from equations 1.52 and 1.54 can be written as

$$\begin{aligned} \frac{1}{\chi - \chi_0} &= \frac{T \pm \theta}{C} \\ \frac{1}{\chi - \chi_0} &= \frac{\pm\theta}{C} + \frac{T}{C} \end{aligned} \tag{1.55}$$

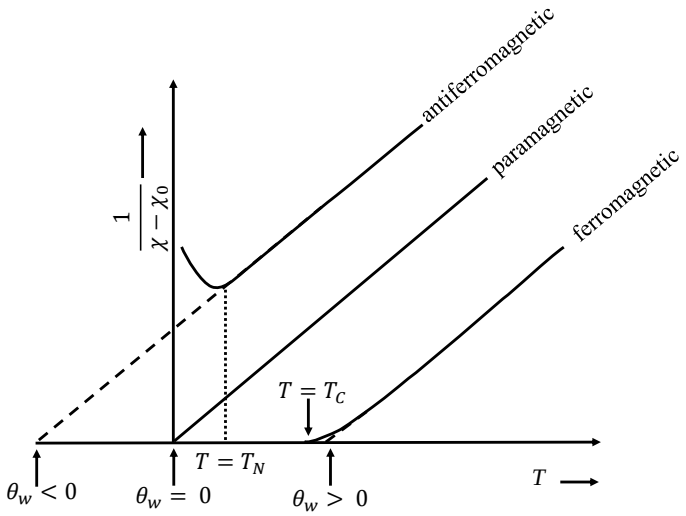

Figure 1.9 Curie Weiss plot for magnetic materials. The temperature corresponding to the end point of the straight line data segment provide approximate Curie T_C and Néel T_N temperatures and corresponding X-intercepts provide corresponding Weiss temperatures. The Weiss temperature is positive for a ferromagnet and negative for an antiferromagnetic material.

where $\theta = T_C = C\lambda$ for a ferromagnetic material and $-\theta = T_N = -C\lambda$ for an antiferromagnetic material. This relation in equation 1.55 is valid for ferrimagnetic as well as multiple sites magnetic formula units ferromagnetic and antiferromagnetic materials. The schematic Curie-Weiss plot for magnetic materials is shown in Fig. 1.9. The Curie-Weiss plot exhibits a positive Y-intercept for antiferromagnetic materials whereas it is negative for ferromagnetic materials. For a Curie-paramagnetic material, it passes through the origin. The X-intercept of the inverse Curie-Weiss plot provides a rough estimate of Curie temperature for a ferromagnetic material. The temperature corresponding to the lower end of the linear section of the antiferromagnetic Curie-Weiss plot provides a rough estimate for the Néel temperature. The slope of the Curie-Weiss plot provides the effective moment of magnetic ion given as

$$\text{slope} = \frac{1}{\text{C}} \tag{1.56}$$

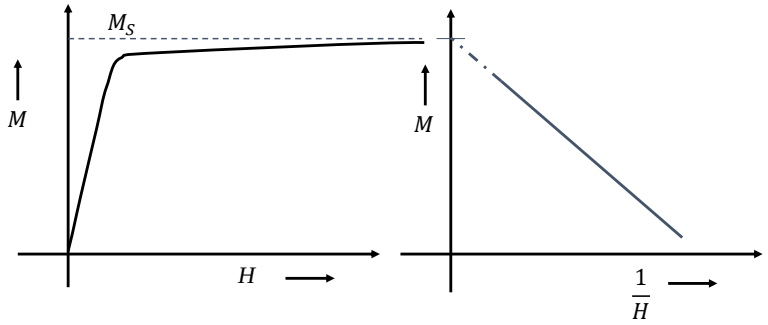

Figure 1.10 Method of obtaining the saturation magnetization (ordered moment) of a ferromagnetic material. Since the laboratory fields can not achieve the perfect saturation (asymptotic magnetization) at a finite field as shown in left panel, the Y-intercept of M vs $\frac{1}{H}$ plot provides the saturation magnetization [35].

For convenience, the molar Curie constant as expressed in equation 1.27 could be expressed to slope of the Curie-Weiss plot as following

$$C_{molar} = \frac{N_A g^2 \mu_B^2 J(J+1)}{3k_B} = \frac{N_A(\mu_{eff}\mu_B)^2}{3k_B}$$

$$\text{Or, } \mu_{\text{eff}} = \sqrt{\frac{3\text{k}_\text{B}\, C_{\text{mol}}}{\text{N}_\text{A}\mu_\text{B}^2}} = \sqrt{\frac{3 * 1.38 * 10^{-16}\ \text{erg/K}\ C_{\text{mol}}}{6.023 * 10^{23}\ \text{mol}^{-1} * (9.27 * 10^{-21}\ \text{erg/G})^2}} \approx \sqrt{8\text{C}_{\text{mol}}}$$

$$\text{Or, } \mu_{\text{eff}} = \sqrt{\frac{8}{\text{slope}}} \tag{1.57}$$

For a ferromagnetic sample, the saturated moment (moment related with low temperature saturation magnetization) could be estimated with the Y-intercept of the linear fit of M vs $\frac{1}{H}$ as shown in Fig. 1.10. Theoretically, H should be sufficiently large to achieve the perfect saturation magnetization which was not possible in our laboratory setting. As $H \to \infty$, $\frac{1}{H} \to 0$ and M attains the saturation magnetization M_S [35].

When the effective moment μ_{eff} and low temperature ordered moment $M_{Saturated}$ are obtained for a magnetic ion, one can determine whether the magnetism is local moment or an itinerant type.

Mathematically, the local or itinerant nature of a magnetic material is measured in terms of the Rhode-Wohlfarth ratio ($RWR = \frac{M_C}{M_{sat}}$). Here $M_C = gJ$ (high temperature case) and $M_{sat} = gJ$ (low temperature case) are the total angular momenta associated with low temperature saturated moment and Curie-Weiss susceptibility respectively [36]). In other word, the RWR is the ratio of the total angular momentum J value derived from the the Curie-Weiss constant to the J value associated with the base temperature ordered moment. Here, low temperature ordered moment is associated with angular momentum $M_{sat} = gJ$ at low temperature as: $M_{\text{Saturated}} = -\frac{N}{V}gJ\mu_B = -\frac{N}{V}M_{\text{sat}}\mu_B$ [36]. The high temperature Curie susceptibility angular momentum $M_C = gJ$ are related to Curie constant as: $C = \frac{N}{V}\frac{\mu_{eff}^2}{3k_B} = \frac{N}{V}\frac{\mu_B^2 g^2 J(J+1)}{3k_B} = \frac{N}{V}\frac{\mu_B^2 gJ(gJ+g)}{3k_B} = \frac{N}{V}\frac{\mu_B^2 M_c(M_c+2)}{3k_B}$ setting $g = 2$ [36]. A compound is considered local moment system if $RWR \approx 1$ and itinerant for RWR>1. The magnetic moment of a local moment ion nearly agrees with Hund's rule estimation ($\mu = -gJ\mu_B$) whereas the itinerant system moment per ion is much smaller than provided by Hund's rules provided that there is no orbital quenching due to crystal electric field.

Curie temperature determination: The Curie temperature of a ferromagnetic system is the temperature at which the spin ordered state transforms into a spin disordered paramagnetic state. This happens when the thermal energy per electron k_BT becomes larger than the exchange interaction between electrons in neighbouring sites i.e., $k_BT > J$. Various methods of obtaining the Curie temperature of the ferromagnetic samples are discussed in various references [37, 38, 39, 40, 41, 42, 43]. Although a quick method of accessing experimental value of Curie temperature from the low-field magnetization data is to take the temperature of the minimum in the temperature derivative $\frac{dM}{dT}$, the phase transition anomaly is often broadened and reliable Curie temperature becomes difficult to access. The Arrott plot method is a convenient technique which provides reliable Curie temperature from the magnetization data.

To derive the Arrott plot equation, Once again, it is convenient to start from the magnetization derived from the molecular field theory (see equations 1.16, 1.47 and 1.48),

$$M = N_A g J \mu_B B_J(\frac{gJ\mu_B(H+\lambda M)}{k_B T})$$
$$M = M_0[\frac{2J+1}{2J}\coth(\frac{2\mathrm{J}+1}{2\mathrm{J}}\mathrm{y}) - \frac{1}{2J}\coth(\frac{\mathrm{y}}{2\mathrm{J}})] \tag{1.58}$$

Where $M_0 = N_A g J \mu_B$. Now, expanding Brillouin function in the small limit of its argument $y = \frac{gJ\mu_B(H+\lambda M)}{k_B T} << 1$ which can be achieved in a low field and high temperature $T \simeq T_C$ condition [44, 45]. A little bit more clarification of validity of the $y << 1$ can be understood as

$$y = \frac{gJ\mu_B(H+\lambda M)}{k_B T} = \frac{gJ\mu_B(H+\frac{T_C}{C}M)}{k_B T}$$
$$y = \frac{gJ\mu_B H}{k_B T} + \frac{3J}{J+1}\frac{T_C}{T}\frac{M}{M_0} \tag{1.59}$$

The first term of equation 1.59 is valid in $H << T$ since $H \approx 1.5$ K per tesla. I have discussed about its magnitude for $J = 1$ in paramagnetic case in equation 1.24. The second term is always $<< 1$ since $M << M_0$ around $T = T_C$ as described in Arrott's original paper [42].

$$M = M_0[\frac{J+1}{3J}y - \frac{[(J+1)^2+J^2](J+1)}{90J^3}y^3 + ...]$$
$$M = Ay - By^3 + ... \tag{1.60}$$

where $A = M_0\frac{J+1}{3J}$ and $B = M_0\frac{[(J+1)^2+J^2](J+1)}{90J^2}$ [44]

Solving for magnetization at $T = T_C$ for small applied field H [46] one can get,

$$M(T = T_C) = M_0(J+1)[\frac{10}{9(1+2J+2J^2)}]^{\frac{1}{3}}H^{\frac{1}{3}} \tag{1.61}$$

This result provides an information that at $T = T_C$, the first term in equation 1.59 i.e., $\frac{gJ\mu_B H}{k_B T_C} = 10^{-4}\frac{JH}{T_C} << 3J[\frac{10}{9(1+2J+2J^2)}]^{\frac{1}{3}}H^{\frac{1}{3}}$ since $T_C >> H \sim 1.5$ K for per tesla. So, in the cubic and higher powers of the expansion, $y = \frac{gJ\mu_B(H+\lambda M)}{k_B T} \approx \frac{gJ\mu_B\lambda M}{k_B T}$ can be used for small applied field and high temperature $T \approx T_C$ [44].

$$M = A(\frac{gJ\mu_B(H+\lambda M)}{k_B T}) - B(\frac{gJ\mu_B\lambda M}{k_B T})^3 \tag{1.62}$$

$$H = (\frac{k_B T}{A g J \mu_B} - \lambda)M + B(\frac{g J \mu_B \lambda M}{k_B T})^3 \tag{1.63}$$

Substituting $A = M_0 \frac{J+1}{3}$ and $\lambda = \frac{T_C}{C}$ (see equation 1.51) above equation takes the form

$$H = (\frac{3 k_B T}{N_A g^2 \mu_B^2 J(J+1)} - \frac{T_C}{C})M + B(\frac{g J \mu_B \lambda M}{k_B T})^3 \tag{1.64}$$

Again, using the coefficient of the temperature T on the first term of right hand side of the equation 1.64 is the Curie constant $C = \frac{N_A g^2 \mu_B^2 J(J+1)}{3 k_B}$ (see equation 1.27), equation 1.64 takes the form

$$H = (\frac{T}{C} - \frac{T_C}{C})M + [B(\frac{g J \mu_B \lambda}{k_B T})^3]M^3 \tag{1.65}$$

By substituting $a_0 = \frac{1}{C}$ and $b = [B(\frac{g J \mu_B \lambda}{k_B T})^3]$ (The temperature term is not absorbed in coefficient a_0 to indicate the first term vanishes at $T = T_C$ and temperature is absorbed in the coefficient b so that Arrott plots are valid only for constant temperature also known as isotherms)

$$H = a_0(T - T_C)M + bM^3 \tag{1.66}$$

Dividing both sides by bM, the equation takes the form,

$$\frac{H}{bM} = \frac{a_0}{bM}(T - T_C)M + M^2 \tag{1.67}$$

On further manipulating an Arrott plot from the mean field theory can be achieved as

$$M^2 = a(T - T_C) + a_1 \frac{H}{M} \tag{1.68}$$

where $a = -\frac{a_0}{b}$ and $a_1 = \frac{1}{b}$. Here both a and a_1 are temperature dependent coefficients. Hence Arrott plots are plotted for known temperatures i.e. isotherms.

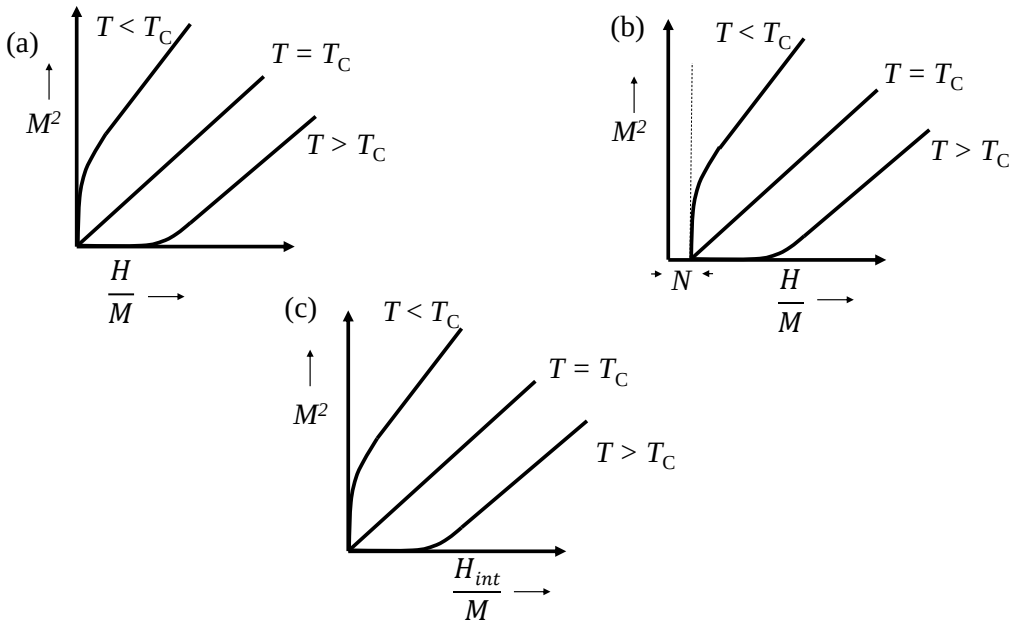

Figure 1.11 (a) Arrott Plots in ideal mean field approach (b) Shifted Arrott plots due to demagnetization factor. (c) Arrott plots after demagnetization correction with average internal field as $H_{\text{int}} = H_{\text{applied}} - NM$ [45, 12, 44]. The calculation of internal field is possible only for regular geometry samples such as cuboids and spheroids.

The Arrott isotherms are generally a straight lines at sufficiently high field and curve at low field as shown in Fig. 1.11(a). This curvy nature at low field is because of the nature of first term in equation 1.68 $a(T-T_C)$ which vanishes at T_C and changes sign above and below it. At the Curie temperature $T = T_C$, the Arrott plot becomes a straight line through origin since the first term of the equation vanishes. If the system does not strictly follow the mean field theory, the Arrott plot at $T = T_C$ might not be a perfectly straight line (see example of Fe_5B_2P [47]).

In an experimental case, the Arrott plots shift a little bit away from the origin due to demagnetization factor of the sample under measurement as shown in Fig. 1.11(b). After the demagnetization factor is corrected with internal field (H_{int}), the Arrott plot is shifted back to the origin as shown in Fig. 1.11(c). The details of the internal field determination is discussed in Chapter 2.1.4. In an Arrott plot, the x-intercept in $\frac{H}{M}$ axis is a beneficial method for a direct determination of the demagnetization factor N for an applied field along the easy axis of magnetization [47]. The basic ideas required for this approach are mentioned in reference [42]. In the mean field approximation, the Arrott isotherms are straight lines and the isotherm corresponding to the Curie temperature passes through the origin. After accounting the effect of the demagnetization factor, Arrott plot is one of the better methods to determine the Curie temperature of a ferromagnetic system which undergoes a second order phase transition, especially if T_C is large and the specific heat feature is small.

1.2.9 Spin wave theory

Spin wave theory explains the temperature variation of magnetization at low temperature. According to spin wave theory, thermal fluctuations are the excitations of the magnetic ground state. A simplest case of excitation could be a single spin flip in a ferromagnetic ground state. However, discrete spin flip costs more energy than a cooperative spin reversal. For the sake of energy minimization, the spin flip is collectively shared along a whole spin assembly in form of spin waves [15]. A typical spin wave formed by collective excitaions of ferromagnetically alligned spins is shown in Fig. 1.12 taken from [48]. Spin waves quanta are called magnons and follow the

Bose-Einstein statistics. Using the three dimensional spin wave model in a ferromagnet, Bloch predicted the low temperature variation of magnetization as [49]

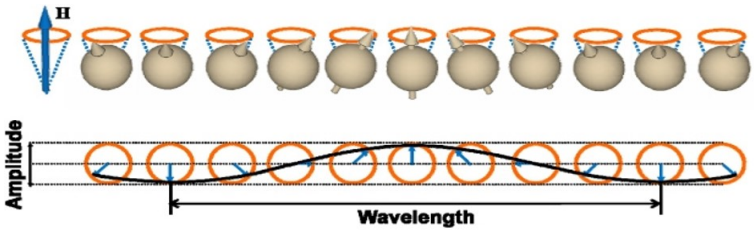

Figure 1.12 A schematic diagram of spin excitations wave showing characteristics wavelength and amplitude taken with permission from [48]. The energy of spin excitation wave is quantized and the energy quanta are called magnons.

$$M(T) = M(0)[1 - (\frac{T}{T_C})^{\frac{3}{2}}] \tag{1.69}$$

where $M(0)$ is the 0 K spontaneous magnetization, and T_C is the Curie temperature of the material. Bloch equation agrees fairly well with the experimentally measured, low temperature magnetization for most of the 3D-ferromagnetic systems.

Although Bloch law is generally developed for a low temperature region, it can be used to estimate the an approximate Curie temperature of a ferromagnetic system whose magnetization gets smeared due to sample degradation or structural phase transition near the high Curie temperature. In this thesis, Bloch law was applied to get an approximate Curie temperature in case of $Ce_{14.3}Ta_{1.0}Co_{62.0}Fe_{12.3}Cu_{10.4}$ sample which tend to thermally degrade around 800 K.

1.2.10 Pauli Paramagnetism

In a metal, valence electrons are delocalized throughout the bulk size of material volume V. These electrons can be treated as an independent electrons gas with statistical mixture of spins $\pm\frac{1}{2}$ which could be represented by a density of states as shown in Fig. 1.13(a). When an external field is applied, the statistical mixture polarizes into spin up and spin down bands as shown in Fig. 1.13(b) [20]. After the sufficient interaction time between spins and field, the spin polarization

equlibriates as shown in Fig. 1.13(c) [11]. The net magnetization density due to an electron is either -μ_B/V or μ_B/V depending up on parallel or anti-parallel to applied field H. Hence net magnetization density is

$$M = -\mu_B(n_\uparrow - n_\downarrow) \tag{1.70}$$

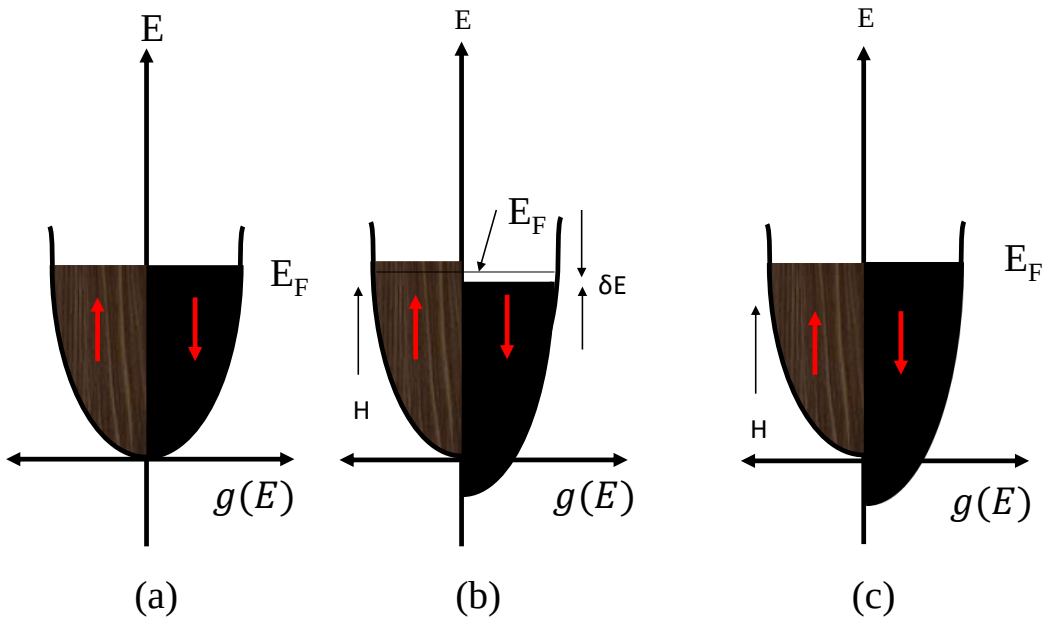

Figure 1.13 (a) Equilibrium band structure of metal (b) Non-equilibrium spin band splitting of metal in an applied field (c) Equilibrium spin band splitting of metal in an applied field.

where $n_\uparrow$ is the density of electrons with spin moment parallel to field H and vice versa [12]. In terms of density of states in Fermi surface $g(E_F)$, the density of polarized electrons can be estimated

using Fermi Dirac statistics as

$$n_\uparrow = \frac{1}{2}\int_0^\infty g(E+\mu_B H)f(E)dE$$
$$n_\downarrow = \frac{1}{2}\int_0^\infty g(E-\mu_B H)f(E)dE \tag{1.71}$$

where $f(E)$ is Fermi Dirac distribution given as

$$f(E) = \frac{1}{exp\frac{(E-\mu)}{k_B T}+1} \tag{1.72}$$

The density of states can be expanded around the non-magnetic Energy E as $g(E \pm \mu_B H) = g(E) \pm \mu_B H \frac{dg(E)}{dE}$ (since $\mu_B H \approx 1.5$ K is a very small energy) and the magnetization density in equation 1.70 takes the form

$$M == -\mu_B(n_\uparrow - n_\downarrow) = \mu_B^2 H \int_0^\infty (-\frac{dg(E)}{dE})f(E)dE \tag{1.73}$$

Using integration by parts and the relation for the derivative of the Fermi function with respect to energy as $\frac{df(E)}{dE} = \delta(E-E_F)$ [12] the magnetization takes the form

$$M = \mu_B^2 H \int_0^\infty \delta(E-E_F)g(E)dE = \mu_B^2 g(E_F)H \tag{1.74}$$

which produces temperature independent susceptibility

$$\chi = \frac{\partial M}{\partial H} = \mu_B^2 g(E_F) \tag{1.75}$$

1.2.11 Stoner model

As derived in the previous section, the alkali and alkaline earth metals are exhibit Pauli paramagnetism since they have broad s-bands. However, transition metals like Fe, Co, and Ni are ferromagnetic at room temperature due to their narrow $3d$ bands which generate high electrostatic repulsion among electrons to generate necessary condition for spontaneous electronic spins band splitting [11]. This metallic ferromagnetism could be understood from the capability of certain

metals to meet the Stoner criterion $Ug(E_F) \geq 1$, where U is coulomb repulsion among electrons and $g(E_F)$ is the density of states at the Fermi level. Physically, Stoner's criterion means the condition of spontaneous splitting of electronic spins bands so that spontaneous magnetization develops in metals.

A schematic condition for ferromagnetism in $3d$ transition metals is shown in Fig. 1.14. If the Fermi level is crossing both spin up and down $3d$ bands such as in Fe, weak ferromagnetism condition is achieved whereas strong band ferromagnetism is achieved if the Fermi level crosses only minority spin bands such as in Co and Ni [11]. The magnetization of Fe is stronger than Co and Ni because of its larger moment. The derivation of Stoner criterion is adopted from reference [19].

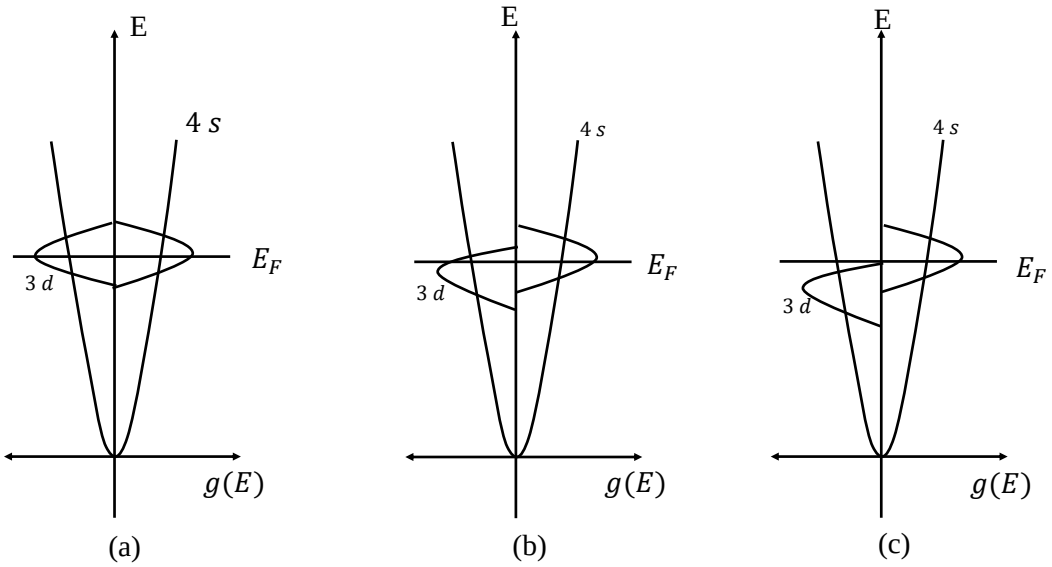

Figure 1.14 Fermi level in (a) a hypothetical transition metal before exchange splitting (b) condition of a weak itinerant ferromagnetism where both majority and minority spin bands are intersected by the Fermi level and (c) condition of a strong itinerant ferromagnetism where only minority $3d$-band is intersected by Fermi level [11]

In the second quantization theory, itinerant electron system in an external field B could be expressed as

$$H = \sum_{k\sigma} \epsilon_k \hat{n_{k\sigma}} + U \sum_j \hat{n_{j\uparrow}} \hat{n_{j\downarrow}} - \frac{g\mu_B H}{2} \sum_j (\hat{n}_{j\uparrow} - \hat{n}_{j\downarrow}) \tag{1.76}$$

The last term in equation 1.76 accounts for the polarization of spin in an external magnetic field H. Here $\hat{n}_{j\uparrow}$ and $\hat{n}_{j\downarrow}$ are the number of up and down polarized states out of total available states n. If m is the average spin polarization, then the splitted spin densities are given as

$$\begin{aligned} < \hat{n}_{j\uparrow} > &= \frac{n}{2} + m \\ < \hat{n}_{j\downarrow} > &= \frac{n}{2} - m \end{aligned} \tag{1.77}$$

Then the total energy density of the system is given as

$$E(m) = \int_0^{\epsilon_F - \delta} \epsilon g(\epsilon) d\epsilon + \int_0^{\epsilon_F + \delta} \epsilon g(\epsilon) d\epsilon + U(\frac{n^2}{2} - m^2) - g\mu_B H m \tag{1.78}$$

where

$$n_\sigma = \int_0^{\epsilon_F \pm \delta} g(\epsilon) d\epsilon = \frac{n}{2} \pm g(\epsilon_F)\delta = \frac{n}{2} \pm m \tag{1.79}$$

with $\sigma = \downarrow$ *or* $\uparrow$ and δ is the shift in energy bands edges from the Fermi level due to exchange splitting. The energy shift due to polarization (as shown in Fig. 1.14) is evaluated as

$$\begin{aligned} \Delta E(m) &= E(m) - E(o) \\ &\approx \int_{-\delta}^{+\delta} \epsilon g(\epsilon) d\epsilon + U(\frac{n^2}{2} - m^2) - g\mu_B H m \\ &= g(\epsilon_F) \int_{-\delta}^{+\delta} \epsilon d\epsilon + U(\frac{n^2}{2} - m^2) - g\mu_B H m \\ &\approx \frac{m^2}{g(\epsilon_F)} - U m^2 - g\mu_B H m \end{aligned} \tag{1.80}$$

Where $\delta = \frac{m}{g(\epsilon_F)}$. For the magnetization density $M = g(\epsilon_F)\mu_B m$ the energy shift takes the form

$$\Delta E(m) = \frac{M^2}{\mu_B^2 g(\epsilon_F)} - U M^2 - g\mu_B H M \tag{1.81}$$

The minimization of the energy shift gives the susceptibility as

$$\chi = \frac{M}{H} = \frac{\mu_0 \mu_B^2 g(\epsilon_F)}{1 - U g(\epsilon_F)} = \frac{\chi_P}{1 - U g(\epsilon_F)} \tag{1.82}$$

where $\chi_P = \mu_0 \mu_B^2 g(\epsilon_F)$ is the Pauli susceptibility and the factor $\frac{1}{(1-Ug(\epsilon_F))}$ is called the Stoner enhancement factor. Here the Stoner enhancement factor $\frac{1}{(1-Ug(\epsilon_F))}$ enhancing magnetic susceptibility which literally could be understood enhancing the exchange integral needed for the ferromagnetic spin alignment. Assume a situation when the denominator of the susceptibility tends to zero such as

$$\begin{aligned} 1 - U g(\epsilon_F) &= 0 \\ U g(\epsilon_F) &= 1 \end{aligned} \tag{1.83}$$

provides a condition of diverging magnetic susceptibility called the Stoner criterion.

1.2.12 Magnetic anisotropy

The magnetic moment of a ferromagnetic system acquires a particular equilibrium direction to minimize the magnetic free energy. This orientation could be easy axis, easy plane or any three dimensional Heisenberg type magnetization. For permanent magnet applications, the anisotropy should be strictly an uniaxial anisotropy. To readily identify the easy magnetization direction, single crystalline samples are needed. The easy direction of magnetization saturates with a minimum magnetizing field. To rotate the direction of spontaneous magnetization away from the preferred direction (axial or planer), extra energy is needed which is called magnetocrystalline anisotropy energy. The maximum energy of rotation of spontaneous magnetization falls at 90° of the preferred direction (either axial or planer) in a uniaxial system. The hard axis makes 90° with the easy axis. There exist several types of magnetic anisotropies such as magnetocrystalline anisotropy, shape anisotropy, stress anisotropy and induced anisotropy. Among these anisotropies, the shape and magnetocrystalline anisotropis are of greater importance for permanent magnet materials. The shape anisotropy originates from the dipolar interactions of the moments and depends on the sample geometry. The magnetocrystalline anisotropy, in general, is the largest in magnitude and originates

from the spin orbit coupling effect. A crystal electric field effect (CEF) favours a particular orbital of the magnetic system and magnetic moment acquires an equilibrium orientation [11]. However in highly anisotropic ferromagnetic materials, CEF anisotropy contribution can be considered only a perturbative correction due to its relatively small contribution in comparison to exchange interaction. If the CEF effect is significant, then a noticeable anisotropy is observed in the paramagnetic state as well as the magnetically ordered state. This effect is distinctly visible in susceptibility of rare-earth based antiferromagnetic compounds such as $TbNi_2Ge_2$ [50, 51].

(i) **Dipole-dipole interaction and shape anisotropy:** A ferromagnetic material could be considered as a crystal lattice of a magnetic dipole moment μ_i situated at site i. The magnetostatic energy of this magnetic lattice structure could be estimated as

$$E_M = -\frac{1}{2}\sum_i \mu_i \cdot h_i = -\frac{1}{2}\oint M \cdot h_i d\tau \tag{1.84}$$

where h_i is the magnetic field at lattice point i due to all other magnetic dipoles [45]. The factor $\frac{1}{2}$ is to account the repetition in counting and the summation is converted to integral for very large number of magnetic dipoles along with volume element $d\tau$. The magnetic field h_i can be estimated using Lorentz construction in which the i^{th} dipole is considered to be situated at the center of a small cavity with inside and outside (surface of the sample) dipoles [52, 45] as

$$h_i = H_{\text{cavity}} + H_L + H_d \tag{1.85}$$

The field H_{cavity} is generated by dipoles inside the cavity. The Lorentz field $H_L = \frac{4\pi}{3}M$ is created by magnetization at the surface of the cavity. The demagnetization field H_d is generated by surface magnetization and is proportional to volume magnetization M as $H_d = -NM$ [45, 12]. Here N is a tensor quantity related to crystalline structure.

Then the magnetostatic energy takes the form

$$E_M = -\frac{1}{2}\oint M \cdot (H_{\text{cavity}} + H_L + H_d) d\tau \tag{1.86}$$

The magnetostatic energy due to $H_{\text{cavity}} + H_L$ terms is called dipolar crystalline anisotropy which is proportional to square of magnetization (i.e., crystalline anisotropy $\propto M^2V$, V being the magnetic volume) and quantatively not important among all magnetic anisotropies [52]. Here the M^2 term is independent of direction which is main concern of anisotropy. The contribution due to H_d term is called shape anisotropy. Finally, the shape anisotropy energy is given as

$$\begin{aligned} E_{\text{shape}} &= -\frac{1}{2}\oint M \cdot H_d d\tau \\ E_{\text{shape}} &= -\frac{1}{2}\oint M \cdot N \cdot M d\tau \end{aligned} \tag{1.87}$$

By accounting the tensor property of the magnetization, the the shape anisotropy is expressed as [52]

$$E_{\text{shape}} = K^2_{\text{shape}} sin^2\theta \tag{1.88}$$

where K^2_{shape} is shape anisotropy energy density and θ is the angle between particular sample facet and direction of magnetization. The quantity K^2_{shape} is very complicated and can be analytically calculated for regular shapes such as spheroids and cuboids. The simplest case is a uniformly magnetized infinite sheet with magnetization direction perpendicular to plate. Using symmetry analysis for the perpendicular magnetization, the demagnetization tensor for takes the form

$$\begin{pmatrix} 0 & 0 & 0 \\ 0 & 0 & 0 \\ 0 & 0 & 1 \end{pmatrix} \tag{1.89}$$

Then shape anisotropy energy density for an infinite plane sheet is $\frac{1}{2}\mu_0 M_S^2$ in SI unit ($2\pi M_S^2$ in CGS unit) [12, 52, 45].

(ii) **Spin orbit interaction and magnetocrystalline anisotropy:** The variation of magnetization of a material with crystallographic orientation is called magnetocrystalline anisotropy property. The cause of large magnetocrystalline anisotropy is spin-orbit interaction [15, 14, 45].

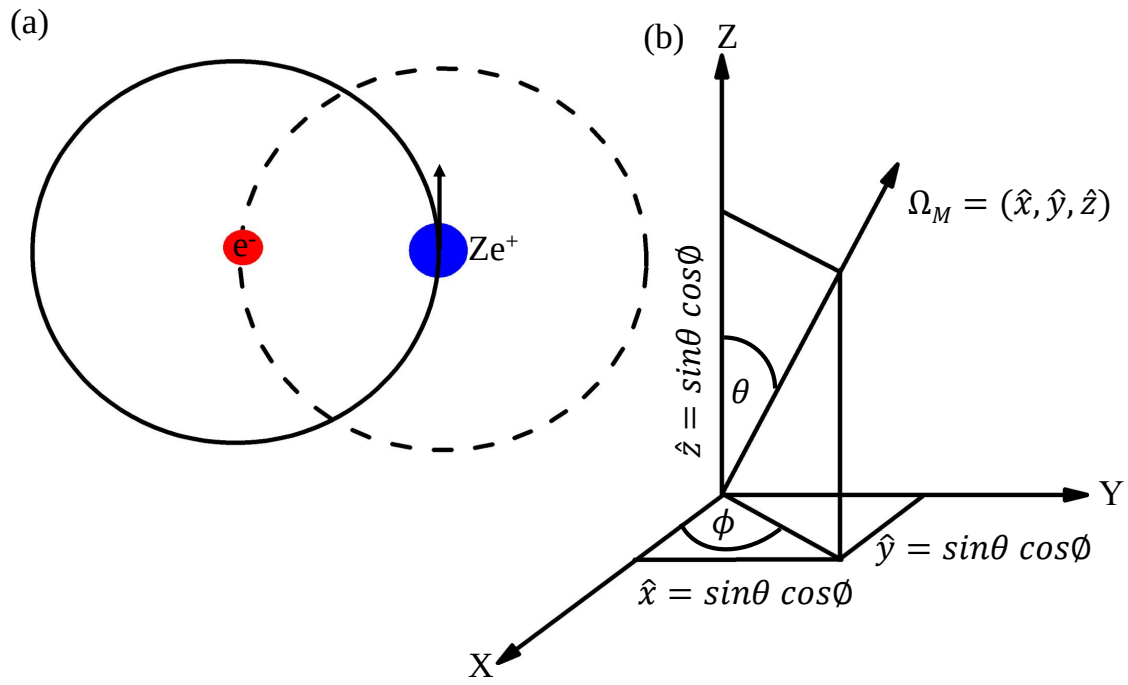

Figure 1.15 (a) Illustration of spin orbit interaction in e^- rest frame of reference. (b) Direction cosines of magnetization with crystallographic principal axes.

The crystalline anisotropy of a material is microscopically related with crystal structure (i.e., crystal electric field). The rare earth elements are the good source of magnetocrystalline anisotropy since the rare-earth elements exhibit large spin orbit interaction and the localized $4f$ electronic orbitals which are less effected by crystal electric environment than d-orbital electron density. In a given crystal field environment, if the unique axis (c-axis of tetragonal or hexagonal system) of the crystallographic axis is surrounded by oblate electronic orbitals with large z-component of angular momentum then the material will have uniaxial anisotropy where as the prolate nature tends to provide a planer anisotropy [53].

The most of the magnetic properties of a ferromagnetic materials could be explained correctly with non-relativistic quantum mechanics [52]. The relativistic effect is necessary to correctly account the anisotropic magnetic properties which is related to spin-orbit interaction in materials. In

the electron rest frame of reference as shown in Fig. 1.15(a), the magnetic field $\overrightarrow{B}$ experienced by electron is given by [52, 54]

$$\overrightarrow{B} = -\frac{1}{2m_e r}\frac{dV(r)}{dr}\frac{\hbar\hat{l}}{c^2} = \frac{2\xi(r)}{\mu_B}\hat{\Omega}_M \tag{1.90}$$

where

$$\xi(r) = \frac{\mu_B}{2m_e r c^2}\frac{dV(r)}{dr} \tag{1.91}$$

is the radial average of the spin-orbit splitting constant which is function of Bohr magneton (μ_B), electronic mass (m_e), velocity of light (c) and radial potential gradient ($\frac{dV(r)}{dr}$). $\hat{\Omega}_M = (\sin\theta\cos\phi,\ \sin\theta\sin\phi,\ \cos\theta)$ is direction of the magnetic field experienced by electron.

To get the magneto-crystalline anisotropy formula in a convenient way, concept of magnetic susceptibility $\overrightarrow{M} = \chi\overrightarrow{B}$, here χ is a diagonalized tensor quantity, can be introduced as

$$E_{SO} = -\overrightarrow{M}\cdot\overrightarrow{B} = -\overrightarrow{B}\chi\cdot\overrightarrow{B} \tag{1.92}$$

For uniaxial systems (e.g., tetragonal, hexagonal and trigonal) the anisotropic susceptibility can be expressed in terms of second rank matrix where two planer components are equal but the axial component is different as

$$\chi = \begin{bmatrix} \chi_a & 0 & 0 \\ 0 & \chi_a & 0 \\ 0 & 0 & \chi_c \end{bmatrix} \tag{1.93}$$

Then equation 1.92 takes the form

$$\begin{aligned} E_{SO} &= -(\frac{2\xi(r)}{\mu_B})^2\hat{\Omega}_M\chi\cdot\hat{\Omega}_M \\ or, E_{SO} &= -(\frac{2\xi(r)}{\mu_B})^2(\chi_a\sin^2\theta + \chi_c\cos^2\theta) \\ E_{SO} &= -(\frac{2\xi(r)}{\mu_B})^2[\chi_c + (\chi_a - \chi_c)\sin^2\theta] \\ E_{SO} &= K_0 + K_1\sin^2\theta \end{aligned} \tag{1.94}$$

Where $K_0 = -(\frac{2\xi(r)}{\mu_B})^2\chi_c$ is isotropic magnetic free energy and $K_1 = -(\frac{2\xi(r)}{\mu_B})^2(\chi_a - \chi_c)$ is magneto-crystalline anisotropy. This formula for K_1 shows that magnetocrystalline anisotropy is proportional to the spin orbit interaction factor $(\frac{2\xi(r)}{\mu_B})^2$. If higher order of susceptibility and magnetization is considered, higher order anisotropy constants are obtained as

$$E_{SO} = K_0 + K_1 \sin^2\theta + K_2 \sin^4\theta + ... \tag{1.95}$$

If all K_1, K_2 .. are all zeros, the system is isotropic. For uniaxial system, if $K_1 > 0$ and $K_2 > -K_1$ then the unique axis is called easy axis magnetization (here c-axis). For a planer system, $K_1 > 0$ and $K_2 < -K_1$ [52].

1.2.13 Domain theory

Intially, Weiss purposed that ferromagnetic substructures inside a bulk magnetic sample could explain the net zero magnetization in a bulk ferromagnetic sample without mentioning the word domain [55]. Soon after, these substructures with uniform magnetization and arbitrary orientations inside a bulk ferromagnetic materials were identified as domains. Domain theory explains the mechanism of formation of ferromagnetic domains, their refinement and their influence on the magnetic properties of materials. Surface patterns of the ferromagnetic domains are observed using image acquisition techniques such as Bitter decoration, magneto-optical techniques (Faraday and Kerr effects) and various microscopy techniques (Lorentz and magnetic force). Domain theory uses the available surface domain patterns and predicts the three dimensional domain structures which minimizes the total magnetic energy of the system [55].

In a ferromagnet, the exchange interaction favors the parallel alignment of the spins so as to minimize the total energy, thereby forming a single ferromagnetic domain. However, a bulk ferromagnetic domain give rise to the magnetostatic energy which again raises the total energy. A schematic diagram of magnetic poles formation in a bulk ferromagnetic sample is demonstrated in Fig. 1.16(a) - (b). Fig. 1.16(c) shows that the direction of field lines outside the ferromagnetic sample is opposing the magnetization direction inside the sample. These field lines could be considered

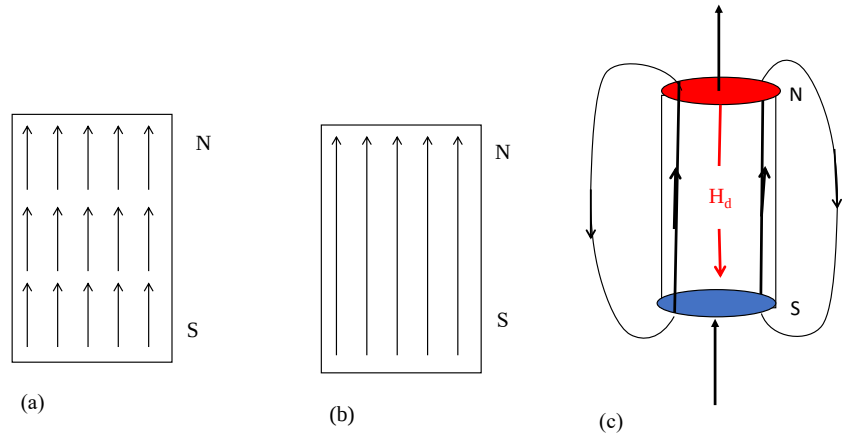

Figure 1.16 Demonstration of the mechanism of formation of magnetic poles in a uniformly magnetized sample that are responsible for magnetostatic energy. (a) A ferromagnetic sample showing the perfect alignment of the atomic magneticmagnetic moments. (b) Coupling of the atomic magnets inside the magnetic volume leaves only north pole in the upper end and the south pole in the lower end of the sample (c) The magnetic field lines outside the magnetic volume oppose the direction of magnetic moments inside. This could be considered to be equivalent to the field lines inside the magnetic volume due to the virtual magnetic poles localized at the end of the sample. This field is called demagnetization field H_d (see chapter 2 for additional discussion.)

passing inside the bulk ferromagnet due to virtual monopoles created at the extermities of the magnetized volume [12]. The competition between the exchange interaction and magnetostatic energy drives the magnetic system in to a multiple domains structure so as to minimize the total energy of the magnetic system [55, 20, 15, 12, 45]. This was the reason that, historically, steel or Alnico magnets were fabricated into horse shoe or toroidal shapes so as to avoid the magnetostatic demagnetization due to poles formation. There are several additional factors associated such as magnetocrystalline anisotropy and magnetostrictive energies which play a vital role in shape and size refinement of the domains and nature of domain walls.

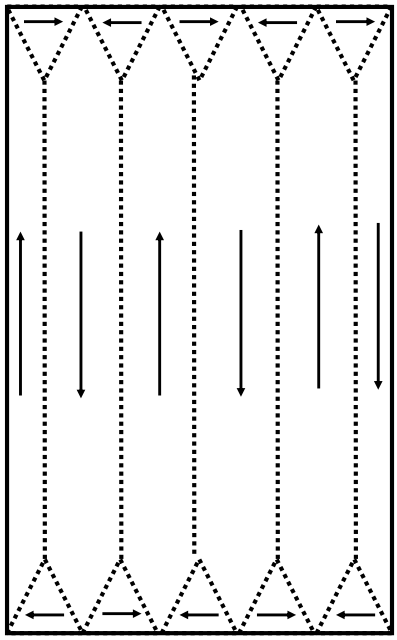

Figure 1.17 Free pole avoidance mechanism in a bulk ferromagnet. The primary domains align parallel or antiparallel to the preferred direction of magnetization whose poles are cancelled by triangular closure domains.

The dominant factor that controls the shape of the ferrromagnetic domains is magnetocrystalline anisotropy energy. Although the magnetostatic energy renders the ferromagnetic samples in multi-domains, the exchange interaction inside a domain is minimum when all the spins inside the individual domains point along the preferred direction. This is achieved by formation of multiple large domains, also known as primary domains, aligned either parallel or anti-parallel to preferred direction with the principle of avoidance of free pole formation [45] via closure domain as shown in Fig 1.17 [20]. The principle of the avoidance of the pole formation requires the minimization of the magnetostatic energy by attaining the minimum magnetic surface charge ($\mathbf{M} \cdot \hat{n}$, $\hat{n}$ being normal to the magnetization surface) configuration in a ferromagnetic sample. A perfect pole avoidance geometry is toroidal shape, however in a real sample the optimized closure domains minimize the magnetostatic energy [45].

The contraction or extension of the length of a ferromagnetic materials due to magnetization is called magnetostriction [56]. The extension and contraction are called positive and negative magnetostriction respectively. The magnetostriction influences all three major competing factors namely exchange interaction, magnetocrystalline and magnetostatic energies. Generally, the change in length is very small about tens of parts per million however magnetostriction is large enough to deform the magnetic domains [20].

1.2.14 Domain walls

The competition between exchange interaction, magnetocrystalline and magnetostatic energies prevails down to the boundary region between domains. So the ordering of the magnetic moments within these boundaries is not abruptly changing as sketched in Fig. 1.17, rather there occurs a gradual rotation of magnetization for sake of total energy minimization. These boundaries regions between domains with gradually rotating magnetic moments are called domain walls.

In 180° rotation of magnetization in neighbouring domains, a domain wall is called Bloch wall if the magnetization is rotating perpendicular to the domain wall. The width (δ) and energy (σ) associated with Bloch wall are given as [12]

$$\delta = \pi\sqrt{\frac{A}{K}} \tag{1.96}$$

and

$$\sigma = \pi\sqrt{AK} \tag{1.97}$$

Here $A = 2JS^2\frac{z}{a}$ is called stiffness constant [13] which is related with exchange integral J, number of atom per unit cell z and lattice parameter a. K is magnetocrystalline anisotropy energy density.

If a magnetic materials forms a thin film, there is great reduction in in-plane shape anisotropy and the magnetization gradually rotates within the domain wall called a Néel wall [20].

Similarly, there exist a sharp 90° rotation of magnetization in the closure domain as shown in Fig. 1.17. In such 90° rotation of magnetization, the magnetization in a domain wall makes a constant 45° angle both with wall-plane [20].

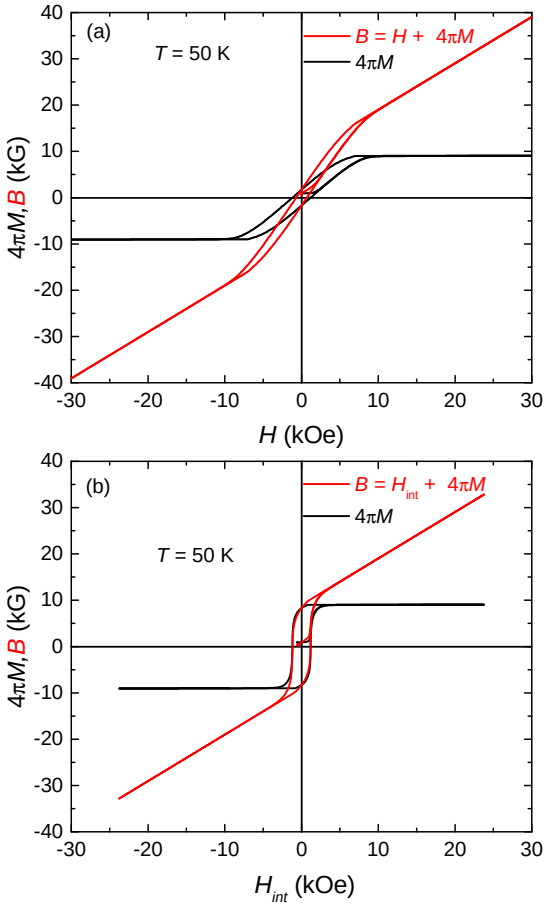

Figure 1.18 Relation between B, H and M in the CGS unit. (a) Without demagnetization effect correction (b) With demagnetization effect correction.

1.2.15 High performance permanent magnets

In the remaining subsections of this chapter, specific parameters needed for a ferromagnetic material to be applicable for high strength permanent magnets are discussed. A high performance permanent magnet is characterized by a large magnetization hysteresis loop and high Curie temperature. A hysteresis loop is a five quadrant magnetization *M(H)* data set, or, equivalently, a magnetic induction *B(H)* loop. Fig. 1.18 (both (a) and (b)) shows hysteresis loops for as-grown single crystalline $Ce_{0.86}Ta_{0.06}Co_{3.72}Fe_{0.73}Cu_{15.9}$ sample at 50 K. The details of the sample is discussed in Chapter 10. Figs. 1.18(a) and 1.18(b) show the relation between B and H without (a)

and with (b) the demagnetization effect correction. The magnetic induction B and H are related as $B = \mu_0(H + M)$ in the SI or $B = H + 4\pi M$ in the CGS unit, where M is the magnetization.

An enlarged, hypothetical, *B(H)* loop is shown in Fig. 1.19 to explain its various elements. The magnetization slowly increases, linearly in the beginning, and then saturates in a sufficiently large field as represented with point A. During the reversal of the field, as the magnetizing field decreases, the induced magnetization does not follow the same path as it does in the first quadrant. When the magnetizing field is reduced to zero, there is finite residual induced magnetization B_r called remanence. When the magnetizing field is increased in the reverse direction, the remanence continuously decreases and reduces to zero. The corresponding reverse magnetizing field H_C is called coercivity. The larger the coercivity and remanence, the better the energy product $(BH)_{max}$ which is the maximum energy density that can be stored in a permanent magnet [57]. Mathematically, $(BH)_{max}$ is the maximum square that can be inscribed in the second quadrant of the hysteresis loop and the corresponding point (B_0, H_0) is called operating point of the permanent magnet. The straight line joining operating point with the origin is called loadline or the demagnetization line [58]. Upon further increasing of the magnetizing field, the magnetization saturates in an opposite direction at point C. When the field begins to increase at point C, it again follows a different path and produces the same negative remanence in the third quadrant and finally saturates at point A again. In additional cycles, *B-H* curve follows the outer loop. If the sample is passed through the magnetization loops of insufficiently large field to saturate, then the sample passes through a un-optimized loop called a minor loop.

1.2.16 Magnetic hysteresis in domain theory viewpoint

The shape of the ferromagnetic hysteresis loop shown in Fig. 1.19 can be understood using domain theory as illustrated in Fig. 1.20(a). Initially at point O, the ferromagnet is in net zero moment condition. As soon as small field is applied, larger domains tend to form in the field direction in expense of reverse domains [20]. The domain wall dynamic is reversible upto point A_1 and no hysteresis is achieved.

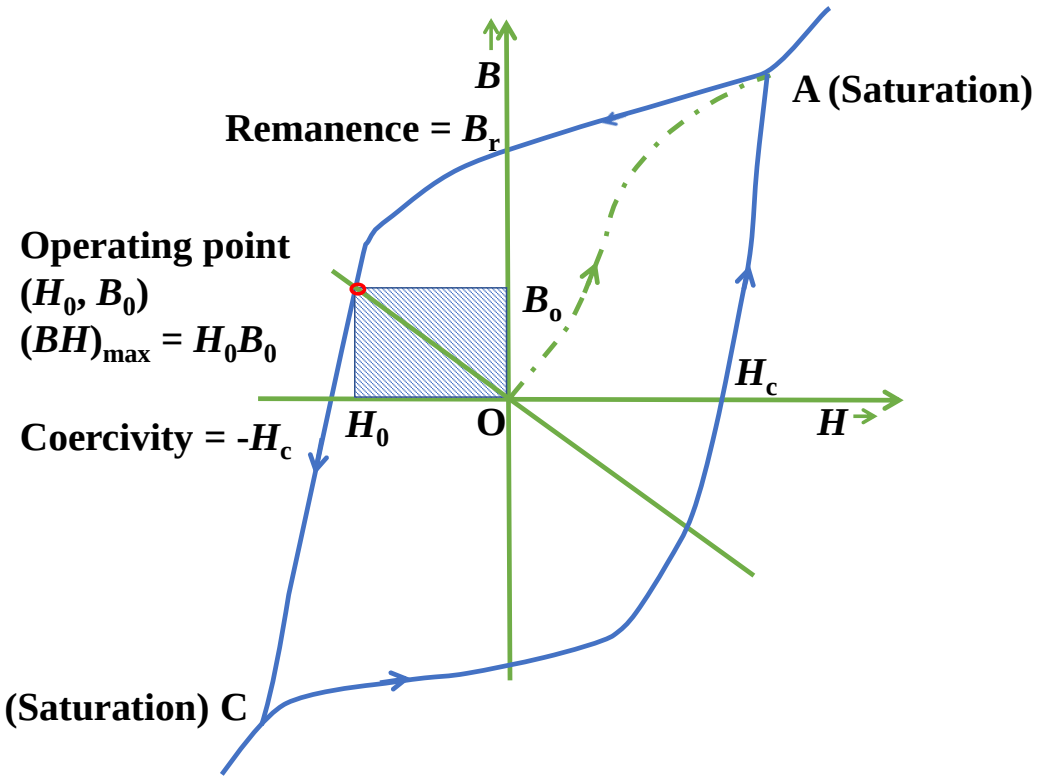

Figure 1.19 Permanent magnet hysteresis loop.

On further increasing the field, domain walls tend to move and get pinned by imperfections such as grain boundaries, impurities sites, dislocations and faults. Domains walls are pinned by imperfections as they neutralize the locally available magnetostatic energy as a result of free poles as shown in Fig. 1.20(b). During this magnetostatic energy neutralization process, the domain wall forms closure domains around the defect site as shown in Fig. 1.20(c). As the field is further increased, the domain walls begin to move past the pining potentials via deformation of closure domains as shown in Fig. 1.20(d). As coercive field is reached, the domain wall moves off and the closure domains transform to spike domains as shown in Fig. 1.20(e) [20]. Finally, the magnetostatic energy restores with the disappearance of the spike domains. Past the coercive field, the magnetization is discontinuous due to domains boundary motion known as Barkhausen effect [12, 20].

In a sufficiently large field, a saturation is obtained removing all the domain walls as indicated in uniformly magnetized single domain magnet as shown in point A in Fig. 1.20(a). As the field is removed it follows the reversible path down to saturation magnetization point A due to dipole rotation triggered by demagnetization field. The demagnetization process becomes irreversible soon after the field decreases below the saturation point since the demagnetization field can not overcome the ferromagnetic domain pinning.

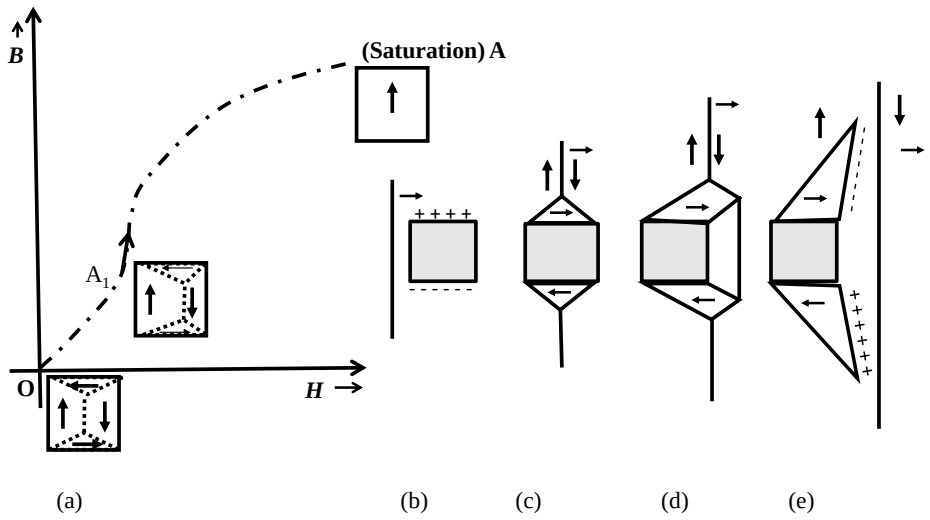

Figure 1.20 (a) Explanation of the hysteresis phenomena using domain theory (b) The + and − symbols are used to represent the magnetostatic energy around a defect in a permanent magnet. (c) When a domain wall moves through a defect, the domain wall is pinned in the impurity creating local energy minimum around the defect via closure domains formation [20]. (d) As the field makes the wall to move further, the nature of closure domains deform (e) As the domain wall passes by, the magnetostatic energy redevelops around the defects forming spike domains [20]

1.2.17 Requirements of ferromagnetic materials to be useful permanent magnets

High flux permanent magnets design needs several fabrication steps after the identification of potential ferromagnetic materials. The energy product is a complex function of above mentioned

intrinsic magnetic properties and extrinsic properties such as microstructures development to generate significant domain pinning. Additionally, chemical stability of materials is also a key factor for a permanent magnets. Depending upon the energy product of commercial magnets, there are two major families of permanent magnets currently in use, namely rare-earth based high flux permanent magnets which have energy product greater then 200 kJ/m^3 and low flux Alnico and ferrites with energy product as low as 38 kJ/m^3[5].

With the sudden rise in the price of rare-earth elements, a family of magnets that could fulfill the need for energy product in between low flux (e.g., Alnico and Ferrites) and critical rare-earth based high-flux permanent magnets conveniently defined as "gap magnets" are drawing a considerable amount of attention. To develop a potential gap magnet, we need to find ferromagnetic materials with (i) high Curie temperature (at least greater than 550 K) (ii) high saturation magnetization (at lease greater than 0.5 Tesla) and (iii) large uniaxial anisotropy ($\geq$ 5 Tesla at room temperature) [11]. However, these criteria alone are not enough to get high flux permanent magnets. It needs tremendous amount of research to develop a stable permanent magnet. For example, MnBi has been identified as a potential rare-earth free permanent magnet material for a long time [59]. Still, no robust permanent magnet has been developed out of it due to stability and microstructures development issues. To get new robust non-critical element-based permanent magnets, the starting point is the identification of new uniaxial ferromagnetic materials with the above mentioned three major intrinsic properties.

1.3 References

[1] S. Constantinides. The demand for rare earth free materials in permanent magnets. *Arnold Magnetic Technologies*, 2012.

[2] Yutaro Takaya, Kazutaka Yasukawa, Takehiro Kawasaki, Koichiro Fujinaga, Junichiro Ohta, Yoichi Usui, Kentaro Nakamura, Jun-Ichi Kimura, Qing Chang, Morihisa Hamada, Gjergj Dodbiba, Tatsuo Nozaki, Koichi Iijima, Tomohiro Morisawa, Takuma Kuwahara, Yasuyuki Ishida, Takao Ichimura, Masaki Kitazume, Toyohisa Fujita, and Yasuhiro Kato. The tremendous potential of deep-sea mud as a source of rare-earth elements. *Scientific Reports*, 8(5763), 2018.

[3] Claire L. McLeod and Mark. P. S. Krekeler. Sources of Extraterrestrial Rare Earth Elements: To the Moon and Beyond. *Resources*, 6(40), August 2017.

[4] D. Bauer, D. Diamond, J. Li, D. Sandalow, P. Telleen, and B. Wanner. U.S. Department of Energy Critical Materials Strategy. 2010.

[5] J. M. D. Coey. Permanent magnets: Plugging the gap. *Scripta Materialia*, 67(6):524–529, sep 2012.

[6] A. J. Freeman and R. E. Watson. Theoretical investigation of some magnetic and spectroscopic properties of rare-earth ions. *Phys. Rev.*, 127:2058–2075, Sep 1962.

[7] M.I. Bartashevich, T. Goto, R.J. Radwanski, and A.V. Korolyov. Magnetic anisotropy and high-field magnetization process of $CeCo_5$. *Journal of Magnetism and Magnetic Materials*, 131(1):61 – 66, 1994.

[8] Teresa Matich. A new use for cerium? Investing News Network, Dig Media Inc., April 2015.

[9] Zoe Budrikis. Magnetism: Doping rehabilitates failed materials. *Nature Reviews Materials*, 3(18018), Mar 2018.

[10] D.J. Griffiths. *Introduction to Electrodynamics*. Prentice Hall, 1999.

[11] J. M. D. Coey. *Magnetism and Magnetic Materials*. Cambridge University Press, 2010.

[12] Stephen Blundell. *Magnetism in Condensed Matter*. Oxford University Press, 2001.

[13] Adrian Ionescu, Justin Llandro, and Kurt R. A. Ziebeck. *Magnetism, Magnetic Materials, and Nanoparticles*, pages 1 – 51. Cambridge University Press, 2019.

[14] Neil W. Ashcroft and N. David Mermin. *Solid State Physics*. Thompson Books/Cole, 2007.

[15] Charles Kittel. *Introduction to Solid State Physics*. Wiley, seventh edition, 2004.

[16] J. H. Van Vleck. *The Theory of Electric and Magnetic Susceptibilities*. Oxford University Press, London, 1932. Chapter VI.

[17] Assa Auerbach. *Interacting Electrons and Quantum Magnetism*. Springer-Verlag, 1994.

[18] Yoshiro Kakehashi. *Modern Theory of Magnetism in Metals and Alloys*. Springer, 2012.

[19] Patrick Fazekas. *Lecture Notes on Electron Correlation and Magnetism*. World Scientific Publishing Company, Singapore, 1999.

[20] Nicola A. Spaldin. *Paramagnetism*, page 4864. Cambridge University Press, 2 edition, 2010.

[21] Charles Kittel. *Introduction to Solid State Physics 8E.* John Wiley and Sons Ltd, 2004.

[22] G. Grosso and G.P. Parravicini. *Solid State Physics.* Elsevier Science, 2013.

[23] E. A. Goremychkin, R. Osborn, E. D. Bauer, M. B. Maple, N. A. Frederick, W. M. Yuhasz, F. M. Woodward, and J. W. Lynn. Crystal Field Potential of $PrOs_4Sb_{12}$: Consequences for Superconductivity. *Phys. Rev. Lett.*, 93:157003, Oct 2004.

[24] K Gatterer and H P Fritzer. Magnetic susceptibility of the Van Vleck paramagnet $Cs_5Eu(N_3)_8$. *Journal of Physics: Condensed Matter*, 4(19):4667–4673, May 1992.

[25] Yusuke Takikawa, Shuji Ebisu, and Shoichi Nagata. Van Vleck paramagnetism of the trivalent Eu ions. *Journal of physics and chemistry of solids*, 71(11):1592–1598, Nov 2010.

[26] M. Tovar, D. Rao, J. Barnett, S. B. Oseroff, J. D. Thompson, S-W. Cheong, Z. Fisk, D. C. Vier, and S. Schultz. Eu_2CuO_4: An anisotropic Van Vleck paramagnet. *Phys. Rev. B*, 39:2661–2663, Feb 1989.

[27] A. A. Loginov, E. N. Khatsko, A. S. Cherny, B. N. Baumer, A. I. Rykova, P. S. Kalinin, and A. Sulpis. Magnetic properties of the singlet antiferromagnet $KTb(WO_4)_2$. *Low Temperature Physics*, 32(1):68–76, 2006.

[28] P. W. Anderson. Antiferromagnetism. theory of superexchange interaction. *Phys. Rev.*, 79:350–356, Jul 1950.

[29] M. A. Ruderman and C. Kittel. Indirect exchange coupling of nuclear magnetic moments by conduction electrons. *Phys. Rev.*, 96:99–102, Oct 1954.

[30] Tadao Kasuya. A Theory of Metallic Ferro- and Antiferromagnetism on Zener's Model. *Progress of Theoretical Physics*, 16(1):45–57, 07 1956.

[31] Kei Yosida. Magnetic Properties of Cu-Mn Alloys. *Phys. Rev.*, 106:893–898, Jun 1957.

[32] C. Kittel. Indirect exchange interactions in metals. volume 22 of *Solid State Physics*, pages 1 – 26. Academic Press, 1969.

[33] E.Y. Tsymbal and D.G. Pettifor. Perspectives of giant magnetoresistance. volume 56 of *Solid State Physics*, pages 113 – 237. Academic Press, 2001.

[34] H. Köhler and J. Sticht and J. Kübler. Spin waves and Heisenberg exchange constants for -iron. *Physica B: Condensed Matter*, 172(1):79 – 84, 1991.

[35] M. ElMassalami, D. da S. Oliveira, and H. Takeya. On the ferromagnetism of $AlFe_2B_2$. *J. Magn. Magn. Mater.*, 323(16):2133 – 2136, 2011.

[36] P. Rhodes and E. P. Wohlfarth. The effective Curie-Weiss constant of ferromagnetic metals and alloys. *Proc. Roy. Soc. A. Mathematical, Physical and Engineering Sciences*, 1963.

[37] Bruce M. Moskowitz. Methods for estimating Curie temperatures of titanomaghemites from experimental $J_s - T$ data. *Earth and Planetary Science Letters*, 53(1):84 – 88, 1981.

[38] K. Fabian, V. P. Shcherbakov, and S. A. McEnroe. Measuring the Curie temperature. *Geochemistry, Geophysics, Geosystems*, 14(4):947–961, 2013.

[39] John Hasier, Maria Annichia Riolo, and Philip Nash. Curie temperature determination via thermogravimetric and continuous wavelet transformation analysis. *EPJ Techniques and Instrumentation*, 4, 2017.

[40] Williams, Henry W. and Chamberland, Bertrand L. Determination of Curie, Néel, or crystallographic transition temperatures via differential scanning calorimetry. *Analytical Chemistry*, 41(14):2084–2086, 1969.

[41] D. L. Connelly, J. S. Loomis, and D. E. Mapother. Specific Heat of Nickel near the Curie Temperature. *Phys. Rev. B*, 3:924–934, Feb 1971.

[42] Anthony Arrott. Criterion for ferromagnetism from observations of magnetic isotherms. *Phys. Rev.*, 108:1394–1396, Dec 1957.

[43] Anthony Arrott and John E. Noakes. Approximate equation of state for nickel near its critical temperature. *Phys. Rev. Lett.*, 19:786–789, Oct 1967.

[44] Soshin Chikazumi. *Physics of Ferromagnetism*. Oxford Science Publications, second edition, 1997.

[45] A. Aharoni. *Introduction to the Theory of Ferromagnetism*. International Series of Monographs on Physics. Clarendon Press, 2000.

[46] David C. Johnston. Unified molecular field theory for collinear and noncollinear Heisenberg antiferromagnets. *Phys. Rev. B*, 91:064427, Feb 2015.

[47] Tej N. Lamichhane, Valentin Taufour, Srinivasa Thimmaiah, David S. Parker, Sergey L. Bud'ko, and Paul C. Canfield. A study of the physical properties of single crystalline Fe_5B_2P. *J. Magn. Magn. Mater.*, 401:525 – 531, 2016.

[48] Sang-Koog Kim. Micromagnetic computer simulations of spin waves in nanometre-scale patterned magnetic elements. *Journal of Physics D: Applied Physics*, 43(26):264004, Jun 2010.

[49] F. Bloch. Zur theorie des ferromagnetismus. *Zeitschrift für Physik*, 61(3):206–219, Mar 1930.

[50] S.L. Bud'ko, Z. Islam, T.A. Wiener, I.R. Fisher, A.H. Lacerda, and P.C. Canfield. Anisotropy and metamagnetism in the RNi_2Ge_2 (R=Y, La - Nd, Sm - Lu) series. *Journal of Magnetism and Magnetic Materials*, 205(1):53 – 78, 1999.

[51] T. A. Wiener, I. R. Fisher, S. L. Bud'ko, A. Kracher, and P. C. Canfield. Design of a metallic Ising spin glass in the $Y_{1-x}Tb_xNi_2Ge_2$ system. *Phys. Rev. B*, 62:15056–15066, Dec 2000.

[52] Patrick Bruno. *Ferienkurse des Forschungszentrums Julich Chapter: 24*, chapter Physical Origins and Theoretical Models of Magnetic Anisotropy, pages 24.1 –24.28. 1993.

[53] Ralph Skomski. *Simple Models of Magnetism*. Oxford Graduate Texts. Oxford University Press, Oxford, 2008.

[54] Herbert Kroemer. The Thomas precession factor in spinorbit interaction. *American Journal of Physics*, 72(1):51–52, 2004.

[55] A. Hubert, R. Schäfer, and A. Rudolf Schafer. *Magnetic Domains: The Analysis of Magnetic Microstructures*. Springer, 1998.

[56] E W Lee. Magnetostriction and magnetomechanical effects. *Reports on Progress in Physics*, 18(1):184–229, Jan 1955.

[57] J. M. D. Coey. New permanent magnets manganese compounds. *Journal of Physics: Condensed Matter*, 26(6):064211, Jan 2014.

[58] Herbert A. Leupold and Ernest Potenziani II. An overview of modern permanent magnet design. Research and development technical report SLCET-TR-90-6, Electronics Technology And Devices Laboratory, Aug 1990.

[59] J Cui, J P Choi, G Li, E Polikarpov, J Darsell, N Overman, M Olszta, D Schreiber, M Bowden, T Droubay, M J Kramer, N A Zarkevich, L L Wang, D D Johnson, M Marinescu, I Takeuchi, Q Z Huang, H Wu, H Reeve, N V Vuong, and J P Liu. Thermal stability of MnBi magnetic materials. *Journal of Physics: Condensed Matter*, 26(6):064212, Jan 2014.

CHAPTER 2. EXPERIMENTAL METHODS

2.1 Introduction

Exploratory material synthesis (both single and polycrystalline samples) combined with basic characterization is a powerful technique for the discovery of novel materials. Such synthesis requires an in-depth knowledge of the physical and chemical properties of the constituent elements as well as their equilibrium states via phase equilibrium diagrams. However, the reported phase diagrams sometime contain inaccuracies and may contain poorly explored or missing composition fields. In exploratory synthesis, the existing phase diagrams can only provide necessary information for the initial planning. In the next few paragraphs, I will discuss the basic concepts about binary phase diagrams which are very useful in polycrystalline as well as high temperature single crystalline solution growth techniques, in reference to a Ce-Co binary phase diagram [1].

The atomic percentage-temperature phase diagrams have their crucial importance in materials synthesis strategies. In a binary phase diagram, the x-axis shows atomic percentages of the elements and y-axis shows temperature. A recent version of Ce-Co binary phase diagram [1] is presented in Fig. 2.1. Along the x-axis, pure Ce is at the far left while pure Co is at the far right. The blue color on the top shows a high temperature region representing a homogeneous-liquid state (L). Around 24 and 33 atomic percentages of Co, the low melting composition points A and B are called eutetic points as shown in Fig 2.1. The low melting temperature eutectic points' compositions can be used as a solvent (flux) in a crystal growth process.

All the vertical lines in the phase diagram represent elements or stoichiometric compounds. The stoichiometric compounds melt either congruently or incongruently. For example, $Ce_{24}Co_{11}$ melts congruently at 446 °C. In a congruent melting, a solid melts in the liquid of the same composition without any decomposition. In contrast, in the incongruently melting the solid phase decomposes into another compound (of different composition) and a liquid. All the compounds between $CeCo_2$

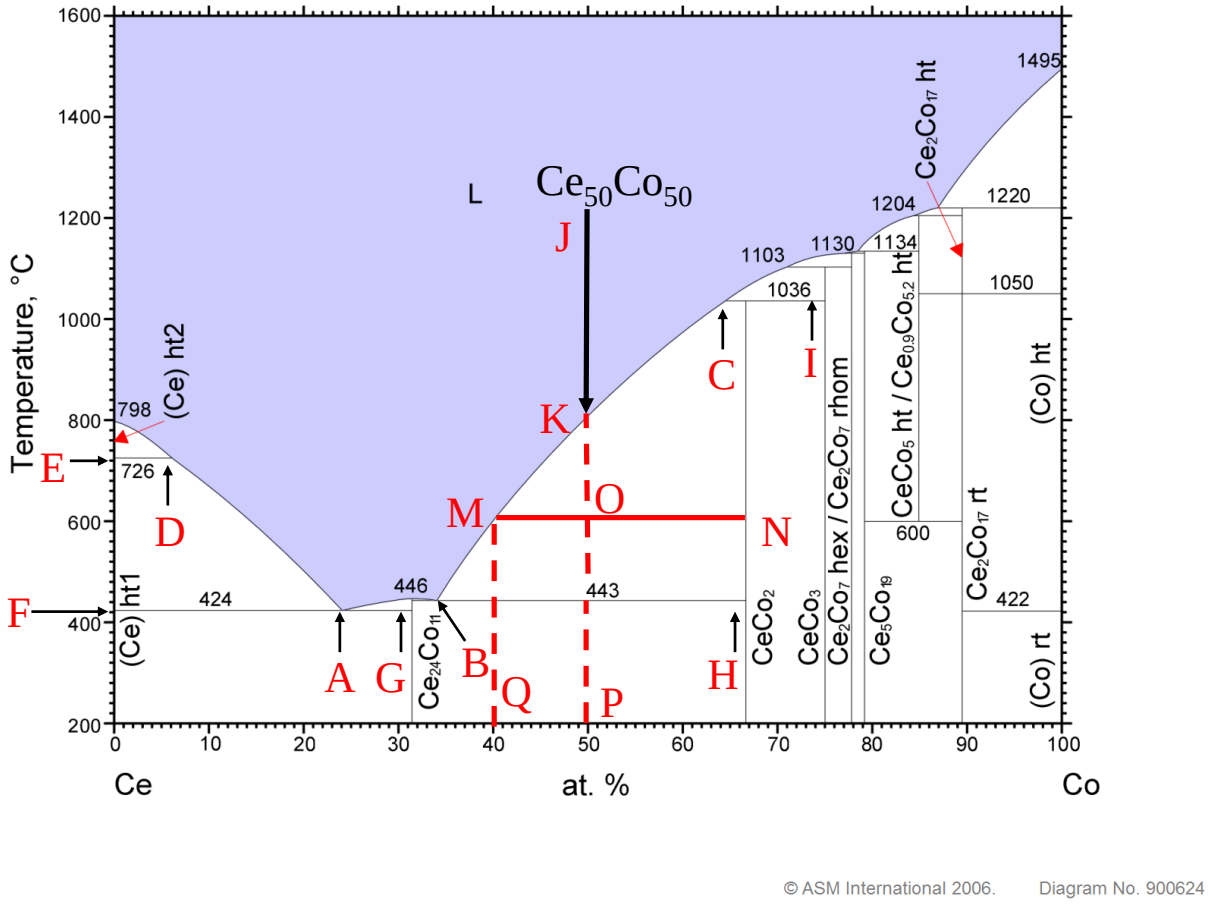

Figure 2.1 Ce-Co binary phase diagram taken from ASM International with permission (phase diagram number 900624) [1]. The points A-K and M-Q presented in red colours are the added points to facilitate the explanation of basic terminologies in synthesis. Similarly the black colored arrows and red solid and dotted straight lines are added to display the lever rule to estimate the atomic percentages of the solid and liquid phases.

and Ce_2Co_{17} melt incongruently. In such compounds, a horizontal line corresponding to that decomposition temperature which is called a peritectic line. The boundary between homogeneous-liquid phase and mixed solid-liquid phase regions is the liquidus line such as segments AD and BC. The solid horizontal lines are called solidus lines (e.g. FA, AG, and BH) which represents the minimum temperature at which liquids are stable.

2.1.1 Sample preparation

In this thesis, most of the materials under study are synthesized in single-crystalline form using high temperature solution growth techniques [2, 3, 4]. Single crystalline samples are required mainly for the characterization of intrinsic anisotropic physical properties. Occasionally, poly-crystalline samples were synthesized to initially verify the existence of the target compounds/chemical compositions via arcmelting and solid state reactions. In some functional materials, such as permanent magnets, polycrystalline samples are required to obtain the desired properties through controlled microstructure effects.

The phase diagram in Fig. 2.1 can be used to plan initial crystal growths. A case study of heating and cooling of $CeCo_2$ is discussed in this chapter. $CeCo_2$ decomposes into $CeCo_3$ and a liquid at 1036°C. Heating further, $CeCo_3$ gradually dissolves into the liquid between 1036 and about 1060 °C (the liquidus temperature). To make the complete dissolution of the decomposed high melting phases, the best approach is to heat up the melt higher than melting point of the decomposition generated new phases. In case of CeCo2, the growth was heated to 1200 °C so that any possible high melting phases such as $CeCo_3$ and Ce_2Co_7 will completely melt. However, there should be no chemical reaction reaction between crucibles and growth materials at the highest achievable temperature. The growth assembly holder such as amorphous silica ampoule and quartz wool also should safely withstand up to 1200 °C so that this growth process becomes possible.

However, if we examine a $CeCo_2$ solution upon cooling, it becomes a mixture of $CeCo_3$ crystalline nucleates and and roughly $Ce_{37}Co_{63}$ composition liquid at 1036°C. On further cooling of the $Ce_{37}Co_{63}$ composition liquid, crystals of $CeCo_2$ nucleate and become larger and larger as the

cooling proceeds further down. In general, a slower cooling rate increases the chances of obtaining larger crystals. As $CeCo_2$ crystallize out, with further cooling, the liquid becomes richer in Ce and finally reaches to roughly $Ce_{66}Co_{34}$ composition represented by point B. Upon further cooling, the eutectic composition solidifies. The solidified eutectic composition contains solid compounds that lie on the left and right of the eutectic point such as $Ce_{24}Co_{11}$ and $CeCo_2$ in this case. Sometime, eutectic compositions decompose into stripes of alternative phases as observed in Fe-Si eutectic point [5]. The nucleation of $CeCo_3$ crystal above the peritectic line at 1036°C and $CeCo_2$ below it produces mixed phases crystals. In several experiments, mixed phase crystals were easily distinguishable using crystal morphologies. In some cases, the minority phase might reside as an inclusion or nucleates on the surface of the majority phase crystals. Generally, the crystals with larger yield is the majority phase and smaller yield is the minority phase.

As a second example, we can study $CeCo_3$. If $CeCo_3$ is heated up, it first decomposes into a mixture of hex/rhom Ce_2Co_7 and a liquid ($\sim Ce_{29}Co_{71}$) at 1103 °C. On further heating to 1130 °C, it forms a homogeneous liquid. While cooling down 1103 °C, it forms a mixture of about 40 and 60 atomic percentages of liquid and solid hex/rhom Ce_2Co_7 as mixed phases respectively. On further cooling the remaining liquid it will crystallize out $CeCo_3$ down to 1036 °C and the liquid phase with the composition corresponding to point C. On further cooling the remaining liquid at point C below 1036 °C, $CeCo_2$ crystallizes out where the remaining liquid at the eutectic point gets solidified ultimately as explained above.

To synthesize a single phase, single crystalline $CeCo_2$ sample, we need to select a composition that will intersect the liquidus line for $CeCo_2$ below the peritectic line (e.g., line CI as shown in Fig. 2.1).

To quickly estimate the proportion of the $CeCo_2$ crystalline phase and existing liquid, the lever rule can be used. To understand the lever rule, imagine a case of cooling down the liquid phase of $Ce_{50}Co_{50}$ composition down to $\sim$ 600°C represented by the line MN called a tie line. Assuming the intersection point "O" of vertical line KP and horizontal line MN as a fulcrum of a lever, the atomic phase fraction of solid ($CeCo_2$) and liquid($\sim Ce_{60}Co_{40}$) phases are estimated as:

Atomic % of $CeCo_2 = \frac{MO}{MN} \approx \frac{10.0}{26.5} = 37.60\%$

Atomic % of liquid $Ce_{60}Co_{40} = \frac{ON}{MN} \approx \frac{16.5}{26.5} = 62.40\%$

One can easily find out that the sum of the percentages of phase fractions is 100 in total. To show a quick demonstration of the conservation of number of atoms, writing the composition of two phases at 600 °C, we have the liquid phase of $Ce_{60}Co_{40}$ which provides 62.40% of its atoms and the solid phase composition is $CeCo_2 = Ce_{33}Co_{70}$ which provides 37.60% of atoms of the total atoms to form $Ce_{50}Co_{50}$. Now adding up the fraction of the atomic percentages of both phases for each type of atoms one can get: $Ce_{60\times0.624+33\times0.376}Co_{40\times0.624+67\times0.376} = Ce_{50}Co_{50}$, the initial atomic composition of the homogeneous melt.

An example of a solution growth using Ta-crucibles ($CeCo_2$): $CeCo_2$ single crystals were grown to check the interaction of Ce and Co with Ta crucibles and to utilize it as an absorption standard in energy dispersive x-ray spectroscopy (EDS) along with $MgCo_2$ to quantify the composition of $Ce_{3-x}Mg_xCo_9$ solid solutions. Al_2O_3 crucibles are a common choice for a flux growth, but they are unsuitable for some compositions including those with higher rare-earth concentrations. In general, systems with greater than 10-15 atom% rare-earth attack the Al_2O_3 crucible at processing temperatures forming complex metal oxides. This kind of reduction of metal oxide with reactive metals is called thermite reaction which produces excessive heat during reaction. A Ta crucible often hold up better in these cases.

The Co rich composition such as $Co_{67}Ce_{33}$ is not appropriate for single phase $CeCo_2$ growth since it has a relatively high melting temperature as well as it crosses a peritectic line at 1036 °C. Any initial composition that contains less than 63 atom % of Co can be used for $CeCo_2$ single crystals growth to avoid the peritectic line during crystal growth. The larger the cooling temperature window, larger the single crystals could be grown with a sufficiently slow cooling rate. However, the crystals tend to inter-grow if the growth composition is very close to the crystal stoichiometry. As a test case, the $Ce_{50}Co_{50}$ initial composition was used to synthesize cubic single crystalline $CeCo_2$. The $Ce_{50}Co_{50}$ starting composition was packed inside a sealed Ta crucible and growth ampoule was formed as shown in Fig. 2.2. All the details of the Ta-crucibles assembly and ampule formation is

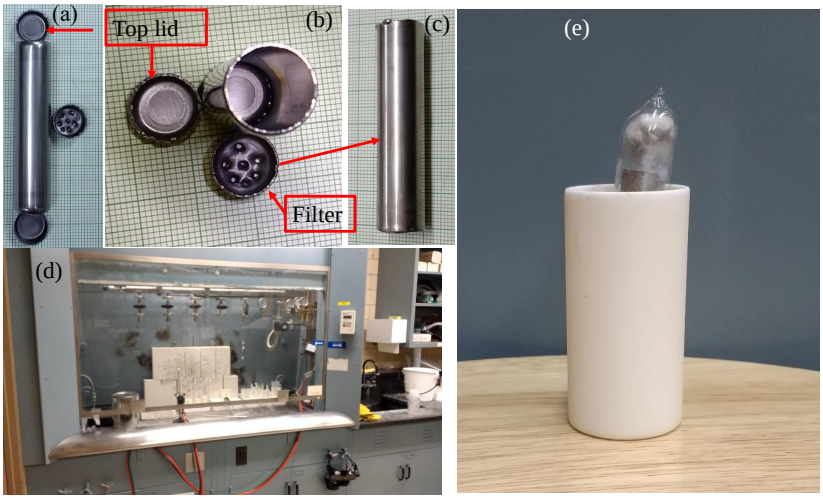

Figure 2.2 Pictorial demonstration of high temperature Ta-crucible and growth ampule preparation for the solution growth. (a) Four machined major parts of a pure elemental Ta to prepare a Ta crucible. The millimeter grid on the background provides information about the size of the parts. Small rectangular Ta-sheets were machined in a cup shape using a hydraulic press. The middle lid is pierced with a nail to make a strainer which separates flux and crystals during centrifuging. (b) Ta crucible formed after sealing the bottom lid by electric discharge melting under Ar-atmosphere (c) The Ta crucible with about 5 g of $Ce_{50}Co_{50}$ growth materials at the bottom, strainer in the middle as shown with red arrow and top sealed with another Ta lid with ∼10 psi Ar pressure in it. (d) Glass bench connected with purging Ar and oxygen-hydrogen blow-torch to soften the amorphous silica. (e) Ready to heat growth ampoule inside a 50 ml alumina crucible containing a Ta crucible inside an amorphous silica jacket under $\frac{1}{3}$ an Ar atmosphere

explained in the caption of Fig. 2.2(a) - (e). Thus prepared ampoule is passed through an appropriate temperature growth profile such that it is homogeneous liquid at the highest temperature 1200°C. The ampule was held at 1200°C around 10 h to allow sufficient time to dissolve Co in the melt and cooled down to 600°C for over 75 h. To separate crystals from the remaining flux a centrifuge was used. The crystal growth temperature profile and crystals separation scheme using centrifuge is shown in Fig. 2.3.

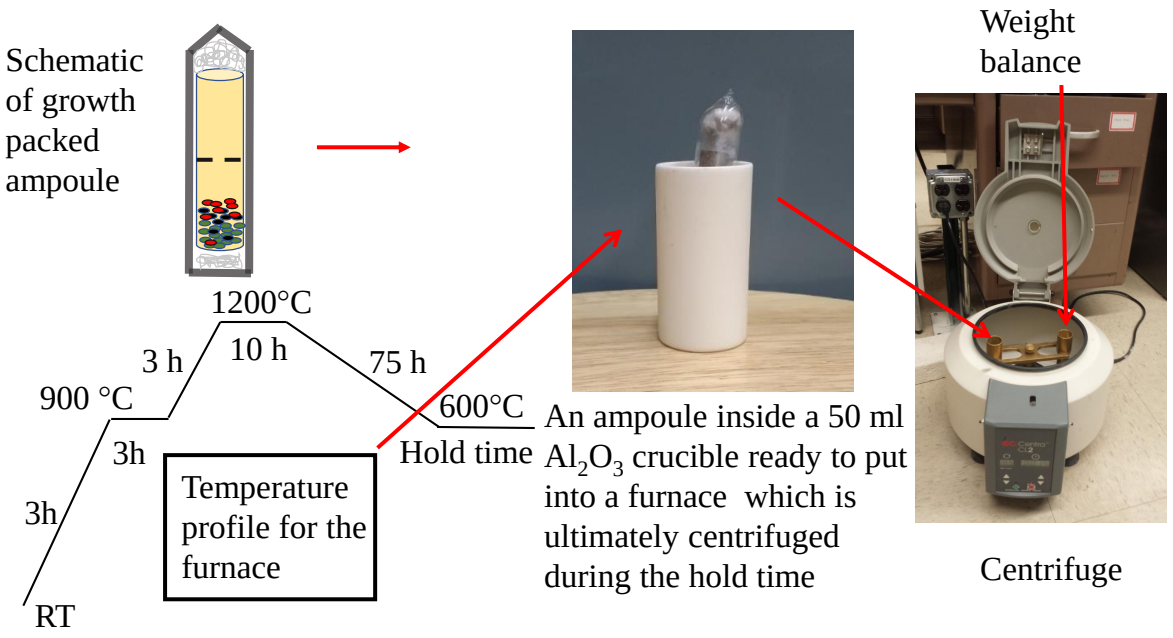

Figure 2.3 $CeCo_2$ single crystal growth temperature profile and growth ampoule inside a 50 ml alumina crucible. During the hold time, the growth is quickly pulled out of furnace and centrifuged within 3-5 seconds.

2.1.1.1 A survey on single crystalline samples synthesis methods

There are several bulk crystal growth methods which can be broadly classified as crystal growth out of melts, solutions, vapours and solids [6, 7]. Among these methods, the Verneuli process is considered one of the oldest method which successfully provide decent sized single crystals out of the melt. The Verneuli process does not require a growth crucible which keeps the single crystals free from contamination of sample from the crucible material. However, a possibility of a large temperature gradient in Crucible free environment could generate large stress in the crystals. Similar to Verneuli process, zone melting, Skull melting, and optical float zone growth processes do not need growth crucibles. In contrast Bridgmann, Czochralski, and Kyropoulos techniques need growth crucibles. Similarly, in the solid state single crystal synthesis, an appropriate annealing or sintering method of micro-structured powder is adopted to enhance the single grain formation

of desired compound by avoiding the multiple grains development in the matrix [8]. The solid state single crystal synthesis method could be used to synthesize commercially useful, net shaped single crystals or textured ceramics (e.g., sapphire, variants of ferroelectric perovskite $BaTiO_3$ and transparent neodymium-doped yttrium aluminum garnet) [8]. In a vapour transport method, a volatile transport agent is used to decompose the target material into volatile components and transport them to crystal growth region. In solution growth techniques, either low melting flux or eutectic mixtures are used to dissolve the high melting elements to form the homogeneous growth liquid which is later cooled down to crystallize the bulk crystals. A short summary of the major single crystals synthesis techniques and comparison of the exploratory solution growth technique is presented below.

Verneuli process: The Verneuli process is a flame-fusion growth process [9] out of melt in which polycrystalline powder of the desired single crystal material is constantly dropped down to a earthen very hot rod with help of O_2 gas flow and the container vibration. The precursor powder flowing with O_2 is passed through a very hot channel (2000 °C) along with flow of H_2 gas to maintain the flame fusion condition. The powder grains melt to form small droplets and coalesce together on the earthen crystal growth rod holding either a seed crystal or suitable substrate to support a boule shaped single crystalline sample. The Verneuli process works best for the congruently melting compounds. This method was widely used in production of artificial gem stones such as corundum and spinels.

Czochralski process: In the Czochralski process, a growth rod containing a seed crystal is pulled upward out of a molten, high-purity material under a controlled rotation rate, displacement and temperature gradient. The Czochralski process also works best for the congruently melting compounds. Most of industrial semiconductors like Si, Ge and GaAs single crystals are grown using this method.

Bridgman process: In the Bridgman process, a crucible containing molten material is cooled by moving it through a temperature gradient in a controlled fashion. This method provides low cost single crystalline samples but works for selected congruently melting compounds.

Optical float zone process: The optical float zone process uses a high intensity light source and multiple curved mirrors to focus light to produce a molten zone in the crystal growth ingot [10]. This method is not often appropriate for metallic single crystal growth since metals are highly reflective. Single crystallinity is achieved using seed crystal in the starting end of the crystal holding rod [11]. The molten zone is gradually moved upward in a controlled fashion. In this process, the possible contamination from the crucible is avoided by passing a ultra high purity polycrystalline ingot through an appropriate temperature gradient zone. The size of the single crystalline sample is often limited by surface tension of the molten material.

Vapour transport process: The vapour transport method is appropriate for the preparation of the high quality crystals of compounds that contain volatile elements, or, in some cases for deeply embedded compounds in a phase diagram, i.e. compounds with small or no exposed liquidus surfaces, or for compounds that undergo structural transitions on heating before melting (e.g., FeSe). In the vapour transport method, nonvolatile precursors are decomposed into volatile components and either self transported or transported with some transport agent to either hot or cold ends of the growth tube, depending on energy balance and phase equilibria of the various components. The temperature and pressure gradients are the major factors that controls the crystal growth kinetics [12].

2.1.2 Solution growth technique

The solution growth technique is one of the oldest single crystalline sample growth technique. A high temperature solution growth with a metallic flux is considered to be started by as early as 19^{th} century when Henri Moissan attempted to grow artificial diamonds using Fe flux [13]. Instead SiC was found to be synthesized also known as moissanite after his name. Slow cooling of high temperature solutions was extensively employed in between 1950 and 1970 to produce several bulk single crystalline samples [6]. Although the crystals are not large enough for many applications, they are often sufficient for characterization of physical properties of new compounds. The major

exploratory synthesis features that are available in solution growth techniques are summarized in following points.

(i) Relatively small sample size makes the search cheaper. Solution growth can be carried out in 2 ml and 5 ml ceramic or refractory metallic crucibles and greatly reduce the price of search similar to solid state reactions. Moreover, relatively simpler growth equipment (e.g., crucibles, ampoules and furnaces) make the growth cheaper.

(ii) Confirmation of the homogeneous melt at highest temperature: At highest temperature, the growth ampoule can be centrifuged decanting all the growth materials passing through the crystal separator filter in the catch crucible without loss of growth materials, which can be easily recycled if frit-disc crucible set is used for the flux growth [3]. The undissolved component can be fractionalized out to start the new growth or the information could be used to identify the appropriate composition for next crystal growth trails.

(iii) Easier crystal growth method for peritectic and volatile compounds: In the solution growth technique, the peritectic decomposition temperature could be easily avoided by selecting the starting growth composition that intersects liquids well below the peritectic line. For example, peritectic decomposition range of $CeCo_2$ could be avoided with a binary growth composition that contains greater than 30 atomic percentage of Ce. Similarly in Fe_5B_2P [14], dealing with high vapour pressure element P needs additional cautions. In our experiment, Fe and B powders were soaked in the molten P and slowly heated up allowing the solid state reaction which avoids the excessive boiling of P before it forms a homogeneous liquid with the reactants. This method is not possible in crystal growth methods out of melts such as Czochralski, Verneuli, Bridgman and optical floating zone process. A separate encapsulated chamber is necessary to generate the higher pressure than the partial pressure of volatile component to avoid its evaporation. For example, a liquid encapsulated modified Czochralski method is employed to deal with compounds containing a volatile or a high vapour pressure element [15].

(iv) Correction of the existing phase diagrams and discovery of new compounds: The existing experimental phase diagrams for various elements are only the suggestions of reality. The accuracy

of every reported reactions depends on variables such as purity of elements, accuracy and sensitivity of temperature probes, characterization probes etc. Solution growth provides quick verification of, or correction of, the local segment of the phase diagrams with relatively small amount of growth materials. Sometime it can reveal new compounds, probably peritectically forming, in phase diagrams which even could have very small exposed liquidus region such as RCd_x quasicrystals [16].

2.1.2.1 An example of fractionation of the melt in $AlMn_2B_2$ solution growth using Canfield Crucible Sets

Traditionally, a single crystal solution growth is carried out in ceramic crucibles which lack a ceramic filter. Often, the separation of crystals and flux was achieved by using a quartz wool plug inside the catch crucibles [2]. This method sacrifices the flux which could be recycled for future growths or used for successive growths to scan the phase diagrams. To overcome this limitation, Canfield et al. have recently come up with a special crystal growth assembly known as a frit-disc crucible set as shown in Fig. 2.4 in which a ceramic filter that fits well in between the growth and the catch crucible [17]. These are sold by LSA Ceramics as Canfield Crucible Sets (CCS).

CCS are very useful for exploratory binary, ternary and even quarternary single crystals growth using the solution-growth technique. In a CCS set, the frit and crucibles are so well aligned that the fractionated melt could be reused and recycled for multiple growth attempts [3]. CCS were used to grow $AlMn_2B_2$ single crystals out of the Al rich starting composition $Al_{68}Mn_{22}B_{10}$ as explained below.

Al shots (Alfa Aesar 99.999%), B pieces (Alfa Aesar 99.5% metal basis) and Mn pieces (Alfa Aesar 99.9% metal basis) after surface oxidation cleaning as described elsewhere [18] were used for the crystal growth process. We started with an Al rich composition, $Al_{68}Mn_{22}B_{10}$, and arc-melted it at least 4 times under an Ar atmosphere (mass loss less than 2%) to make sure the dissolution of B in the melt. The button was then cut with a metal cutter and re-arcmelted if some unreacted B pieces were found. After the button appeared to be homogeneous, it was packed in a fritted alumina crucible set [17] and sealed under a partial pressure of argon inside an amorphous silica

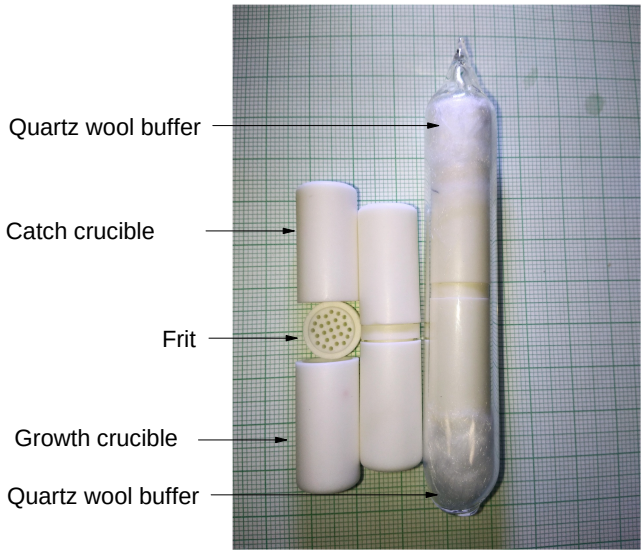

Figure 2.4 Left and middle: CCS on a millimeter grid. Right: Crystal growth ampoule formed with growth materials loaded CCS under partial pressure of Ar. The quartz wool at the top and bottom of the ampoule protects it from differential thermal expansion during heating and cooling and from mechanical shock during centrifuging.

jacket to form a growth ampoule as shown in Fig. 2.4. The growth ampoule was then heated to 1200 °C over 2 h and soaked there for 10 h before decanting using a centrifuge. Due to the high melting point of boron containing compounds, a single phase, homogeneous liquid was not formed at 1200 °C. The undissolved polycrystalline MnB and Al-Mn binary compounds were separated at 1200 °C via centrifuging. The catch crucible that collected the homogeneous melt fraction of this initial step at 1200 °C was then again sealed in another fritted alumina crucible set under Ar atmosphere to form second growth ampoule. This second ampoule was heated to 1200 °C over 2 h, held there for another 10 h and cooled down to 1100 °C over 50 h and spun using centrifuge to separate the crystals. The second growth attempt produced a mixture of the targeted $AlMn_2B_2$ phase along with MnB crystals. To avoid this MnB contamination, the catch crucible of this second growth step was used for a third growth and sealed again, as a part of CCS, under a partial pressure of Ar. For this stage, to make sure there are no other nucleated crystals, the third growth growth was heated to 1200 °C over 2 h and soaked there for 2 h. It was then cooled down to 1100 °C

over 1 h and stayed there for 1 h followed by slow cooling to 990 °C over 120 h and centrifuged to separate large, single phased $AlMn_2B_2$ crystals with dimensions as large as 4 x 2 x 0.1 mm^3 as shown in Fig. 2.5. The remaining flux, on the surface of the crystals, was removed via etching in concentrated NaOH.

Figure 2.5 Fractionated melt flux grown, NaOH etched $AlMn_2B_2$ crystals

It should be noted that predominantly single phase $AlMn_2B_2$ crystals could be (and were) grown in single growth attempt using initial $Al_{84}Mn_8B_8$ composition however the crystals were smaller than those shown in Fig. 2.5, due to multiple nucleation sites possibly due to tiny grains of undissolved B.

2.1.3 Structural, composition and orientation characterizations

Powder x-rays diffraction: The most convenient technique to take a structural finger print of materials is x-rays diffraction (XRD). The wavelength of x-rays naturally matches with the inter-planer spacing (d_{hkl}) between the lattice planes and x-rays are diffracted following the Bragg's law [19]

$$2d_{hkl}\ \sin\theta_{\mathrm{n}} = \mathrm{n}\lambda \tag{2.1}$$

where (hkl) are the Miller indices of a diffraction plane, n is the order of the diffraction peak and λ is the wave length of incident x-rays. The physical principle of x-rays diffraction is the interference of coherent x-ray wave fronts diffracted from different layers of lattice of particular inter-planer spacing d_{hkl}. The constructive diffraction peaks are observed at particular angle $2\theta_n$ which provides a unique signature for a compound. By matching these diffraction patterns with a vast collection of structural database, the structure and composition of the compounds can be identified. With the known structure and powder diffraction pattern, the lattice parameters can be extracted for the compounds using the Le Bail fitting of the pattern [20]. The powder diffraction pattern is sufficient to study the structural aspects of solid solutions since they follow the Vegard's law, which states that the lattice parameter vary proportional to the concentration of the dopant [21]. For all the compounds studied in this thesis, powder XRD was carried out using Rigaku MiniFlex II diffractrometer in a Bragg-Brantano ($\theta - 2\theta$) geometry. Besides lattice parameters and particle sizes, Bragg-Brentano diffractrometer could be use to identify the crystallographic orientation information of the single crystals and lattice parameter corresponding to plate like facet [22]. The measured powder XRD patterns were analyzed using GSAS [23], EXPGUI [24] and Fullprof [25] software packages.

Laue Diffraction: The Laue diffraction principle is exactly the same as the Bragg's diffraction except (i) it is a three dimensional diffraction and (ii) the x-ray is from a broad-wavelength source. The Laue diffraction condition could be conveniently displayed in an Ewald sphere construction as shown in Fig. 2.6. In the Ewald sphere, the center of the sphere is the real diffracting crystal, the incident (k_i) and diffracted (k_f) wave vectors are chosen to end up in the intersection of reciprocal lattices points and the Ewald circle itself. In terms of vector notation:

$$\vec{k}_i - \vec{k}_f = \vec{\Delta k} = \vec{G} \tag{2.2}$$

When Laue back-scattered photographs are taken, we observe the projection of reciprocal lattice points on the detector screen. Then the reciprocal lattice system is analyzed in combination with

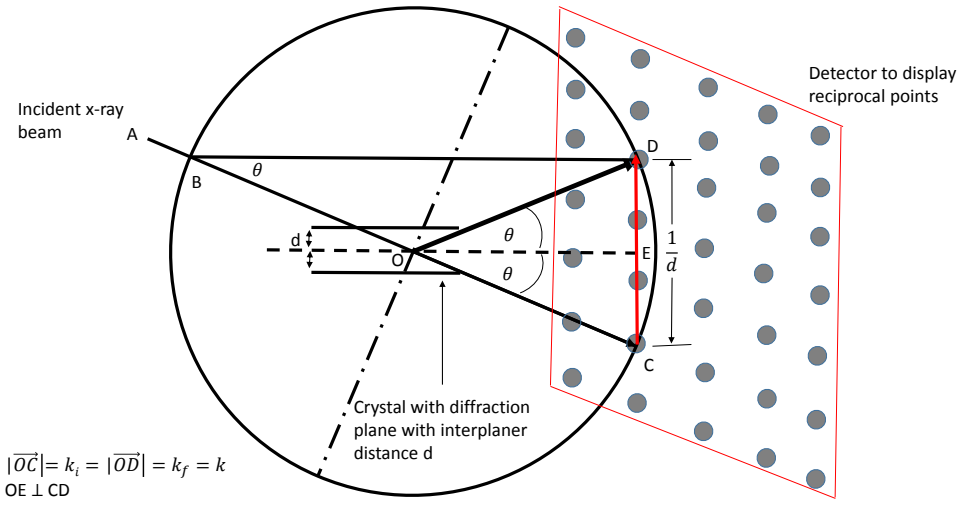

Figure 2.6 Schematic construction for an Ewald sphere. The incident x-ray beam is diffracted elastically from a plane making a glancing angle θ with it. The direct crystal plane OE is perpendicular to the reciprocal lattice plane CD.

intuitive symmetry analysis and using software packages such as Orient Express [26] and Laue Clip [27].

To alternatively verify the Laue back-scattered results analysis, monochromatic x-ray diffraction from the crystal surface in a Bragg-Brentano geometry [22] was employed in crystallographic orientation characterization of ZrMnP, HfMnP [18], $Ce_{3-x}Mg_xCo_9$ [28], $AlFe_2B_2$ [29] and $AlMn_2B_2$ [30].

2.1.4 Electrical transport properties

Electrical transport is a key measurable quantity to identify materials temperature dependent resistance properties and associated phase transition phenomena. It identifies whether a material is a metal or an insulator. The resistivity of semiconductors exponentially increases with decreasing temperature ($\rho(T)_{semi} \propto e^{\beta\Delta}$, $\beta = \frac{1}{k_B T}$, where Δ is the band-gap and k_B is Boltzmann constant) whereas it monotonically decreases for simple metals. The electrical resistivity of a typical metal is associated with several scattering sources including a defect and impurity scattering term ρ_0, electron-electron scattering (ρ_{el-el}), spin-spin scattering in magnetic materials (ρ_{S-S}), interacting

magnetic impurities in a nonmagnetic host known as Kondo scattering (ρ_{Kondo}), and electron-phonon interaction (ρ_{el-ph}) given as:

$$\rho(T) = \rho_0 + \rho_{el-el} + \rho_{s-S} + \rho_{Kondo} + \rho_{el-ph} \tag{2.3}$$

The imperfection scattering term (ρ_0) is temperature independent and can provide some basic information about the sample quality. The base temperature residual resistance ρ_0 and residual resistivity ratio (RRR) $\frac{R(300K)}{R(2K)}$ can provide initial insight about the purity of the material: the higher the value of RRR, the better the quality of the material. The imperfection scattering term ρ_0 could be of the order of few $\mu\Omega cm$ (e.g., generic metallic element can have ρ_0 on the order of 0.1 - 1.0 $\mu\Omega cm$) The second term in equation 2.3 ρ_{el-el} is associated with Fermi liquid behaviour which is proportional to T^2 ($\rho_{el-el} = AT^2$) [31]. In a Fermi liquid, electrons only around Fermi level (E_F) can be excited with thermal energy (k_BT) with a scattering probability proportional to $\frac{k_BT}{E_F}$. The proportionality constant is given as $A = \frac{\hbar}{e^2}\frac{k_B^2}{E_F^2}l_{quad}$ where $\hbar$ is Plank constant per unit 2π, e is electronic charge and l_{quad} is characteristic length scale for a material under study which depends electronic density of states [31]. By fitting the experimental data within $0 - 12$ K temperature range, the magnitude of the coefficient A for V, Pt and Cu was reported to be 370, 110 and 3 $\frac{f\Omega m}{\mathrm{K}^2}$ respectively [32]. In most simple metals, then, this is very small term even at 4 K.

The spin spin scattering term ρ_{s-S} occurs due to scattering of conduction electrons due to spins of bound electrons in magnetic ions. These magnetic ions electrons are interacting via exchange interaction in a magnetic material. The nature of conduction electron scattering depends on whether these bound electrons are in paramagnetic regime or in an ordered state. At a high temperature paramagnetic regime, there is inelastic spin scattering due to non periodic nature of the spins. As soon as the magnetic ordering takes place, the scattering between the conduction electrons and the bound spins becomes elastic [33] and the there is noticeable difference in conduction electron scattering. This difference in scattering becomes visible in terms of an anomaly in electrical resistivity around paramagnetic to magnetic phase transition temperature of a magnetic material via temperature derivative of resistivity $\frac{d\rho(T)}{dT}$. The nature of the temperature variation

of the spin-spin scattering term depends on the details of the magnetic order of the system. For example, the spin-spin scattering term (ρ_{s-S}) for transition metal, itinerant ferromagnets exhibit a T^2 behaviour due to inter-band spin-flip electron scattering by magnons in a low temperature regime [34].

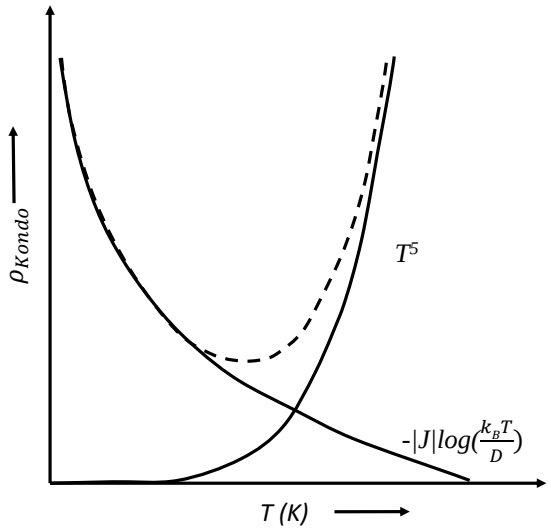

Figure 2.7 Typical resistivity characteristics (the dotted line) associated with dilute local moment magnetic impurities embedded in metallic hosts. The minimum in the resistivity generally occurs around some low temperature (e.g. 10 K for CeB_6 [35]) where the Kondo contribution (proportional to - $|J|\log\frac{k_BT}{D}$ [36]) and electron-phonon term (proportional to T^5) intersect each-other.

For a material with very dilute randomly substituted local moment magnetic impurity ions in a nonmagnetic metallic host such as lightly Mn doped Cu, the resistivity increases with the decreasing temperature as a result of incoherent electron scattering known as Kondo scattering effect. In the Kondo scattering effect, Kondo singlet state is formed between local moment and conduction electrons as the temperature is reduced [37, 38]. Using the second order perturbation in impurity ion and conduction electron interaction Hamiltonian, Kondo derived the high temperature (sufficiently higher than Kondo temperature T_K) resistivity of the system (ρ_m) which is proportional to cubic power of antiferromagnetic contact interaction (J) [37], density of states in Fermi level (ρ_F) and logarithmic proportional to temperature as

$$\rho_m = A|J|^2 S(S+1)[1 - |J|\rho_F \log\frac{k_B T}{D}] \tag{2.4}$$

where A is proportionality constant, S is the impurity spin and D is the cutoff corresponding to conduction bandwidth [37] related to Kondo temperature T_K by following relation

$$k_B T_K = D\ \exp(-\frac{1}{|2J\rho_F|}) \tag{2.5}$$

The above formula can also be expressed in terms of $\frac{T}{T_K}$ ratio as

$$\frac{\rho_m}{\rho_0} \propto -\log\frac{T}{T_K} \tag{2.6}$$

Because of the negative exchange integral J for an antiferromagnetic type coupling, the resistivity of Kondo impurity system decreases with increasing temperature which competes with low temperature electron-phonon contribution (T^5) to produce a shallow minimum in the resistivity [39]. A schematic of temperature characteristics of inelastic Kondo resistivity is presented in Fig. 2.7. However, if the concentration of magnetic impurity is increased in a metallic host so as to form a periodic Kondo singlet lattice, then the material behaves as a periodic system again and the resistivity will decrease as T^2 Fermi liquid behaviour as in a heavy fermion compounds such as $CeCu_6$ [35] and $CeCoIn_5$ [40] before they undergo phase transitions, if any, at low temperature. Although, all the materials studied in this thesis were magnetic materials, they had Kondo temperatures that were effectively zero and therefore no Kondo like resistivity features were observed in their resistances. The discussion of the Kondo effect does help in understanding of the origin and nature of spin scattering in magnetic systems. One can find the additional information about Kondo lattices phenomena in these two references and more references there in [37, 41].

Finally, the last term ρ_{el-ph} term is associated with the scattering of electrons with lattice vibration quanta known as phonons. The electron phonon scattering contribution is proportional to T well above the Debye temperature and T^5 at low temperature. In a combined form, the

electron phonon scattering contribution is given by the Bloch-Grunisen formula as

$$\rho_{el-ph} = B(\frac{T}{\Theta_R})^5 \int_0^{\frac{\Theta_R}{T}} \frac{x^5}{(e^x - 1)(1 - e^{-x})} dx \tag{2.7}$$

where B is a proportionality constant and Θ_R is the Debye temperature [42]. At very high temperature until melting, the resistivity becomes constant as soon as mean free path of electron scattering saturates [19].

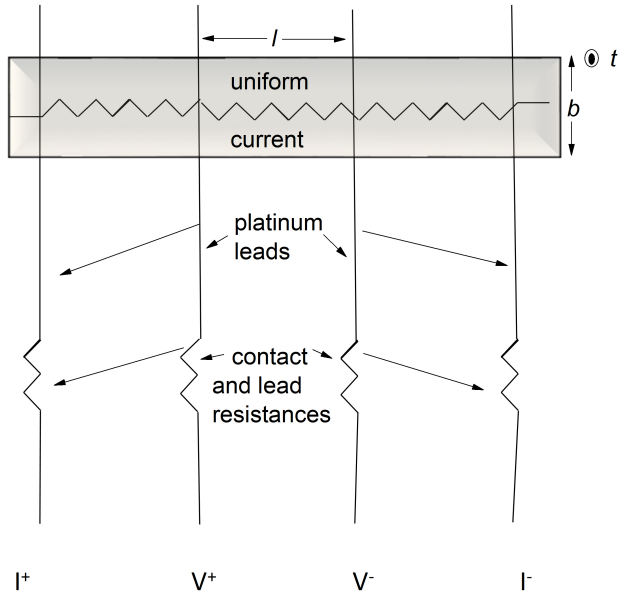

Figure 2.8 Schematic diagram of four-probe resistance measurement. The outer platinum leads I^+ and I^- provide current and inner platinum leads V^+ and V^- collect the voltage from the uniform current flowing region of the sample. The resistivity at a given temperature is determined as $\rho(T) = \frac{R \times b \times t}{l}$ where l is length of sample between voltage leads, b is breadth and t is thickness of the resistance bar.

To measure an electrical resistance of single crystalline samples, traditional four-probe resistance bars were prepared and temperature dependent electrical resistance was measured using an ac resistance bridge LR 700 (1 mA excitation current with f = 17Hz). A Quantum Design (QD) Magnetic Property Measurement System (MPMS) was used for the temperature control and the data acquisition purposes.

A schematic block diagram for a four probe sample arrangement is shown in Fig. 2.8. A polished sample bar is connected with four Pt wires to construct a resistance measurement assembly. The inner Pt wires are the voltage leads and outer wires are current leads. For the connection, silver paint, or epoxy, was used. These contacts generate the contact resistance in each lead. In each experimental assembly, the contact resistance was less than 2 Ω. The contact resistance is detrimental to the resistivity measurement since it can locally generate Joule heating effect($H = I^2R$).

2.1.5 Magnetic properties measurements

In chapter 1, several microscopic concepts of magnetization were discussed. Experimentally, a magnetizing field (H) is applied and induced magnetization (M) is measured as a moment per unit mass or volume. The magnetic susceptibility of a material is defined as:

$$\chi = \lim_{H \to 0} \frac{dM}{dH} \tag{2.8}$$

There are five major sources of magnetic susceptibility as: (i) Core diamagnetism (χ_{core}) (ii) Pauli paramagnetism (χ_{Pauli}) (iii) Landau diamagnetism (χ_{Landau}) (iv) Van Vleck paramagnetism (χ_{VV}) and (V) Curie-Weiss (χ_{CW}) susceptibility i.e.,

$$\chi_T = \chi_{\text{core}} + \chi_{\text{Pauli}} + \chi_{\text{Landau}} + \chi_{\text{VV}} + \chi_{\text{CW}} \tag{2.9}$$

The susceptibility of a material is either dominated by one of the above types or the combined effect of multiple types of susceptibilities.

The initial three types of susceptibilities are roughly temperature independent if there is no phase transition over the temperature ranges commonly measured ($T \leq 300$) K or even higher temperature ranges ($T \leq 1000$ K). The core diamagnetism is associated with completely filled electronic states and these states tend to oppose the magnetizing field via Lenz's law. The core diamagnetic susceptibility is a characteristic constant for a material and proportional to effective

atomic number times the average square of electronic orbital radius ($Z_{eff} < r^2 >$) [36] (see derivations in subsections 1.2.4 and 1.2.6). The Pauli paramagnetic susceptibility is a small temperature independent positive term associated with the magnetization of conduction electrons. It is proportional to electronic density of states in the Fermi surface ($g(E_F)$) and given as $\chi_{\text{Pauli}} = \mu_B^2 g(E_F)$ (see derivation in section 1.2.13). The Landau diamagnetism is associated with the orbital motion of conduction electrons around the axis of the external magnetic field. The conduction electronic states are quantized in cylindrical tubes like states (degeneracy $p = \frac{2e\phi}{h}$) known as Landau levels, ϕ being the magnetic flux through the system [36]. Of course, these completely filled Landau levels contribute toward the diamagnetic susceptibility given as

$$\chi_{\text{Landau}} = -(\frac{m_e}{m_e^*})^2 \frac{\chi_{\text{Pauli}}}{3} \tag{2.10}$$

where $\chi_{\text{Pauli}} = \mu_B^2 g(E_F)$. m_e and m_e^* are free and effective electron masses respectively [36].

The Van Vleck susceptibility (χ_{VV}) becomes temperature independent in the low temperature regime due to the narrowly separated excited states ($k_B T << \Delta$ even at low temperature) with the singlet ground state [43]. In such a situation, the total effective angular momentum number J becomes zero only at low temperature such that $\Delta \sim k_B T_{<J>=0}$. This situation could be originated from one electron less than half field magnetic ions such as Eu^{3+} or Sm^{+2} or crystal field detected singlet ground state with narrowly separated excited states as in a Pr compound [44] (see explanation in section 1.2.7). From an experiment point of view, one can identify the Van Vleck susceptibility if it is temperature independent at low temperature, then exhibits Curie-like crossover at higher temperature.

Finally, the susceptibility associated with local magnetic moments, which has thermal energy greater than ordering energy $k_B T > J$, that decays inversely with temperature is called Curie susceptibility given as

$$\chi(T) = \frac{N}{V} \frac{g^2 \mu_B^2}{3} \frac{J(J+1)}{k_B T} \tag{2.11}$$

where $C = \frac{N}{V}\frac{g^2\mu_B^2}{3}\frac{J(J+1)}{k_B}$ is called Curie constant (see derivation in section 1.2.7). The modification of the temperature dependence of the susceptibility with exchange interaction is called Curie-Weiss susceptibility modified as $\chi_{CW} = \frac{C}{T \pm \theta}$, θ being the Weiss temperature. Additional details in χ_{CW} is explained in section 1.2.8 in the discussion of mean field theory.

The magnetic property of a material depends upon the resultant effect of all kinds of the susceptibilities. A Pauli paramgnetic material is characterized with a positive temperature-independent magnetic susceptibility meaning that the conduction electrons spins are playing dominant role in its magnetism. Elemental Cu is diamagnetic despite its unpaired $4s^1$ electron. This is the result of the core diamagnetic contribution exceeding the Pauli paramagnetic susceptibility. Similarly, the diamagnetism of Bi is explained with the larger Landau diamagnetic contribution than its Pauli paramagnetic counterpart due to its small effective mass $m_e^* = 0.01m_e$ [36]. The Curie susceptibility of the noninteracting local moments decreases inversely with temperature.

Ferromagnetism is characterized by the evolution of spontaneous magnetization below Curie temperature. The magnetic susceptibility in terms of initial slope of magnetization can not be defined in case of ferromagnetism.

To measure a sample's magnetization, a Quantum Design MPMS was used in the temperature range 1.8 - 300 K. In a MPMS, liquid helium was used as a cryogenic medium with a boiling temperature of 4.2 K. To reach the 1.8 K temperature, the sample chamber is pumped down to a lower pressure [46]. The polycrystalline and needle-like single-crystalline samples were mounted in and between clear, uniform straws as shown in Fig. 2.9(a)-(c) and attached to the MPMS sample rod with help of a dental floss. For plate like samples, either teflon (not preferred) or an acrylic disk was used to support the sample for the measurement of magnetization perpendicular to plates, as shown in Figs. 2.9 (c) and (d). Whenever disc mounting was used (Fig. 2.9 d), background magnetization was subtracted if the magnetization was found to be sufficiently weak. The best result of the background subtraction is obtained if the magnetization of the disc is obtained for the same measurement sequence for the sample. Otherwise, additional numerical interpolation is necessary.

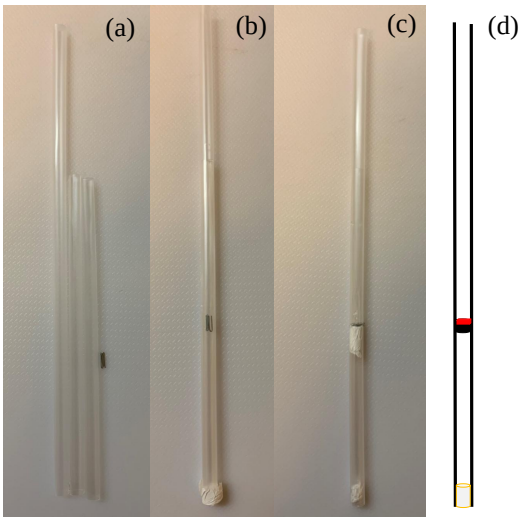

Figure 2.9 MPMS sample mounting using plastic straws and teflon tape and mounting disc. (a) One longer intact straw and two laterally oneside opened straws along with needle like magnetic sample (b) mounting of needle-like samples in the layers of one side opened straws and inserted inside the longer intact straw followed by teflon taping on the lower end (c) mounting the needle like samples to measure the magnetization perpendicular their length (d) Schematic of a cuboid sample on the mounting disc inside the straw.

A Quantum Design physical property measurement system (PPMS) VersaLab vibrating Sample Magnetometer (VSM) was used to measure the magnetization in the 50 - 1000 K range. A VSM that could generate 3 Tesla magnetic field using NbTi superconducting solenoid with 20 A current was used in these measurements [47]. It uses a compressed helium gas cryocooler to cool down to the operating temperature of the superconducting magnet ($\sim$ 4K) and the sample chamber (down to 50 K). The VSM incorporates either a standard option (50 - 400 K) or an oven option (300 - 1000 K) mode as shown in Fig. 2.10 (a) - (c). The sample holder of the oven option mode is connected to electric heating circuit whereas standard option does not require heating assembly. High temperature magnetization measurement uses a platinum thin film heater stick [47] and Zircar alumina cement is used to mount the magnetization measurement sample on the heater stick. Polycrystalline chunks or naturally flat faced samples can be readily mounted. Single crystalline

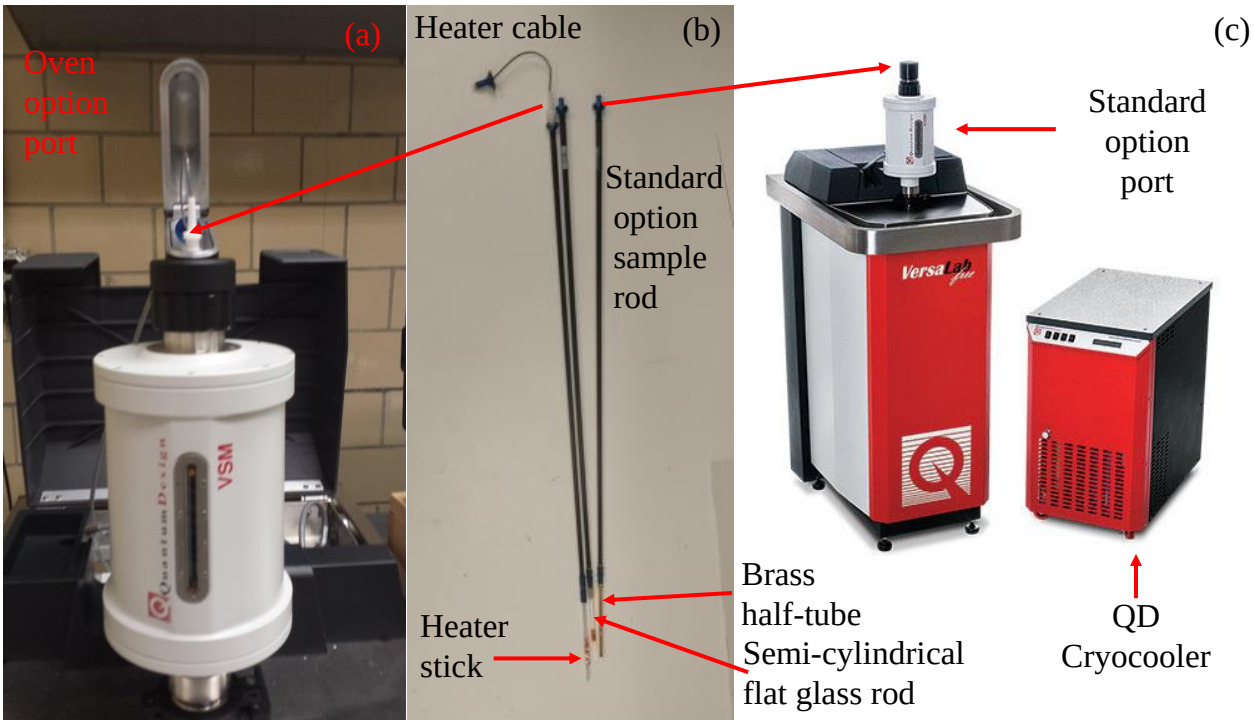

Figure 2.10 VSM (a) oven option port (b) sample mounting rods with heater stick for the oven option, semicylindrical flat glass rod and half-brass tube for the standard option (c) picture of a complete VSM standard option mode setup along with a QD cryocooler on the right, Images © 2019, Quantum Design, Inc. (included with permission) [45].

samples were cut or polished in cuboid shapes so that (i) they could be properly mounted on the platinum heater stick using Zircar cement and (ii) the associated demagnetization effect could be appropriately accounted for. The desired alignment of the prismatic samples was often achieved on the heater stick under a microscope. The mounted sample on the heater stick was covered with approximately one inch long copper foil to avoid the radiation loss and reduce the temperature gradient between platinum heater and top surface of the sample.

The sample rod installation process was done as quick as possible so that contamination of sample chamber with atmospheric dust and moisture could be avoided. Similarly, proper sealing of the various O-rings could reduce the diffusion of the moisture and atmospheric gases in the cryocooler cycle. Attaining the required high vacuum for the oven option is the most challenging

job in the oven option application. This could be achieved relatively easier if the sample chamber and O-rings are regularly cleaned and O-rings are properly greased with a high vacuum grease. Inside the cryocooler compression cycle, a charcoal chamber is used to absorb the diffused gases. When the charcoal is saturated with permeated gases, it should be heated to high temperature to remove the trapped gases. This process is called regeneration [47].

In the standard option, GE varnish, permabond, loctite glue, teflon tape and Kapton tape were used to to mount the samples. The background correction were employed if found necessary (greater than 2% difference). A lot of additional relevant information of sample mounting could be found in the QD application note 1096-306 [48].

2.1.5.1 Spontaneous Magnetization determination

The spontaneous magnetization well below the Curie temperature was determined by the linear fit of the saturated high-field-magnetization data as shown in Fig. 2.12 ($M_S \sim 24\mu_B/f.u.$ for $Sm_2Co_{16.69}Ta_{0.31}$ at 2 K). In this diagram, the Y-intercept of linearly fitted red line for the horizontal magnetization section of the c-axis magnetization provides the spontaneous magnetization. The spontaneous magnetization for the easy axis magnetization and saturation magnetization are approximately equal at sufficiently low temperature in comparison to the Curie temperature of the sample. Additional examples and explanation of spontaneous magnetization determination can be found in the references [28, 49]. The spontaneous magnetization near the critical region i.e. in the vicinity of transition temperature was determined using the Y-intercept of the Arrott plot or $\frac{H_{int}}{M}$ vs M^4 [50, 29]. The $\frac{H_{int}}{M}$ vs M^4 graph becomes essential when the Arrott plot are not straight enough to provide an unambiguous Y-intercept. Generally, Arrott plots are straight lines only for ideally mean field ferromagnets. The spontaneous magnetization is useful for estimation of Curie temperature using the power laws fitting such as generalized Bloch law ($M(T) = M(0)[1 - (\frac{T}{T_c})^{\frac{3}{2}}]$) [51] and the estimation of the maximum theoretical energy product of permanent magnets [$(BH)_{\max} = \frac{M_S^2}{4\mu_0}$] [52].

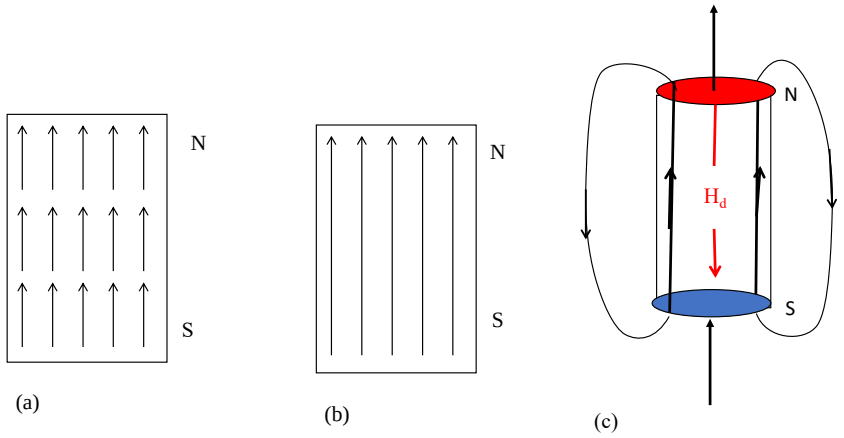

Figure 2.11 Demonstration of the mechanism of formation of magnetic poles in a uniformly magnetized sample that are responsible for magnetostatic energy. (a) A ferromagnetic sample showing the perfect alignment of the atomic magnetic moments. (b) Coupling of the atomic magnets inside the magnetic volume leaves only north pole in the upper end and the south pole in the lower end of the sample (c) The magnetic field lines outside the magnetic volume oppose the direction of magnetic moments inside. This could be considered to be equivalent to the field lines inside the magnetic volume due to the virtual magnetic poles localized at the end of the sample. This field is called demagnetization field H_d.

2.1.5.2 Demagnetization factor determination

The origin of demagnetization effect in ferromagnetic sample is the shape anisotropy which exists due to the magnetostatic field of magnetic poles located on the extremities of a magnetized sample as shown in Fig. 2.11(a) - (c) for a rectangular sample. The magnitude of the demagnetization field inside a ferromagnetic sample can be understood using the second Maxwell equation

$$\nabla . B = 0 \tag{2.12}$$

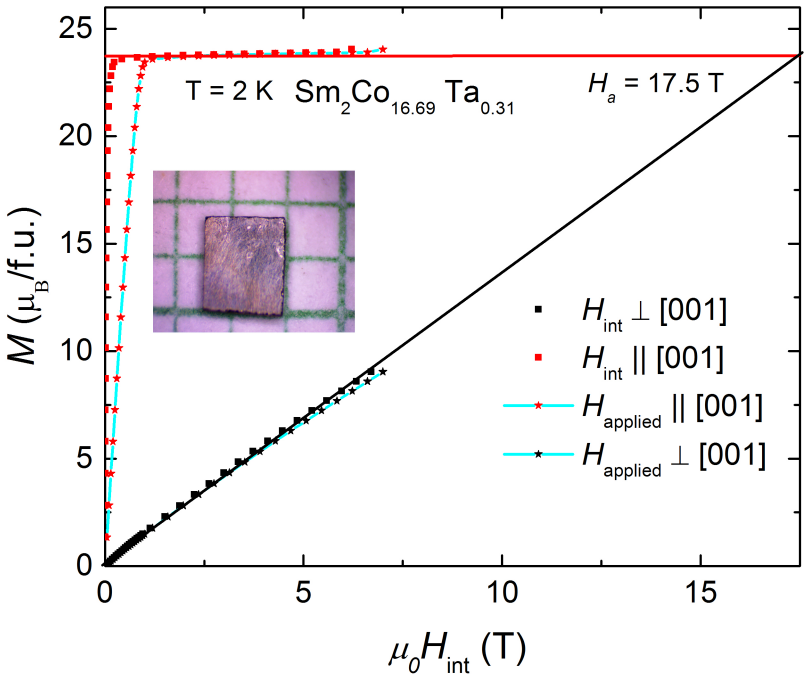

Figure 2.12 Determination of an anisotropy field at 2 K using an extrapolation of magnetization data for $Sm_2Co_{16.69}Ta_{0.31}$. The magnetic field corresponding to the intersection of extrapolation of higher field magnetization data of easy and hard axis magnetization is the anisotropic magnetic field ($\sim$ 17.5 T). The demagnetization field $H_d = |NM|$ could be read from the easy axis magnetization data around 1 T field. The inset shows the polished sample to facilitate the dimensions measurement to calculate demagnetization factors [53].

Since $B = \mu_0(H + M)$

$$\nabla.\mu_0(H + M) = 0$$

$$\nabla.H = -\nabla.M \tag{2.13}$$

Though B is solonoidal i.e. perfect dipolar, H is not. The magnetic monopoles are required to satisfy the equation 2.13. Experimentally magnetic monopoles are not detected yet. Hence the free end of the sample acts as magnetic poles as demonstrated in Fig. 2.11(c). The magnetostatic field (demagnetization field H_d) of these magnetic poles oppose the magnetic field lines inside the sample volume and is proportional to net magnetization i.e.,

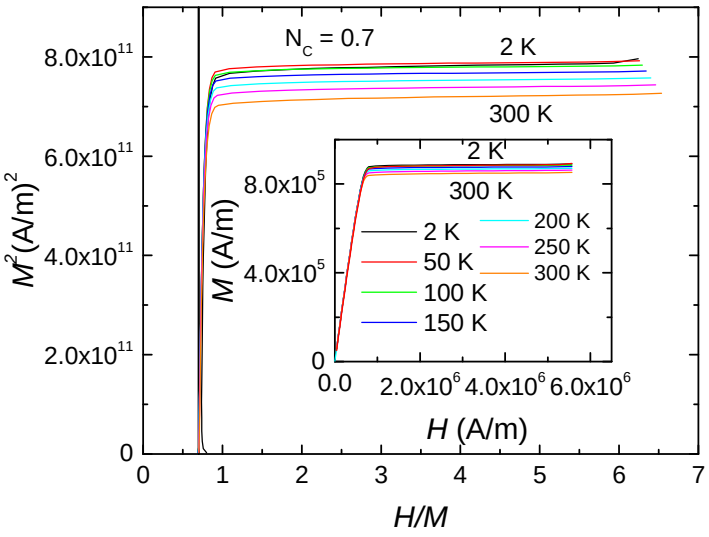

Figure 2.13 Low temperature easy axis Arrott plot of $Sm_2Co_{16.69}Ta_{0.31}$ to estimate the experimental demagnetization factor. The x-intercept of M^2 vs $\frac{H}{M}$ for H = 0 provides the demagnetization factor $N_C = 0.7$. The inset shows the corresponding *M(H)* data.

$$H_d \propto -M$$

$$\therefore H_d = -NM \tag{2.14}$$

Here N is the proportionality constant also known as demagnetization tensor. This relation is strictly valid for the spheroidal samples in which demagnetization field in all directions. If this relation is used for the prismatic samples, it is assumed that the demagnetization field is the average within the whole geometry. In matrix form the demagnetization field can be expressed as

$$(H_d)_i = -\sum_{ij} N_{ij} M_j \tag{2.15}$$

The off diagonal elements of demagnetization tensor could be reduced to zero if an external magnetic field is applied parallel to the principal axes of the regular shaped magnetic samples.

$$N = \begin{pmatrix} N_x & 0 & 0 \\ 0 & N_y & 0 \\ 0 & 0 & N_z \end{pmatrix} \tag{2.16}$$

The trace of diagonalized tensor satisfies a relation Trace (N_{ij}) = D(r) [54] where D(r) is called a shape function. The shape function is defined as

$$\begin{aligned} D(r) &= 1 \quad \text{inside the sample} \\ D(r) &= 0 \quad \text{outside} \end{aligned} \tag{2.17}$$

The shape function takes the unity value under certain assumptions such as the demagnetization effect depends only on the sample geometry and magnetization is uniform throughout the samples. However, the problem of demagnetization requires further studies. For example, the magnetization inside the most of the experimental samples is nonuniform, specially it varies appreciably near the sharp sample boundaries. The demagnetization factors also depend on the permeability of the samples [55].

Throughout this thesis, we estimated the approximate demagnetization factors that accounts only the major shape effect of demagnetization for the measured samples (which were cut and polished into the prismatic shape of known dimensions) using the micromagnetic approach as outlined by Aharoni [53]. To better track the demagnetization factors in different directions, measurements samples were polished in a regular parallelepiped shapes often with facets parallel to principle crystallographic planes as shown in the upper left inset of Fig. 2.12. The easy axis demagnetization effect is independent of temperature as shown in Fig. 2.13. This behaviour is manifested in the overlapping of the easy axis Arrott plot isotherms at low temperature and helps to experimentally determine the easy axis demagnetization factor N_{easy} (N_C in case of $Sm_2Co_{16.69}Ta_{0.31}$) [14]. Once N_{easy} is determined, the square shaped sample provides a guide line to calculate the demagnetization factor as $N_{other\ axis} = \frac{1-N_{easy}}{2}$ on the basis of the formula $N_A + N_B + N_C = 1$ [36].

Finally, the demagnetization effect is corrected by determining the internal field in the sample:

$$H_{int} = H_{applied} - N * M \tag{2.18}$$

where N is the demagnetization factor and M is the magnetization.

2.1.5.3 Anisotropy field determination

A anisotropy field is the magnitude of the field which saturates the hard axis magnetization. An example of the anisotropic field determination for $Nd_2Fe_{14}B$ by Bolzoni et al. clearly demonstrate how to get the anisotropy field if sufficiently large magnetizing field is applied [56]. In case of very large anisotropy and unavailability of large enough field, extrapolation of the magnetization to estimate the anisotropy field was adopted in various systems including Ta substituted $Sm_2Co_{16.69}Ta_{0.31}$ as shown in Fig. 2.12. This extrapolation method generally provides a minimum estimate of the anisotropy field since the extrapolation for the hard axis magnetization is often started from the higher slope region. In an uniaxial system, the first anisotropy constant can be estimated using the anisotropy field H_a and saturation magnetization M_S as $K_1 = \frac{H_a * M_S}{2}$ which is technically the area between the easy and hard axis magnetization curves in the first quadrant as shown in Fig. 2.12.

2.1.5.4 Anisotropy Energy density determination

The magnetocrystalline anisotropy energy (MAE) for a single crystalline sample is expressed in equation (1.73) plus the Zeeman term provides the total MAE of a single crystalline sample in an external magnetic field H as [57]:

$$E_{\mathrm{MAE}} = K_0 + K_1 \sin^2\theta + \mathrm{K}_2 \sin^4\theta + ... + M_{\mathrm{S}}\ H \cos(\frac{\pi}{2} - \theta) \tag{2.19}$$

where M_S is the saturation magnetization and θ is the angle between easy axis and magnetization direction. $\frac{\pi}{2} - \theta$ is the angle between hard axis and magnetization. In an equilibrium, total MAE remains uniform i.e.

$$\frac{\partial E_{\mathrm{MAE}}}{\partial \theta} = 0 \Rightarrow 4K_2 \sin^3\theta \cos\theta + 2\ K_1 \sin\theta \cos\theta = M_{\mathrm{S}}\ H \cos\theta$$

Using $\sin\theta = \frac{M_\perp}{M_S}$ we get,

$$\frac{H}{M_\perp} = \frac{2K_1}{M_S^2} + \frac{4K_2}{M_S^4} M_\perp^2 \tag{2.20}$$

This equation is famous Sucksmith-Thompson equation to estimate the MAE. The intercept of the equation 2.20 determines the anisotropy constant as Intercept = $\frac{2K_1}{M_S^2}$ and slope = $\frac{4K_2}{M_S^4}$. After the proper demagnetization correction, Sucksmith-Thompson equation 2.20 takes the form:

$$\frac{H_{int}}{M_\perp} = \frac{2K_1}{M_S^2} + \frac{4K_2}{M_S^4} M_\perp^2 \tag{2.21}$$

For the easy axis isotherm, Sucksmith-Thompson relation takes a form [57]:

$$\frac{H_{int}}{M_\parallel} = \frac{2(K_1 + 2K_2)}{M_S^2} + \frac{4K_2}{M_S^4} M_\parallel^2 \tag{2.22}$$

2.2 References

[1] Okamoto H. Cerium-cobalt binary phase diagram. ASM Alloy Phase Diagram Database, P. Villars, editor-in-chief; H. Okamoto and K. Cenzual, section editors, 1990.

[2] P. C. Canfield and Z. Fisk. Growth of single crystals from metallic fluxes. *Philos. Mag.*, 65(6):1117–1123, 1992.

[3] Paul C. Canfield, Tai Kong, Udhara S. Kaluarachchi, and Na Hyun Jo. Use of frit-disc crucibles for routine and exploratory solution growth of single crystalline samples. *Philos. Mag.*, 96(1):84–92, 2016.

[4] Paul C. Canfield and Ian R. Fisher. High-temperature solution growth of intermetallic single crystals and quasicrystals. *Journal of Crystal Growth*, (225):155 – 161, 2001.

[5] Wade A. Jensen, Naiming Liu, Eva Rosker, Brian F. Donovan, Brian Foley, Patrick E. Hopkins, and Jerrold A. Floro. Eutectoid transformations in Fe-Si alloys for thermoelectric applications. *Journal of Alloys and Compounds*, 721:705 – 711, 2017.

[6] Peter Capper. *Bulk Crystal Growth: Methods and Materials*. Springer International Publishing, 2017.

[7] K.Seevakan and S.Bharanidharan. Different types of crystal growth methods. *International Journal of Pure and Applied Mathematics*, 119:5743–5758, 2018.

[8] Suk-Joong L. Kang, Ji-Hoon Park, Seok-Young Ko, and Ho-Yong Lee. Solid-state conversion of single crystals: The principle and the state-of-the-art. *Journal of the American Ceramic Society*, 98(2):347–360, 2015.

[9] R. Falckenberg. *The Verneuil Process*, pages 109–184. Springer US, Boston, MA, 1978.

[10] S.M. Koohpayeh, D. Fort, and J.S. Abell. The optical floating zone technique: A review of experimental procedures with special reference to oxides. *Progress in Crystal Growth and Characterization of Materials*, 54(3):121 – 137, 2008.

[11] S.M. Koohpayeh, J.-J. Wen, B.A. Trump, C.L. Broholm, and T.M. McQueen. Synthesis, floating zone crystal growth and characterization of the quantum spin ice $Pr_2Zr_2O_7$ pyrochlore. *Journal of Crystal Growth*, 402:291 – 298, 2014.

[12] Peer Schmidt, Michael Binnewies, Robert Glaum, and Marcus Schmidt. *Chemical Vapor Transport Reactions-Methods, Materials, Modeling*, chapter 9. IntechOpen, Feb 2013.

[13] Henri Moissan. *The Electric Furnace*. London : Edward Arnold, 1904.

[14] Tej N. Lamichhane, Valentin Taufour, Srinivasa Thimmaiah, David S. Parker, Sergey L. Bud'ko, and Paul C. Canfield. A study of the physical properties of single crystalline Fe_5B_2P. *J. Magn. Magn. Mater.*, 401:525 – 531, 2016.

[15] J. Friedrich. Methods for bulk growth of inorganic crystals: Crystal growth. In *Reference Module in Materials Science and Materials Engineering*. Elsevier, 2016.

[16] Alan I. Goldman, Tai Kong, Andreas Kreyssig, Anton Jesche, Mehmet Ramazanoglu, Kevin W. Dennis, Sergey L. Budko, and Paul C. Canfield. A family of binary magnetic icosahedral quasicrystals based on rare earths and cadmium. *Nature Materials*, 12:714–718, June 2013.

[17] Paul C. Canfield, Tai Kong, Udhara S. Kaluarachchi, and Na Hyun Jo. Use of frit-disc crucibles for routine and exploratory solution growth of single crystalline samples. *Philosophical Magazine*, 96(1):84 – 92, November 2016.

[18] Tej N. Lamichhane, Valentin Taufour, Morgan W. Masters, David S. Parker, Udhara S. Kaluarachchi, Srinivasa Thimmaiah, Sergey L. Bud'ko, and Paul C. Canfield. Discovery of ferromagnetism with large magnetic anisotropy in ZrMnP and HfMnP. *Appl. Phys. Lett.*, 109(9):092402, 2016.

[19] Neil W. Ashcroft and N. David Mermin. *Solid State Physics*. Thompson Books/Cole, 2007.

[20] Armel Le Bail. Whole powder pattern decomposition methods and applications: A retrospection. *Powder Diffraction*, 20(4):316326, 2005.

[21] A. R. Denton and N. W. Ashcroft. Vegard's law. *Phys. Rev. A*, 43:3161–3164, Mar 1991.

[22] A. Jesche, M. Fix, A. Kreyssig, W. R. Meier, and P. C. Canfield. X-ray diffraction on large single crystals using a powder diffractometer. *Philos. Mag.*, 96(20):2115–2124, 2016.

[23] A. C. Larson and R. B. Von Dreele. General structure analysis system. *Los Alamos National Laboratory Report No. LAUR 86-748*, 2004.

[24] Brian H. Toby. *EXPGUI*, a graphical user interface for *GSAS*. *Journal of Applied Crystallography*, 34(2):210–213, Apr 2001.

[25] Juan Rodrguez-Carvajal. *An introduction to the program Fullprof 2000.* Laboratoire Léon Brillouin (CEA-CNRS), 2001.

[26] Jean Laugier and Bernard Bochu. LMGP-Suite Suite of Programs for the interpretation of X-ray Experiments. *ENSP/Laboratoire des Matèriaux et du Gènie Physique, BP 46. 38042 Saint Martin d'Hères, France.*

[27] Olaf Jochen Schumann. *Structural Investigations on layered Manganites and Ruthenates.* PhD thesis, Universität zu Köln, 2010.

[28] Tej N. Lamichhane, Valentin Taufour, Andriy Palasyuk, Qisheng Lin, Sergey L. Bud'ko, and Paul C. Canfield. $Ce_{3-x}Mg_xCo_9$: Transformation of a Pauli Paramagnet into a Strong Permanent Magnet. *Phys. Rev. Applied*, 9:024023, Feb 2018.

[29] Tej N. Lamichhane, Li Xiang, Qisheng Lin, Tribhuwan Pandey, David S. Parker, Tae-Hoon Kim, Lin Zhou, Matthew J. Kramer, Sergey L. Bud'ko, and Paul C. Canfield. Magnetic properties of single crystalline itinerant ferromagnet $AlFe_2B_2$. *Phys. Rev. Materials*, 2:084408, Aug 2018.

[30] Tej N. Lamichhane, Khusboo Rana, Qisheng Lin, Sergey L. Bud'ko, Yuji Furukawa, and Paul C. Canfield. Near room temperature antiferromagnetic ordering with a potential low-dimensional magnetism in $AlMn_2B_2$. *Phys. Rev. Materials*, 3:064415, Jun 2019.

[31] D. van der Marel, J. L. M. van Mechelen, and I. I. Mazin. Common Fermi-liquid origin of T^2 resistivity and superconductivity in n-type $SrTiO_3$. *Phys. Rev. B*, 84:205111, Nov 2011.

[32] D. B. Poker and C. E. Klabunde. Temperature dependence of electrical resistivity of vanadium, platinum, and copper. *Phys. Rev. B*, 26:7012–7014, Dec 1982.

[33] Tineke Van Peski-Tinbergen and A.J. Dekker. Spin-dependent scattering and resistivity of magnetic metals and alloys. *Physica*, 29(9):917 – 937, 1963.

[34] B. Raquet, M. Viret, E. Sondergard, O. Cespedes, and R. Mamy. Electron-magnon scattering and magnetic resistivity in 3*d* ferromagnets. *Phys. Rev. B*, 66:024433, Jul 2002.

[35] A. Takase, K. Kojima, T. Komatsubara, and T. Kasuya. Electrical resistivity and magnetoresistance of CeB_6. *Solid State Communications*, 36(5):461 – 464, 1980.

[36] Stephen Blundell. *Magnetism in Condensed Matter.* Oxford University Press, 2001.

[37] Piers Coleman. Heavy Fermions and the Kondo Lattice: a 21st Century Perspective. 2015.

[38] B Coqblin. *Kondo Effect (Theory)*, chapter K, pages 61 – 65. Elsevier Ltd., 2005.

[39] Jun Kondo. Resistance Minimum in Dilute Magnetic Alloys. *Progress of Theoretical Physics*, 32(1):37–49, 07 1964.

[40] C Petrovic, P G Pagliuso, M F Hundley, R Movshovich, J L Sarrao, J D Thompson, Z Fisk, and P Monthoux. Heavy-fermion superconductivity in $CeCoIn_5$ at 2.3 K. *Journal of Physics: Condensed Matter*, 13(17):L337–L342, Apr 2001.

[41] Leo Kouwenhoven and Leonid Glazman. Revival of the Kondo effect. *Physics World*, 14(1):33–38, Jan 2001.

[42] J. M. Ziman. *Principles of the Theory of Solids*. Cambridge University Press, 2 edition, 1972.

[43] J. H. Van Vleck. *The Theory of Electric and Magnetic Susceptibilities*. Oxford University Press, London, 1932. Chapter VI.

[44] E. A. Goremychkin, R. Osborn, E. D. Bauer, M. B. Maple, N. A. Frederick, W. M. Yuhasz, F. M. Woodward, and J. W. Lynn. Crystal Field Potential of $PrOs_4Sb_{12}$: Consequences for Superconductivity. *Phys. Rev. Lett.*, 93:157003, Oct 2004.

[45] VersaLab^{TM} 3 Tesla, Cryogen-free Physical Property Measurement System. Quantum Design, Inc.

[46] A. H. Cooke and R. A. Hull. Experiments on pumping liquid helium to low temperatures. *Nature*, (143):799800, 1939.

[47] Quantum Design Inc. *VersaLab user's manual, part number 1300-001, B2.*

[48] VSM sample mounting techniques, application note 1096-306, rev. b1. Technical report, Quantum Design Inc., 2016.

[49] Tej N. Lamichhane, Michael T. Onyszczak, Olena Palasyuk, Saba Sharikadze, Tae-Hoon Kim, Qisheng Lin, Matthew J. Kramer, R.W. McCallum, Aleksander L. Wysocki, Manh Cuong Nguyen, Vladimir P. Antropov, Tribhuwan Pandey, David Parker, Sergey L. Bud'ko, Paul C. Canfield, and Andriy Palasyuk. Single-crystal permanent magnets: Extraordinary magnetic behavior in the Ta-, Cu-, and Fe-substituted $CeCo_5$ systems. *Phys. Rev. Applied*, 11:014052, Jan 2019.

[50] Bin Chen, JinHu Yang, HangDong Wang, Masaki Imai, Hiroto Ohta, Chishiro Michioka, Kazuyoshi Yoshimura, and MingHu Fang. Magnetic Properties of Layered Itinerant Electron Ferromagnet Fe_3GeTe_2. *J. Phys. Soc. Jpn.*, 82(12):124711, 2013.

[51] F. Bloch. Zur theorie des ferromagnetismus. *Zeitschrift für Physik*, 61(3):206–219, Mar 1930.

[52] J. M. D. Coey. New permanent magnets manganese compounds. *Journal of Physics: Condensed Matter*, 26(6):064211, Jan 2014.

[53] Amikam Aharoni. Demagnetizing factors for rectangular ferromagnetic prisms. *J. Appl. Phys.*, 83(6):3432–3434, 1998.

[54] M. Beleggia and M. De Graef. On the computation of the demagnetization tensor field for an arbitrary particle shape using a fourier space approach. *Journal of Magnetism and Magnetic Materials*, 263(1):L1 – L9, 2003.

[55] R. Prozorov and V. G. Kogan. Effective demagnetizing factors of diamagnetic samples of various shapes. *Phys. Rev. Applied*, 10:014030, Jul 2018.

[56] F. Bolzoni, O. Moze, and L. Pareti. First order field induced magnetization transitions in single crystal $Nd_2Fe_{14}B$. *J. Appl. Phys.*, 62(2):615–620, 1987.

[57] W. Sucksmith and J. E. Thompson. The Magnetic Anisotropy of Cobalt. *Proceedings of the Royal Society of London A: Mathematical, Physical and Engineering Sciences*, 225(1162):362–375, 1954.

CHAPTER 3. A STUDY OF THE PHYSICAL PROPERTIES OF SINGLE CRYSTALLINE Fe_5B_2P

A paper published in *Journal of Magnetism and Magnetic Materials*

Tej N Lamichhane[1,2], Valentin Taufour[2] , Srinivasa Thimmaiah[2], David S. Parker[3], Sergey L. Bud'ko[1,2] and Paul C. Canfield[1,2]

1: Department of Physics and Astronomy, Iowa State University, Ames, Iowa 50011, U.S.A.

2: Ames Laboratory, Iowa State University, Ames, Iowa 50011, U.S.A.

3: Materials Science and Technology Division, Oak Ridge National Laboratory, Oak Ridge, TN 37831

3.1 Abstract

Single crystals of Fe_5B_2P were grown by self-flux growth technique. Structural and electrical and magnetic anisotropic properties are studied. The Curie temperature of Fe_5B_2P is determined to be 655$\pm$2 K. The saturation magnetization is determined to be 1.72 μ_B/Fe at 2 K. The temperature variation of the anisotropy constant K_1 is determined for the first time, reaching $\sim$ 0.50 MJ/m^3 at 2 K, and it is comparable to that of hard ferrites. The saturation magnetization is found to be larger than the hard ferrites. The first principle calculations of saturation magnetization and anisotropy constant are found to be consistent with the experimental results.

Keywords: single crystal, magnetization, demagnetization factor, Arrott plot, transition temperature, anisotropy constant

3.2 Introduction

The existence of the ternary Fe_5B_2P phase was first reported in 1962[1, 2]. The first reference reported the detailed structural information and the Curie temperature for the Fe_5B_2P phase.The

second reference reported the structural details using X-ray and chemical analysis. Its structural prototype is tetragonal Cr_5B_3 with the space group $D^{ls}_{4h} - I4/mcm$. The Curie temperature was reported to fall between 615 K to 639 K, depending upon the B content. In 1967, another study reported a Curie temperature of 628 K and a saturation magnetization of 1.73 μ_B/Fe [3]. The Fe_5B_2P phase was also studied using Mössbauer spectroscopy and X-ray diffraction in 1975 [4]. In addition to confirming the Curie temperature range as well as the average saturation magnetic moment per Fe atom, the Mössbauer study identified the average moment contributed by each of the Fe lattice sites in the Fe_5B_2P unit cell. The Fe(2) (or 4c) sites contribute 2.2 μ_B/Fe. The Fe(1) (or 16l) sites contribute 1.6 μ_B/Fe. The average extrapolated moment of the both sites at 0 K was reported to be 1.73 μ_B/Fe.

Fe_5B_2P is specifically interesting as a possible high transition temperature, rare earth free, hard ferromagnetic material. Given that all prior work on Fe_5B_2P was made on polycrystalline samples, we developed a single crystal growth protocol, measured thermodynamic and transport properties of single crystalline samples, and determined the magnetic anisotropy of this material. The anisotropy constant K_1 is positive, indicating that the c axis is the easy axis of magnetization, and has a comparable size and temperature dependence as hard ferrites such as $SrFe_{12}O_{19}$ and $BaFe_{12}O_{19}$.

3.3 Experimental Details

3.3.1 Crystal growth

As part of our effort to search for new, or poorly characterized ferromagnetic compounds, we have developed single crystal growth protocols for transition metal rich, chalcogenide and pnictide binary and ternary phases. In a manner similar to some of our earlier transition metal - sulphur work, [5, 6] we started by confirming our ability to contain Fe-P binary melts in alumina crucibles sealed in amorphous silica ampules. As outlined by Canfield and Fisk [7] and Canfield, [8] sealed ampoules were decanted after slow cooling by use of a centrifuge. Crucibles with alumina filters [9, 10] were used to allow assessment and even reuse of the decanted liquid. For this experiment, a

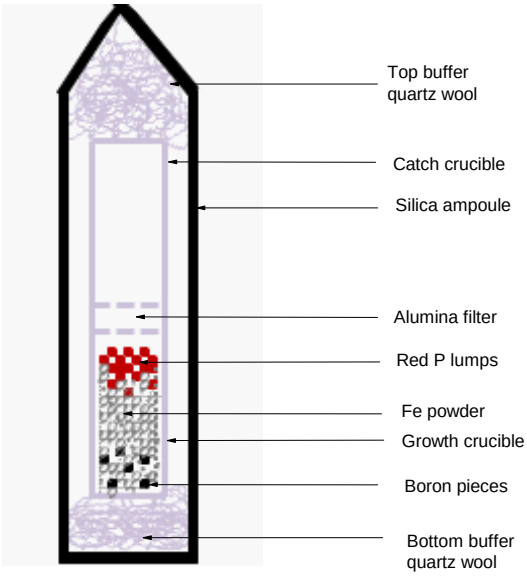

Figure 3.1 A schematic assembly of the crystal growth ampoule.

mixture of freshly ball milled iron powder and red phosphorous lumps were placed in an alumina crucible in an atomic ratio of Fe : P = 0.83 : 0.17. A homogenous liquid exists at 1060 (i.e. there was no crystal growth upon cooling from 1200 to 1060 and all of the material decanted). For similar temperature profiles, an initial melt of $Fe_{0.86}P_{0.14}$ lead to the growth of dendritic Fe whereas for initial melts of $Fe_{0.81}P_{0.19}$, $Fe_{0.79}P_{0.21}$ and $Fe_{0.77}P_{0.23}$ faceted Fe_3P was grown. These data are all consistent with the binary phase diagram [11] and indicate that the Fe-P binary melt does not have a significant partial pressure of phosphorous and does not react with alumina.

Figure 3.2 (a) The acid etched single crystals image of Fe_5B_2P (b) Laue pattern along the hard axis [100] and (c) Laue pattern along the easy axis [001] of magnetization.

After some optimization, an initial stoichiometry of $Fe_{72}P_{18}B_{10}$ was used to grow single phase Fe_5B_2P plates. Ball milled Fe (Fe lumps obtained from Ames lab), red phosphorous lumps (Alfa Aesar, 99.999% (metal basis)), and crystalline boron pieces (Alfa Aesar, 99.95%) were placed in an

alumina crucible / filter assembly, sealed in a partial pressure of Ar in an amorphous silica tube (as shown schematically in figure 3.1). The ampoule was heated over 3 hours to 250 , remained at 250 for 3 hours, heated to 1200 over 12 hours, held at 1200 for 10 hours, and then cooled to 1160 over 75 hours. After cooling to 1160 the ampoule was decanted using a centrifuge and plate like single crystals of Fe_5B_2P could be found on the growth side of the alumina filter. In order to confirm that the growth of crystals took place from a complete liquid, we decanted one growth at 1200 , instead of cooling to 1160 , and indeed found all of the material decanted.

After growth, single crystals were cleaned by etching in a roughly 6 molar HCl solution. Figure 3.2(a) shows a picture of the etched single crystals.

3.3.2 Physical properties measurement

The crystal structure and lattice parameters of Fe_5B_2P were determined with both single crystal and powder x-ray diffraction (XRD). The crystal structure of Fe_5B_2P was determined from single-crystal XRD data collected with the use of graphite monochromatized MoKα radiation ($\lambda = 0.71073$ Å) at room temperature on a Bruker APEX2 diffractometer. Reflections were gathered by taking four sets of 360 frames with 0.5° scans in ω, with an exposure time of 25 s per frame and the crystal-to-detector distance was 5 cm. The measured intensities were corrected for Lorentz and polarization effects. The intensities were further corrected for absorption using the program SADABS, as implemented in Apex 2 package [12].

For powder XRD, etched single crystals of Fe_5B_2P were selected and finely powdered. The powder was evenly spread over the zero background single crystal silicon wafer sample holder with help of a thin film of Dow Corning high vacuum grease. The powder diffraction pattern was recorded with Rigaku Miniflex diffractrometer using copper K_α radiation source over 8.5 hours (at a rate of 3 sec dwell time for per 0.01° to cover the 2θ value up to 100°).

To identify the crystallographic orientation of the single crystal plates, Laue diffraction patterns were obtained using a Multiwire Laboratories, Limited spectrometer. The resistivity anisotropy

data were measured in a four-probe configuration using a Quantum Design Magnetic Property Measurement System (MPMS) for temperature control and the external device control option to interface with a Linear Research, Inc. ac (20mA, 16 Hz) resistance bridge (LR 700). To make the resistivity anisotropy data more reliable, resistivity bar for both [100] and [001] axes were taken from the same crystal as shown in the inset of figure 3.5.

The sample preparation for magnetization measurements is a major step in a magnetic anisotropy study. The etched crystal was cut into a rectangular prismatic shape and the dimensions were determined with a digital Vernier caliper.

Temperature and field dependent magnetization was measured using the MPMS up to room temperature and a Quantum Design Versalab Vibration Sample Magnetometer (VSM) with an oven option for higher temperature ($T < 1000$ K). In MPMS, plastic straw was used to align the sample in desired directions. The sample was glued to the VSM sample heater stick with Zircar cement obtained from ZIRCAR Ceramics Inc.. While gluing, the sample was pushed into the thin layer of Zircar paste spread on the heater stick to ensure a good thermal contact with the heater stick. When the sample was firmly aligned with the desired direction it was covered with Zircar cement uniformly. Finally, the VSM heater stick, with the sample glued on it, was covered with a copper foil so as to (i) better control the heat radiation in the sample chamber, (ii) maintain a uniform temperature inside the wrapped foil (due to its good thermal conductivity), and (iii) further secure the sample throughout the measurement.

In the VSM, both zero field cooled (ZFC) as well as field cooled (FC) magnetizations were measured and found to be almost overlapping. The difference between the measured data in the VSM and the MPMS was found to be less than 3% at 300 K (i.e. at the point of data overlap). We normalized the magnetization data from the MPMS with FC VSM data to get a smooth curve for the corresponding applied field.

3.3.3 Determination of demagnetization factor for transition temperature and anisotropy constant measurement

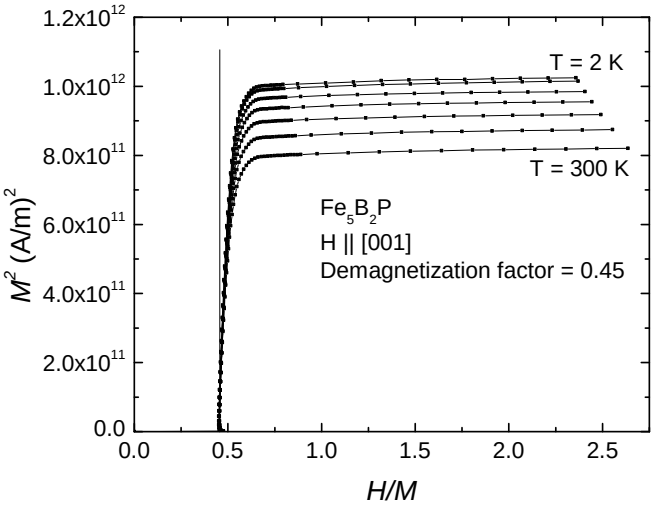

Figure 3.3 An analysis of M(H) isotherms taken at T = 2, 50, 100, 150, 200, 250, 300 K and plotted as M^2 versus H/M to determine the demagnetization factor. The H/M axis intercept at 0.45 is the experimental demagnetization factor for easy axis of magnetization.

The demagnetization factors along different directions were determined by using a formula developed by Aharoni [13]. The calculated demagnetization factors for the field along a, b, and c axes were determined to be 0.21, 0.29, and 0.50 respectively. To verify that demagnetization factors were accurate, we prepared a M^2 versus $\frac{H}{M}$ plot for the lower temperature M(H) data along the easy axis of magnetization as shown in figure 3.3. The X-intercept gives the directly measured experimental value of the demagnetization factor along the easy magnetization axis [14]. In figure 3.3, we can clearly see that all the M^2 curves are overlapping near the M^2 axis indicating that the demagnetization factor along the easy magnetization direction does not depend on temperature. A value of demagnetization factor of 0.45 was determined along the c axis which is not that different from the value of 0.50 inferred from the sample dimensions. Based on this result, we readjusted the two hard

axes demagnetization factors in proportion such that the total sum of all 3 of them is 1. The experimentally readjusted values for demagnetization factors were 0.231, 0.319 and 0.45 along a, b and c axes respectively. With the benefit of fourfold symmetry of Fe_5B_2P unit cell perpendicular to its c axis, magnetization was measured along a and c axes and corresponding demagnetization factors were used to calculate the corrected internal magnetic field (H_{int}). Here $H_{\text{int}} = H_{\text{applied}} - NM$, where N is the demagnetization factor and M is the magnetization.

3.4 Results and discussion

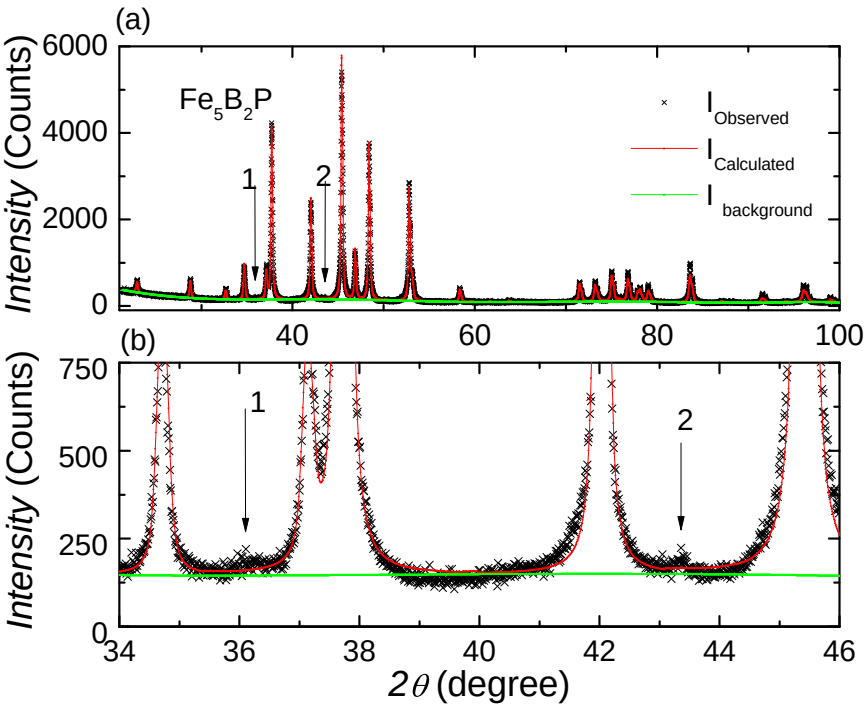

Figure 3.4 (a) Powder x-ray diffraction pattern of Fe_5B_2P (b) Enlarged powder X-ray diffraction pattern in between 2θ value of 34° to 46° to show the weak impurity peaks 1 and 2.

3.4.1 Lattice parameters determination

The structure solution and refinement for single crystal data was carried out using SHELXTL program package [15]. The final stage of refinement was performed using anisotropic displacement parameters for all the atoms. The refined composition was $Fe_5B_{2.12}P_{0.88(1)}$ with residual $R1 = 2.3\%$ (all data). The off-stoichiometry was due to partial replacement of phosphorus by boron on 4a site in the structure. According to the previous report [4] Fe_5B_2P shows a considerable phase width. All the details about the atomic positions, site occupancy factors, and displacement parameters for crystal of $Fe_5B_{2.12}P_{0.88(1)}$ are given in tables 8.1, and 8.2.

Fe_5B_2P has a tetragonal unit cell with lattice constants a = 5.485 (3) Åand c = 10.348(3) Å. While analysing the powder pattern, the CIF file obtained from single crystal data was used and the powder pattern was fitted with Rietveld analysis using GSAS EXPGUI software package [16, 17]. During the Rietveld analysis, Fe sites were supposed to be fully occupied and thermally rigid whereas P and B occupation number were released between each other with help of constraints. Finally, a well fitted powder diffraction pattern with $R_p = 0.0828$ was obtained as shown in figure 3.4(a). The lattice parameters from this measurement are in close agreement (less than 0.2 % deviation) with our single crystal data as well as previously reported data [2, 4]. A final stoichiometry of the powder sample was determined to be $Fe_5B_{2.11}P_{0.89}$. This stoichiometry is in agreement with our single crystal XRD composition of $Fe_5B_{2.12}P_{0.88(1)}$. Two tiny unidentified peaks denoted by 1 and 2 in figure 3.4 were noticed in all batches of Fe_5B_2P measured. A possible origin for these peaks is an excess amount of unreacted boron trapped in crystal. We suspected boron because it has many overlapping diffraction peaks with Fe_5B_2P as well as with these two tiny humps denoted by 1 and 2 and enlarged in figure 3.4(b).

Here we don't believe that the traces of unreacted boron can affect the magnetic properties of the sample in a significant manner because boron is non-magnetic. It is possible that boron impurities are responsible for the residual resistivity being rather large (17-35 micro-ohm cm), although

Table 3.1 Crystal data and structure refinement for Fe_5B_2P.

Empirical formula	$Fe_5B_{2.12}P_{0.88}$
Formula weight	329.42
Temperature	293(2) K
Wavelength	0.71073 Å
Crystal system, space group	Tetragonal, $I4/mcm$
Unit cell dimensions	a=5.485(3) Å
	b = 5.485(3) Å
	c = 10.348(6) Å
Volume	311.3(4) $Å^3$
Z, Calculated density	4, 7.029 g/cm^3
Absorption coefficient	22.905 mm^{-1}
F(000)	615
Crystal size	0.01 x 0.05 x 0.08 mm^3
θ range (°)	3.938 to 31.246
Limiting indices	$-7 \leq h \leq 7$
	$-7 \leq k \leq 7$
	$-14 \leq l \leq 14$
Reflections collected	2113
Independent reflections	152 [R(int) = 0.0433]
Completeness to $\theta = 25.242°$	100.00%
Absorption correction	multi-scan, empirical
Refinement method	Full-matrix least-squares on F^2
Data / restraints / parameters	152 / 0 / 17
Goodness-of-fit on F^2	1.101
Final R indices [I> 2σ(I)]	$R1 = 0.0140$, $wR2 = 0.0289$
R indices (all data)	$R1 = 0.0180$, $wR2 = 0.0299$
Extinction coefficient	0.0243(3)
Largest diff. peak and hole	0.485 and -0.474 e.$Å^{-3}$

Table 3.2 Atomic coordinates and equivalent isotropic displacement parameters (A^2) for Fe_5B_2P. U(eq) is defined as one third of the trace of the orthogonalized U_{ij} tensor.

atom	Occ	x	y	z	U_{eq}
Fe1	1	0.0000	0.0000	0.0000	0.005(1)
Fe2	1	0.1701(1)	0.6701(1)	0.1403(1)	0.005(1)
P3	0.88(1)	0.0000	0.0000	0.2500	0.004(1)
B3	0.12(1)	0.0000	0.0000	0.2500	0.004(1)
B4	1	0.6175(2)	0.1175(2)	0.0000	0.005(1)

this can also come from the small off-stoichiometry due to partial replacement of phosphorus by boron on 4a site in the structure.

3.4.2 Identification of crystallographic orientation

The Laue diffraction pattern shown in figure 3.2(b) was obtained with the X-ray beam parallel to the plane of the plate [100]. The Laue pattern shown in figure 3.2(c) was obtained with the X-ray beam perpendicular to the plane of the plate [001]. The obtained Laue diffraction patterns were analysed with the OrientExpress analysis software [18]. The Laue pattern analysis revealed that the crystals facets were grown along [100], [010], and [001] directions.

3.4.3 Resistivity measurement

The resistivity data of a single crystalline sample helps to test its quality. The resistivities of Fe_5B_2P with currents parallel to [100] and [001] directions are measured from room temperature down to 2 K; the resistivity is found to be metallic in nature as shown in figure 3.5. The residual resistivity ratio ($RRR = \rho(300\text{ K})/\rho(2\text{ K})$) of the Fe_5B_2P sample is estimated to be nearly 3.6 in [100] direction and 2.8 in [001] direction. The resistivity for easy axis of magnetization [001] is found to be greater than hard axis [100] of magnetization. The electrical anisotropy is found to be opposite than magnetic anisotropy for Fe_5B_2P. It is hard to correlate the magnetic and electrical anisotropic properties of Fe_5B_2P. The residual resistivity $\rho(2\text{ K})$ is roughly 17 $\mu\Omega$cm in

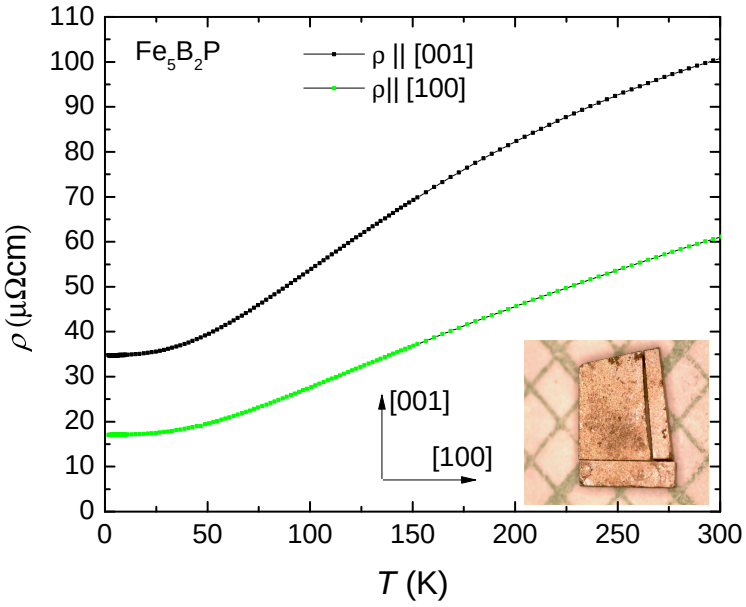

Figure 3.5 Resistivity of Fe_5B_2P below the room temperature with an excitation current being parallel to [100] and [001] directions. The inset picture shows the electrical resistivity bars obtained from the same single crystal to measure the electrical resistivity anisotropy property.

[100] direction and 35 $\mu\Omega$cm in [001] direction respectively. These values are consistent with some residual disorder in the sample (e.g. the P an B site disorder on the P_3 site).

3.4.4 Measurement of magnetization and saturation magnetization

The temperature dependent magnetization of Fe_5B_2P along the easy [001] and hard [100] axes in various magnetizing field strengths in terms of μ_B/Fe are reported in figure 3.6. As the field strength increases, the moment increases and saturates. The saturating field for the easy axis was found to be nearly 0.8 T and $M(T)$ data in an applied field of 1 T is the same as saturation magnetization obtained from $M(H)$ isotherms data (not shown here). The magnetization along the hard axis has not reached saturation in an external field of 1 T and forms a concave parabola

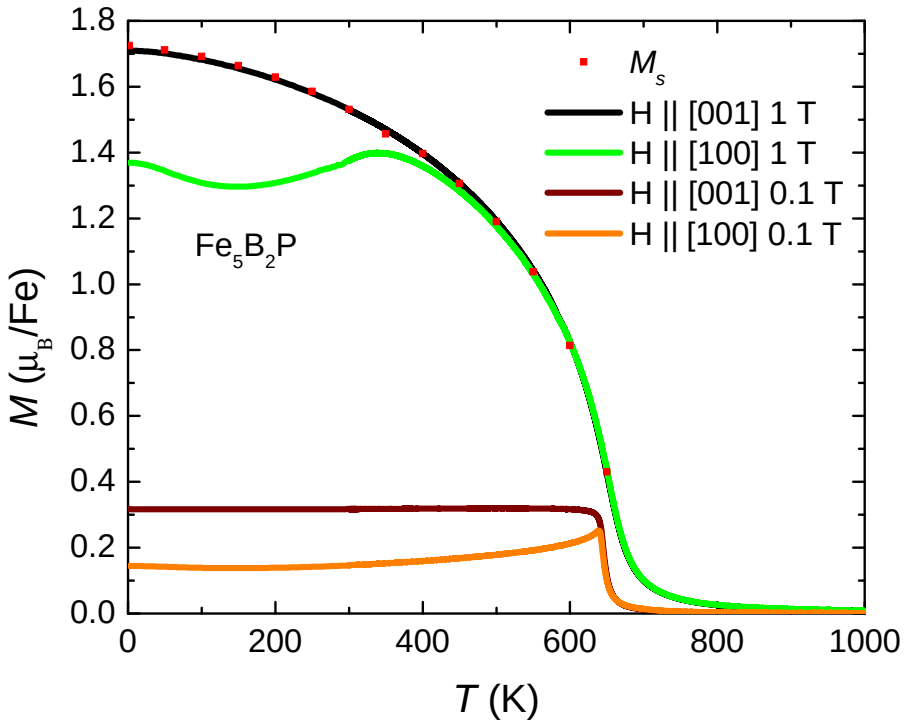

Figure 3.6 Temperature dependent magnetization of Fe_5B_2P at various magnetizing field along [100] and [001] directions and saturation magnetization, M_s, inferred from M(H) isotherms.

around 150 K as shown in the green curve of figure 3.6. We have not systematically investigated the origin of the parabolic curve below 400 K for M(T) with $H = 1T||[100]$. It reaches to saturation with higher applied magnetic field and looks like the magnetization curve along the easy axis of magnetization. One possible explanation for a low applied field and low temperature region valley in magnetization curve is the following. As the sample is cooled down, the anisotropy field (H_a) increases (typically H_a (T) varies as $M_s(T)^2$) resulting in a decrease of the sample macroscopic magnetization. Indeed, for $H_\perp < H_a$, we have $M_\perp = H_\perp * M_s/H_a$ which gives a curve similar to the one observed for M(T) with $H = 0.1\ T||[100]$. When taking into account the demagnetization factor, $N_\perp$, we have $M_\perp = H_\perp * M_s/(H_a + N_\perp * M_s)$. As the domains are becoming more elongated, $N_\perp$ will decrease upon cooling. This can give rise to a parabolic curve with a minimum as the one

observed for $H = 1T|||[100]$. Another explanation is that such parabolic curve could originate from a peculiar high value of the higher order anisotropy constant K_2 (T) which was assumed to be zero at higher temperature.

Below the Curie temperature, the $M(T)$ curves at low field are almost constant because the applied field is less than the demagnetizing field. The saturation magnetization (M_s) data were determined from the Y-intercept of linear fit of $M(H)$ isotherms plateau (as shown in figure 3.8) at 2 K, 50 K and in an interval of 50 K up to 650 K. The saturation magnetization at 2 K was found to be 1.72 μ_B/Fe which is very close to the previously reported value of 1.73 μ_B/Fe [3, 4].

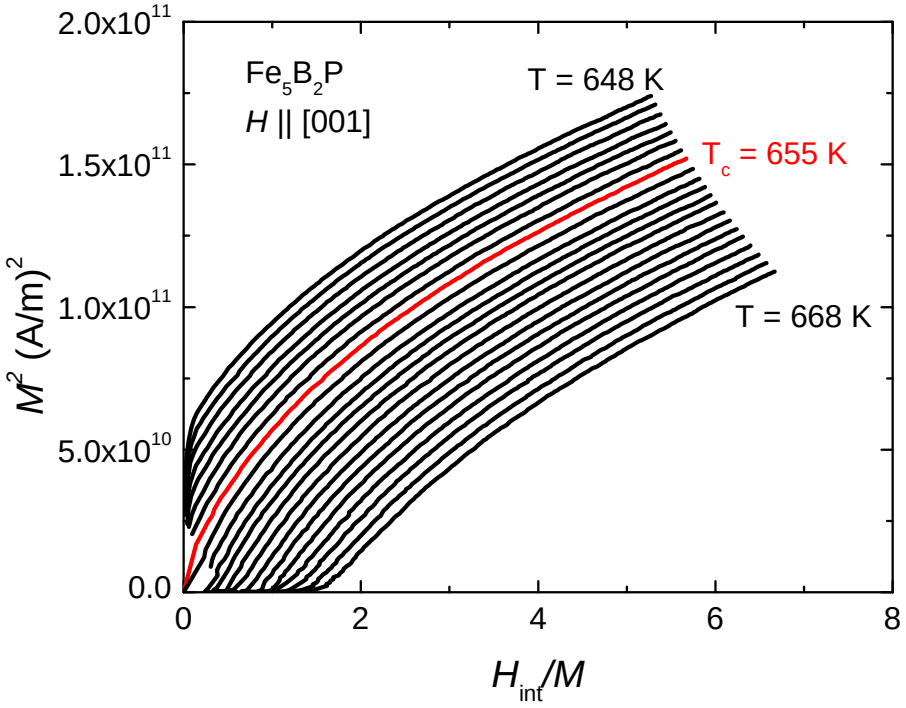

Figure 3.7 The Arrott plot of Fe_5B_2P. Here M(H) isotherms were measured for the prismatic sample from 648 K to 668 K with a spacing of 1 K. Internal magnetic field (H_{int}) was determined with an experimentally measured demagnetization factor (0.45) for the easy axis of magnetization. The temperature corresponding to M^2 versus H_{int}/M isotherm passing through origin gives the Curie temperature. The Curie temperature is determined to be 655 ± 2 K.

3.4.5 Determination of transition temperature

A M^2 versus H_{int}/M Arrott plot was used to determine the Curie temperature. The Curie temperature corresponds to Arrott plot curve that passes through the origin. For our sample, the Arrott curve corresponding to 655 K is passing through the origin as shown in figure 3.7). Hence the Curie temperature of Fe_5B_2P is determined to be 655 ± 2 K, where the error includes an instrumental uncertainty of ± 1 K inherent to such a high temperature measurement in a VSM and a reproducibility error due to sample gluing process on the heater stick resulting in a variation in thermal coupling. This Curie temperature is a little bit higher than the previously reported window of 615 K to 639 K [3, 4].

To make sure our measurement was correct, magnetization of a piece of a nickel wire obtained from the Alfa Aesar company (99.98 % metal basis) was measured with the same VSM heater stick. Using the criterion from reference [19], the Curie temperature of nickel sample was determined to be 625 ± 2 K which is in agreement with VSM Tech Note [20]. The Curie temperature of nickel is reported to fall between 626 to 633 K [21]. These results confirm the accuracy of measured Curie temperature.

3.4.6 Determination of anisotropy constant K_1

The anisotropy constant K_1 is the measure of anisotropy energy density and strongly depends on the unit cell symmetry and temperature. One of the conceptually simplest methods of measuring the anisotropy constant of an uniaxial system is to determine the area between the easy and hard axes M(H) isotherms [22]. Here we measured both the easy and hard axes isothermal M(H) curves starting from 2 K. Then we measured M(H) curves from 50 K to 800 K in 50 K intervals. A typical example of determination of the anisotropy constant by measuring the anisotropy area between two magnetization curves is shown in figure 3.8.

The temperature dependence of K_1 is shown in Fig. 3.9. K_1 is positive, indicating that the c axis is the easy axis of magnetization, in agreement with a previous calculation using a simple point charge model [4].

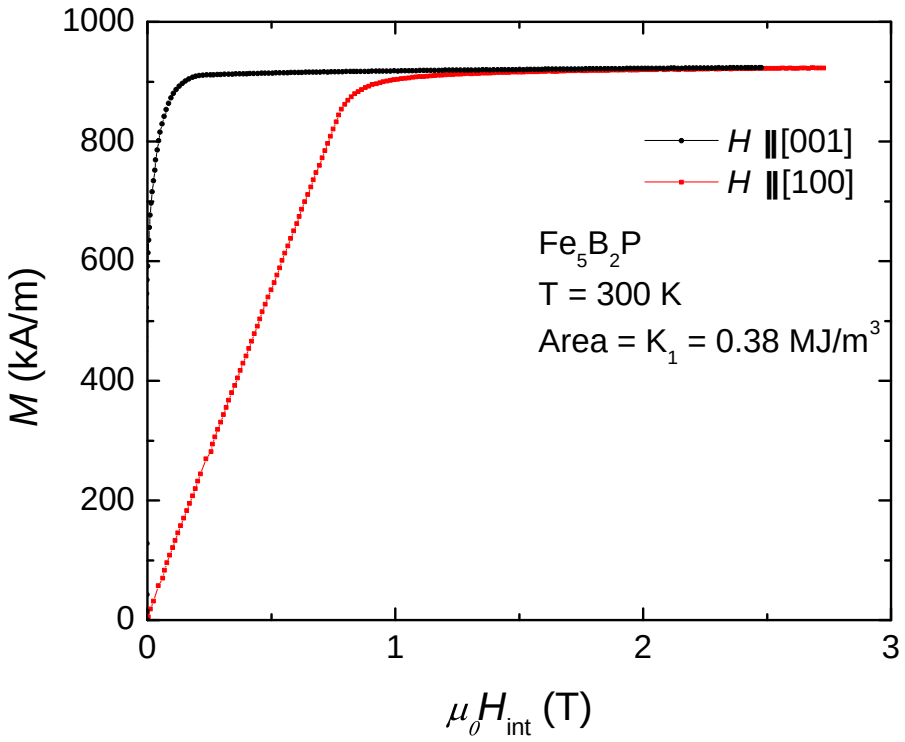

Figure 3.8 An example of determination of K_1 at 300 K with an appropriate axes units so as to obtain the area in terms of MJ/m^3 unit.

We have compared the anisotropy constant K_1 and saturation magnetization M_s of Fe_5B_2P with the single crystal data of hard ferrites $SrFe_{12}O_{19}$ and $BaFe_{12}O_{19}$ [23]. The anisotropy constant of Fe_5B_2P is greater at low temperature than either of these ferrites. The Fe_5B_2P sample becomes comparable to that of $SrFe_{12}O_{19}$ at room temperature but decreases slightly faster than both $BaFe_{12}O_{19}$ and $SrFe_{12}O_{19}$ above room temperature as shown in figure 3.9. However, the nature of variation of the saturation magnetization of Fe_5B_2P is different than the hard ferrites as shown in figure 3.10. Both of the ferrites show a roughly linear decrease of saturation magnetization with increasing temperature whereas the saturation magnetization of Fe_5B_2P is found to be significantly non-linear in T and also significantly larger for $T < 600$ K. The saturation magnetization of Fe_5B_2P is 1.53 μ_B/Fe at 300 K, which is already larger than the value of 1.16 μ_B/Fe in $SrFe_{12}O_{19}$. Since

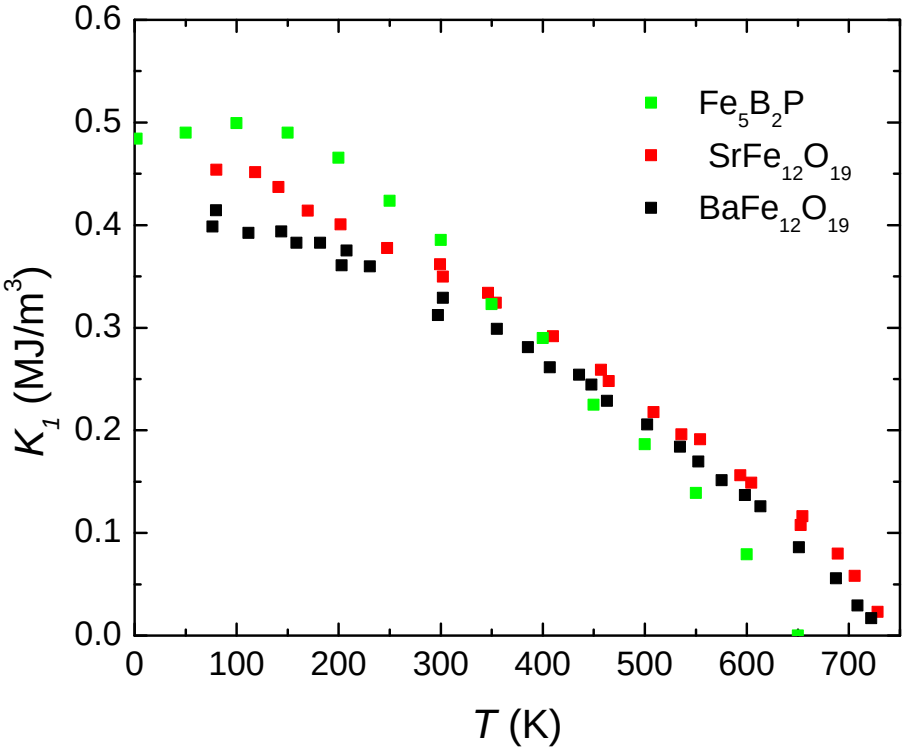

Figure 3.9 Temperature variation of the anisotropy constant K_1 of Fe_5B_2P and comparison with $SrFe_{12}O_{19}$ and $BaFe_{12}O_{19}$ from ref. [23].

Fe_5B_2P contains less non-magnetic elements, the volume magnetization of 915 kA/m for Fe_5B_2P is more than twice that of $SrFe_{12}O_{19}$ (377 kA/m [23]).

3.5 First principles calculations

In an effort to understand the observed magnetic properties - in particular, the saturation magnetization and magnetocrystalline anisotropy - of Fe_5B_2P, we have performed first principles calculations using the augmented plane-wave density functional theory code WIEN2K [24] within the generalized gradient approximation (GGA) of Perdew, Burke and Ernzerhof [25]. Sphere radii of 1.77, 2.15 and 2.06 Bohr were used for B, Fe and P, respectively, and an RK_{max} of 7.0 was employed, where RK_{max} is the product of the smallest sphere radius and the largest plane-wave

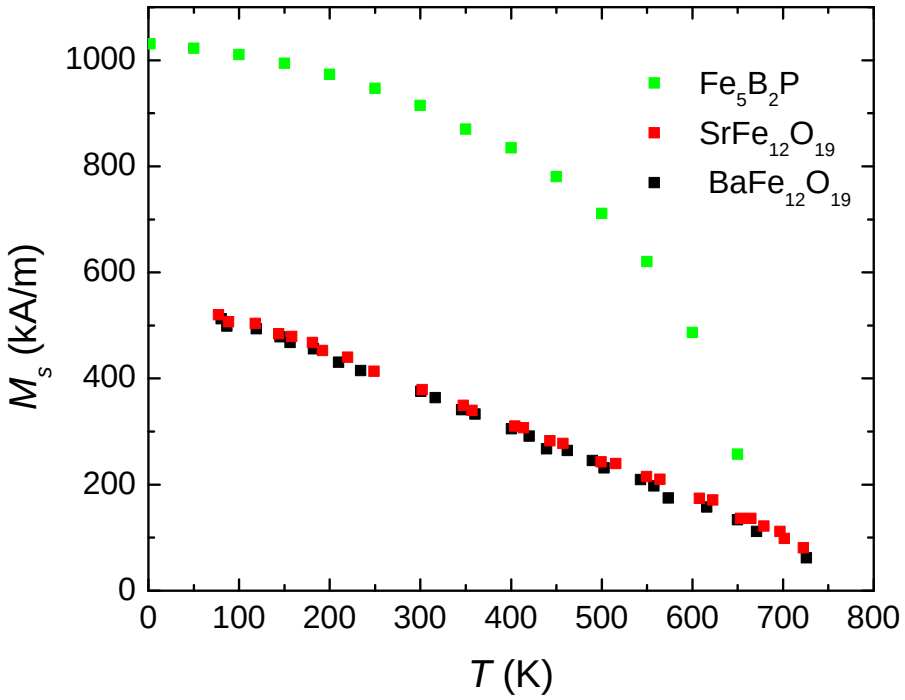

Figure 3.10 Temperature variation of the saturation magnetization M_s of Fe_5B_2P and comparison with $SrFe_{12}O_{19}$ and $BaFe_{12}O_{19}$ from ref. [23].

expansion wave vector. The experimental lattice parameters from Ref. [2] were used and all internal coordinates were relaxed. All calculations, the internal coordinate relaxation excepted, employed spin-orbit coupling and a total of approximately $10,000$ k-points in the full Brillouin zone were used for the calculation of magnetic anisotropy. For these calculations we computed total energies for the magnetic moments parallel to (100) and (001) and computed the anisotropy as the difference in these energies.

As in the experimental work we find a strong ferromagnetic behavior in Fe_5B_2P, with a saturation magnetic moment of 1.79 μ_B per Fe, which includes an average orbital moment of approximately 0.03 μ_B for each of the Fe sites. We present the calculated density-of-states in Fig. 3.11. The theoretical saturation value is in good agreement with the experimental 2 K moment of 1.72 μ_B per Fe. Small negative moments of -0.1 μ_B and -0.06 μ_B per atom are found for the B and P

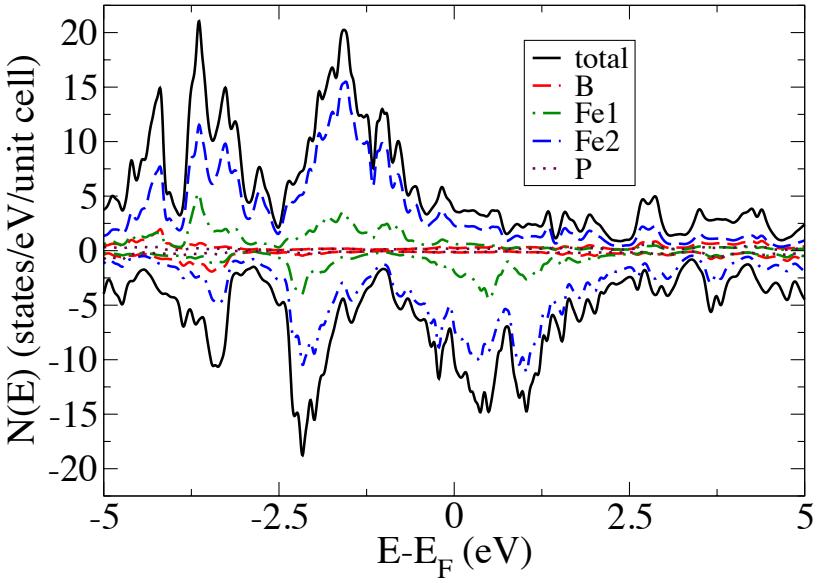

Figure 3.11 The calculated density-of-states of $Fe5PB_2$

atoms respectively, while the spin moments for the three distinct inequivalent Fe atoms are 1.79, 1.79 and 2.08 μ_B. These are significantly smaller than the values for bcc Fe (approximately 2.2 μ_B) and for the Fe atoms in hexagonal Fe_3Sn (approximately 2.4 μ_B/Fe [26]), limiting the potential performance as a hard magnetic material. Figure 3.11 displays the reason for this, with the spin-minority DOS substantially larger than the spin-majority DOS around the Fermi energy, reducing the moment.

As in the experiment, the calculated easy axis of the magnetization is the c-axis, with a $T = 0$ value for the first anisotropy constant K_1 of 0.46 MJ/m^3, which is in excellent agreement with the experimental value of 0.48 MJ/m^3. On a per-Fe basis this is 44 μeV. This is much larger than the ~ 1 μeV value for bcc Fe [27], as might be expected given the non-cubic symmetry of Fe_5B_2P, but is roughly consistent with the 60 μeV/Co value for hcp Co. This is again indicative of the usual requirement of an anisotropic crystal structure for significant magnetic anisotropy. Regarding the

structure itself, in the perfectly ordered Fe_5B_2P structure, eight of the ten Fe atoms have three boron nearest neighbors and two next-nearest phosphorus neighbors, with the other two Fe atoms having four boron nearest neighbors. There are no nearest-neighbor Fe-Fe bonds, which is perhaps surprising in a structure which is over 60 atomic percent Fe. One may suppose that a variegated bonding configuration, with a range of atoms bonding with the Fe atoms, might be favorable for the magnitude, though not necessarily the *sign* (i.e. axial or planar) of the anisotropy, but this is apparently not realized in this material. In any case, the theoretical calculations are generally quite consistent with the results of the experimental work performed.

3.6 Conclusions

Single crystals of Fe_5B_2P were grown using a self-flux growth method within a 40 window of cooling. The electrical and magnetic anisotropy properties were studied. The Curie temperature of Fe_5B_2P was determined to be 655 ± 2 K. The saturation magnetization was determined to be 1.72 μ_B/Fe at 2 K. The temperature variation of the anisotropy constant K_1 was determined for the first time, reaching ~ 0.50 MJ/m^3 at 2 K, and found to be comparable to that of hard ferrites. The saturation magnetization, in unit of kA/m is found to be larger than the hard ferrites. The first principle calculation values of saturation magnetization and anisotropy constant using augmented plane-wave density functional theory code were found to be consistent with experimental work.

3.7 Acknowledgement

We thank T. Kong, U. Kaluarachchi, K. Dennis, and A. Sapkota for useful discussion. The research was supported by the Critical Material Institute, an Energy Innovation Hub funded by U.S. Department of Energy, Office of Energy Efficiency and Renewal Energy, Advanced Manufacturing Office. This work was also supported by the Office of Basic Energy Sciences, Materials Sciences Division, U.S. DOE. The first principle calculation of this work was performed in Oak Ridge National Laboratory.

3.8 References

[1] E. Fruchart, A.-M. Triquet, R. Fruchart, and A. Michale. Two New Ferromagnetic Compounds in the Ternary System Iron-Phosphorous-Boron (in French). *Compt. Rend. Acad. Sci. Paris*, 255:931–933, 1962.

[2] S. Rundqvist. X-Ray Investigation of the Ternary System Fe-P-B. Some Features of the System Cr-P-B, Mn-P-B and Ni-P-B. *Acta Chem. Scand.*, 16:1, 1962.

[3] A. M. Blanc, E. Fruchart, and R. Fruchart. Magnetic and Crystallographic Studies of the $(Fe_{1-x}Cr_x)_3P$ Solution Solids and the Ferromagnetic Phase Fe_5B_2P (in French). *Ann. Chim., t.2 (1967)*, 1967.

[4] L. Häggström, R. Wäppling, E. Ericsson, Y. Andersson, and S. Rundqvist. Mössbauer and X-ray studies of Fe_5PB_2. *J. Solid State Chem.*, 1975.

[5] Xiao Lin, Sergey L. Bud'ko, and Paul C. Canfield. Development of viable solutions for the synthesis of sulfur bearing single crystals. *Philos. Mag.*, 92(19-21):2436–2447, 2012.

[6] Qisheng Lin, Valentin Taufour, Yuemei Zhang, Max Wood, Thomas Drtina, Sergey L. Budko, Paul C. Canfield, and Gordon J. Miller. Oxygen trapped by rare earth tetrahedral clusters in Nd_4FeOS_6: Crystal structure, electronic structure, and magnetic properties. *J. Solid State Chem.*, 229(0):41 – 48, 2015.

[7] P. C. Canfield and Z. Fisk. Growth of single crystals from metallic fluxes. *Philos. Mag.*, 65(6):1117–1123, 1992.

[8] Paul C. Canfield. Solution Growth of Intermetallic Single Crystals: A Beginners Guide, Properties and Appl ications of Complex Intermetallics. *(World Scientific, Singapore, 2010)*, pages 93–111, 2010.

[9] Paul C. Canfield, Tai Kong, Udhara S. Kaluarachchi, and Na Hyun Jo. Use of frit-disc crucibles for routine and exploratory solution growth of single crystalline samples. *Philos. Mag.*, 96(1):84–92, 2016.

[10] Cedomir Petrovic, Paul C. Canfield, and Jonathan Y. Mellen. Growing intermetallic single crystals using in situ decanting. *Philos. Mag.*, 92(19-21):2448–2457, 2012.

[11] H. Ohtani, N. Hanaya, M. Hasebe, S.I. Teraoka, and M. Abe. Fe-P Phase Diagram, ASM Alloy Phase Diagrams Database, P. Villars, editor-in-chief; H. Okamoto and K. Cenzual, section editors. *ASM International, Materials Park, OH, USA, 2006-2015*, 2006-2015.

[12] Bruker. APEX-2, Bruker AXS Inc., Madison, Wisconsin, USA, 10th ed. (2013). 2013.

[13] Amikam Aharoni. Demagnetizing factors for rectangular ferromagnetic prisms. *J. Appl. Phys.*, 83(6):3432–3434, 1998.

[14] Anthony Arrott. Criterion for ferromagnetism from observations of magnetic isotherms. *Phys. Rev.*, 108:1394–1396, Dec 1957.

[15] *SHELXTL-v2008/4, Bruker AXS Inc., Madison, Wisconsin, USA, 2013.*

[16] A.C. Larson and R.B. Von Dreele. "General Structure Analysis System (GSAS)". *Los Alamos National Laboratory Report LAUR*, pages 86–748, 1994.

[17] B. H. Toby. EXPGUI, a graphical user interface for GSAS. *J. Appl. Cryst.*, 34:210–213, 2001.

[18] Jean Laugier and Bernard Bochu. LMGP-Suite Suite of Programs for the interpretation of X-ray Experiments. *ENSP/Laboratoire des Matèriaux et du Gènie Physique, BP 46. 38042 Saint Martin d'Hères, France.*

[19] Anthony Arrott and John E. Noakes. Approximate equation of state for nickel near its critical temperature. *Phys. Rev. Lett.*, 19:786–789, Oct 1967.

[20] *Quantum Design, Tech Note 1097-202, Measured Curie Temperature of the VSM Oven Nickel Standard Sample* .

[21] B. Legendre and M. Sghaier. Curie temperature of nickel. *Journal of Thermal Analysis and Calorimetry*, 105(1):141–143, 2011.

[22] R. M. Bozorth. Determination of ferromagnetic anisotropy in single crystals and in polycrystalline sheets. *Phys. Rev.*, 50:1076–1081, Dec 1936.

[23] B. T. Shirk and W.R. Bussem. Temperature dependence of M_s and K_1 of $BaFe_{12}O_{19}$ and $SrFe_{12}O_{19}$ single crystals. *J. Appl. Phys.*, 1969.

[24] P. Blaha, K. Schwarz, G. Madsen, D. Kvasnicka, and J. Luitz. WIEN2k, An Augmented Plane Wave + Local Orbitals Program for Calculating Crystal Properties (K. Schwarz, Tech. Univ. Wien, Austria, 2001). *WIEN2k, An Augmented Plane Wave + Local Orbitals Program for Calculating Crystal Properties (K. Schwarz, Tech. Univ. Wien, Austria, 2001).*

[25] Perdew, John P. and Burke, Kieron and Ernzerhof, Matthias. Generalized Gradient Approximation Made Simple. *Phys. Rev. Lett.*, 77:3865–3868, Oct 1996.

[26] B. C. Sales and B. Saparov and M. A. McGuire and D. J. Singh and D. S. Parker. Ferromagnetism of Fe_3Sn and alloy. *Sci Rep.*

[27] G. H. O. Daalderop, P. J. Kelly, and M. F. H. Schuurmans. First-principles calculation of the magnetocrystalline anisotropy energy of iron, cobalt, and nickel. *Phys. Rev. B*, 41:11919–11937, Jun 1990.

CHAPTER 4. DISCOVERY OF FERROMAGNETISM WITH LARGE MAGNETIC ANISOTROPY IN ZrMnP AND HfMnP

A paper published in *Applied Physics Letter*

Tej N. Lamichhane,[1,2] Valentin Taufour,[1,2] Morgan W. Masters,[1] David S. Parker,[3] Udhara S. Kaluarachchi,[1,2] Srinivasa Thimmaiah,[2] Sergey L. Budko,[1,2] and Paul C. Canfield[1,2]

[1]Department of Physics and Astronomy, Iowa State University, Ames, Iowa 50011, USA

[2] The Ames Laboratory, US Department of Energy, Iowa State University, Ames, Iowa 50011, USA

[3] Materials Science and Technology Division, Oak Ridge National Laboratory, Oak Ridge, Tennessee 37831, USA

4.1 Abstract

ZrMnP and HfMnP single crystals are grown by a self-flux growth technique and structural as well as temperature dependent magnetic and transport properties are studied. Both compounds have an orthorhombic crystal structure. ZrMnP and HfMnP are ferromagnetic with Curie temperatures around 370 K and 320 K respectively. The spontaneous magnetizations of ZrMnP and HfMnP are determined to be 1.9 μ_B/f.u. and 2.1 μ_B/f.u. respectively at 50 K. The magnetocaloric effect of ZrMnP in term of entropy change (ΔS) is estimated to be -6.7 kJm^{-3}K^{-1} around 369 K. The easy axis of magnetization is [100] for both compounds, with a small anisotropy relative to the [010] axis. The anisotropy field along the [001] axis is $\sim$ 4.6 T for ZrMnP and $\sim$ 10 T for HfMnP at 50 K. Such large magnetic anisotropy is remarkable considering the absence of rare-earth elements in those compounds. The observed magnetic properties are studied using first principle calculations and most of the results are consistent with experimental results. More importantly, our calculations

suggest that the large magnetic anisotropy comes primarily from the Mn atoms suggesting that similarly large anisotropies may be found in other 3d transition metal compounds.

4.2 Introduction

In recent years, both the increase in the price of rare-earths used in magnets and adverse environmental impacts associated with their mining and purification have made the search for rare-earth-poor or rare-earth-free permanent magnets crucial. In an attempt to look for potential rare-earth-free alternatives, we studied the magnetocrystalline anisotropy of the Fe-rich compounds $(Fe_{1-x}Co_x)_2B$ [1] and Fe_5B_2P [2]. Specifically, $(Fe_{0.7}Co_{0.3})_2B$ has drawn a lot of attention as a possible permanent magnet because of its axial magnetocrystalline anisotropy [3, 4, 5]. Fe_5B_2P has a comparable magnetocrystalline anisotropy [2].

Mn, like Fe, offers some of the highest ordered moment values, but finding Mn-based ferromagnets is challenging. Fortunately Mn is known to form ferromagnetic phases such as MnX, where X is a pnictogen. Recently MnBi, both in pure form and in a high temperature phase, stabilized with Rh [6, 7, 8, 9], has been studied as a possible Mn-based ferromagnet with moderate magnetic anisotropy.

Given the existence of Mn-X ferromagnetism and our recent efforts to discover new ternary ferromagnets through the surveys of transition metal - pnictogen and chalcogen ternary compounds, we used the Mn-rich, Mn-P eutectic as a starting point for a search for new Mn-P-X ternary ferromagnets. During our survey (X = B, Al, Si, Ti, Fe, Co, Ni, Ge, Y, Zr, Nb, Rh, Pd and Hf), we discovered that ZrMnP and HfMnP are ferromagnetic at room temperature. Both ZrMnP and HfMnP have the orthorhombic crystal structure [space group: Pnma (62)] [10, 11]. These are bi-transition metal phosphides with TiNiSi-type structure which is an anti-$PbCl_2$ type superstructure [11]. In this paper, we report the magnetic properties (both experimental and first principle calculations) of single crystalline HfMnP and ZrMnP for the first time. We found a large magnetic anisotropy in particular for HfMnP.

The ZrMnP and HfMnP single crystals were grown by a solution growth technique [12, 13, 14] as described below.

4.3 Crystals growth

4.3.1 Initial test

ZrMnP and HfMnP single crystals were grown by a solution growth technique using the Mn-rich Mn-P eutectic composition ($Mn_{87}P_{13}$) as a starting solution [12]. Establishing the safe handling of the Mn-P solution for the crystal growth process was carried out in a manner similar to our previous phosphorous-based works [2, 15]. Freshly ball-milled Mn powder (Alfa Aesar, 99.9%) and red P lumps (Alfa Aesar, 99.999%) were mixed in the eutectic composition in a fritted alumina crucible set [13, 14] and sealed in an amorphous silica tube under a partial pressure of Ar. The Mn powder was covered with red P lumps in the growth crucible. Then the ampoule was heated up to 250 °C over 3 h and kept at 250 °C for 3 h. These steps are taken to avoid the vaporization of P by immediately mixing the molten P with Mn powder. The ampoule was then slowly heated to 1150 °C over 12 h and held there for 3 h to better homogenize the melt. Finally, the ampoule was cooled down to 1000 °C over 50 h and decanted with the help of a centrifuge. All the content was recovered in the catch crucible clearly demonstrating that all material forms a liquid at 1000°C and above. Given that there was no evidence of significant P-vapour pressure, this confirmed the safe and controlled handling of Mn-P solution for single crystal growth.

4.3.2 Mn cleaning

Elemental Mn tends to oxidize, and a surface layer of MnO forms on exposure to the atmosphere. If the Mn used contains a significant amount of MnO, a shift of the exact stoichiometry can result in growth of Mn_3P crystals in the above-mentioned eutectic test. To reduce the MnO content of the Mn used, Mn plates were heat-treated inside an amorphous SiO_2 tube under a partial Ar atmosphere. The mechanism of Mn cleaning is the following [16]:

$2MnO+SiO_2 \xrightarrow{950\ ^\circ C \text{ under partial pressure of Ar (Up to 75 h)}} Mn_2SiO_4$ with the resulting Mn_2SiO_4 deposited on the interior wall of the tubing.

4.3.3 Single Crystal Growth

The cleaned Mn plates were ball-milled using an agate ball-milling set for 2 minutes. In the ternary crystal growth attempts, various amounts of elemental metal pieces (Zr or Hf) were covered with Mn powder and P lumps, in the same fashion as in our eutectic test. To make sure that the second transition metal was dissolved in the melt, the growth ampoules were heated up to 1180 ° C and held there for 3 h. The growth ampoules were then cooled down to 1025 ° C over 180 h where the flux was decanted via centrifuge. By careful observation of crystals sizes, 1.25% of Zr or Hf metal in the Mn-P eutectic was found to be the optimal stoichiometry ($Zr_{1.25}Mn_{85.90}P_{12.85}$ and $Hf_{1.25}Mn_{85.90}P_{12.85}$) to get larger (but still relatively small) crystals. The crystals were partially covered with flux and etched with 1 molar HCl solution. The acid-etched needle like single crystals of ZrMnP and HfMnP are shown in FIG. 4.1(a) and 4.2(a) respectively.

4.4 Structural characterization

The single crystal XRD data were obtained using a Bruker APEX2 diffractometer. Single crystals of ZrMnP and HfMnP were mounted on a goniometer head of a Bruker Apex II CCD diffractometer and measured using graphite-monochromatized MoK_α radiation ($\lambda = 0.71073A^\circ$). Reflections were gathered at room temperature by taking four sets of 360 frames with 0.5° scans in ω, with an exposure time of 20 s (ZrMnP) or 30 s (HfMnP) per frame. The crystal-to-detector distance was 50 mm. The reflections were collected over the range of $4.2 < \theta < 31.3^\circ$ and corrected for Lorentz and polarization effects. The intensities were further corrected for absorption using the program SADABS, as implemented in Apex 2 package [17].

The structure solution and refinement of ZrMnP and HfMnP were carried out using SHELXTL [18] in the space group Pnma [10, 11]. The final stage of refinement was performed using anisotropic displacement parameters for all the atoms. The refined composition of ZrMnP was found to be stoichiometric within two standard deviations, whereas HfMnP showed off-stoichiometric composition i.e., $Hf_{1.04(1)}Mn_{1.06(1)}P_{0.90(1)}$. Tables I, II and III summarize data collection, lattice parameters, atomic positions, site occupancy factors, and displacement parameters for crystals of ZrMnP and HfMnP.

Table 4.1 Crystal data and structure refinement for ZrMnP and HfMnP.

Empirical formula	ZrMnP	$Hf_{1.04(1)}$ $Mn_{1.06(1)}$ $P_{0.90(1)}$
Formula weight	177.13	271.37
Temperature	293(2) K	293(2) K
Wavelength	0.71073 Å	0.71073 Å
Crystal system, space group	Orthorhombic, Pnma	Orthorhombic, Pnma
Unit cell dimensions	a=6.4170(17) Å	a=6.3257(17) Å
	b = 3.6525(10) Å	b = 3.6298(10) Å
	c = 7.5058(19) Å	c = 7.409(2) Å
Volume	175.92(8) $Å^3$	170.13(8) $Å^3$
Z, Calculated density	4, 6.688 g/cm^3	4, 10.595 g/cm^3
Absorption coefficient	13.415 mm^{-1}	71.333 mm^{-1}
F(000)	320	459
Crystal size	0.06 x 0.04 x 0.02 mm^3	0.05 x 0.07 x 0.02 mm^3
θ range (°)	4.178 to 31.307	4.236 to 31.405
Limiting indices	$-8 \leq h \leq 9$	$-8 \leq h \leq 8$
	$-5 \leq k \leq 5$	$-5 \leq k \leq 5$
	$-10 \leq l \leq 10$	$-10 \leq l \leq 10$
Reflections collected	2507	2443
Independent reflections	317 [R(int) = 0.0216]	305 [R(int) = 0.0673]
Completeness to $\theta = 25.242°$	100.00%	100.00%
Absorption correction	multi-scan, empirical	multi-scan, empirical
Refinement method	Full-matrix least-squares on F^2	Full-matrix least-squares on F^2
Data / restraints / parameters	317 / 0 / 20	305 / 0 / 22
Goodness-of-fit on F^2	1.216	1.080
Final R indices [I> 2σ(I)]	$R1 = 0.0135$, $wR2 = 0.0286$	$R1 = 0.0247$, $wR2 = 0.0460$
R indices (all data)	$R1 = 0.0144$, $wR2 = 0.0291$	$R1 = 0.0359$, $wR2 = 0.0494$
Extinction coefficient	0.0376(17)	0.0088(2)
Largest diff. peak and hole	0.542 and -0.756 e.$Å^{-3}$	2.381 and -2.526 e.$Å^{-3}$

Table 4.2 Atomic coordinates and equivalent isotropic displacement parameters (A^2) for ZrMnP. U(eq) is defined as one third of the trace of the orthogonalized U_{ij} tensor.

atom	Occ.	x	y	z	U_{eq}
Zr1	1	0.0310(1)	0.2500	0.6746(1)	0.004(1)
Mn2	1	0.1373(1)	0.2500	0.0592(1)	0.004(1)
P3	1	0.2670(1)	0.2500	0.3708(1)	0.004(1)

Table 4.3 Atomic coordinates and equivalent isotropic displacement parameters (A^2) for $Hf_{1.04}$ $Mn_{1.06}$ $P_{0.90}$. U(eq) is defined as one third of the trace of the orthogonalized U_{ij} tensor.

atom	Occ.	x	y	z	U_{eq}
Hf1	1	0.0314(1)	0.2500	0.6741(1)	0.003(1)
Mn2	0.96(1)	0.1400(1)	0.2500	0.0593(1)	0.005(1)
Hf2	0.04(1)				
P3	0.90(1)	0.2670(2)	0.2500	0.3697(2)	0.004(1)
Mn3	0.10(1)				

To get the powder XRD data, several etched single crystalline needles of each phosphide were finely powdered and spread over a zero background single crystalline silicon wafer with help of a thin film of Dow Corning high vacuum grease and scanned using Rigaku Miniflex X-ray diffractometer with Cu K_α radiation source. Scans were performed over 90° in 0.01° increments and data was acquired over 5 sec exposures. The atomic co-ordinate information from the single crystal measurements were used to refine the powder XRD patterns (Rietveld analyses) of ZrMnP and HfMnP samples. The R_p for both Rietveld analyses were less than 0.081. The Rietveld analysed powder XRD patterns for ZrMnP and HfMnP are shown in FIG. 4.1(e) and 4.2(e) respectively.

4.5 Crystallographic orientation

The crystallographic orientations of single crystalline samples were determined by analysing backscattered Laue photographs using the OrientExpress software package [19] and the diffraction of monochromatic X-ray beam from the sample facets over the Bragg Brentano Geometry with the beam direction parallel to the scattering vector . The normal to the flat facets of the as-grown rods is [101] or equivalent direction (see Laue photographs of ZrMnP and HfMnP sample in of the FIG. 4.1(b) and 4.2(b)) and the long axis of the rod is [010]. To confirm the normal to the flat faces is [101] or [−101], X-ray diffraction peaks from single crystal facets of ZrMnP and HfMnP were obtained from the powder XRD machine (Bragg Brentano Geometry on Rigaku Miniflex diffractrometer). The X-ray diffraction on the single crystal facets gave the four diffraction peaks of $\{i0i\}$ type as shown in FIG. 4.1(d) and 4.2(d). Then the samples facing [101] direction toward the X-Ray beam were rotated 49° in anti-clockwise direction with the help of a goniometer to get [001] Laue patterns as shown in FIG. 4.1(c) and 4.2(c).

4.6 Resistivity measurements

The ZrMnP and HfMnP needles were suitable for resistivity measurement. The four probe measurement technique was employed to measure the resistivity. Electrical contacts were prepared by gluing platinum wires with H20E EPO-TEK epoxy. Quantum Design (QD) Magnetic Property

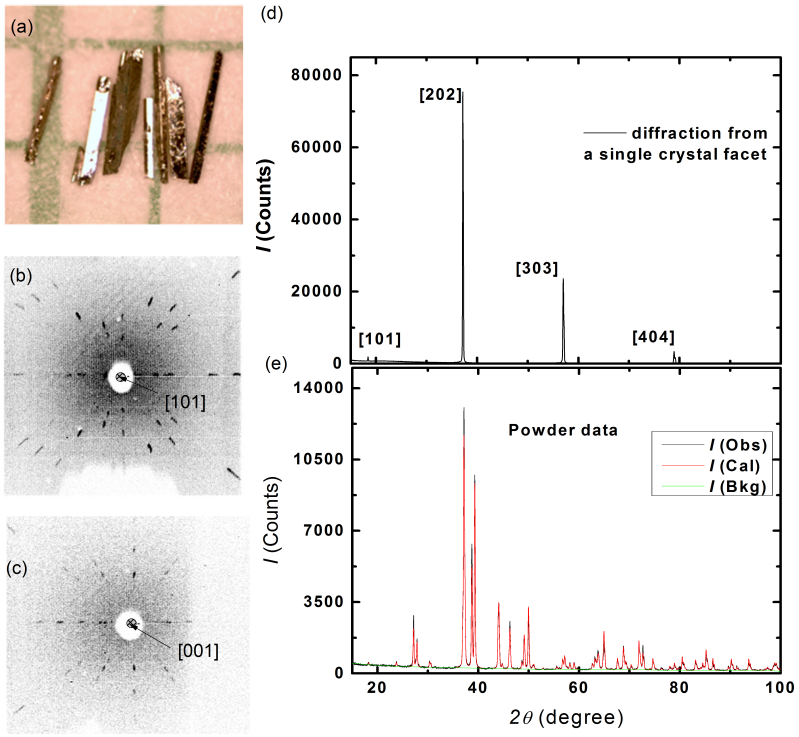

Figure 4.1 (a) Single crystals of ZrMnP (b) Back-scattered Laue pattern from facet [101] (c) Back-scattered Laue pattern [001] which was obtained at an angle of $\approx 49^{\circ}$ in an anti-clockwise direction to [101] (d) X-ray diffraction from a single crystal facet keeping the Rigaku Miniflex XRD puck fixed (e) Rietveld refined powder XRD data.

Measurement System (MPMS) was used as a temperature environment during the resistivity measurement. The MPMS was interfaced with a Linear Research, Inc. ac resistance bridge (LR 700).

The resistivity of both compounds was measured along the [010] direction. The resistivity data for ZrMnP and HfMnP are shown in FIG. 4.3. The resistivity of either compound is fairly metallic in nature. The residual resistivity ratio (RRR=$\frac{\rho(300K)}{\rho(2K)}$) was determined to be 5.6 and 5.4 for ZrMnP and HfMnP respectively. Although the RRR values for both of the compounds are comparable, HfMnP has a residual resistivity, ρ_0, that is over 50% higher, consistent with a slightly off-stoichiometric composition.

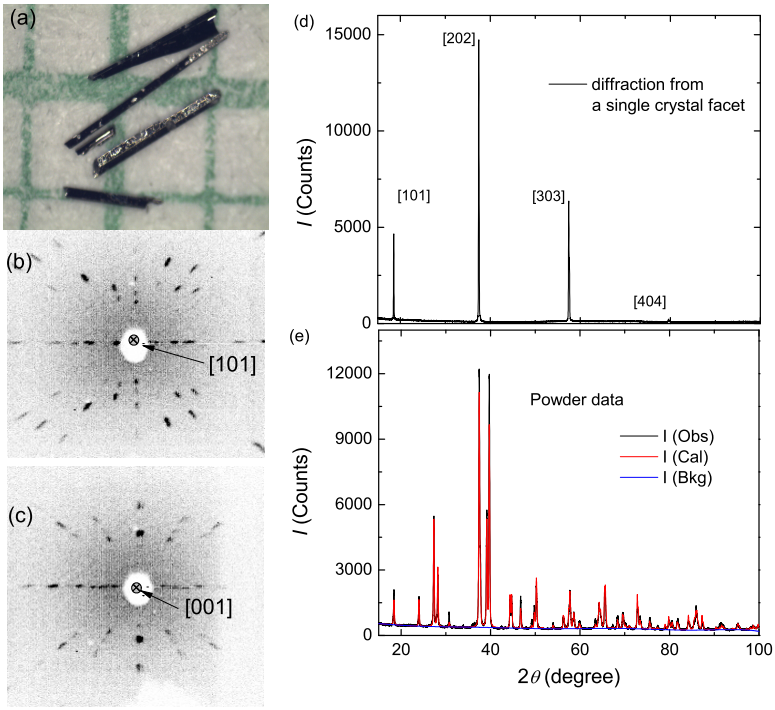

Figure 4.2 (a) Single crystals of HfMnP (b) Back-scattered Laue pattern from a facet [101] (c) Back-scattered Laue pattern pattern [001] which was obtained at an angle of $\approx 49^{\circ}$ in an anti-clockwise direction to [101] (d) X-ray diffraction from a single crystal facet keeping the Rigaku Miniflex XRD puck fixed (e) Reitveld refined powder XRD data.

In the case of HfMnP, a change in slope of resistivity occurs at ~ 320 K, which is consistent with a ferromagnetic phase transition at that temperature. This can be seen more clearly in FIG. 4.4(a) where a loss of spin-disorder-scattering feature is clearly found for $T_{\mathrm{C}} \sim 320$ K. A similar value can be inferred from the low-field (0.1 T magnetization data shown in FIG. 4.4(b) (The thermal hystersis is due to heating/cooling at 3 K/minute). Based on these data, T_{C} is determined to be around 320 K for HfMnP.

4.7 Magnetization measurements

The magnetic properties of the samples were measured using QD Versalab Vibrating Sample Magnetometer (VSM) in standard option from 50 K to 400 K. We used GE 7031 Varnish to glue

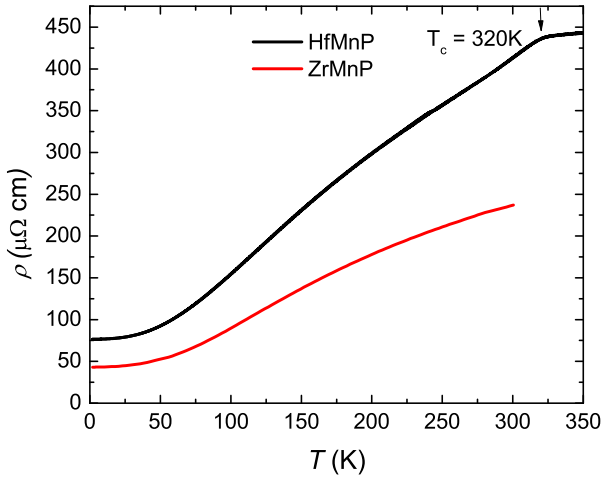

Figure 4.3 Resistivity of ZrMnP and HfMnP with an excitation current along [010] direction

the sample on the VSM quartz stick. The etched, rod-like samples were used for magnetization measurements. Both the temperature-dependent magnetization *M(T)* (at 1 T) and field-dependent magnetization *M(H)* data (starting at 50 K in steps of 50 K) were measured for each sample. The sample glued with GE varnish was further secured with teflon tape.

4.7.1 Identification of easy axis of magnetization and demagnetization factor

Experimental identification of the easy axis of magnetization for a needle-like crystal is not straightforward because of demagnetization effects, particularly if it is not along the axial direction. In addition, the small sample size makes the alignment difficult. The strongest criteria for the determination of the easy axis of magnetization are: (i) the highest saturation magnetization at low applied field and (ii) overlapping of Arrott plot curves at low-temperature isotherms. None of the faceted [101] or axial [010] directions of the ZrMnP and HfMnP crystals were found to be the easy axis of magnetization. So to align the [100] or [001] axis in the field direction, a delrin sample holder with 45° slope was prepared so that each facet is aligned with an error of ±4°. The

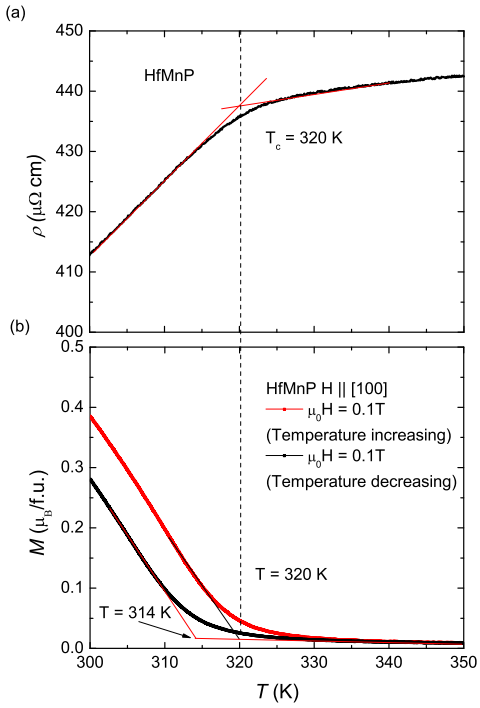

Figure 4.4 Curie Temperature determination for HfMnP. (a) Enlarged resistivity data near the anomaly in resistivity (b) Enlarged temperature dependent magnetization data near the ferromagnetic transition. The temperature of slope change in resistivity data (T_C = 320 K) equals to the upper limit of the temperature range of the slope change in *M(T)* data along [100] direction for 0.1 T field.

magnetization of the delrin sample holder was subtracted from the measurements.

Arrott plots for all 3 principle directions of the orthorhombic rods for ZrMnP sample are shown in FIG. 4.5. The detailed explanation of Arrott plot analysis for field along the easy axis of magnetization is in our previous work [2]. The Arrott curves at low temperatures along [100] direction overlap for ZrMnP, indicating this as the easy axis of magnetization. Between the two hard axes, [010] is an easier direction of magnetization than [001].

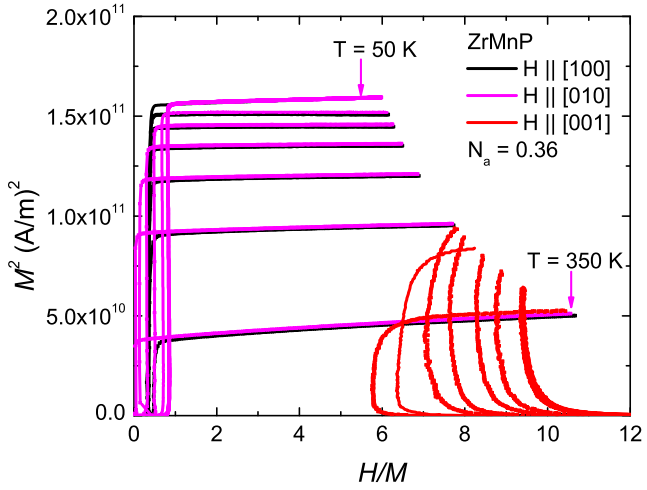

Figure 4.5 Determination of demagnetization factor for the easy axis of magnetization of ZrMnP sample: The highest value of M^2 curve corresponds to 50 K and lowest valued M^2 curve corresponds to 350 K, all others taken at intervals of 50 K for all directions measured. The overlapping of M^2 curves with minimum intercept in $\frac{H}{M}$ axis at low-temperature isotherms is considered to occur along the easy axis (here [100]) of the magnetization. The demagnetization factor for the [100] direction was determined to be $N_a = 0.36$.

To determine the anisotropy axes and fields for HfMnP at 50 K, more sensitive and higher field (7 T) QD MPMS equipped with angular magnetization measurement was used. FIG. 4.6 shows the variation of magnetization of HfMnP sample with respect to the rotation angle. Starting from the [101] facet, it reaches to its minimum when [001] direction aligns with field and maximum when [100] direction aligns, consistent with the results obtained from the Arrott plot measurements in ZrMnP.

4.7.2 Curie temperature determination

Arrot plot analyses were made for the easy axis (along [100]) of magnetization of ZrMnP to determine the Curie temperature. In an Arrott plot, M^2 isotherms are plotted as a function of $\frac{H_{int}}{M}$ where $H_{int} = H\text{-N}^*M$ is the internal field of the magnetization sample after the correction of the demagnetization effect. N is the demagnetization factor which can be experimentally determined

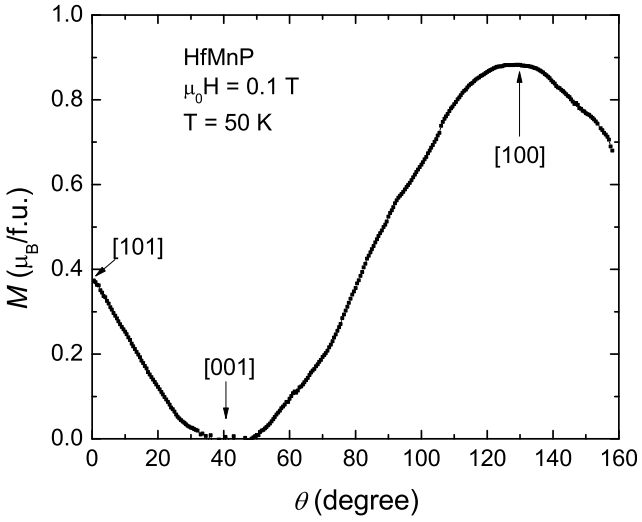

Figure 4.6 Angular magnetization of HfMnP measured at 50 K in a 0.1 T applid field.

for the easy axis of magnetization [2]. N_a was determined to be 0.36 for ZrMnP (see FIG. 4.5). In the mean field approximation, the Arrott curve at the Curie temperature is a straight line passing through origin. The Curie temperature of ZrMnP was determined to be $\sim$ 370 K as shown in FIG. 4.7.

4.7.3 Determination of the magneto-caloric effect

The isothermal entropy change can be determined from magnetization measurements using the following equations:

$$\Delta S_{\text{iso}}(T, \Delta H) = \int_{H_i}^{H_f} dS = \int_{H_i}^{H_f} \left.\frac{\partial S}{\partial H}\right|_T dH$$

Using the Maxwell relation $\left.\frac{\partial S}{\partial H}\right|_T = \mu_0 \left.\frac{\partial M}{\partial T}\right|_H$, we have:

$$\Delta S_{\text{iso}}(T, \Delta H) = \mu_0 \int_{H_i}^{H_f} \left.\frac{\partial M}{\partial T}\right|_H dH$$

For small enough temperature steps at T_u and T_l around T, we can approximate:

$$\left.\frac{\partial M}{\partial T}\right|_H \approx \frac{M(T_u, H) - M(T_l, H)}{T_u - T_l}$$

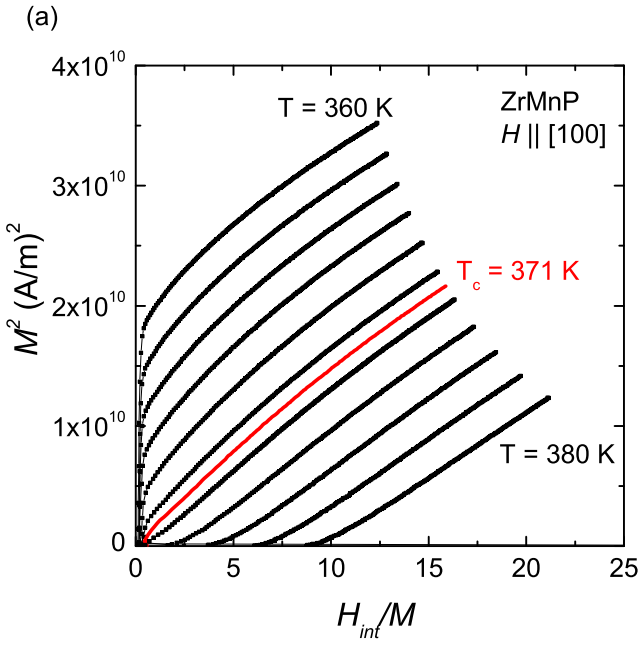

Figure 4.7 Determination of Curie temperature of ZrMnP from *M(H)* data along [100]. All black colored Arrott curvers are taken at a step of 2 K temperature.

So that we have:

$$\Delta S_{\text{iso}}(T, \Delta H) \approx \frac{\mu_0}{T_u - T_l} \int_{H_i}^{H_f} M(T_u, H) - M(T_l, H) dH \quad \text{(S 1)}$$

The magnetization isotherms near T_C as shown in FIG. 4.7 can be used with Eq. 5.1 to determine $\Delta S_{\text{iso}}(T, \Delta H)$.

4.8 Additional details of first-principles calculations

Calculations were performed using the experimental lattice parameters and all internal coordinates not dictated by symmetry were relaxed until internal forces were less than 2 mRyd/Bohr. Sphere radii (in Bohr) for ZrMnP of 1.86 for P, 2.36 for Mn and 2.5 for Zr were used; for HfMnP sphere radii of 1.97 for P, 2.3 for Mn and 2.5 for Hf were used. An RK_{max} (the product of the smallest sphere radius, i.e. P, and the largest planewave expansion wavevector) of 7.0 was used

and the linearized augmented plane-wave basis was used throughout. In general all calculations used sufficient numbers of k-points - a minimum of $1,000$ k points in the full Brillouin zone for convergence, and as many as $30,000$ k-points for the calculations of magnetic anisotropy. For this anisotropy convergence was carefully checked; the difference in anisotropy energies calculated using 10,000 and 30,000 k-points was less than 2 percent.

Figure 4.8 Temperature dependent (solid lines) and spontaneous magnetization M_s (corresponding squares) of ZrMnP and HfMnP.

Figure 4.8 shows the spontaneous magnetization (M_s) and temperature dependent magnetization of ZrMnP and HfMnP. M_s was determined by the linear extrapolation from the high-field region of the easy axis [100] *M(H)* isotherm to zero field. The spontaneous magnetization of HfMnP ($2.1\mu_B$ /f.u. at 50 K) is slightly higher than ZrMnP ($1.9\mu_B$ /f.u. at 50 K). The temperature dependent magnetization is reported for the [100] direction in a 1 T applied field. Both ZrMnP and HfMnP undergo a ferromagnetic transition between 300 K and 400 K. More precise determinations of the Curie temperatures using Arrott plots or change in slope of temperature dependent electrical resistivity (see SI) give T_C around 370 K and 320 K for ZrMnP and HfMnP respectively.

The anisotropy field between [100] and [010] for ZrMnP was determined to be 0.40 T at 50 K as shown in FIG. 4.9 (a). In HfMnP, the anisotropy field between [100] and [010] was determined to be 0.66 T at 50 K as shown in FIG. 4.9 (b). The anisotropy field between the hardest axis [001] and two almost degenerate axes [100] and [010] is estimated by extrapolation of tangents from the linear region of *M(H)* curves. The anisotropy field for [001] axis for ZrMnP was determined to be 4.6 T for ZrMnP and 10 T for HfMnP. Such an anisotropy field is remarkably high anisotropy for a rare-earth-free magnet.

Comparisons for the low-temperature anisotropy of HfMnP are not abundant in the literature. $Nd_2Fe_{14}B$ has an anisotropy field around 8.2 T at room temperature [20]. Examples of reported rare-earth free permanent magnets include: Mn_xGa thin-film (H_a = 15 T)[21], CoPt (H_a = 14 T)

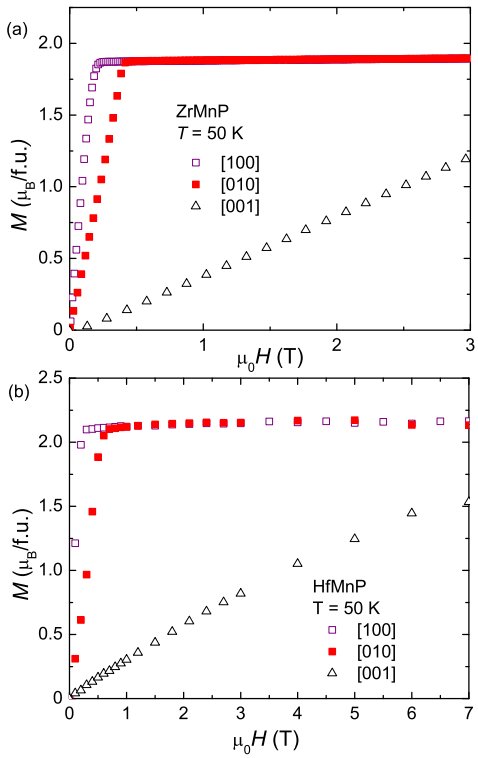

Figure 4.9 Anisotropic magnetization of ZrMnP and HfMnP along salient directions at 50 K.

[22], FePt (H_a = 10 T) [23], FePd (H_a = 4 T at 4 K) [24], MnBi (H_a = 5 T) [25] and MnAl ($H_a \approx 3$ T) [26]. The HfMnP magnetocrystalline aniostropy falls in-between those values. The 10 T anisotropy of HfMnP at 50 K nearly equals with the magnetocrystalline anisotropy of $Nd_2Fe_{14}B$ at 247 K [20].

For ZrMnP, we have studied the magnetocaloric effect from the magnetization isotherms. The results (in terms of magnetic entropy change (ΔS)) are shown in FIG. 4.10. The relevant mathematical calculation is presented in SI. The largest effect is observed near 369 K with -6.7 kJ m^{-3} K^{-1}, which is not so low considering that the transition is reversible and that ZrMnP does not contain rare-earth element. For comparison, the value for Gd at 294 K is -22 kJ m^{-3} K^{-1} [27, 28], and

the value of $La_{0.8}Na_{0.2}MnO_3$ at 337 K is -10.7 kJ m^{-3} K^{-1} [29]. This result indicates that ZrMnP might be a promising candidate as a magnetic refrigerant above room temperature.

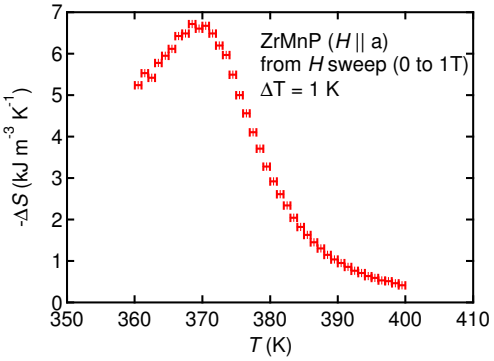

Figure 4.10 Magnetic entropy change (ΔS) of ZrMnP with the field change of 1 T applied along the a axis, determined from magnetization measurements.

To understand the observed magnetic behavior we have performed first principles calculations of ZrMnP and HfMnP using the plane-wave density functional theory code WIEN2K [30], employing the generalized gradient approximation of Perdew, Burke and Ernzerhof [31]. Additional details are given in SI. For HfMnP, calculations were run for two scenarios, since the experimental results find some disorder in the sample. The first run assumes perfect stoichiometry. For the second run we have used the virtual crystal approximation (VCA) as follows. We assume P and Mn to be trivalent and Hf tetravalent, so that the 10 percent Mn occupancy of the P site is assumed isoelectronic and the 4 percent Hf occupancy on the Mn site is modeled by adding 0.04 electrons per Mn and taking the Mn ion core to have charge 25.04. Unless mentioned explicitly, the HfMnP results refer to this VCA result.

We find saturation magnetic moments of 2.02 and 1.99 μ_B/f.u. for the Zr and Hf compounds, respectively. This total includes orbital moments for the Zr compound of 0.034 per Mn and 0.008 per Zr, and for HfMnP of 0.060 per Mn and 0.012 per Hf. These totals are in reasonably good agreement with the experimental values presented previously (1.9 μ_B/f.u. for ZrMnP and 2.1 μ_B/f.u. for HfMnP). We suspect that the slight theoretical understatement for the Hf compound is related to

the non-stoichiometry of the HfMnP sample. For the Zr compound we have also estimated the Curie point by computing the energy difference (relative to the groundstate) of a configuration with nearest neighbor Mn pairs anti-aligned; one third this energy difference is taken as the Curie point, which we calculate as 654 K. This is significantly above the experimental value of around 370 K and suggests, as often occurs, that thermal fluctuations beyond the mean-field approach are important here.

Magnetic anisotropy for an orthorhombic system is characterized by total energy calculations for the magnetic moments along each of the three principal axes [32]. To first order, one can expand this energy as

$$E = E_0 + K_{aa}k_a^2 + K_{bb}k_b^2 + K_{cc}k_c^2 \tag{4.1}$$

where k_{ii} is the magnetic moment direction cosine along axis i and K_{ii} the corresponding anisotropy constant. One can eliminate one of the K_i using the Pythagorean theorem. To simplify matters, however, we shall simply speak of energy differences relative to the groundstate.

For ZrMnP, we find, in good agreement with experiment, the [010] and [100] axes to be the 'easy' directions, separated by just 0.012 meV per Mn (in the calculation the [010] axis is the easy axis). The [001] direction is the 'hard' direction, falling some 0.136 meV per Mn above the [010] axis. On a volumetric basis this last energy difference is 0.49 MJ/m^3. The calculated saturation magnetic moment is 0.53 T and yields a calculated anisotropy field of 2.3 T. This is somewhat less than the 4.6 T anisotropy field observed in the experiment. One recalls a similar discrepancy in the MnBi ferromagnet [33, 34, 8], which has been argued as arising from correlation or lattice dynamics effects; it is possible that similar effects are at work here.

For HfMnP (in the VCA calculation) we find, again in good agreement with experiment, the [010] and [100] axes as the 'easy' directions, separated by 0.041 meV/Mn; as with ZrMnP the [010] axis is calculated to be the easy axis. The [001] direction lies some 0.47 meV per Mn above the [010] direction. This is a much larger anisotropy than found in the Zr compound and could suggest the importance of the Hf atoms in the anisotropy. To check this we have run a calculation in which spin-orbit coupling (the source of magnetocrystalline anisotropy) is turned off for the Mn atom, and

computed the anisotropy. In fact we find from this calculation that just 30 percent of the magnetic anisotropy arises from the Hf atom - fully 70 percent arises from the Mn atom. This is a surprising result given that it is widely assumed that heavy elements (such as the rare earth elements) are indispensable for magnetic anisotropy. Here it is in fact the $3d$ element Mn that generates most of the anisotropy.

On a volumetric basis the total anisotropy is 1.78 MJ/m^3, yielding an anisotropy field of 8.1 T. This is in reasonable agreement with the 10 T value from the experiment, and the discrepancy could arise from the effects mentioned for ZrMnP, or perhaps from the disorder in the sample. It is worth noting that our calculation of disorder-free HfMnP finds a significantly smaller anisotropy of 1.43 MJ/m^3. This suggests the importance of disorder to the anisotropy, and surprisingly suggests that additional disorder might in fact *increase* the anisotropy from the substantial values already found.

It is of interest to understand this large magnetic anisotropy. Presented in FIG. 4.11 is the calculated VCA bandstructure of HfMnP in the orthorhombic Brillouin zone in the ferromagnetic state, with spin-orbit coupling included (this mixes spin-up and spin-down states so that the bands presented contain both characters). Two facts are immediately evident from the plot; firstly, there are a large number of Fermi-level crossings, despite the general transfer of spectral weight away from the Fermi level associated with the magnetic transition. Secondly, and more importantly, there are a number of band crossings (indicated by the red ovals) that fall virtually *at* the Fermi level.

Magnetic anisotropy arises from spin-orbit coupling and involves a sum of matrix elements connecting occupied and unoccupied states *at the same wavevector*, divided by the energy difference of these states (see Ref. [35] for the exact expression). From this fact it is clear that magnetic materials that have a large amount of band crossings very near E_F will generally have a larger magnetic anisotropy, since this allows the coupling of occupied and unoccupied states with the same wavevector and small energy denominator. HfMnP has several such features and it is most likely these that cause the large magnetic anisotropy. We note also that the magnetic anisotropy

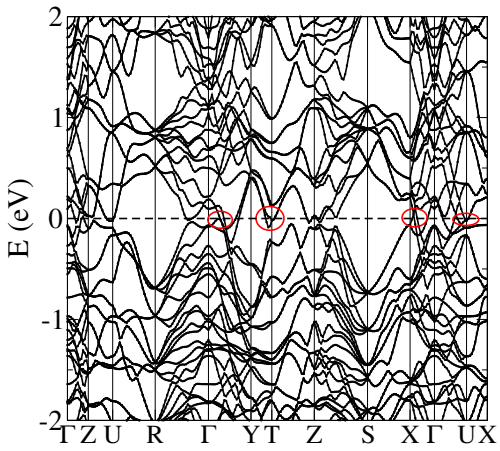

Figure 4.11 The calculated bandstructure of HfMnP; note the multiple band crossings near E_F indicated by red ovals.

effect of these crossings will be sensitive to their exact position relative to E_F and thus it is plausible that disorder effects on the anisotropy are substantial, as we observe.

Perhaps the most important finding from the theoretical part the work is the large magnetic anisotropy - 0.47 meV per Mn - found for HfMnP. On a per atom basis this is nearly *eight* times the experimental value [36] of 0.06 meV per atom for hcp Cobalt. It is probable that this large anisotropy is not specific to Mn, but originates in the unusual electronic structure anisotropic orthorhombic structure. If it were possible to stabilize a 3*d*-based ferromagnet with this anisotropy, but a higher proportion of the 3*d* element, one might obtain a very useful magnetic material without the need for expensive rare-earth elements. Since materials with high proportions of Mn tend towards antiferromagnetism, rather than the desired ferromagnetic alignment, such a magnetic material might best be based on Fe, which often aligns ferromagnetically. One example of such a material is Fe_2P, which shows an MAE of 2.32 MJ/m^3 [35], although this material is also affected by a low Curie temperature.

In summary, HfMnP and ZrMnP single crysals were grown by a self-flux growth technique and their structural, transport and magnetic properties were studied. Both of the phosphides are ferromagnetic at room temperature. The Curie temperatures of ZrMnP and HfMnP are around

370 K and 320 K respectively. The easy axis of magnetization is [100] for both compounds with a small anisotropy field along [010] axes. The anisotropy field along [001] axes is found to be 4.5 T and 10 T for ZrMnP and HfMnP respectively. The spontaneous magnetizations of ZrMnP and HfMnP at 50 K are determined to be $1.9\mu_B$/f.u. and $2.1\mu_B$/f.u. respectively. The magnetic entropy change (ΔS) of ZrMnP is found to be -6.7 kJm^{-3}K^{-1} near its Curie temperature. The observed magnetic properties are consistent with the first principle calculation results.

Acknowledgement

We would like to thank T. Kong, G. Drachuck and W. Meier for useful discussions. Dr. Warren Straszheim is acknowledged for doing WDS on various samples. The research was supported by the Critical Materials Institute, an Energy Innovation Hub funded by the U.S.Department of Energy, Office of Energy Efficiency and Renewable Energy, Advanced Manufacturing Office. This work was also supported by the Office of Basic Energy Sciences, Materials Sciences Division, U.S. DOE. This work was performed at the Ames Laboratory, operated for DOE by Iowa State University under Contract No. DE-AC02-07CH11358.

4.9 References

[1] Kirill D Belashchenko, Liqin Ke, Markus Däne, Lorin X Benedict, Tej Nath Lamichhane, Valentin Taufour, Anton Jesche, Sergey L Bud'ko, Paul C Canfield, and Vladimir P Antropov. Origin of the spin reorientation transitions in $(Fe_{1-x}Co_x)_2B$ alloys. *Appl. Phys. Lett.*, 106(6):062408, 2015.

[2] Tej N. Lamichhane, Valentin Taufour, Srinivasa Thimmaiah, David S. Parker, Sergey L. Bud'ko, and Paul C. Canfield. A study of the physical properties of single crystalline Fe_5B_2P. *J. Magn. Magn. Mater.*, 401:525 – 531, 2016.

[3] Hong Jian, Konstantin P Skokov, Michael D Kuz'min, Iliya Radulov, and Oliver Gutfleisch. Magnetic properties of (Fe, Co)$_2$ B alloys with easy-axis anisotropy. *Magnetics, IEEE Transactions on*, 50(11):1–4, 2014.

[4] A. Edström, M. Werwiński, D. Iuşan, J. Rusz, O. Eriksson, K. P. Skokov, I. A. Radulov, S. Ener, M. D. Kuz'min, J. Hong, M. Fries, D. Yu. Karpenkov, O. Gutfleisch, P. Toson, and

J. Fidler. Magnetic properties of $(Fe_{1-x}Co_x)_2B$ alloys and the effect of doping by $5d$ elements. *Phys. Rev. B*, 92:174413, Nov 2015.

[5] Markus Däne, Soo Kyung Kim, Michael P Surh, Daniel berg, and Lorin X Benedict. Density functional theory calculations of magnetocrystalline anisotropy energies for (Fe_{1-x} Co_x) $_2$ B. *J. Phys.: Condens. Matter*, 27(26):266002, 2015.

[6] Jun Cui, Jung-Pyung Choi, Evgueni Polikarpov, Mark E. Bowden, Wei Xie, Guosheng Li, Zimin Nie, Nikolai Zarkevich, Matthew J. Kramer, and Duane Johnson. Effect of composition and heat treatment on MnBi magnetic materials. *Acta Mater.*, 79:374–381, OCT 15 2014.

[7] K. V. Shanavas, David Parker, and David J. Singh. Theoretical study on the role of dynamics on the unusual magnetic properties in MnBi. *Sci Rep*, 4:7222, NOV 27 2014.

[8] V. P. Antropov, V. N. Antonov, L. V. Bekenov, A. Kutepov, and G. Kotliar. Magnetic anisotropic effects and electronic correlations in MnBi ferromagnet. *Phys. Rev. B*, 90:054404, Aug 2014.

[9] Valentin Taufour, Srinivasa Thimmaiah, Stephen March, Scott Saunders, Kewei Sun, Tej Nath Lamichhane, Matthew J. Kramer, Sergey L. Bud'ko, and Paul C. Canfield. Structural and Ferromagnetic Properties of an Orthorhombic Phase of MnBi Stabilized with Rh Additions. *Phys. Rev. Applied*, 4:014021, Jul 2015.

[10] Ya. F. Lomnitskaya and R. R. Korolishin. Reaction of phosphorus and zirconium with chromium or manganese. *Izvestiya Akademii Nauk SSSR, Neorganicheskie Materialy*, 23(1):77–80, 1987.

[11] Ya.F. Lomnytska and Yu.B. Kuz'ma. New phosphides of {IVa} and Va group metals with TiNiSi-type . *J. Alloys Compd.*, 269(12):133 – 137, 1998.

[12] H. Okamoto. Mn-P phase diagram. *ASM International, Alloy Phase Diagram Section, Materials Park, Ohio, U.S.A.*, 2006-2015.

[13] Cedomir Petrovic, Paul C. Canfield, and Jonathan Y. Mellen. Growing intermetallic single crystals using in situ decanting. *Philos. Mag.*, 92(19-21):2448–2457, 2012.

[14] Paul C. Canfield, Tai Kong, Udhara S. Kaluarachchi, and Na Hyun Jo. Use of frit-disc crucibles for routine and exploratory solution growth of single crystalline samples. *Philos. Mag.*, 96(1):84–92, 2016.

[15] Gil Drachuck, Anna E. Böhmer, Sergey L. Bud'ko, and Paul C. Canfield. Magnetization and transport properties of single crystalline RPd_2P_2 (R=Y, La - Nd, Sm - Ho, Yb). *J. Magn. Magn. Mater.*, 417:420 – 433, 2016.

[16] J. J. Moore. Chapter 5: Slag chemistry. chemical metallurgy. second edition, 1990.

[17] Bruker. APEX-2, Bruker AXS Inc., Madison, Wisconsin, USA, 10th ed. (2013). 2013.

[18] *SHELXTL-v2008/4, Bruker AXS Inc., Madison, Wisconsin, USA, 2013.*

[19] Jean Laugier and Bernard Bochu. LMGP-Suite Suite of Programs for the interpretation of X-ray Experiments. *ENSP/Laboratoire des Matèriaux et du Gènie Physique, BP 46. 38042 Saint Martin d'Hères, France.*

[20] F. Bolzoni, O. Moze, and L. Pareti. First-order field-induced magnetization transitions in single-crystal $Nd2_2Fe_{14}B$. *J. Appl. Phys.*, 62(2):615–620, 1987.

[21] L. J. Zhu, D. Pan, S. H. Nie, J. Lu, and J. H. Zhao. Tailoring magnetism of multifunctional Mn_xGa films with giant perpendicular anisotropy. *Appl. Phys. Lett.*, 102(13), 2013.

[22] H. Shima, K. Oikawa, A. Fujita, K. Fukamichi, K. Ishida, S. Nakamura, and T. Nojima. Magnetocrystalline anisotropy energy in $L1_0$-type CoPt single crystals. *J. Magn. Magn. Mater.*, 290291, Part 1:566 – 569, 2005. Proceedings of the Joint European Magnetic Symposia (JEMS' 04).

[23] K. Inoue, H. Shima, A. Fujita, K. Ishida, K. Oikawa, and K. Fukamichi. Temperature dependence of magnetocrystalline anisotropy constants in the single variant state of $L1_0$-type FePt bulk single crystal. *Appl. Phys. Lett.*, 88(10), 2006.

[24] H. Shima, K. Oikawa, A. Fujita, K. Fukamichi, K. Ishida, and A. Sakuma. Lattice axial ratio and large uniaxial magnetocrystalline anisotropy in $L1_0$-type FePd single crystals prepared under compressive stress. *Phys. Rev. B*, 70:224408, Dec 2004.

[25] Michael A. McGuire, Huibo Cao, Bryan C. Chakoumakos, and Brian C. Sales. Symmetry-lowering lattice distortion at the spin reorientation in MnBi single crystals. *Phys. Rev. B*, 90:174425, Nov 2014.

[26] Haruaki Saruyama, Mikihiko Oogane, Yuta Kurimoto, Hiroshi Naganuma, and Yasuo Ando. Fabrication of $L1_0$-ordered MnAl films for observation of tunnel magnetoresistance effect. *Jpn. J. Appl. Phys.*, 52(6R):063003, 2013.

[27] S. Yu. Dan'kov, A. M. Tishin, V. K. Pecharsky, and K. A. Gschneidner. Magnetic phase transitions and the magnetothermal properties of gadolinium. *Phys. Rev. B*, 57:3478–3490, Feb 1998.

[28] K A Gschneidner Jr, V K Pecharsky, and A O Tsokol. Recent developments in magnetocaloric materials. *Reports on Progress in Physics*, 68(6):1479, 2005.

[29] M. Wali, R. Skini, M. Khlifi, E. Dhahri, and E. K. Hlil. A giant magnetocaloric effect with a tunable temperature transition close to room temperature in Na-deficient $La_{0.8}Na_{0.2-x}\square_xMnO_3$ manganites. *Dalton Trans*, 44:12796–12803, 2015.

[30] P. Blaha, K. Schwarz, G. Madsen, D. Kvasnicka, and J. Luitz. WIEN2k, An Augmented Plane Wave + Local Orbitals Program for Calculating Crystal Properties (K. Schwarz, Tech. Univ. Wien, Austria, 2001). *WIEN2k, An Augmented Plane Wave + Local Orbitals Program for Calculating Crystal Properties (K. Schwarz, Tech. Univ. Wien, Austria, 2001).*

[31] Perdew, John P. and Burke, Kieron and Ernzerhof, Matthias. Generalized Gradient Approximation Made Simple. *Phys. Rev. Lett.*, 77:3865–3868, Oct 1996.

[32] Wilfred Palmer. Magnetocrystalline anisotropy of magnetite at low temperature. *Phys. Rev.*, 131:1057–1062, Aug 1963.

[33] T. J. Williams, A. E. Taylor, A. D. Christianson, S. E. Hahn, R. S. Fishman, D. S. Parker, M. A. McGuire, B. C. Sales, and M. D. Lumsden. Extended magnetic exchange interactions in the high-temperature ferromagnet MnBi. *Appl. Phys. Lett.*, 108(19), 2016.

[34] K. V. Shanavas, David S. Parker, and David J. Singh. Theoretical study on the role of dynamics on the unusual magnetic properties in MnBi. *Scientific Reports*, 4(7222):7222, 2014.

[35] M. Costa, O. Grånäs, A. Bergman, P. Venezuela, P. Nordblad, M. Klintenberg, and O. Eriksson. Large magnetic anisotropy of Fe_2P investigated via *ab initio* density functional theory calculations. *Phys. Rev. B*, 86:085125, Aug 2012.

[36] G. H. O. Daalderop, P. J. Kelly, and M. F. H. Schuurmans. First-principles calculation of the magnetocrystalline anisotropy energy of iron, cobalt, and nickel. *Phys. Rev. B*, 41:11919–11937, Jun 1990.

CHAPTER 5. MAGNETIC PROPERTIES OF SINGLE CRYSTALLINE ITINERANT FERROMAGNET $AlFe_2B_2$

A paper published in *Physical Review Materials*

Tej N. Lamichhane,[1,2] Li Xiang,[1,2] Qisheng Lin,[1] Tribhuwan Pandey,[3] David S. Parker,[3] Tae-Hoon Kim,[1] Lin Zhou,[1] Matthew J. Kramer,[1] Sergey L. Bud'ko,[1,2] and Paul C. Canfield[1,2]

[1]Ames Laboratory, U.S. DOE, Ames, Iowa 50011, USA

[2]Department of Physics and Astronomy, Iowa State University, Ames, Iowa 50011, USA

[3]Materials Science and Technology Division, Oak Ridge National Laboratory, Oak Ridge, Tennessee 37831, USA

5.1 Abstract

Single crystals of $AlFe_2B_2$ have been grown using the self flux growth method and then measured the structural properties, temperature and field dependent magnetization, and temperature dependent electrical resistivity at ambient as well as high pressure. The Curie temperature of $AlFe_2B_2$ is determined to be 274 K. The measured saturation magnetization and the effective moment for paramagnetic Fe-ion indicate the itinerant nature of the magnetism with a Rhode-Wohlfarth ratio $\frac{M_C}{M_{sat}} \approx 1.21$. Temperature dependent resistivity measurements under hydrostatic pressure shows that transition temperature T_C is suppressed down to 255 K for $p = 2.24$ GPa pressure with a suppression rate of ~ -8.9 K/GPa. The anisotropy fields and magnetocrystalline anisotropy constants are in reasonable agreement with density functional theory calculations.

5.2 Introduction

In recent years, $AlFe_2B_2$ has attracted a growing research interest as a rare-earth free ferromagnet that might have potential as a magneto-caloric material [1, 2]. It is a layered material

that has been identified as an itinerant ferromagnet [3]. $AlFe_2B_2$ was first reported by Jeitschko[4] and independently by Kuz'ma and Chaban [5] in 1969. $AlFe_2B_2$ crystallizes in an orthorhombic structure with space group *Cmmm* (Mn_2AlB_2 structure type). The Al atoms located in $2a$ crystallographic position (0,0,0) form a plane which alternately stacks with Fe-B slabs formed by Fe atoms; located at $4j$(0, 0.3554, 0.5) and B atoms located at $4i$ (0,0.1987,0) positions [6]. A picture of unit cell for $AlFe_2B_2$ is shown in Fig. 5.1(a). $AlMn_2B_2$ and $AlCr_2B_2$ are the other two known iso-structural transition metal compounds. The magnetic nature of $AlMn_2B_2$ and $AlCr_2B_2$ is not clearly understood [7]. Among these 3 members only $AlFe_2B_2$ is ferromagnetic; however the reported magnetic parameters for $AlFe_2B_2$ show a lot of variation [3, 1, 6, 2, 8]. A good summary of all these variations is presented tabular form in a very recent literature [9].

For example, the Curie temperature of this material is reported to fall within a window of 274 - 320 K depending up on the synthesis route. Initial work indicates that, the Curie temperature of $AlFe_2B_2$ was 320 K [3]. The Curie temperature of Ga-flux grown $AlFe_2B_2$ was reported to be 307 K and for arcmelted, polycrystalline samples it was reported to be 282 K [1]. The Curie temperature for annealed, melt-spun ribbons was reported to be 312 K [6]. A Mössbauer study on arc-melted and annealed sample has reported the Curie temperature of 300 K [2]. At the lower limit, the Curie temperature of spark plasma sintered $AlFe_2B_2$ was reported to be 274 K [8]. The reported saturation magnetic moment also manifests up to 25% variation from the theoretically predicted saturation moment of 1.25 μ_B/Fe. The first reported saturation magnetization and effective moment values for $AlFe_2B_2$ were 1.9(2) μ_B/f.u. at 4.2 K and 4.8 μ_B/Fe respectively [3]. Similarly Du et al. has reported the saturation magnetization moment of 1.32 μ_B/Fe at 5 K [10]. Recently, Tan et al. has reported the saturation magnetization of 1.15 μ_B/Fe and 1.03 μ_B/Fe for before and after the HCl etching of an arcmelted sample [1]. The lower saturation moment, after the acid etching, suggested either the inclusion of Fe-rich magnetic impurities in the sample or degradation of the sample with acid etching. Recently, a study pointed out that the content of impurity phases decreases with excess of Al in the as cast alloy and by annealing [11]. The main reason for the variation in reported magnetic parameters is the difficulty in preparing pure single crystal, single

phase $AlFe_2B_2$ samples. To this end, detailed measurements on single phase, single crystalline samples will provide unambiguous magnetic parameters and general insight into $AlFe_2B_2$.

In this work, we investigated the magnetic and transport properties of self-flux grown single crystalline $AlFe_2B_2$. We report single crystalline structural, magnetic and transport properties of $AlFe_2B_2$. We find that $AlFe_2B_2$ is an itinerant ferromagnet with $\frac{M_C}{M_{sat}} \approx 1.14$ and the Curie temperature is initially linearly suppressed with hydrostatic pressure at rate of $\frac{dT_C}{dp} \sim -8.9$ K/GPa. The magnetic anisotropy fields of $AlFe_2B_2$ are ~ 1 T along [010] and ~ 5 T along [001] direction. The first magneto-crystalline anisotropic constants (K_1s) at base temperature are determined to be $K_{010} \approx 0.23$ MJ/m^3 and $K_{001} \approx 1.8$ MJ/m^3 along [010] and [001] directions respectively (The subscript 1 is dropped for simplicity.).

5.3 Experimental Details

5.3.1 Crystal growth

Single crystalline samples were prepared using a self-flux growth technique[12]. First we confirmed that our initial stochiometry $Al_{50}Fe_{30}B_{20}$ was a single phase liquid at 1200 °C. Starting composition $Al_{50}Fe_{30}B_{20}$ with elemental Al (Alfa Aesar, 99.999%), Fe (Alfa Aesar, 99.99%) and B (Alfa Aesar, 99.99%) was arcmelted under an Ar atmosphere at least 4 times. The ingot was then crushed with a metal cutter and put in a fritted alumina crucible set [13] under the partial pressure of Ar inside an amorphous SiO_2 jacket for the flux growth purpose. The growth ampoule was heated to 1200 °C over 2-4 h and allowed to homogenize for 2 hours. The ampoule was then placed in a centrifuge and all liquid was forced to the catch side of crucible. Given that all of the melt was collected in catch crucible, this confirms that $Al_{50}Fe_{30}B_{20}$ is liquid at 1200 °C.

Knowing that the arcmelted $Al_{50}Fe_{30}B_{20}$ composition exists as a homogeneous melt at 1200 °C , the cooling profile was optimised as following. The homogeneous melt at 1200 °C was cooled down to 1180 °C over 1 h and slowly cooled down to 1080 °C over 30 h at which point the crucible limited, plate-like crystals were separated from the remaining flux using a centrifuge. The large plate-like

crystals had some $Al_{13}Fe_4$ impurity phase on their surfaces which was removed with dilute HCl etching [8]. The as-grown single crystals are shown in the insets of Fig. 5.2(a).

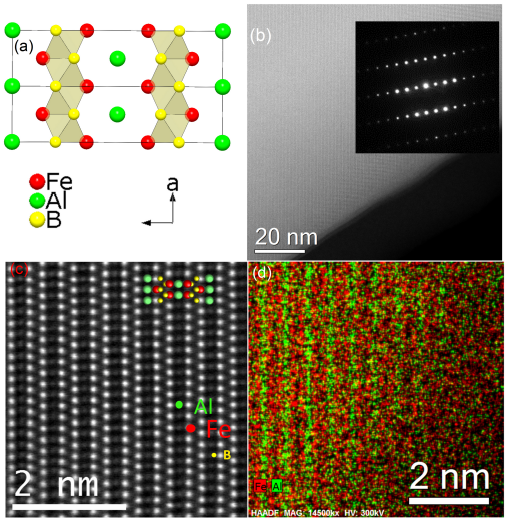

Figure 5.1 (a) $AlFe_2B_2$ unit cell (b) HAADF STEM image shows uniform chemistry of the $AlFe_2B_2$ crystal. The inset is a corresponding selected-area electron diffraction pattern. (c) High resolution HAADF STEM image of $AlFe_2B_2$ taken along [101] zone axis along with projection of a unit cell represented with Fe (red), Al(green) and B (yellow) spheres. The structural pattern of Al and FeB slab layers are also visible in unit cell shown in pannel (a). (d) EDS elemental mapping without account of B scattering effect where green stripes are Al and red stripes are Fe distributions.

5.3.2 Characterization and physical properties measurements

The crystal structure of $AlFe_2B_2$ was characterized with both single crystal X-ray diffraction (XRD) and powder XRD. The single crystal XRD data were collected within a 4°-29° angle value of 2θ using Bruker Smart APEX II diffractometer with graphite-monochromatized Mo-K_α radiation source ($\lambda = 0.71073$ $\AA$). The powder diffraction data were collected using a Rigaku MiniFlex II diffractometer with Cu-K_α radiation. The acid etched $AlFe_2B_2$ crystals were ground to fine powder and spread over a zero background, Si-wafer sample holder with help of a thin film of Dow Corning

high vacuum grease. The diffraction intensity data were collected within a 2θ interval of 5°-100° with a fixed dwelling time of 3 sec and a step size of 0.01°.

The as-grown single crystalline sample was examined with a transmission electron microscopy to obtain High-angle-annular-dark-field (HAADF) scanning transmission electron microscopy (STEM) images, corresponding selected-area electron diffraction pattern and high resolution HAADF STEM image of $AlFe_2B_2$ taken under [101] zone axis.

The anisotropic magnetic measurements were carried out in a Quantum Design Magnetic Property Measurement System (MPMS) for 2 K $\leq T \leq$ 300 K and a Versalab Vibrating Sample Magnetometer (VSM) for 50 K$\leq T \leq$700 K.

The temperature dependent resistivity of $AlFe_2B_2$ was measured in a standard four-contact configuration, with contacts prepared using silver epoxy. The excitation current was along the crystallographic a-axis. AC resistivity measurement were performed in a Quantum Design Physical Property Measurement System (PPMS) using 1 mA; 17 Hz excitation, with a cooling at a rate of 0.25 K/min. A Be-Cu/Ni-Cr-Al hybrid piston-cylinder cell similar to the one described in Ref. [14] was used to apply pressure. Pressure values at the transition temperature T_C were estimated by linear interpolation between the room temperature pressure $p_{300\mathrm{K}}$ and low temperature pressure $p_{T\leq 90\mathrm{K}}$ values [15, 16]. $p_{300\mathrm{K}}$ values were inferred from the 300 K resistivity ratio $\rho(p)/\rho(0\,\mathrm{GPa})$ of lead [17] and $p_{T\leq 90\mathrm{K}}$ values were inferred from the $T_c(p)$ of lead [18]. Good hydrostatic conditions were achieved by using a 4:6 mixture of light mineral oil:n-pentane as a pressure medium; this mixture solidifies at room temperature in the range $3-4$ GPa, i.e., well above our maximum pressure [14, 19, 16].

5.4 Experimental results

5.4.1 Structural characterization

The HAADF STEM image along with selected area diffraction pattern in the inset and high resolution HAADF STEM image of $AlFe_2B_2$ taken under [101] zone axis and EDS Al-Fe elmental

mapping are presented in pannels (b), (c) and (d) of Fig. 5.1. Taken together they strongly suggest the uniform chemical composition of $AlFe_2B_2$ through out the sample.

The crystallographic solution and parameters refinement on the single crystalline XRD data was performed using SHELXTL program package [20]. The Rietveld refined single crystalline data are presented in TABLES 8.1, and 8.2. Using the atomic coordinates from the crystallographic information file obtained from single crystal XRD data, powder XRD data were Rietveld refined with $R_P = 0.1$ using General Structure Analysis System [21] (Fig. 5.2 (a)). The lattice parameters from the powder XRD are: a = 2.920(4) $\mathring{A}$, b = 11.026(4) $\mathring{A}$ and c = 2.866(7) $\mathring{A}$ which are in reasonable agreement with the single crystal data analysis values.

To confirm the crystallogrpahic orientation of the $AlFe_2B_2$ crystals, monochromatic Cu-K_α XRD data were collected from the flat surface of the crystals and found to be {020} family as shown in Fig. 5.2 (b), i.e. the [010] direction is perpendicular to the plate. However finding a thick enough, flat, as grown facet with [100] and [001] direction was made difficult by the thin, sheet-like morphology of the sample and its crucible limited growth nature. A [001] facet was cut out of large crucible limited crystal as shown in the inset of Fig. 5.2(c). The monochromatic Cu-K_α XRD pattern scattered from the cut surface confirms the [001] direction displaying the [001] and [002] peaks (Fig. 5.2 (c)). To better illustrate the crystallographic orientations, powder XRD, and monochromatic surface XRD patterns from the plate surface and cut edge are plotted together in Fig. 5.2 (d). This plot clearly identifies that direction perpendicular to the plate is [010] and cut edge surface is (001). Slight displacement of the surface XRD peaks is the result of the sample height in the Bragg Brentano geometry. The splitting of [080] peak is observed by distinction of Cu-K_α satellite XRD patterns usually observed at high diffraction angles.

5.5 Magnetic properties

The anisotropic magnetization data were measured using a sample with known crystallographic orientation. The temperature dependent magnetization *M(T)* data along [100] axis is presented in

Table 5.1 Crystal data and structure refinement for $AlFe_2B_2$.

Empirical formula	$AlFe_2B_2$
Formula weight	160.3
Temperature	293(2) K
Wavelength	0.71073 Å
Crystal system, space group	Orthorhombic, *Cmmm*
Unit cell dimensions	a=2.9168(6) Å
	b = 11.033(2) Å
	c = 2.8660(6) Å
Volume	92.23(3) 10^3 Å^3
Z, Calculated density	2, 5.75 g/cm^3
Absorption coefficient	31.321 mm^{-1}
F(000)	300
θ range (°)	3.693 to 29.003
Limiting indices	$-3 \leq h \leq 3$
	$-14 \leq k \leq 14$
	$-3 \leq l \leq 3$
Reflections collected	402
Independent reflections	7 [R(int) = 0.0329]
Absorption correction	multi-scan, empirical
Refinement method	Full-matrix least-squares on F^2
Data / restraints / parameters	74 / 0 / 12
Goodness-of-fit on F^2	1.193
Final R indices [I> 2σ(I)]	$R1 = 0.0181$, $wR2 = 0.0467$
R indices (all data)	$R1 = 0.0180$, $wR2 = 0.0467$
Largest difference peak and hole	0.679 and -0.880 e.Å^{-3}

Table 5.2 Atomic coordinates and equivalent isotropic displacement parameters (A^2) for $AlFe_2B_2$. U(eq) is defined as one third of the trace of the orthogonalized U_{ij} tensor.

atom	Wyckoff site	x	y	z	U_{eq}
Fe	4(j)	0.0000	0.3539(1)	0.5000	0.006(6)
Al	2(a)	0.0000	0.0000	0.0000	0.006(7)
B	4(i)	0.0000	0.2066(5)	0.0000	0.009(7)

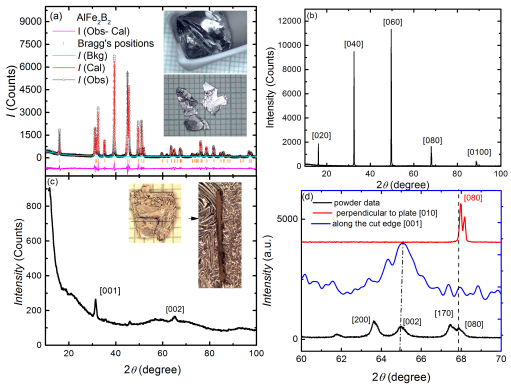

Figure 5.2 (a) Powder XRD for $AlFe_2B_2$. I(Obs), I(Cal) and I(Bkg) stands for experimental powder diffraction, Rietveld refined and instrumental background data. The green vertical lines represent the Bragg reflection peaks and the I(Obs-Cal) is the differential intensity between I(Obs) and I(Cal). The upper inset picture shows the crucible limited growth nature of $AlFe_2B_2$. The lower inset picture is the pieces of as grown plate-like crystals. (b) Monochromatic XRD pattern from the plate surface of $AlFe_2B_2$. (c) Monochromatic XRD pattern from cut surface [001] collected using Bragg-Brentano geometry. The left inset photo shows the as grown $AlFe_2B_2$ crystal. The right inset picture is the photograph of the cut section of the crystal parallel to (001) plane. The middle unidentified peak might be due to a differently oriented shard of cut $AlFe_2B_2$ crystal. (d) Comparison of the monochromatic surface XRD patterns from (b) and (c) with powder XRD pattern from (a) within extended 2θ range of 60 - 70° to illustrate the identification scheme of the crystallographic orientation.

Fig. 5.3(a). Both the Zero Field Cooled Warming (ZFCW) and Field Cooled(FC) *M(T)* data are almost overlapping for 0.01 T applied field. The *M(T)* data suggest a Curie temperature (T_C) of $\sim$ 275 K using an inflection point of *M(T)* data as a criterion. This value will be determined more precisely below to be $T_C = 274$ K using easy axis *M(H)* isotherms around Curie temperature.

Figure 5.3(b) shows the anisotropic, field-dependent magnetization at 2 K. The saturation magnetization (M_{sat}) at 2 K is determined to be 2.40 μ_B/f.u., i.e. roughly half of bulk BCC Fe moment. The anisotropic *M(H)* data at 2 K show [100] is the easy axis, [010] axis is a harder axis with an anisotropy field of $\approx$ 1 T and [001] is the hardest axis of magnetization with an anisotropy field of $\approx$ 5 T. A Sucksmith-Thompson plot [22], using $M(H)$ data along [001], is shown

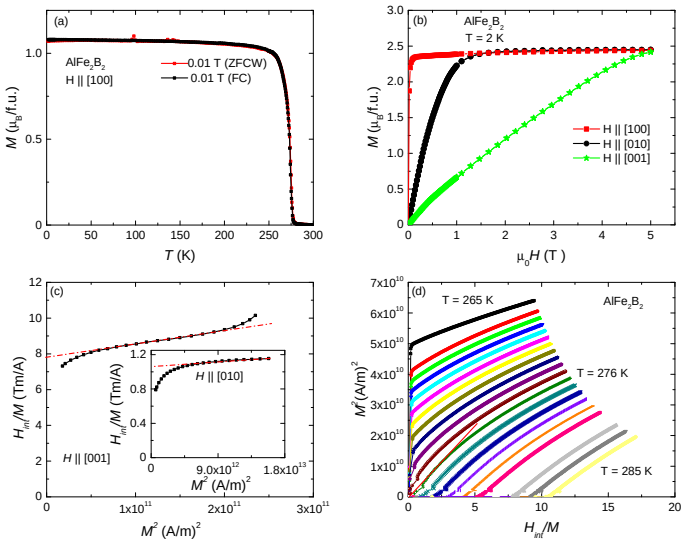

Figure 5.3 (a) Temperature dependent magnetization with 0.01 T applied field along [100] direction (b)) Field dependent magnetization along principle directions at 2 K. [100] is the easy axis with smallest saturating field , [010] is the intermediate axis with 1 T anisotropy and [001] is the hardest axis with $\sim$ 5 T anisotropy field. (c) Sucksmith-Thompson plot for *M(H)* data along [001] direction (and along [010] in the inset) to estimate the magneto-crystalline anisotropy constants. The red dash-dotted line is the linear fit to the hard axes isotherms at high field region ($>$ 3 T) whose Y-intercept is used to estimate the anisotropy constant K. (d) Arrott plot obtained with easy axis isotherms within the temperature range of 265-285 K at a step of 1 K. The straight line through the origin is the tangent to the isotherm corresponding to the transition temperature.

in Fig. 5.3(c). The inset to Fig. 5.3(c) shows data for H along [010]. In a Sucksmith-Thompson plot, the Y-intercept of the linear fit of hard axis $\frac{H_{int}}{M}$ vs M^2 isotherm provides the magneto-crystalline anisotropy constant ($intercept = \frac{2K_1}{{M_S}^2}$, M_S being saturation magnetization at 2 K) of the material. From these plots we determined $K_{010} = 0.23$ MJ/m^3 and $K_{001} = 1.78$ MJ/m^3 respectively.

Given that $AlFe_2B_2$ has $T_C \sim$ room temperature, and is formed from earth abundant elements, it is logical to examine it as a possible magnetocaloric material. The easy axis, [100], *M(H)* isotherms around the Curie temperature (shown for the Arrott plot in Fig. 5.3(d)) were used to estimate the magnetocaloric property for $AlFe_2B_2$ in-terms of entropy change using following equation [1, 23]:

$$\Delta S(\frac{T_1+T_2}{2}, \Delta H) \approx \frac{\mu_0}{T_2-T_1}\int_{H_i}^{H_f} M(T_2,H) - M(T_1,H)dH \quad (5.1)$$

where H_i, H_f are initial and final applied fields and $T_2 - T_1$ is the change in temperature. For this formula to be valid, $T_2 - T_1$ should be small. Here $T_2 - T_1$ is taken to be 1 K. The entropy change calculation scheme in one complete cycle of magnetization and demagnetization is estimated in terms of area between two consecutive isotherms between the given field limit as shown in Fig. 5.4(a). The measured entropy change as a function of temperature is presented in Fig. 5.4(b). The entropy change in 2 T and 3 T applied fields is maximum around 276 K being 3.78 $Jkg^{-1}K^{-1}$ and 4.87 $Jkg^{-1}K^{-1}$respectively. The 2 T applied field entropy change data of this experiment agrees very well with reference [9], shown as 2 T* data in Fig. 5.4(b). The entropy change values for our single crystalline samples are in close agreement with previously reported polycrystalline sample measured values as well [1, 6].

Although, $AlFe_2B_2$ is a rare-earth free material, its magnetocaloric property is larger than lighter rare-earth RT_2X_2 (R = rare earth T = transition metal, X = Si,Ge) compounds with $ThCr_2Si_2$-type structure (space group I4/mmm) namely $CeMn_2Ge_2$($\sim$ 1.8 $Jkg^{-1}K^{-1}$) [24], $PrMn_2Ge_{0.8}Si_{1.2}$($\sim$ 1.0 $Jkg^{-1}K^{-1}$) [25] and $Nd(Mn_{1-x}Fe_x)_2Ge_2$($\sim$ 1.0 $Jkg^{-1}K^{-1}$) [26]. The entropy change of $AlFe_2B_2$ is significantly smaller than $Gd_5Si_2Ge_2$($\sim$ 13 $Jkg^{-1}K^{-1}$), it has comparable entropy change with elemental Gd($\sim$ 5.0 $Jkg^{-1}K^{-1}$) [27]. These results shows that $AlFe_2B_2$ has the potential to be used for magnetocaloric material considering the abundance of its constituents.

To precisely determine the Curie temperature, an Arrott plot was constructed using a wider range of *M(H)* isotherms along the [100] direction (Fig. 5.3(d)). In an Arrott plot M^2 is plotted as a function of $\frac{H_{int}}{M}$. H_{int}= H_{app}-N*M is internal field inside the sample after the demagnetization field is subtracted. In this case the experimental demagnetization factor along the easy axis of the sample was found to be almost negligible because of its thin, plate-like shape with the easy axis lying along the longest dimension of the sample. The detail of determination of the exper-

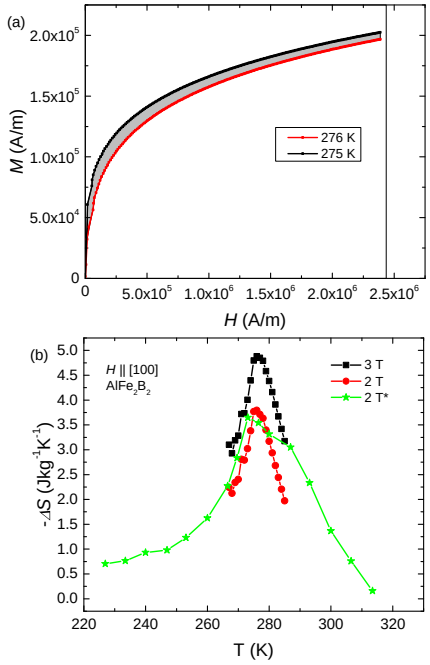

Figure 5.4 Magnetocaloric effect in $AlFe_2B_2$ obtained using *M(H)* isotherms along [100]. (a) showing the change in entropy (ΔS) evaluation scheme at its highest value (b) change in entropy with 2 T and 3 T applied fields using easy axis [100] isotherms. For the sake of comparison, the 2 T* field data are taken from the reference [9].

imental demagnetization factors and their comparison with theoretical data is explained in the references [23] and [28]. The Arrott plots have a positive slope indicating the transition is second order [29]. In the mean field approximation, in the limit of low fields, the Arrott isotherm corresponding to the Curie temperature is a straight line and passes through the origin. In Fig. 5.3(d), the isotherm corresponding to 276 K passes through the origin but it is not a perfectly straight line. This suggests that the magnetic interaction in $AlFe_2B_2$ does not obey the mean-field theory. In the mean-field theory, electron correlation and spin fluctuations are neglected, but these can be significant around the transition temperature of an itinerant ferromagnet.

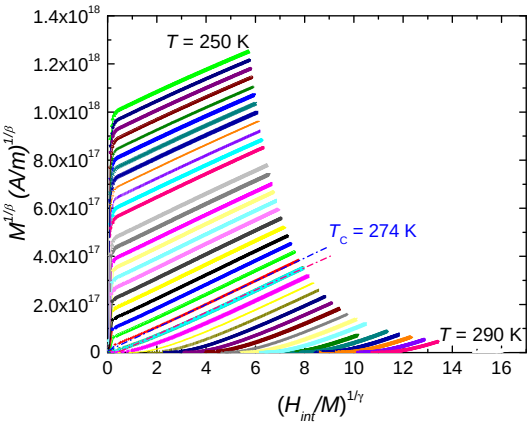

Figure 5.5 Generalized Arrott plot of $AlFe_2B_2$ with magnetization data along [100] direction within temperature range of 250 - 290 K at a step of 1 K. The $\beta = 0.30 \pm 0.04$ and $\gamma = 1.180 \pm 0.005$ were determined from the Kouvel–Fisher method. The two dash-dot straight lines are drawn to visualize the intersection of the isotherms with the axes.

Since the Arrott plot data are not straight lines, a generalized Arrott plot is an alternative way to better confirm the Curie temperature. The generalized Arrott plot derived from the equation of the state [30]

$$(\frac{H_{int}}{M})^{1/\gamma} = a\frac{T - T_C}{T} + bM^{1/\beta} \tag{5.2}$$

is shown in Fig. 5.5. The critical exponents β and γ used in equation of state are derived from the Kouvel-Fisher analysis[31, 32]. To determine β, the equation used was:

$$M_S[\frac{d}{dT}(M_S)]^{-1} = \frac{T - T_C}{\beta} \tag{5.3}$$

where the slope is $\frac{1}{\beta}$. The value of the spontaneous magnetization around the transition temperature was extracted from the Y-intercept of the M^4 vs $\frac{H}{M}$ [33] exploiting their straight line nature with clear Y-intercept. The experimental value of β was determined to be 0.30 ± 0.04 as shown in Fig. 5.6. The uncertainty in β was determined with fitting error as $\Delta\beta = \frac{\delta slope}{slope^2}$.

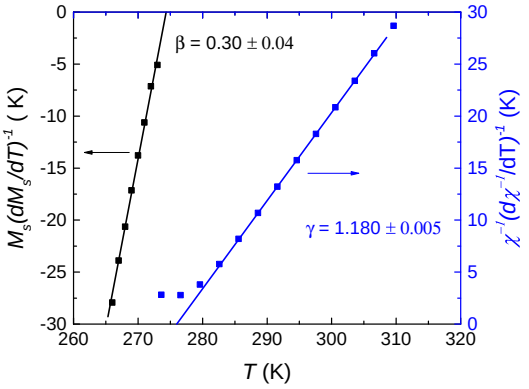

Figure 5.6 Determination of the critical exponents (β and γ)using Kouvel-Fisher plots. See text for details.

Similarly, the value of critical exponent γ was determined with the equation:

$$\chi^{-1}[\frac{d}{dT}(\chi^{-1})]^{-1} = \frac{T - T_C}{\gamma} \tag{5.4}$$

where the slope is $\frac{1}{\gamma}$ and $\chi^{-1}(T)$ is the initial high temperature inverse susceptibility near the transition temperature. The experimental value of the γ was determined to be 1.180 ± 0.005 as shown in Fig. 5.6.

Finally the third critical exponent δ was determined using the equation:

$$M \propto H^{1/\delta} \tag{5.5}$$

by plotting $\ln(M)$ vs $\ln(H)$ (Fig. 5.7) corresponding to Curie temperature 274 K. The experimental value of the δ was determined by fitting $\ln(M)$ vs $\ln(H)$ over different ranges of applied field H. Taking the average of the range of the δ value as shown in Fig. 5.7 we determine δ to be 4.9 ± 0.1 which was closely reproduced (4.93 ± 0.03) with Widom scaling theory $\delta = 1 + \frac{\gamma}{\beta}$.

Additionally, the validity of Widom scaling theory demands that the magnetization data should follow the scaling equation of the state. The scaling laws for a second order magnetic phase transition relate the spontaneous magnetization $M_S(T)$ below T_C, the inverse initial susceptibility $\chi^{-1}(T)$ above T_C, and the magnetization at T_C with corresponding critical amplitudes by the following power laws:

$$M_S(T) = M_0(-\epsilon)^{\beta}, \epsilon < 0 \tag{5.6}$$

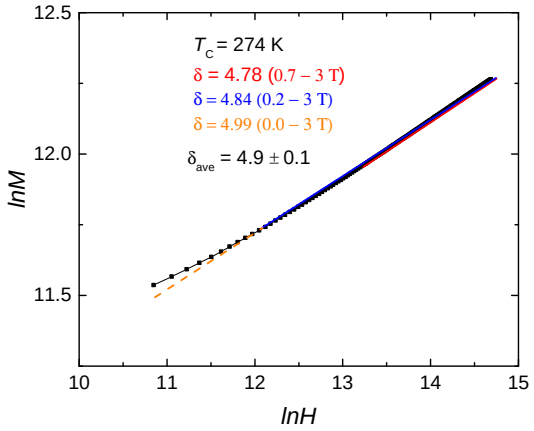

Figure 5.7 Determination of the critical exponent δ using Kouvel-Fisher plots using *M(H)* isotherm at T_C to check the consistency of β and γ via Widom scaling. The data used for determining the exponent δ are highlighted with the red curve in corresponding *M(H)* isotherm. The data in the low field region slightly deviate from the linear behaviour in the logarithmic scale as shown in the inset. The range dependency of the value of δ is illustrated with different colors tangents. The field range for the fitted data is indicated in the parenthesis along with the value of δ. See text for details.

$$\chi^{-1}(T) = \Gamma(\epsilon)^{\gamma}, \epsilon > 0 \tag{5.7}$$

$$M = XH^{\frac{1}{\delta}} \tag{5.8}$$

Where M_0, Γ and X are the critical amplitudes and $\epsilon = \frac{T-T_C}{T_C}$ is the reduced temperature [34]. The scaling hypothesis assumes the homogeneous order parameter which with scaling hypothesis can be expressed as

$$M(H,\epsilon) = \epsilon^{\beta} f_{\pm}(\frac{H}{\epsilon^{\beta+\gamma}}) \tag{5.9}$$

Where f_+(T> T_C) and f_-(T< T_C) are the regular functions. With new renormalised parameters, m = $\epsilon^{-\beta}M(H,\epsilon)$ and h = $\epsilon^{-(\beta+\gamma)}M(H,\epsilon)$ equation 5.9 can be written as

$$m = f_{\pm}(h) \tag{5.10}$$

Up to the linear order, the scaled m vs h graph is plotted as shown in Fig. 5.8 along with an inset in log-log scale which clearly shows that all isotherms converge to the two curves one for T> T_C and other for T< T_C. This graphically shows that all the critical exponents were properly renormalized.

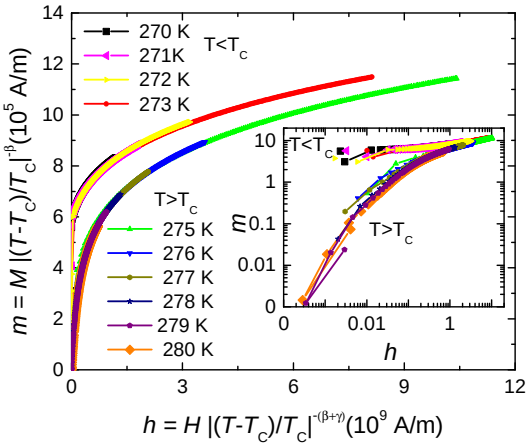

Figure 5.8 Normalized isotherms to check the validity of scaling hypothesis. The isotherms in between 270-273 K are converged to higher value ($T<T_C$) and isothems inbetween 275-280 K are converged to lower value($T>T_C$). The inset shows the corresponding log-log plot clearly bifurcated in two branches in low field region.

Finally the consistency of the critical exponents β and γ is demonstrated (shown in Fig. 5.9(a)) by reproducing the initial spontaneous magnetization M_S and $\chi^{-1}(T)$ near the transition temperature using the Y and X-intercept of generalized Arott plots as shown in Fig. 5.5 which overlaps with M_S obtained by M^4 vs $\frac{H}{M}$ [33] and and initial inverse susceptibility $\chi^{-1}(T)$ with 1 T applied field. The extracted data well fit [34] with corresponding power laws in equation (6) and (7) as shown in Fig. 5.9(b) giving $\beta = 0.295 \pm 0.002$ and $\gamma = 1.210 \pm 0.003$ which closely agree with previously obtained K-F values.

The experimental value of the $AlFe_2B_2$ critical exponents ($\gamma = 1.18$, $\beta = 0.30$, $\delta = 4.93$) are comparable to those of the 3 dimensional (3D) Ising model ($\gamma = 1.25$, $\beta = \frac{5}{16}$, $\delta = 5$) [35] and 3D-XY model ($\gamma = 1.32$, $\beta = 0.35$, $\delta = 4.78$) [36] rather than those of the mean-field model ($\gamma = 1$, $\beta = 0.5$, $\delta = 3$). Further experimental measurements and theoretical would be needed to further clarify the universality class of this material.

To measure the effective moment (M_{eff}) of the Fe above the Curie temperature, a Curie-Weiss plot was prepared as shown in Fig. 5.9. The effective moment of the Fe-ion above the Curie

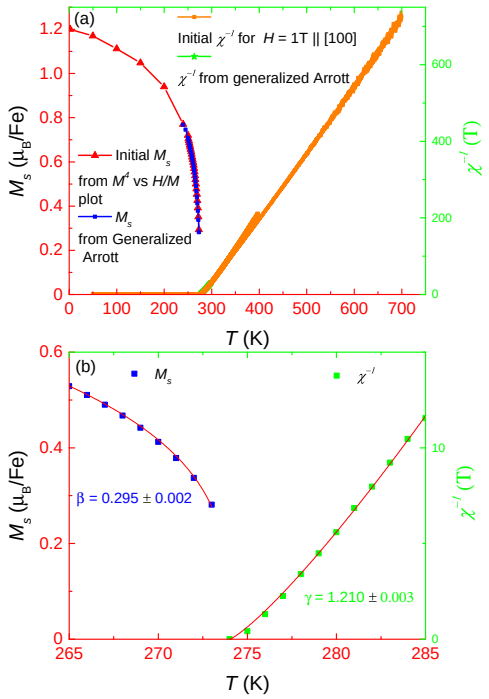

Figure 5.9 Illustration of the consistency of the critical exponents β and γ used for generalizes Arrott plot (a) by reproducing the initial spontaneous magnetization M_S and $\chi^{-1}(T)$ via Y and X-intercept of the generalized Arrott plot. (b) Fitting of the extracted data (squares) from generalized Arrott plot with corresponding power laws (red lines) in equation 6 and 7.

temperature was determined to be 2.15 μ_B. Since the effective moment above the Curie temperature is almost equal to BCC Fe (2.2 μ_B) and the ordered moment at 2 K is significantly smaller than Fe-ion (1.2 μ_B/Fe) giving the Rhode-Wohlfarth ratio ($\frac{M_C}{M_{sat}}$) nearly equal to 1.21, where effective moment $\mu_{eff} = \sqrt{(8 * C)}$ and C is the Curie-Weiss constant given as $C = \frac{(\mu_B)^2}{3*R} * M_C(M_C + 2)$, this compound shows signs of an itinerant nature in its magnetization [37].

Itinerant magnetism, in general, can be tuned (meaning the size of magnetic moment and Curie temperature can be altered significantly and sometime even suppressed completely) with an

external parameter like pressure or chemical doping. As a case study, we investigated the influence of the external pressure on the ferromagnetism of $AlFe_2B_2$.

Figure 5.10 shows the pressure dependent resistivity of single crystalline $AlFe_2B_2$ with current applied along the crystallographic a-axis. It shows metallic behaviour with a residual resistivity of 60 $\mu\Omega$ cm. The metalic behavior was also predicted in density functional calculation as well [38]. The ambient pressure temperature dependent resistivity of $AlFe_2B_2$ shows a kink around 275 K, indicating a loss of spin disorder scattering associated with the onset of ferromagnetic order. As pressure is increased to 2.24 GPa the temperature of this kink is steadily reduced. To determine the transition temperature T_C, the maximum in the temperature derivative $d\rho/dT$ is used, as shown in the inset of Fig. 5.10. The pressure dependence of T_C, the temperature - pressure phase diagram of $AlFe_2B_2$ is presented in Fig. 5.11. The transition temperature, T_C, is suppressed from 275 K to 255 K when pressure is increased from 0 to 2.24 GPa, giving a suppression rate of -8.9 K/GPa. Interestingly, Curie temperature suppression rate of $AlFe_2B_2$ is found to be comparable to the model itinerant magnetic materials like helimagnetic MnSi (~ -15 K/GPa) [39], and weak ferromagnets $ZrZn_2$ (~ -13 K/GPa) [40] and Ni_3Al (~ -4 K/GPa) [41]. A linear fitting of the data as shown in Fig. 5.11 indicates that to completely suppress the T_C around 31 GPa would be required. Usually such linear extrapolation provide an upper estimate of the critical pressure.

First principles calculations

Theoretical calculations for $AlFe_2B_2$ were performed using the all electron density functional theory code WIEN2K [42, 43, 44]. The generalized gradient approximation according to Perdew, Burke, and Ernzerhof (PBE) [45] was used in our calculations. The sphere radii (RMT) were set to 2.21, 2.17, and 1.53 Bohr for Fe, Al, and B, respectively. RK_{max} which defines the product of the smallest sphere radius and the largest plane wave vector was set to 7.0. All calculations were performed with the experimental lattice parameters as reported in reference [46] (which are consistent with our results) and all internal coordinates were relaxed until internal forces on atoms were less than 1 mRyd/Bohr-radius. All the calculations were performed in the collinear spin

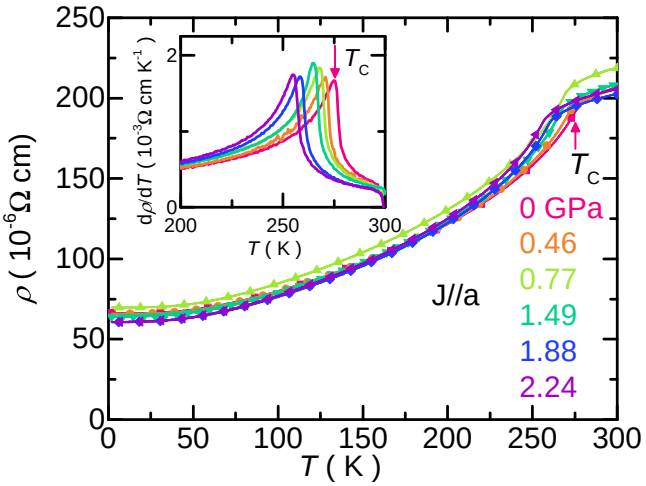

Figure 5.10 Evolution of the single crystal $AlFe_2B_2$ resistivity with hydrostatic pressure up to 2.24 GPa. Pressure values at T_C were estimated from linear interpolation between the P_{300K} and $P_{T\leq 90K}$ values (see text). Current was applied along the crystallographic a-axis. Inset shows the evolution of temperature derivative $d\rho/dT$ with hydrostatic pressure. The peak positions in the derivative were identified as transition temperature T_C. Examples of T_C are indicated by arrows in the figure.

alignment. The magnetic anisotropy energy (MAE) was obtained by calculating the total energies of the system with spin-orbit coupling (SOC) with the magnetic moment along the three principal crystallographic axes. For these MAE calculations the k-point convergence was carefully checked, and the calculations reported here were performed with 120,000 k-points in the full Brillouin zone.

Similar to the experimental observation, $AlFe_2B_2$ is calculated to have ferromagnetic behaviour, with a saturation magnetic moment (we do not include the small Fe orbital moment) of 1.36 μ_B/Fe. This is in reasonable agreement with the experimentally measured value of 1.21μB/Fe. Interestingly this calculated magnetic moment on Fe, is significantly lower than the moment on Fe in BCC Fe (2.2 μ_B/Fe) further suggesting a degree of itinerant behaviour. The calculated density of states is shown in Fig. 5.12. As expected for a Fe-based ferromagnet, the electronic structure in the vicinity of the Fermi level is dominated by Fe d orbitals and we observe a substantial exchange splitting of 2-3 eV.

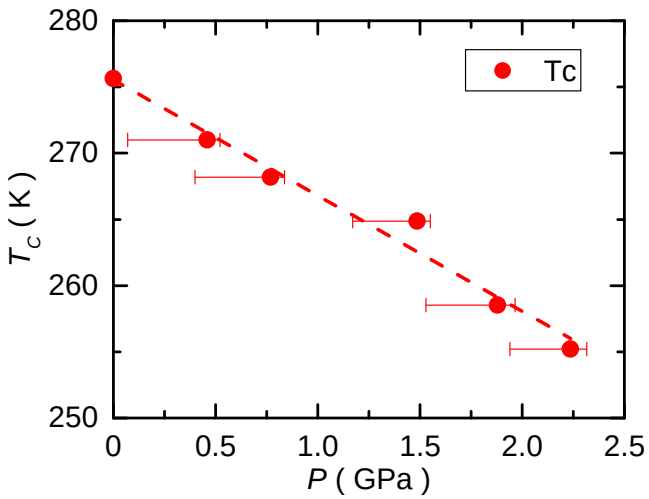

Figure 5.11 Temperature - pressure phase diagram of $AlFe_2B_2$ as determined from resistivity measurement. Pressure values were estimated as being described in Fig. 5.10 and in the text. Error bars indicate the room temperature pressure P_{300K} and low temperature pressure $P_{T\leq 90K}$. As shown in the figure, in the pressure region of $0 - 2.24$ GPa the ferromagnetic transition temperature T_C is suppressed upon increasing pressure, with suppressing rate around -8.9 K/GPa.

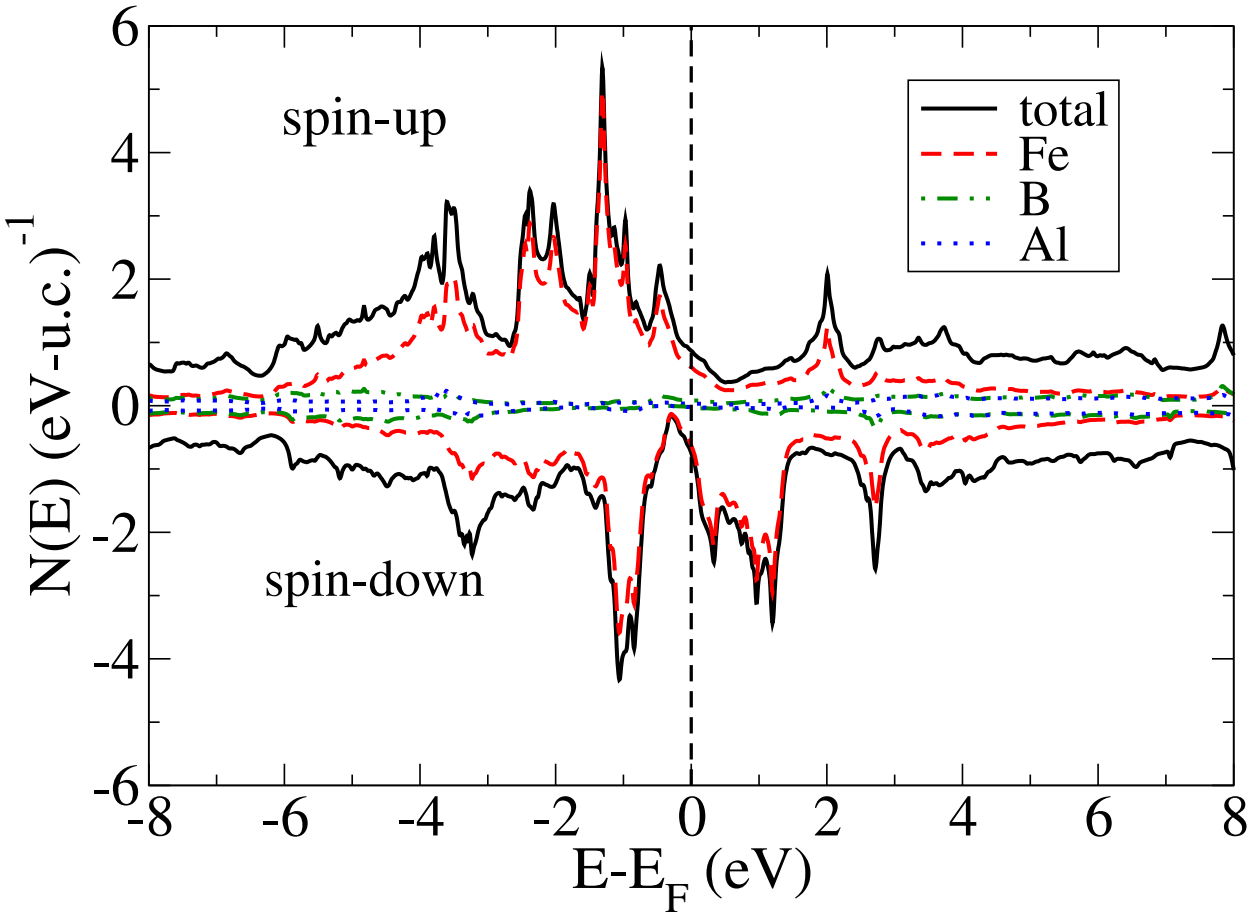

Figure 5.12 The calculated density-of-states of $AlFe_2B_2$.

For an orthorhombic crystal structure, the magnetic anisotropy energy is described by total energy calculations for the magnetic moments along each of the three principal axis [47]. For $AlFe_2B_2$ we find, the [100] and [010] axes to be the "easy" directions, separated by just 0.016 meV per Fe, with [100] being the easiest axis. The [001] direction is the "hard" direction, which lies 0.213 meV per Fe above the [100] axis. As in our previous work on HfMnP [23], this value is much larger than the 0.06 meV value for hcp Co and likely results from a combination of the orthorhombic crystal structure and the structural complexity associated with a ternary compound. The 0.213 meV energy difference on a volumetric basis corresponds to a anisotropy constant K_1 as 1.48 MJ/m^3. (Note that we use the convention of the previous work and simply *define* K_1 for

an orthorhombic system as the energy difference between the hardest and easiest directions.) This magnetic anisotropy constant describes the energy cost associated with the changing the orientation of the magnetic moments under the application of a magnetic field, and is an essential component for permanent magnets. It is noteworthy that this anisotropy is comparable to the value of 2 MJ/m^3 proposed by Coey for an efficient permanent magnet [48], despite containing no heavy elements, using the approximation that $H_a \approx 2\mu_0 K_1/M_s$, with K as 1.48 MJ/m^3 and M$_s$ as 0.68 T, yields an anisotropy field of 5.4 T, which is in excellent agreement with the experimentally measured value of 5 T and $K_{001} \approx 1.8$ MJ/m^3.

5.6 Conclusions

Single crystalline $AlFe_2B_2$ was grown by self-flux-growth technique and structural, magnetic and transport properties were studied. $AlFe_2B_2$ is an orthorhombic, metallic ferromagnet with promising magnetocaloric behaviour. The Curie temperature of $AlFe_2B_2$ was determined to be 274 K using the generalized Arrott plot method along with estimation of critical exponents using Kouvel-Fisher analysis. The ordered magnetic moment (M_{sat}) at 2 K is 1.20μ_B/Fe at 2 K which is much less than paramagnetic Fe-ion moment at high temperature (2.15μ_B/Fe) indicating itinerant magnetism. The magnetization in $AlFe_2B_2$ responds to the hydrostatic pressure with $\frac{dT_C}{dP} \sim -8.9$ K/GPa. A linear extrapolation of this $T_C(P)$ trend leads to an upper estimate of $\sim$ 30 GPa required to fully supress the transition. The saturation magnetization and anisotropic magnetic field predicted by first principle calculations are in close agreement with the experimental results. The magneto-crystalline anisotropy fields were determined to be 1 T along [010] and 5 T along [001] direction w. r. to easy axis [100]. The magneto-crystalline anisotropy constants at 2 K are determined to be $K_{010} \approx 0.23$ MJ/m^3 and $K_{001} \approx 1.8$ MJ/m^3.

5.7 Acknowledgement

We would like to thank Drs. W. R. McCallum and L. H. Lewis for drawing attention to this compound and Dr. A. Palasyuk for useful discussions. This research was supported by the Critical

Materials Institute, an Energy Innovation Hub funded by the U.S. Department of Energy, Office of Energy Efficiency and Renewable Energy, Advanced Manufacturing Office. This work was also supported by the office of Basic Energy Sciences, Materials Sciences Division, U.S. DOE. Li Xiang was supported by W. M. Keck Foundation. This work was performed at the Ames Laboratory, operated for DOE by Iowa State University under Contract No. DE-AC02-07CH11358.

5.8 References

[1] Xiaoyan Tan, Ping Chai, Corey M. Thompson, and Shatruk Michael. Magnetocaloric Effect in $AlFe_2B_2$: Toward Magnetic Refrigerants from Earth-Abundant Elements. *J. Am. Chem. Soc.*, 135(25):9553–9557, 2013.

[2] Johan Cedervall, Lennart Häggström, Tore Ericsson, and Martin Sahlberg. Mössbauer study of the magnetocaloric compound $AlFe_2B_2$. *Hyperfine Interactions*, 237(1):47, 2016.

[3] M. ElMassalami, D. da S. Oliveira, and H. Takeya. On the ferromagnetism of $AlFe_2B_2$. *J. Magn. Magn. Mater.*, 323(16):2133 – 2136, 2011.

[4] Wolfgang Jeitschko. The crystal structure of Fe_2AlB_2. *Acta Cryst.*, B(25):163–165, June 1969.

[5] Yu. B. Kuz'ma and N.F. Chaban. Crystal Structure of the Compound Fe_2AlB_2. *Inorg. Mater.*, 5:321–322, 1969.

[6] Qianheng Du, Guofu Chen, Wenyun Yang, Jianzhong Wei, Muxin Hua, Honglin Du, Changsheng Wang, Shunquan Liu, Jingzhi Han, Yan Zhang, and Jinbo Yang. Magnetic frustration and magnetocaloric effect in $AlFe_{2-x}$ Mn_x B_2 (x = 0 - 0.5) ribbons. *Journal of Physics D: Applied Physics*, 48(33):335001, 2015.

[7] Ping Chai, Sebastian A. Stoian, Xiaoyan Tan, Paul A. Dube, and Michael Shatruk. Investigation of magnetic properties and electronic structure of layered-structure borides AlT_2B_2 (T=Fe, Mn, Cr) and $AlFe_{2-x}Mn_xB_2$. *Journal of Solid State Chemistry*, 224:52 – 61, 2015.

[8] Sarah Hirt, Fang Yuan, Yurij Mozharivskyj, and Harald Hillebrecht. $AlFe_{2-x}Co_xB_2$ (x = 0 - 0.30): T_C Tuning through Co Substitution for a Promising Magnetocaloric Material Realized by Spark Plasma Sintering. *Inorg. Chem.*, 55(19):9677–9684, 2016. PMID: 27622951.

[9] R. Barua, B.T. Lejeune, L. Ke, G. Hadjipanayis, E.M. Levin, R.W. McCallum, M.J. Kramer, and L.H. Lewis. Anisotropic magnetocaloric response in $AlFe_2B_2$. *J. Alloys Compd.*, 745:505 – 512, 2018.

[10] Qianheng Du, Guofu Chen, Wenyun Yang, Zhigang Song, Muxin Hua, Honglin Du, Changsheng Wang, Shunquan Liu, Jingzhi Han, Yan Zhang, and Jinbo Yang. Magnetic properties of $AlFe_2\ B_2$ and $CeMn_2\ Si_2$ synthesized by melt spinning of stoichiometric compositions. *Japanese Journal of Applied Physics*, 54(5):053003, 2015.

[11] E. M. Levin, B. A. Jensen, R. Barua, B. Lejeune, A. Howard, R. W. McCallum, M. J. Kramer, and L. H. Lewis. Effects of Al content and annealing on the phases formation, lattice parameters, and magnetization of $Al_xFe_2\ B_2$(x = 1.0 , 1.1 , 1.2) alloys. *Phys. Rev. Materials*, 2:034403, Mar 2018.

[12] P. C. Canfield and Z. Fisk. Growth of single crystals from metallic fluxes. *Philos. Mag.*, 65(6):1117–1123, 1992.

[13] Paul C. Canfield, Tai Kong, Udhara S. Kaluarachchi, and Na Hyun Jo. Use of frit-disc crucibles for routine and exploratory solution growth of single crystalline samples. *Philos. Mag.*, 96(1):84–92, 2016.

[14] S.L. Bud'ko, A.N. Voronovskii, A.G. Gapotchenko, and E.S. ltskevich. The fermi surface of cadmium at an electron-topological phase transition under pressure. *J. Exp. Theor. Phys.*, 59(2):454, February 1984.

[15] J. D. Thompson. Low-temperature pressure variations in a self-clamping pressure cell. *Rev. Sci. Instrum.*, 55(2):231–234, 1984.

[16] M. S. Torikachvili, S. K. Kim, E. Colombier, S. L. Budko, and P. C. Canfield. Solidification and loss of hydrostaticity in liquid media used for pressure measurements. *Rev. Sci. Instrum.*, 86(12):123904, 2015.

[17] A Eiling and J S Schilling. Pressure and temperature dependence of electrical resistivity of Pb and Sn from 1-300K and 0-10 GPa-use as continuous resistive pressure monitor accurate over wide temperature range; superconductivity under pressure in Pb, Sn and In. *J. Phys. F: Met. Phys*, 11(3):623, 1981.

[18] B Bireckoven and J Wittig. A diamond anvil cell for the investigation of superconductivity under pressures of up to 50 GPa: Pb as a low temperature manometer. *J Phys E*, 21(9):841, 1988.

[19] S. K. Kim, M. S. Torikachvili, E. Colombier, A. Thaler, S. L. Bud'ko, and P. C. Canfield. Combined effects of pressure and Ru substitution on $BaFe_2As_2$. *Phys. Rev. B*, 84:134525, Oct 2011.

[20] *SHELXTL-v2008/4, Bruker AXS Inc., Madison, Wisconsin, USA, 2013.*

[21] Brian H. Toby. *EXPGUI*, a graphical user interface for *GSAS. J. Appl. Crystallogr.*, 34(2):210–213, Apr 2001.

[22] W. Sucksmith and J. E. Thompson. The Magnetic Anisotropy of Cobalt. *Proc. Royal Soc. A*, 225(1162):362–375, 1954.

[23] Tej N. Lamichhane, Valentin Taufour, Morgan W. Masters, David S. Parker, Udhara S. Kaluarachchi, Srinivasa Thimmaiah, Sergey L. Bud'ko, and Paul C. Canfield. Discovery of ferromagnetism with large magnetic anisotropy in ZrMnP and HfMnP. *Appl. Phys. Lett.*, 109(9):092402, 2016.

[24] M. F. Md Din, J. L. Wang, Z. X. Cheng, S. X. Dou, S. J. Kennedy, M. Avdeev, and S. J. Campbell. Tuneable Magnetic Phase Transitions in Layered $CeMn_2Ge_{2-x}Si_x$ Compounds. *Sci. Rep*, 5(11288), 2015.

[25] J. L. Wang, S. J. Campbell, R. Zeng, C. K. Poh, S. X. Dou, and S. J. Kennedy. Re-entrant ferromagnet $PrMn_2Ge_{0.8}Si_{1.2}$: Magnetocaloric effect. *J. Appl. Phys.*, 105(7):07A909, 2009.

[26] Y.Q. Chen, J. Luo, J.K. Liang, J.B. Li, and G.H. Rao. Magnetic properties and magnetocaloric effect of $Nd(Mn_{1-x}Fe_x)_2Ge_2$ compounds. *J. Alloys Compd.*, 489(1):13 – 19, 2010.

[27] V. K. Pecharsky and K. A. Gschneidner, Jr. Giant Magnetocaloric Effect in $Gd_5(Si_2Ge_2)$. *Phys. Rev. Lett.*, 78:4494–4497, Jun 1997.

[28] Tej N. Lamichhane, Valentin Taufour, Srinivasa Thimmaiah, David S. Parker, Sergey L. Bud'ko, and Paul C. Canfield. A study of the physical properties of single crystalline Fe_5B_2P. *J. Magn. Magn. Mater.*, 401:525 – 531, 2016.

[29] B.K. Banerjee. On a generalised approach to first and second order magnetic transitions. *Phys. Lett.*, 12(1):16 – 17, 1964.

[30] Anthony Arrott and John E. Noakes. Approximate equation of state for nickel near its critical temperature. *Phys. Rev. Lett.*, 19:786–789, Oct 1967.

[31] James S. Kouvel and Michael E. Fisher. Detailed magnetic behavior of nickel near its Curie point. *Phys. Rev.*, 136:A1626–A1632, Dec 1964.

[32] Ch.V Mohan, M Seeger, H Kronmller, P Murugaraj, and J Maier. Critical behaviour near the ferromagnetic-paramagnetic phase transition in $La_{0.8}Sr_{0.2}MnO_3$. *J. Magn. Magn. Mater*, 183(3):348 – 355, 1998.

[33] Bin Chen, JinHu Yang, HangDong Wang, Masaki Imai, Hiroto Ohta, Chishiro Michioka, Kazuyoshi Yoshimura, and MingHu Fang. Magnetic Properties of Layered Itinerant Electron Ferromagnet Fe_3GeTe_2. *J. Phys. Soc. Jpn.*, 82(12):124711, 2013.

[34] A. K. Pramanik and A. Banerjee. Critical behavior at paramagnetic to ferromagnetic phase transition in $Pr_{0.5}Sr_{0.5}MnO_3$: A bulk magnetization study. *Phys. Rev. B*, 79:214426, Jun 2009.

[35] D S Gaunt. The critical isotherm and critical exponents of the three-dimensional ising ferromagnet. *Proceedings of the Physical Society*, 92(1):150, 1967.

[36] Massimo Campostrini, Martin Hasenbusch, Andrea Pelissetto, Paolo Rossi, and Ettore Vicari. Critical behavior of the three-dimensional XY universality class. *Phys. Rev. B*, 63:214503, May 2001.

[37] P. Rhodes and E. P. Wohlfarth. The effective Curie-Weiss constant of ferromagnetic metals and alloys. *Proc. Roy. Soc. A. Mathematical, Physical and Engineering Sciences*, 1963.

[38] Y. Cheng, Z.L. Lv, X.R. Chen, and L.C. Cai. Structural, electronic and elastic properties of $AlFe_2B_2$: First-principles study. *Computational Materials Science*, 92:253–257, 2014.

[39] C. Pfleiderer, D. Reznik, L. Pintschovius, H. v. Löhneysen, M. Garst, and A. Rosch. Partial order in the non-Fermi-liquid phase of MnSi. *Nature*, 427:227231, January 2004.

[40] M. Uhlarz, C. Pfleiderer, and S. M. Hayden. Quantum Phase Transitions in the Itinerant Ferromagnet $ZrZn_2$. *Phys. Rev. Lett.*, 93:256404, Dec 2004.

[41] P. G. Niklowitz, F. Beckers, G. G. Lonzarich, G. Knebel, B. Salce, J. Thomasson, N. Bernhoeft, D. Braithwaite, and J. Flouquet. Spin-fluctuation-dominated electrical transport of Ni_3Al at high pressure. *Phys. Rev. B*, 72:024424, Jul 2005.

[42] P. Blaha, K. Schwarz, G. K. H. Madsen, D. Kvasnicka, and J. Luitz. *WIEN2K, An Augmented Plane Wave + Local Orbitals Program for Calculating Crystal Properties*. Karlheinz Schwarz, Techn. Universität Wien, Austria, 2001.

[43] E Sjostedt, L Nordstrom, and David. J Singh. An alternative way of linearizing the augmented plane-wave method. *Solid State Commun.*, 114(1):15 – 20, 2000.

[44] David J. Singh and L. Nordstrom. *Planewaves Pseudopotentials and the LAPW Method, 2nd ed.* Springer, Berlin, 2006.

[45] John P Perdew, Kieron Burke, and Matthias Ernzerhof. Generalized gradient approximation made simple. *Phys. Rev. Lett.*, 77(18):3865, 1996.

[46] Johan Cedervall, Mikael Svante Andersson, Tapati Sarkar, Erna K Delczeg-Czirjak, Lars Bergqvist, Thomas C Hansen, Premysl Beran, Per Nordblad, and Martin Sahlberg. Magnetic structure of the magnetocaloric compound $AlFe_2B_2$. *J. Alloys Compd.*, 664:784–791, 2016.

[47] Wilfred Palmer. Magnetocrystalline anisotropy of magnetite at low temperature. *Phys. Rev.*, 131(3):1057, 1963.

[48] J. M. D. Coey. Hard magnetic materials: A perspective. *IEEE Trans. Magn.*, 47(12):4671–4681, 2011.

CHAPTER 6. NEAR ROOM TEMPERATURE ANTIFERROMAGNETIC ORDERING WITH A POTENTIAL LOW DIMENSIONAL MAGNETISM IN $AlMn_2B_2$

A paper accepted by *Physical Review Materials*

Tej N. Lamichhane[1], Khusboo Rana[1], Qisheng Lin[2], Sergey L. Bud'ko[1], Yuji Furukawa[1], and Paul C. Canfield[1]

[1] Ames Laboratory, U.S. DOE, and Department of Physics and Astronomy, Iowa State University, Ames, Iowa 50011, USA

[2]Ames Laboratory, U.S. DOE, and Department of Physics and Astronomy, Iowa State University, Ames, Iowa 50011, USA

6.1 abstract

We present self flux growth and characterization of single crystalline $AlMn_2B_2$. It is an orthorhombic (space group Cmmm), layered material with a plate like morphology. The anisotropic bulk magnetization data, electrical transport and ^{11}B nuclear magnetic resonance (NMR) data revealed an antiferromagnetic (AFM) transition at 313 $\pm$ 2 K. In the magnetization data, there is also a broad local maximum significantly above the AFM transition that could be a signature of low dimensional magnetic interactions in $AlMn_2B_2$.

6.2 Introduction

The AlT_2B_2 (T = Fe, Cr, Mn) system crystallizes in the orthorhombic, Cmmm structure and adopts a layer morphology with an internal structure of alternate stacking of Al atom planes and T_2B_2 slabs along the *b*-axis [1]. A representative unit cell of $AlMn_2B_2$ is shown in Fig. 6.1(a) to demonstrate this atomic structure. AlT_2B_2 compounds are interesting, specially for potential rare

earth free magnetocaloric materials and soft magnetic materials. $AlFe_2B_2$ is ferromagnetic and studied for its magneto-caloric and anisotropic magnetic properties [2, 3, 4]. Understanding the magnetic properties of the neighbouring, isostructural compounds can provide further insight in to the series as well as how to tune the magnetocaloric property of the $AlFe_2B_2$ via substitution. We started this work to clarify the magnetic properties of $AlMn_2B_2$ since it was identified as a nonmagnetic material [5]. In addition, some inconsistencies between bulk and local probe magnetic measurements in the $Al(Fe_{1-x}Mn_x)_2B_2$ were observed. A later first principle calculation suggested that $AlMn_2B_2$ should be an anti-ferromagnetic compound [6]. In a recent powder neutron study, $AlMn_2B_2$ is identified as a ceramic AFM compound [7] with Neel temperature around 390 K. A study of lattice parameters variation from room temperature to 1200 K revealed that there is a change in anisotropy nature in a and c lattice parameters around 450 K and a local minimum in b lattice parameters around 400 K [8]. The lack of a clear description of the nature or number of magnetic phase transitions in $AlMn_2B_2$ led us to grow and systematically study single crystalline samples.

This paper reports the synthesis of bulk single crystals via high-temperature solution growth and their characterization via high and low temperature magnetization, NMR, and electrical resistance measurements. We find that $AlMn_2B_2$ is a metallic antiferromagnet with a transition temperature of $T_N = 313 \pm 2$ K. In addition we find that $AlMn_2B_2$ has features associated with pseudo-two-dimensional magnets.

6.3 Experimental Details

6.3.1 Crystal growth

Solution growth is a powerful tool even for compounds with high melting elements like B [9, 3, 10]. The major difficulty associated with solution growth is finding an initial composition that allows for growth of the single phase, desired compound. For example, $CaKFe_4As_4$ growth in single phase form presents an illustrative example [11]. Fortunately, with the innovation of fritted alumina

Table 6.1 Crystal data and structure refinement for $AlMn_2B_2$.

Empirical formula	$AlMn_2B_2$
Formula weight	158.48
Temperature	296(2) K
Wavelength	0.71073 Å
Crystal system, space group	Orthorhombic, *Cmmm*
Unit cell dimensions	a=2.9215(1) Å
	b = 11.0709(6) Å
	c = 2.8972(2) Å
Volume	93.706(9) 10^3 Å^3
Z, Calculated density	2, 5.63 g/cm^3
Absorption coefficient	6.704 mm^{-1}
F(000)	73
θ range (°)	3.693 to 29.003
Limiting indices	$-5 \leq h \leq 5$
	$-22 \leq k \leq 22$
	$-5 \leq l \leq 5$
Reflections collected	1467
Independent reflections	270 [R(int) = 0.0401]
Completeness to theta = 25.242°	98.5%
Absorption correction	multi-scan, empirical
Refinement method	Full-matrix least-squares
Data / restraints / parameters	270 / 0 / 12
Goodness-of-fit on F^2	1.101
Final R indices [I> 2σ(I)]	$R1 = 0.0362$, $wR2 = 0.0817$
R indices (all data)	$R1 = 0.0387$, $wR2 = 0.0824$
Largest diff. peak and hole	2.341 and -1.249 e.Å^{-3}

Table 6.2 Atomic coordinates and equivalent isotropic displacement parameters (A^2) for $AlMn_2B_2$. U(eq) is defined as one third of the trace of the orthogonalized U_{ij} tensor.

atom	Wyckoff site	x	y	z	U_{eq}
Mn	4*j*	0	0.3552(1)	1/2	0.0070(1)
Al	2*a*	0	0	0	0.0067(5)
B	4*i*	0	0.2065(5)	0	0.0070(1)

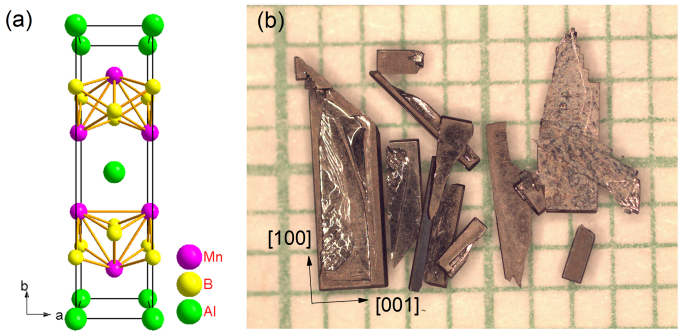

Figure 6.1 (a)$AlMn_2B_2$ unit cell showing Mn_2B_2 slabs stacked with Al layer (b) Concentrated NaOH etched $AlMn_2B_2$ single crystals

crucibles sets [12] we can now reuse decanted melt and essentially fractionate the melt, as described below.

Al shot (Alfa Aesar 99.999%), B pieces (Alfa Aesar 99.5% metal basis) and Mn pieces (Alfa Aesar 99.9% metal basis) after surface oxidation cleaning as described elsewhere [13] were used for the crystal growth process. We started with an Al rich composition, $Al_{68}Mn_{22}B_{10}$, and arc-melted it at least 4 times under an Ar atmosphere. The button was then cut with a metal cutter and re-arcmelted if some not-reacted B pieces were found. After the button appeared to be homogeneous, it was packed in a fritted alumina crucible set [12] and sealed under partial pressure of argon inside amorphous silica jacket to form a growth ampoule. The growth ampoule was then heated to 1200 °C over 2 h and soaked there for 10 h before spinning using a centrifuge. Due to high melting point of B containing compounds, homogeneous liquid was not formed at 1200 °C. Undissolved polycrystalline MnB and Al-Mn binary compounds were separated at 1200 °C via centrifuging. The catch crucible collected the homogeneous melt at 1200 °C was again sealed in a fritted alumina crucible sets under Ar atmosphere to form second growth ampoule. This second ampoule was heated to 1200 °C over 2 h, held there for another 10 h and cooled down to 1100 °C over 50 h and spun using centrifuge to separate the crystals. The second growth attempt produced a mixture of the targeted $AlMn_2B_2$ phase along with MnB crystals. So as to avoid this MnB contamination, the catch crucible of the

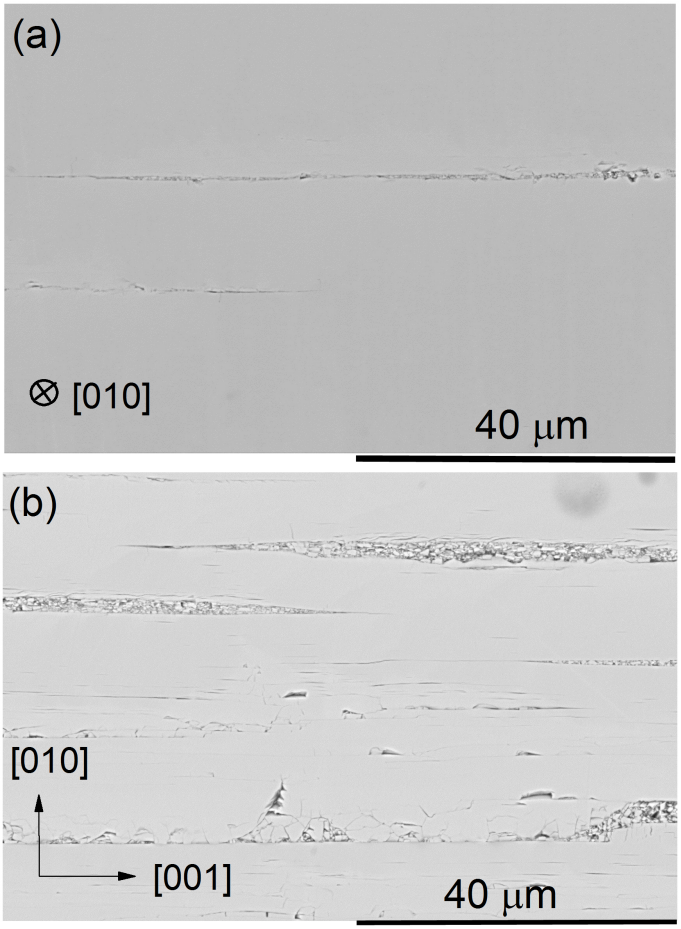

Figure 6.2 (a) SEM image of $AlMn_2B_2$ single crystalline sample along the planar view (with electron beam parallel to [010]) (b) SEM image of $AlMn_2B_2$ in a cross sectional view with electron beam parallel to [100].

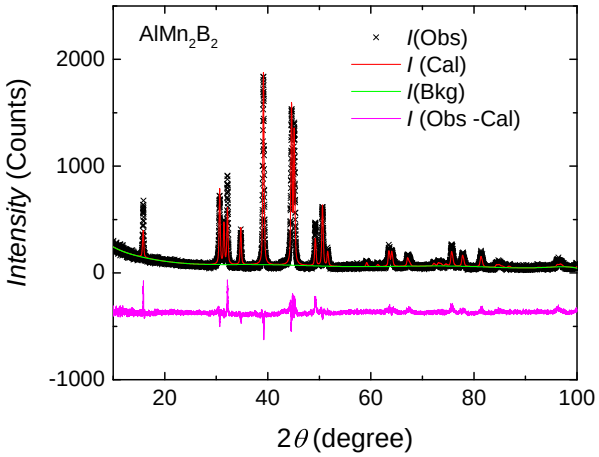

Figure 6.3 Single crystal crushed powder XRD pattern where I (Obs), I(Cal), I(Bkg) and I(Obs-Cal) are observed, calculated, background and differential diffractograms respectively.

second growth was used for a third growth and sealed again under a partial pressure of Ar. For this stage, to make sure there are no other nucleated crystals, the third growth growth was heated to 1200 °C over 2 h and soaked there for 2 h. It was then cooled down to 1100 °C over 1 h and stayed there for 1 h followed by slow cooling to 990 °C over 120 h and centrifuged to separate large, single phased $AlMn_2B_2$ crystals as shown in Fig. 6.1(b). The flux on the surface was removed via concentrated NaOH etching.

It should be noted that predominantly single phase $AlMn_2B_2$ crystals were grown in single growth attempt using initial $Al_{84}Mn_8B_8$ composition however the crystals were small, due to multiple nucleation sites.

6.4 Crystal structure and stoichiometry

As grown single crystals were characterized using a scanning electron microscope (SEM), as well as both powder and single crystal X-ray diffraction (XRD). Figures 6.2(a) and (b) show the planar and cross sectional backscattered SEM images of $AlMn_2B_2$ single crystals which show predomi-

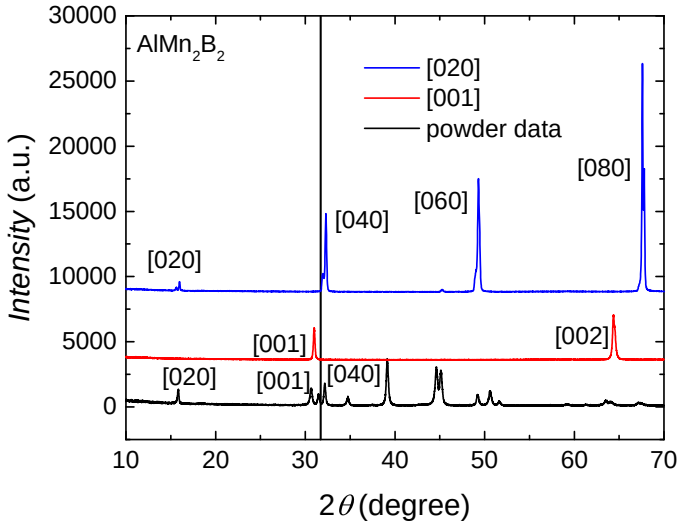

Figure 6.4 Crystallographic orientation characterization of $AlMn_2B_2$ surfaces using monochromatic Cu K_α radiation in Bragg Brentano diffraction geometry. The top curve shows the family of [020] peaks identifying direction perpendicular to plate as [010]. The direction along the thickness of the plates is found to be [001] leaving the direction along the length as [100]. The vertical grid line through the [110] powder diffraction peak (not labeled in diagram) is a reference to identify [001] and [040] peaks observed for different facets.

nantly homogeneous compositions. The small linear grooves are the cracked layers associated with the SEM sample polishing. Being a layered material, it can be easily cleaved and deformed. Boron is difficult to account for correctly in electron dispersive spectroscopy(EDS), as a consequence of this we determined only the Mn:Al ratio for two different batches of single crystalline samples. In first batch, 13 spots were analyzed in EDS with Mn:Al ratio of 2.07 for all characteristics X-ray emissions. Similarly, an 8 spot analysis in the second batch provided the Mn:Al ratio to be 2.12 for characteristics K-lines for all elements. With the L-characteristics-lines analysis, a ratio of 2.51 was obtained for the second batch. Without the creation and use of Mn-Al-B based standards, further characterization by EDS is difficult.

Although the EDS results are qualitatively in agreement with the $AlMn_2B_2$ structure, to more precisely determine the composition and structure, multiple batches of $AlMn_2B_2$ were investigated

using single crystal XRD technique. Single crystalline XRD data were collected with the use of graphite monochromatized Mo K_α radiation (λ=0.71073 Å) at room temperature on a Bruker APEX2 diffractometer. Reflections were gathered by taking five sets of 440 frames with 0.5° scans in ω/θ, with an exposure time of 10 s per frame and the crystal-to-detector distance of 6 cm. The structure solution and refinement for single crystal data was carried out using SHELXTL program package [14]. Attempts to refine occupancies of each site indicated full occupancy($< 3\sigma$). The final stage of refinement was performed using anisotropic displacement parameters for all the atoms. The refinement metrics and atomic coordinates are presented in TABLE 8.1 and 8.2 respectively. The single crystalline refinement showed $AlMn_2B_2$ as a stoichiometric material.

Etched single crystals were finely ground and spread over a zero background silicon wafer sample holder with help of a thin film of Dow Corning high vacuum grease. Powder diffraction data were obtained using a Rigaku Miniflex II diffractometer within a 2θ range of 10 - 100° with a step of 0.02° and dwelling time of 3 seconds for data acquisition. The crystallographic information file from the single crystal XRD solution was used to fit the powder XRD data using GSAS [15] and EXPGUI [16] software packages. Figure 6.3 shows the Rietveld refined powder XRD pattern with R factor of 0.08. Being a relatively hard, layered material, texture is visible along [020] direction although March Dollase texture correction was employed to account for this intensity mismatch.

To identify the crystallographic orientation of the $AlMn_2B_2$ single crystals, we employed the monochromatic X-ray diffraction from the crystallographic surfaces in the Bragg-Brentano geometry [17, 3]. The direction perpendicular to the plate was identified to be [010] since a family of {020} lines were observed in the diffraction pattern as shown in blue curve in Fig. 6.4. The plate was held vertical and the family of {001} peaks were obtained as shown in red curve of Fig. 6.4. The monochromatic x-ray surface diffraction peaks were compared with powder diffraction data to correctly identify their directions. A vertical line through the powder [110] peak was used as a reference point of comparison as shown in Fig. 6.4. Then the last remaining direction was identified to be [100] along the length of the crystals. A reference coordinate system is shown in Fig. 6.1(b) to demonstrate the crystallographic orientations of $AlMn_2B_2$ crystals.

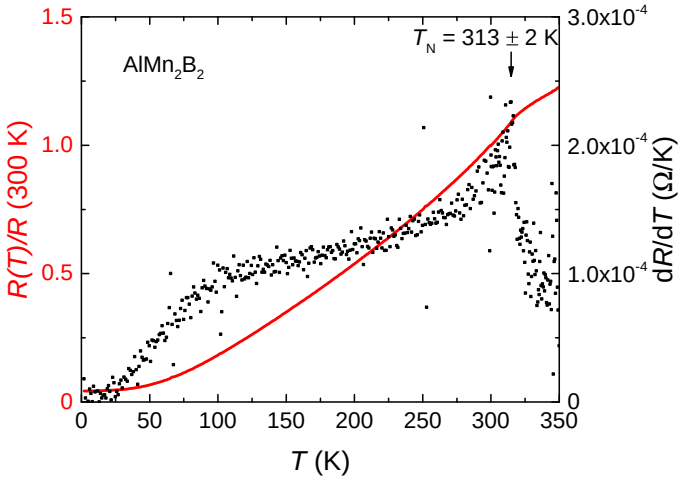

Figure 6.5 Temperature dependent normalized resistance (left axis) and temperature derivative (right axis) of $AlMn_2B_2$. The resistance is metallic in nature. The temperature derivative shows an anomaly at 313 ± 2 K consistent with an AFM phase transition.

6.5 Electric and Magnetic properties

The temperature dependent electrical resistance of $AlMn_2B_2$ was measured in a traditional 4 probe measurement on a NaOH etched, rod like sample using an external device control option to interface with a Linear Research, Inc. ac (1 mA, 17 Hz) resistance bridge (LR 700). Thin platinum wires were attached to the sample using DuPont 4929N silver paint to make electrical contact. Quantum Design Magnetic Property Measurement System (MPMS) was used as a temperature controller. The measured temperature dependent electrical resistance of $AlMn_2B_2$ is shown in Fig. 6.5. These data further confirm that our single crystals are essentially stoichiometric $AlMn_2B_2$; given that the residual resistivity ratio ($\frac{R(350.0K)}{R(2.0K)}$) is 28.5, there is relatively low disorder scattering. In addition, a very clear feature is seen in both R(T) and $\frac{d(R(T))}{dT}$ at T = 313 ± 2 K. Such features are often related to a loss of spin disorder scattering at a magnetic transition [18]. As such, these data are our first suggestion that $AlMn_2B_2$ may indeed have some form of magnetic order below 315 K.

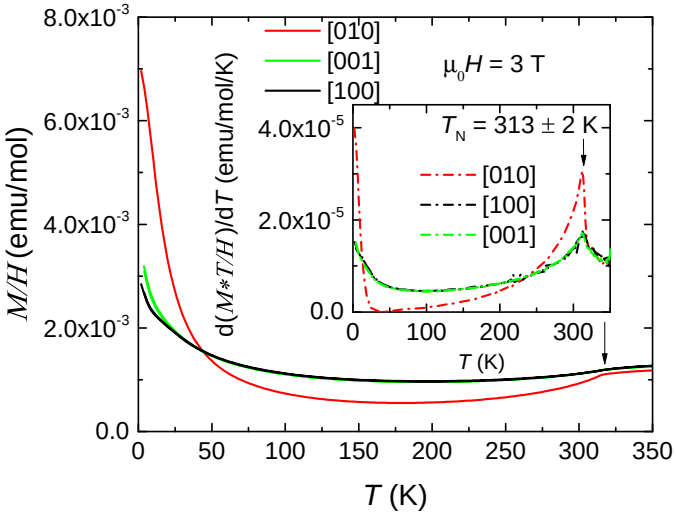

Figure 6.6 Low temperature (2 - 350 K) M/H along various crystallographic axes of $AlMn_2B_2$ sample as outlined in the graph. The inset shows $\frac{d(M*T/H)}{dT}$ as a function of temperature.

The magnetic properties of $AlMn_2B_2$ were studied from a base temperature of 2 K to 700 K. Low temperature anisotropic magnetization data of single crystalline $AlMn_2B_2$ samples were measured within the temperature range 2 - 350 K using a MPMS. High temperature, anisotropic temperature dependent magnetization data were obtained using a Quantum Design VersaLab Vibrating Sample Magnetometer (VSM) over the temperature range 300 - 700 K in an oven option mode.

The low temperature anisotropic susceptibility data, with $H = 3$ T applied field, are presented in Fig. 6.6. Below 50 K, the magnetization data show a low temperature upturn as reported in a previous literature [5]. In all three directions, there is a clear anomaly in susceptibility data around 312 K. The inset shows $\frac{d(M*T/H)}{dT}$ as a function of temperature [19] showing a clear anomaly around 312 K identifying $AlMn_2B_2$ as a AFM material. The observed anomaly in $\frac{d(M*T/H)}{dT}$ coincides with the kink observed in $\frac{dR}{dT}$.

Recently, $AlMn_2B_2$ was reported to be AFM however Neel temperature was reported to be around 390 K [7]. To examine higher temperatures, our high temperature susceptibility data, obtained using our VSM are presented in Fig. 6.7(a) and 6.7(b). Although a broad local maximum

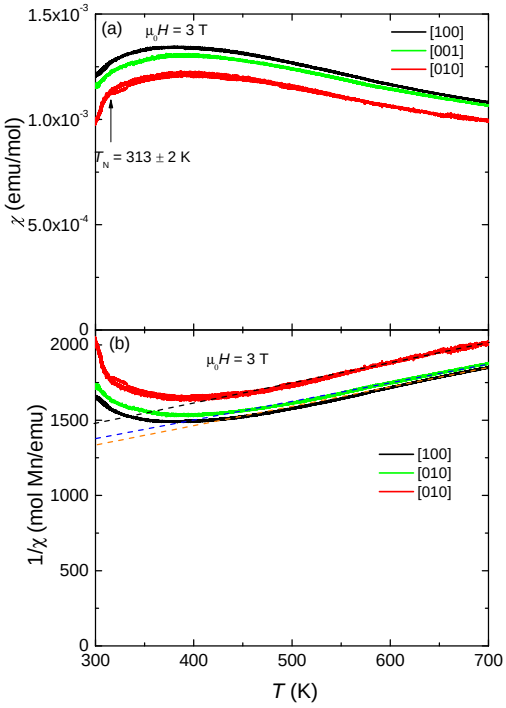

Figure 6.7 (a) High temperature susceptibility data along various axes measured using VSM. There are shallow anomalies present around 313 ± 2 K for each directions. (b) Corresponding Curie Weiss plots identifying $AlMn_2B_2$ as an AFM material with θ_{010} = - 815 K, θ_{100} = - 750 K, and θ_{001} = - 835 K respectively.

of the susceptibility around 350 - 390 K for different axes, consistent to reference[[7]] was found, the $\frac{d(M*T/H)}{dT}$ did not show any anomaly. The only clear and conclusive feature in the high temperature data associated with a magnetic transition is the feature at 313 ± 2 K. The broad local maximum in magnetization well above the transition temperature can be associated with low dimensional, or linear chain anisotropic Heisenberg anitiferromagnetism [20, 21, 22, 23, 24]. The fitted Curie Weiss temperatures for various axes were obtained to be θ_{010} = - 815 K, θ_{100} = - 750 K, and θ_{001} = - 835 K. From the average slope of Curie Weiss plot, the effective moment of Mn is found to be $\sim 2.5 \mu_B$/Mn.

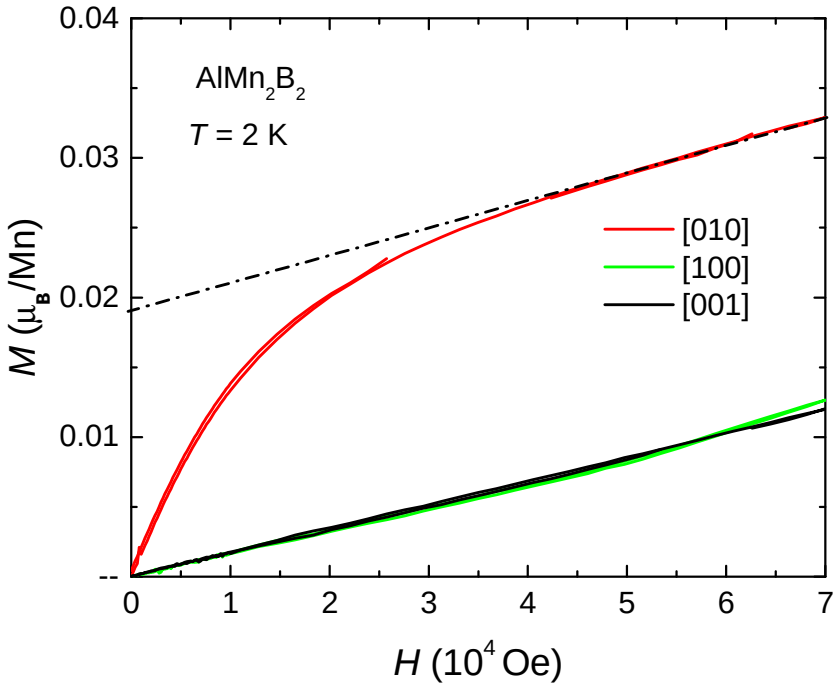

Figure 6.8 Field dependent magnetization *M(H)* of $AlMn_2B_2$ at 2 K. The magnetization along [010] direction shows a saturation magnetization of 0.02 μ_B/Mn with respect to other two principle directions outlined with a linear fit of the high field region data. The *M(H)* data along [010] direction shows no magnetic hysteresis i.e. the almost overlapping 2 red curves for increasing and decreasing field. The At higher field region, all 3 *M(H)* data have the same slopes.

At low temperature, T $\leq$ 50 K, in Fig. 6.6 there is a clear upturn in the *M/H* data, particularly for *H* along the [010] direction. In order to better understand this we measured the anisotropic field dependent magnetization at 2 K as shown in Fig. 6.8. For fields greater than 4 T the slopes of the *M(H)* plots are comparable for all three directions. For $H \parallel$ [010], there is a roughly 0.02 μ_B/Mn offset due to Brillouin function type magnetization for $\mu_0 H \leq 3$ T. The origin of this small, anisotropic contribution is currently not known.

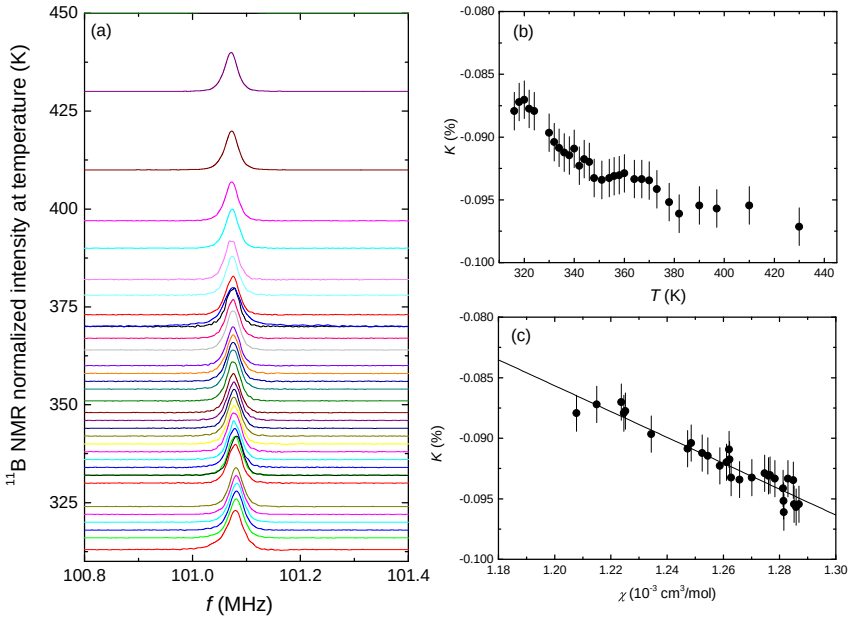

Figure 6.9 ^{11}B-NMR spectra (a) and their Knight Shifts (b) measured at different temperatures from 315 to 430 K with $H = 7.4089$ T. (c) Knight Shift as a function of susceptibility with temperature as an implicit parameter where the black line shows a linear fit.

6.6 Nuclear Magnetic resonance Study

To further investigate the magnetism of $AlMn_2B_2$, we carried out ^{11}B-NMR measurements at various temperatures between 5 K and 430 K as presented in Figs. 6.9 - 6.11. To perform the NMR measurements for the temperature region of $T = 5$ - 295 K, crushed single crystalline powder was enclosed in a weighing paper folded closed cylindrical tube and inserted inside the NMR coil. For the higher temperature NMR measurements up to 430 K from room temperature, the crushed powder was sealed under $\frac{1}{3}$ atmospheric pressure of Ar inside a ~1 mm internal diameter amorphous silica tube. The NMR measurements were carried out using a lab-built phase coherent spin-echo pulsed NMR spectrometer on ^{11}B (nuclear spin $I = \frac{3}{2}$ and gyromagnetic ratio $\frac{\gamma_N}{2\pi} = 13.6552$ MHz/T) nuclei in the temperature range $5 < T < 430$ K. NMR spectra were obtained either by Fourier transform of the NMR echo signals, by sweeping frequency or by sweeping magnetic field. Magnetic phase

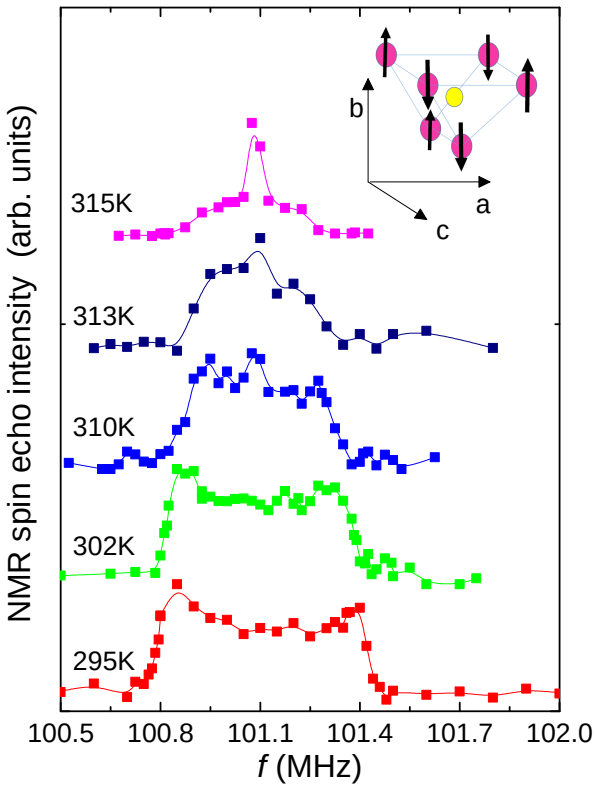

Figure 6.10 ^{11}B-NMR spectra measured at $H = 7.4089$ T by sweeping frequency. Inset shows the six nearest Mn neighbors of B with a possible antiferromagnetic spin orientation [7].

transition was studied analyzing the full width at half maximum ($FWHM$) of ^{11}B-NMR spectra and spin-lattice relaxation rate $\frac{1}{T_1}$. The ^{11}B $\frac{1}{T_1}$ was measured by the conventional single saturation pulse method.

Figure 6.9(a) shows the ^{11}B-NMR spectra obtained by Fourier transform of the NMR spin echo for temperatures in the range 315 - 430 K at $H = 7.4089$ T. Throughout the range of study, the $FWHM$ ~29 kHz is nearly independent of temperature. Figure 6.9(b) shows the temperature dependence of the NMR shift (K) in the paramagnetic state, where K decreases with increasing T. The temperature dependence of K follows that of χ as shown in Fig. 6.9(c) where K is plotted as a function of χ with temperature as an implicit parameter. From the slope of the K-χ plot,

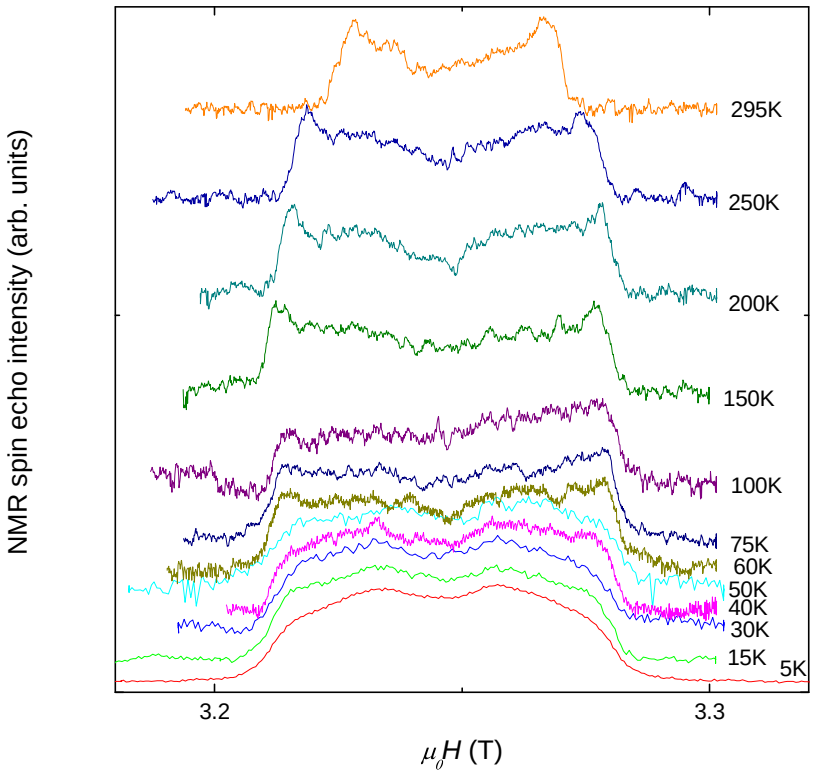

Figure 6.11 ^{11}B-NMR spectra measured at different temperatures between 5 K and 295 K measured using field sweeping method. A noticeable change in shape of ^{11}B-NMR peaks around 50 K coincides with changing the magnetic anisotropy between [100]/[001] and [010] directions as shown in Fig. 6.6.

the hyperfine coupling constant $A_{\rm hf}$ is estimated to be - 12 kOe/$\mu_{\rm B}$ using the relation of $K = A_{\rm hf}$ $\chi/\mu_{\rm B}N_{\rm A}$ where $N_{\rm A}$ is the Avogadro number. The total hyperfine coupling constant at the B site is generally the sum of the transferred hyperfine ($A_{\rm trans}$) and dipolar ($A_{\rm dip}$) couplings produced by the Mn spins: $A_{\rm hf} = zA_{\rm trans} + A_{\rm dip}$ where $z = 6$ is the number of nearest neighbor Mn spins with respect to the B site. The dipolar coupling was calculated to be at most 1 kOe/$\mu_{\rm B}$ which is one order magnitude smaller than the total hyperfine field. This suggests that the dominant contribution of the total hyperfine coupling is due to the transferred hyperfine coupling at the B site. Below 315 K, as shown in Fig. 6.10, the ^{11}B-NMR line broadens abruptly and has an almost rectangular shape at low temperatures. Since the rectangular shape is characteristic of NMR spectrum in AFM ordered

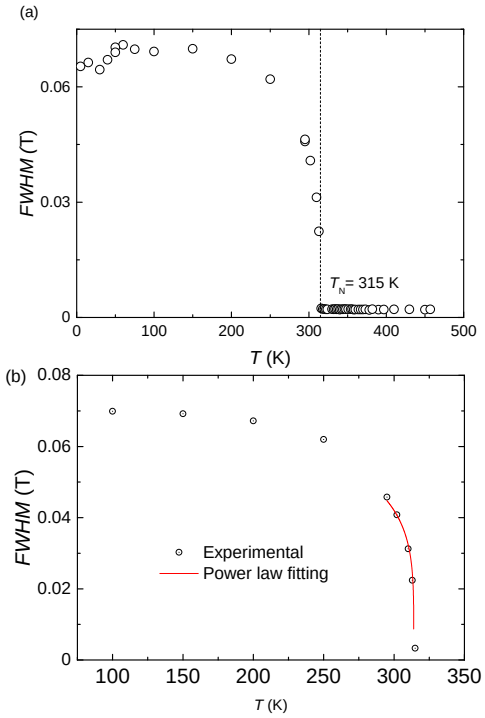

Figure 6.12 (a) Temperature dependence of $FWHM$ ^{11}B-NMR spectra in powdered $AlMn_2B_2$ sample showing AFM transition around 315 K. (b) Power law fitting of the observed temperature variation of ^{11}B $FWHM$ in the temperature range 295 - 315 K as $FWHM \propto [1-(\frac{T}{T_N})]^{\beta}$ with $T_N = 314$ K and $\beta = 0.21 \pm 0.02$.

state for powder sample, the results clearly indicate that the magnetic phase transition around 315 K is AFM. Similar rectangular NMR spectra in AFM state have been observed in $BiMn_2PO_6$ [25], $NaVGe_2O_6$ [26], CuV_2O_6 [27], and $BaCo_2V_2O_8$ [28] .

In the low temperature range between 5 - 295 K, several ^{11}B-NMR spectra were measured at a frequency of $f = 44.32$ MHz by sweeping the magnetic field as shown in Fig. 6.11. The $FWHM$ increases with decreasing temperature and shows nearly constant ($\sim$0.07 T) down to $\sim$50 K. Below 50 K, the $FWHM$ slightly decreases, where the shape of the spectrum changes and the edges of the lines are smeared out. These results suggest a change in magnetic state around 50 K. Although it is not clear at present, it is interesting if the change relates to the strong enhancement of χ_b

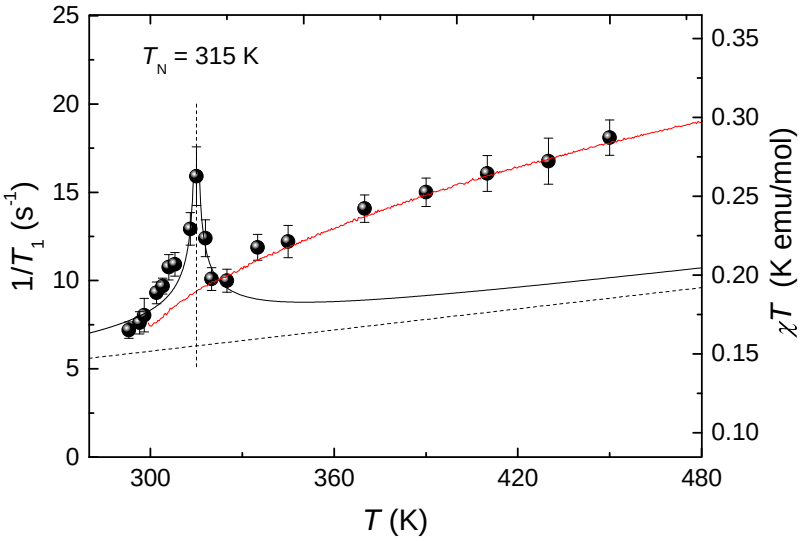

Figure 6.13 The relaxation rate ($\frac{1}{T_1}$) is plotted as a function of T from 293 K to 450 K. The transition temperature at 315 K is evidenced by a sharp peak of $\frac{1}{T_1}$. The black line is the best fit with a weak itinerant antiferromagnet model: ($\frac{1}{T_1} = \frac{0.03T}{|(T-T_N)|^{1/2}} + 0.02T$). The red line shows the temperature dependence of χT. The black dotted line exhibits the contribution of the Korringa-type relation ($\frac{1}{T_1} = 0.02T$) to the weak antiferromagnet model.

below 50 K as shown in Fig. 6.6. NMR measurements on single crystals could provide additional information in this issue. This is the future work.

Figure 6.12(a) shows the temperature variation of the $FWHM$ of the ^{11}B-NMR spectra between 5 - 430 K. Since the $FWHM$ of the powder NMR spectrum in AFM state corresponds to the twice of the internal field ($H_{\rm int}$) at the B site produced by Mn ordered moments [25, 26, 27, 28, 29], the temperature dependence of $FWHM$ reflects the temperature dependence of the Mn sub-lattice magnetization. Therefore, one can obtain the critical exponent (β) of the order parameter using the formula $FWHM \propto (1 - \frac{T}{T_N})^{\beta}$. The maximum value of $\beta = 0.21 \pm 0.02$ with $T_N = 314$ K was obtained by fitting the data points in the range 295 K - 315 K close to T_N as shown in Fig. 6.12(b). Very nominal change was observed in the fitted β parameter with the extension of fitted range toward the low temperature. The observed change in critical exponent β was within the error

bar for all the temperature range. This power law fittings of *FWHM* provided lower value of $\beta = 0.21 \pm 0.02$ (for 3D Heisenberg model $\beta \sim 0.345$) suggesting a low dimensional magnetism as discussed in reference [20].

In general, one may be able to estimate an ordered magnetic moment in the magnetically ordered state if the hyperfine coupling constant and the internal field were known. However, in antiferromagnetic states, the estimation of the ordered magnetic moment is not straightforward due to a cancelation of hyperfine fields. Taking the spin structure from the neutron diffraction measurements [7] shown in the inset of Fig. 6.10 into consideration, a small internal field at the B site is expected due to the cancellation of the transferred hyperfine fields produced by the six nearest neighbor Mn ions in $AlMn_2B_2$. In fact, using the observed internal field ($|H_{\rm int}| \sim 0.35$ kOe) and the total hyperfine coupling constant of -12 kOe/$\mu_{\rm B}$, the ordered moment is estimated to be 0.03 $\mu_{\rm B}$ which is much smaller than the reported value of 0.71 /$\mu_{\rm B}$, evidencing the cancellation of the hyperfine field at the B site in the antiferromagnetic state. If we assume that the transferred hyperfine field at the B site from each Mn ion is the same for the six nearest neighbor Mn ions, zero internal field is expected due to a perfect cancellation. The observed small $H_{\rm int}$ could originate from a nonperfect cancellation of the hyperfine field due to the orthorhombic symmetry where the assumption of the uniform hyperfine field from the six Mn spins is slightly broken down, making the analysis more complicated. The dipolar field may also contribute to the small internal field in the antiferromagnetic state. Further detailed analysis is required to estimate the ordered magnetic moment in $AlMn_2B_2$ using the NMR data, which is beyond the scope of the present manuscript.

To study the dynamical properties of the Mn spins in high temperature range, the spin lattice relaxation rates ($\frac{1}{T_1}$) at the ^{11}B site were measured from room temperature to 430 K. Figure 6.13 shows the temperature dependence of $\frac{1}{T_1}$ where $\frac{1}{T_1}$ shows a clear peak at 315 K, evidencing again the AFM ordering. On the other hand, no clear anomaly in the temperature dependence of $\frac{1}{T_1}$ is observed around 390 K where the magnetic susceptibility exhibits a broad local maximum. Therefore, the broad maximum in the magnetic susceptibility is not associated with a magnetic ordering,

but it could be attributed to a two dimensional magnetic character in $AlMn_2B_2$ as observed in 2D AFM compounds such as $BaMn_2Si_2O_7$ [20].

Finally it is interesting to discuss the nature of the magnetic fluctuations in $AlMn_2B_2$ based on the T_1 data. Since the ordered magnetic moment in the antiferromagnetic state is reported to be $0.71\mu_B$ [7], the compound could be regarded as a weak itinerant antiferromagnet. According to self-consistent renormalization theory [30], $\frac{1}{T_1}$ for weak itinerant antiferromagnets is described as $\frac{1}{T_1} = \frac{aT}{|(T-T_N)|^{1/2}} + bT$ where the first term originates from antiferromagnetic fluctuations around a wavevector q = Q (Q being antiferromagnetic wavevector) and the second term is due to Korringa-type relaxation, characteristic feature of metallic materials [31]. As shown by the black line in Fig. 6.13, although the equation with $a = 0.03$ ($s^{-1}K^{-0.5}$) and $b = 0.02$ ($s^{-1}K^{-1}$) seems to reproduce the data close T_N, the temperature dependence of $\frac{1}{T_1}$ above T ~325 K cannot be well reproduced. Instead, we found the temperature dependence of $\frac{1}{T_1}$ above 325 K is well reproduced by the temperature dependence of χT shown by the red line in Fig. 6.13. Such a behavior of $\frac{1}{T_1} \sim \chi T$ has been observed in many antiferromagnetic insulators with local moments such as $Pb_2VO(PO_4)_2$ [32], $VOMoO_4$ [33] and $BiMn_2PO_6$ [25]. These results suggest that the magnetic fluctuations in the paramagnetic state of $AlMn_2B_2$ are dominated by the uniform paramagnetic fluctuations, similar to the localized spin systems. Further experiments are required to characterize the magnetic fluctuations in the AFM state well below T_N , which will be a future project.

6.7 Conclusions

Structural, electrical transport and magnetic properties were studied on self flux grown single crystalline $AlMn_2B_2$ samples. All these measurements revealed that $AlMn_2B_2$ as an AFM compound with a transition temperature around 313±2 K. At higher temperature broad hump, well above the transition temperature, could be the signature of low dimensional magnetic interaction in $AlMn_2B_2$ above the room temperature.

6.8 Acknowledgement

Dr. Warren Straszheim is acknowledged for doing SEM on various samples. This research was supported by the Critical Materials Institute, an Energy Innovation Hub funded by the U.S. Department of Energy, Office of Energy Efficiency and Renewable Energy, Advanced Manufacturing Office. This work was also supported by the office of Basic Energy Sciences, Materials Sciences Division, U.S. DOE. This work was performed at the Ames Laboratory, operated for DOE by Iowa State University under Contract No. DE-AC02-07CH11358.

6.9 References

[1] Qianheng Du, Guofu Chen, Wenyun Yang, Jianzhong Wei, Muxin Hua, Honglin Du, Changsheng Wang, Shunquan Liu, Jingzhi Han, Yan Zhang, and Jinbo Yang. Magnetic frustration and magnetocaloric effect in $AlFe_{2-x}Mn_xB_2$(x= 0–0.5) ribbons. *Journal of Physics D: Applied Physics*, 48(33):335001, jul 2015.

[2] Xiaoyan Tan, Ping Chai, Corey M. Thompson, and Michael Shatruk. Magnetocaloric Effect in $AlFe_2B_2$: Toward Magnetic Refrigerants from Earth-Abundant Elements. *Journal of the American Chemical Society*, 135(25):9553–9557, 2013. PMID: 23731263.

[3] Tej N. Lamichhane, Li Xiang, Qisheng Lin, Tribhuwan Pandey, David S. Parker, Tae-Hoon Kim, Lin Zhou, Matthew J. Kramer, Sergey L. Bud'ko, and Paul C. Canfield. Magnetic properties of single crystalline itinerant ferromagnet $AlFe_2B_2$. *Phys. Rev. Materials*, 2:084408, Aug 2018.

[4] R. Barua, B.T. Lejeune, L. Ke, G. Hadjipanayis, E.M. Levin, R.W. McCallum, M.J. Kramer, and L.H. Lewis. Anisotropic magnetocaloric response in $AlFe_2B_2$. *Journal of Alloys and Compounds*, 745:505 – 512, 2018.

[5] Ping Chai, Sebastian A. Stoian, Xiaoyan Tan, Paul A. Dube, and Michael Shatruk. Investigation of magnetic properties and electronic structure of layered-structure borides AlT_2B_2 (T=Fe, Mn, Cr) and $AlFe_{2-x}Mn_xB_2$. *Journal of Solid State Chemistry*, 224:52 – 61, 2015.

[6] Liqin Ke, Bruce N. Harmon, and Matthew J. Kramer. Electronic structure and magnetic properties in T_2AlB_2 (T=Fe, Mn, Cr, Co, and Ni) and their alloys. *Phys. Rev. B*, 95:104427, Mar 2017.

[7] D. Potashnikov, E.N. Caspi, A. Pesach, A. Hoser, S. Kota, L. Verger, M.W. Barsoum, I. Felner, A. Keren, and O. Rivin. Magnetic ordering in the nano-laminar ternary Mn_2AlB_2using neutron and X-ray diffraction. *Journal of Magnetism and Magnetic Materials*, 471:468 – 474, 2019.

[8] L. Verger, S. Kota, H. Roussel, T. Ouisse, and M. W. Barsoum. Anisotropic thermal expansions of select layered ternary transition metal borides: MoAlB, Cr_2AlB_2, Mn_2AlB_2, and Fe_2AlB_2. *Journal of Applied Physics*, 124(20):205108, 2018.

[9] Kirill D. Belashchenko, Liqin Ke, Markus Dane, Lorin X. Benedict, Tej Nath Lamichhane, Valentin Taufour, Anton Jesche, Sergey L. Bud'ko, Paul C. Canfield, and Vladimir P. Antropov. Origin of the spin reorientation transitions in $(Fe_{1-x}Co_x)_2B$ alloys. *Applied Physics Letters*, 106(6):062408, 2015.

[10] Paul C. Canfield and Ian R. Fisher. High-temperature solution growth of intermetallic single crystals and quasicrystals. *Journal of Crystal Growth*, (225):155 – 161, 2001.

[11] W. R. Meier, T. Kong, S. L. Bud'ko, and P. C. Canfield. Optimization of the crystal growth of the superconductor $CaKFe_4As_4$ from solution in the FeAS - $CaFe_2As_2$ - KFe_2As_2 system. *Phys. Rev. Materials*, 1:013401, Jun 2017.

[12] Paul C. Canfield, Tai Kong, Udhara S. Kaluarachchi, and Na Hyun Jo. Use of frit-disc crucibles for routine and exploratory solution growth of single crystalline samples. *Philosophical Magazine*, 96(1):84 – 92, November 2016.

[13] Tej N. Lamichhane, Valentin Taufour, Morgan W. Masters, David S. Parker, Udhara S. Kaluarachchi, Srinivasa Thimmaiah, Sergey L. Bud'ko, and Paul C. Canfield. Discovery of ferromagnetism with large magnetic anisotropy in ZrMnP and HfMnP. *Applied Physics Letters*, 109(9):092402, 2016.

[14] *SHELXTL-v2008/4, Bruker AXS Inc., Madison, Wisconsin, USA, 2013.*

[15] A. C. Larson and R. B. Von Dreele. General structure analysis system. *Los Alamos National Laboratory Report No. LAUR 86-748*, 2004.

[16] Brian H. Toby. *EXPGUI*, a graphical user interface for *GSAS*. *Journal of Applied Crystallography*, 34(2):210–213, Apr 2001.

[17] A. Jesche, M. Fix, A. Kreyssig, W. R. Meier, and P. C. Canfield. X-ray diffraction on large single crystals using a powder diffractometer. *Philosophical Magazine*, 96(20):2115–2124, 2016.

[18] Michael E. Fisher and J. S. Langer. Resistive anomalies at magnetic critical points. *Phys. Rev. Lett.*, 20:665–668, Mar 1968.

[19] Michael E. Fisher. Relation between the specific heat and susceptibility of an antiferromagnet. *The Philosophical Magazine: A Journal of Theoretical Experimental and Applied Physics*, 7(82):1731–1743, 1962.

[20] J. Ma, C. D. Dela Cruz, Tao Hong, W. Tian, A. A. Aczel, Songxue Chi, J.-Q. Yan, Z. L. Dun, H. D. Zhou, and M. Matsuda. Magnetic phase transition in the low-dimensional compound $BaMn_2Si_2O_7$. *Phys. Rev. B*, 88:144405, Oct 2013.

[21] A.N Vasil'ev, L.A Ponomarenko, H Manaka, I Yamada, M Isobe, and Y Ueda. Quasi-one-dimensional antiferromagnetic spinel compound $LiCuVO_4$. *Physica B: Condensed Matter*, 284-288:1619 – 1620, 2000.

[22] Y.J. Kim, M. Greven, U.-J. Wiese, and R.J. Birgeneau. Monte-carlo study of correlations in quantum spin chains at non-zero temperature. *The European Physical Journal B - Condensed Matter and Complex Systems*, 4(3):291–297, Aug 1998.

[23] Jill C. Bonner and Michael E. Fisher. Linear magnetic chains with anisotropic coupling. *Physical Review*, 135(3A):640 –658, 1964.

[24] R. Dingle, M. E. Lines, and S. L. Holt. Linear-Chain Antiferromagnetism in $[(CH_3)_4N]$ $[MnCl_3]$. *Phys. Rev.*, 187:643–648, Nov 1969.

[25] R. Nath, K. M. Ranjith, B. Roy, D. C. Johnston, Y. Furukawa, and A. A. Tsirlin. Magnetic transitions in the spin-$\frac{5}{2}$ frustrated magnet $BiMn_2PO_6$ and strong lattice softening in $BiMn_2PO_6$ and $BiZn_2PO_6$ below 200 K. *Phys. Rev. B*, 90:024431, Jul 2014.

[26] B. Pedrini, J. L. Gavilano, D. Rau, H. R. Ott, S. M. Kazakov, J. Karpinski, and S. Wessel. NMR and dc susceptibility studies of $NaVGe_2O_6$. *Phys. Rev. B*, 70:024421, Jul 2004.

[27] Jun Kikuchi, Kazuhiro Ishiguchi, Kiyoichiro Motoya, Masayuki Itoh, Kazunori Inari, Naotoshi Eguchi, and Jun Akimitsu. NMR and Neutron Scattering Studies of Quasi One-Dimensional Magnet CuV_2O_6. *Journal of the Physical Society of Japan*, 69(8):2660–2668, 2000.

[28] Yukiichi Ideta, Yu Kawasaki, Yutaka Kishimoto, Takashi Ohno, Yoshitaka Michihiro, Zhangzhen He, Yutaka Ueda, and Mitsuru Itoh. ^{51}V NMR study of antiferromagnetic state and spin dynamics in quasi-one-dimensional $BaCo_2V_2O_8$. *Phys. Rev. B*, 86:094433, Sep 2012.

[29] A. Yogi, N. Ahmed, R. Nath, A. A. Tsirlin, S. Kundu, A. V. Mahajan, J. Sichelschmidt, B. Roy, and Y. Furukawa. Antiferromagnetism of $Zn_2VO(PO_4)_2$ and the dilution with Ti^{4+}. *Phys. Rev. B*, 91:024413, Jan 2015.

[30] Tôru Moriya and Kazuo Ueda. Nuclear magnetic relaxation in weakly ferro-and antiferromagnetic metals. *Solid State Commun.*, 15(2):169 – 172, 1974.

[31] Yoshio Kitaoka and Hiroshi Yasuoka. NMR Investigations on the Spin Fluctuations in Itinerant Antiferromagnets. I. V_3Se_4 and V_5Se_8. *J. Phys. Soc. Jpn.*, 48(5):1460–1469, 1980.

[32] R. Nath, Y. Furukawa, F. Borsa, E. E. Kaul, M. Baenitz, C. Geibel, and D. C. Johnston. Single-crystal ^{31}P NMR studies of the frustrated square-lattice compound $Pb_2(VO)(PO_4)_2$. *Phys. Rev. B*, 80:214430, Dec 2009.

[33] P. Carretta, N. Papinutto, C. B. Azzoni, M. C. Mozzati, E. Pavarini, S. Gonthier, and P. Millet. Frustration-driven structural distortion in $VOMoO_4$. *Phys. Rev. B*, 66:094420, Sep 2002.

CHAPTER 7. $Ce_{3-x}Mg_xCo_9$: TRANSFORMATION OF A PAULI PARAMAGNET INTO A STRONG PERMANENT MAGNET

A paper published in *Physical Review Applied*

Tej N. Lamichhane,[1,2,*] Valentin Taufour,[1,3] Andriy Palasyuk,[1] Qisheng Lin,[1] Sergey L. Budko,[1,2] and Paul C. Canfield[1,2]

[1]Ames Laboratory, U.S. DOE, Ames, Iowa 50011, USA

[2]Department of Physics and Astronomy, Iowa State University, Ames, Iowa 50011, USA

[3]Department of Physics, University of California Davis, Davis, California 95616, USA

7.1 Abstract

We report on the synthesis of single-crystal and polycrystalline samples of $Ce_{3-x}Mg_xCo_9$ solid solution ($0 \leq x \lesssim 1.4$) and characterization of their structural and magnetic properties. The crystal structure remains rhombohedral in the whole composition range and Mg partially replaces Ce in the $6c$ site of the $CeCo_3$ structure. Ferromagnetism is induced by Mg substitutions starting as low as $x = 0.18$ and reaching a Curie temperature as high as 450 K for $x = 1.35$. Measurements on single crystals with $x = 1.34$ and $T_C = 440$ K indicate an axial magnetic anisotropy with an anisotropy field of 6 T and a magnetization of $6\mu_B$/f.u. at 300 K. Coercicity is observed in the polycrystalline samples consistent with the observed axial magnetic anisotropy. Our discovery of ferromagnetism with large axial magnetic anisotropy induced by substituting a rare-earth element by Mg is a very promising result in the search of inexpensive permanent-magnet materials and suggests that other nonmagnetic phases, similar to $CeCo_3$, may also conceal nearby ferromagnetic phases.

7.2 Introduction

Current rare-earth-based commercial magnets contain local-moment-bearing rare-earth elements, mainly Nd, Sm and Dy whose availability is, according to the United States Department of Energy, important to the clean energy economy and also have an associated supply risk. Alternative to finding a long sought rare earth free, high flux permanent magnet, attempts to find Ce-based permanent magnets or substituting Ce for more critical rare-earth elements could be a pragmatic strategy to address the criticality problem since Ce is a relatively more abundant rare earth [1] with easier extraction chemistry. Ce is relatively easy to separate from the other rare earths since it can easily be oxidised to CeO_2 via roasting from which it can be precipitated out in acidic solutions [2, 3]. Ce can be, in theory as well as experiment, a substitute for critical rare-earths without much compromise in magnetic properties [4]. Because of the volatile price of critical rare-earths, Ce is drawing attention for developing gap-magnets which will populate the gap in energy product (in the range of 10-20 MGOe) in between low flux (Alnico, ferrites) and commercial rare-earth based magnets such as $SmCo_5$ and $Nd_2Fe_{14}B$. Additionally, the study of new Ce based compounds often can reveal interesting physics; Ce exhibits diverse electronic and magnetic properties like local moment bearing Ce^{3+} ion, nonmagnetic Ce^{4+} ion, mixed valency, intermediate valence and itinerant magnetism.

$Ce_{3-x}Mg_xCo_9$ alloys are substitution derivatives of $CeCo_3$ in which Mg partially replace Ce in the $6c$ position. The hydrogenation properties of the compound Ce_2MgCo_9 ($x = 1$) and $Nd_{3-x}Mg_xCo_9$ alloys ($x \leq 1.5$) have been recently investigated [5, 6]. In addition, it was shown that the substitution of Nd by Mg increases the Curie temperature from 381 K for $NdCo_3$ [7] to 633 K for Nd_2MgCo_9 [6].

In this work we present structural and magnetic properties of both single crystalline and polycrystalline $Ce_{3-x}Mg_xCo_9$ for $0 \leq x \lesssim 1.4$. The anisotropic magnetic properties are studied for a single crystal of $Ce_{1.662(4)}Mg_{1.338(4)}Co_9$ (Hereafter we round off the single crystalline composition to 3-significant digits as $Ce_{1.66}Mg_{1.34}Co_9$.). We find a remarkable transformation of a Pauli-

paramagnet $CeCo_3$ (Ce_3Co_9) into the potential permanent magnet $Ce_{3-x}Mg_xCo_9$ which develops 2.2 MJ/m^3 of uniaxial anisotropy energy at 2 K for the $Ce_{1.66}Mg_{1.34}Co_9$.

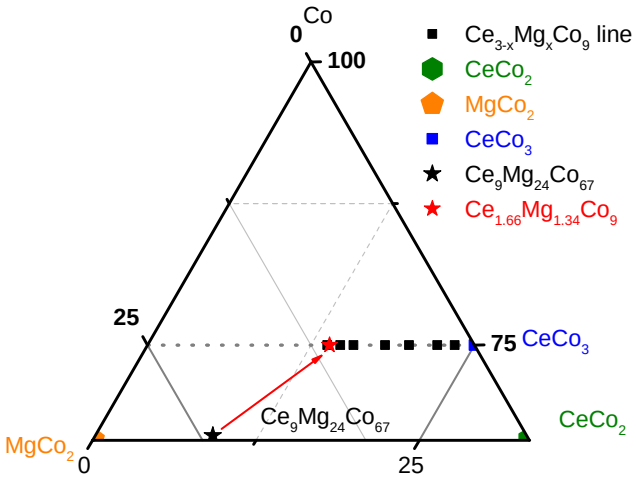

Figure 7.1 Co-rich portion of the Co-Mg-Ce ternary phase diagram showing the $Ce_{3-x}Mg_xCo_9$ solid solution line and 1:2 type impurity phases. $Ce_9Mg_{24}Co_9$ is the optimised initial melt composition for the solution growth of single crystalline $Ce_{1.66}Mg_{1.34}Co_9$. (See text for details.)

7.3 Experimental Methods

To establish the existence range of the solid solution $Ce_{3-x}Mg_xCo_9$, we prepared polycrystals with various nominal compositions of $0 \leq x \leq 2.00$ (see TABLE 7.3 below). Ce metal from the Ames Laboratory Material Preparation Center (purity > 99.99%), Co chunks (99.95%, Alfa Aesar), and Mg (99.95%,Gallium Source, LLC) were packed in a 3-capped Ta crucible [8] under an Ar atmosphere. The Ta crucible was then sealed into an amorphous silica ampoule. The ampoule was heated to 900 °C over 3 hours and held there for 3 hours. This step allows the reaction of Ce and Mg at low temperature and avoids the excessive boiling of Mg inside the Ta crucible. The ampoule was then heated to 1200 °C over 3 hours and held there for 10 hours. At this point, the ampoule was spun in a centrifuge and all the molten growth material was decanted and quenched in catch side of the Ta-tube. This step confirmed that the mixture was forming a homogeneous

melt at 1200 °C. The ampoule was put back into a furnace then annealed at 900 °C for 24 hours. Mg free $CeCo_3$ was also synthesized by arcmelting the stoichiometric composition and annealing at 900 °C for 1 week.

Single crystals of $Ce_{3-x}Mg_xCo_9$ were grown using a solution growth technique. An initial composition of $Ce_9Mg_{24}Co_{67}$ (see FIG. 7.1) was packed in a 3-capped Ta crucible [8] and heated to 1200 °C similar to the polycrystals. The ampoule was then cooled down to 1100 °C over 75 hours after which crystals were separated from the flux by using a centrifuge. Similarly, $CeCo_3$ single crystals were prepared by cooling a $Ce_{30}Co_{70}$ melt from 1200° to 1100 °C in 1 hour and then to 1050 °C over 75 hours[9].

Elemental analysis of the samples was performed using Energy Dispersive Spectroscopy(EDS). Polycrystalline samples were embedded in epoxy resin and finely polished. The polished samples were examined with EDS on 6-10 spots and a statistical average composition is reported. Thin plate-like single crystalline samples, see FIG. 7.2(a), were mounted on a conducting carbon tape. Self-flux grown $MgCo_2$ and $CeCo_2$ single crystals were used as absorption standards for the Ce-Co-Mg alloy composition analyses. Powder X-ray diffraction data were collected at room temperature on a Rigaku MiniFlex II diffractometer with Cu Kα radiation. Data were collected with a 3 seconds dwell time for each interval of 0.01° within a 2θ range of $10-100°$. Lattice parameters were refined by the Rietveld analysis method using GSAS [10] and EXPGUI [11].

Single crystal X-ray diffraction was carried out on a Bruker Smart APEX II diffractometer with graphite-monochromatized Mo-K_α radiation (0.71073 Å). Reflections were gathered at room temperature by taking four sets of 360 frames with 0.5° scans in ω, with an exposure time of 10 s. The crystal-to-detector distance was maintained 60 mm. The reflections were collected over the range of 3° to 62° in 2θ.

Electrical resistivity was measured on single crystals using the 4-probe technique with a Linear Research, Inc. ac resistance bridge (LR700, $f = 17$ Hz). A Quantum Design (QD) Magnetic Property Measurement System (MPMS) was used for the temperature control. Samples were sliced into thin rectangular bars (approximately 0.9 mm x 0.45 mm x 0.04 mm) and platinum wires

were attached to the samples with Dupont 4929N silver paint. The contact resistances were less than 2 Ω.

Magnetization was measured using a QD-VersaLab Vibrating Sample Magnetometer (VSM). The standard option was used in the temperature range 50-400 K and the oven option in the range 300-1000 K. Loctite 435 and Zircar cement were used to attach the samples in the standard and oven options, respectively. Field dependent magnetization isotherms were also measured down to 2 K in a MPMS. The details of sample mounting and experimental determination of demagnetization factor along the easy axis are discussed in references [12] and [13].

7.4 Composition and structural properties

7.4.0.1 Single crystal: Characterization and structure

Table 7.1 Crystallographic data and refinement parameters for $Ce_{1.662(4)}Mg_{1.338(4)}Co_9$.

Empirical formula	$Ce_{1.662(4)}Mg_{1.338(4)}Co_9$
Formula weight	796.32
Crystal system, space group	trigonal, *R-3m* h
Unit cell dimensions	$a = 4.9260(7)$ Å
	$c = 24.019(5)$ Å
Volume	504.75(18) Å^3
Z, Calculated density	3, 7.859 g/cm^3
Absorption coefficient	32.577 mm^{-1}
Reflections collected	2000 [$R_{(int)} = 0.0408$]
Data / restraints / parameters	224 / 0 / 18
Goodness-of-fit on $\|F\|^2$	1.149
Final R indices $[I > 4\sigma(I)]$	$R1 = 0.0204$, $wR2 = 0.0450$
R indices (all data)	$R1 = 0.0226$, $wR2 = 0.0455$
Largest diff. peak and hole	1.917 and -1.477 e.Å^{-3}

A picture of as grown $Ce_{1.66}Mg_{1.34}Co_9$ single crystals, a Laue backscattered photograph and single crystal surface diffracted monochromatic XRD data collected via Rigaku MiniFlex II diffractometer with Bragg-Brentano geometry [14] are presented in pannels (a), (b) and (c) of FIG. 7.2

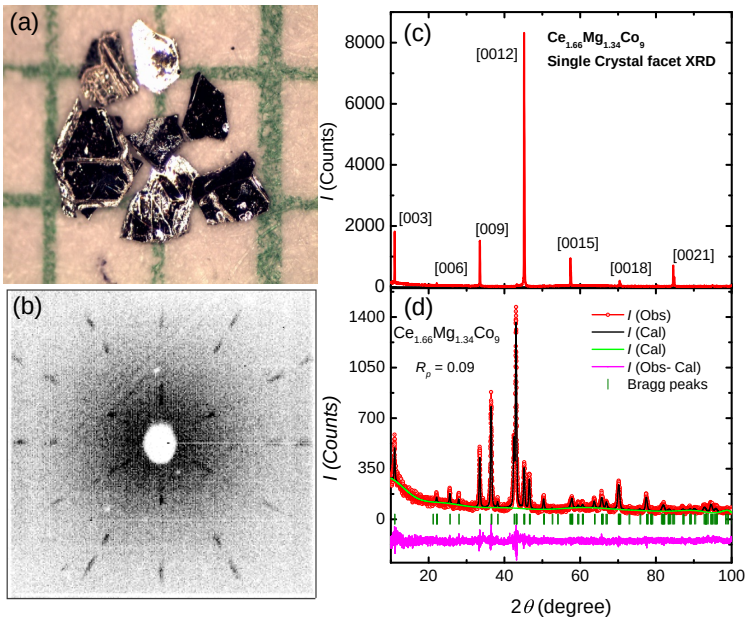

Figure 7.2 (a) Single crystals of $Ce_{1.66}Mg_{1.34}Co_9$. (b) Backscattered Laue photograph of $Ce_{1.66}Mg_{1.34}Co_9$ with X-ray beam perpendicular to plate. (c) Monochromatic X-ray diffraction from the surface of single crystal using Bragg-Brentano geometry. (d) Powder XRD for $Ce_{1.66}Mg_{1.34}Co_9$ where I(Obs), I(Cal) and I(Bkg) are experimental, Rietveld refined and instrumental background data respectively. The lower section of the graph shows the Bragg's peaks positions with olive vertical lines and the differential X-ray diffractrogram I(Obs-Cal).

respectively. Both Laue and monochromatic single crystalline XRD data confirmed that the single crystals grow with a planar morphology with the c-axis perpendicular to the plates.

The crystallographic data obtained from the single crystal X-ray diffraction for $Ce_{1.66}Mg_{1.34}Co_9$ grown out of $Ce_9Mg_{24}Co_{67}$ initial melt are summarized in TABLES. 8.1, and 8.2. FIG. 7.2(d) shows a powder X-ray diffraction pattern of the crushed single crystals which has some noticeable mismatch in observed and Rietveld refined intensity of {00l} families of the peaks, indicating a degree of preferred orientation in the powder sample. As mentioned above, the relatively small crystal size made it difficult to acquire enough powder sample to obtain less noisy XRD data and better statistics in the Rietveld refinement. To reduce the intensity mismatch, a preferred orientation correction was employed in the Rietveld refinement using spherical harmonics up to

Table 7.2 Atomic coordinates and equivalent isotropic displacement parameters ($\AA^2 \times 10^{-3}$) for $Ce_{1.66}Mg_{1.34}Co_9$. $U_{(eq)}$ is defined as one third of the trace of the orthogonalized U_{ij} tensor.

atom	Wyckoff site	Occ	x	y	z	U_{eq}
Ce(1)	$3a$	1	0	0	0	14(1)
Ce(2)	$6c$	0.338 (4)	0	0	0.1414(1)	12(1)
Mg(2)	$6c$	0.662 (4)	0	0	0.1414(1)	12(1)
Co(1)	$3b$	1	0	0	$\frac{1}{2}$	11(1)
Co(2)	$6c$	1	0	0	0.3339(1)	17(1)
Co(3)	$18h$	1	0.5014(1)	0.4986(1)	0.0840(1)	11(1)

12^{th} order and absorption correction for plate like grains in the powder sample. The Rietveld refined lattice parameters for powder XRD data of the single crystal $Ce_{1.66}Mg_{1.34}Co_9$ are $a = 4.923(1)$ $\AA$ and $c = 24.026(1)$ $\AA$ with $R_p = 0.09$ which are in close agreement (within 2-3σ) with single crystal XRD data as shown in TABLE 8.1. The single crystal XRD composition was $Ce_{13.92}Mg_{11.08}Co_{75}$ ($Ce_{1.662(4)}Mg_{1.338(4)}Co_9$). Although we did not make quantitative compositional analysis measurement on the single crystalline sample with EDS (The crystals were too thin to readily polish and small droplets of Mg rich flux was on their surfaces.) we could detect the minor presence of Ta, (up to 1 at.%) most likely caused by slight dissolution of the inner wall surfaces of Ta reaction container and diffusion of Ta atoms into the reaction liquid during the long term dwelling process at the maximum temperature of 1200° C as well as at ramping down to 1100° C over 75 hours. However, an attempt to solve the crystal structure along with inclusion of Ta in any Wyckoff sites or interstitial sites was unsuccessful. We believe that Ta is distributed in our crystals in the form of nano-sized precipitates rather than incorporated into interstices of the crystals structure.

The crystal structure of $Ce_{3-x}Mg_xCo_9$ is rhombohedral and belongs to the $PuNi_3$ type structure[5]. Similar to the $R_{3-x}Mg_xNi_9$ series, the Co-containing structure is an intergrowth of $CaCu_5$-type (A) and $MgCu_2$-type (B) building blocks with a repeating sequence of ABA'B'A"B"A as shown in

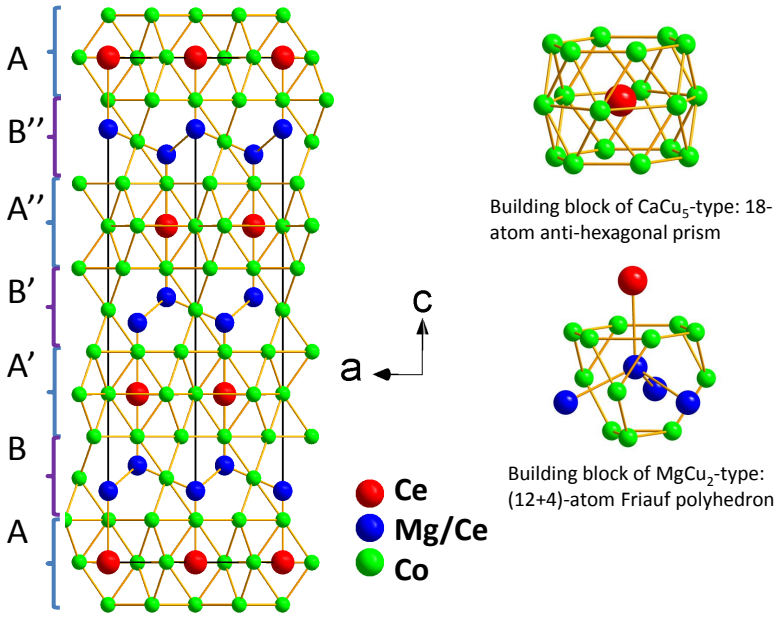

Figure 7.3 The crystal structure for $Ce_{3-x}Mg_xCo_9$ showing the stacking sequence of $CaCu_5$ type plane (A) and $MgCu_2$ type plane (B) visualized along [010] direction.

FIG. 8.1. Here A', B' and A", B" are introduced to show the relative translation of the growth layers with respect to c-axis during stacking. There are two independent sites for Ce atoms in this structure: one $3a$ site is located at the center of a face-shared anti-hexagonal prism defined by 18 Co atoms; the other $6c$ site is surrounded by 12 Co atoms defining a truncated tetrahedron plus four capping atoms at longer distances. As expected from the polyhedra volume, the statistically distributed Ce/Mg mixtures prefer to occupy the Wyckoff $6c$ site with its smaller volume.

7.4.0.2 Polycrystalline samples: Composition and lattice parameters

The nominal and EDS composition of the polycrystalline samples are presented in TABLE 7.3 along with the Rietveld refined percentage of the majority phase in the sample. The SEM images for mixed and predominantly single phase $Ce_{3-x}Mg_xCo_9$ samples are presented in FIG. 7.4.

Table 7.3 The comparison of the loaded compositions with the EDS determined composition. A nominal presence of Ta (up to 1 at.%) was found in the homogeneous $Ce_{3-x}Mg_xCo_9$ samples. Some of the higher-Mg samples showed traces of a $TaCo_3$ impurity phase and low-Mg content samples showed a $TaCo_2$ phase.

Loaded composition (Nominal)	EDS composition	Rietveld Refinement % of majority phase: $Ce_{3-x}Mg_xCo_9$
$CeCo_3$ (arcmelted and annealed at 900°C for 7 days)	$CeCo_3$ + $CeCo_2$	$\geq$ 88%
$Ce_{2.75}Mg_{0.25}Co_9$	$Ce_{2.82}Mg_{0.18}Co_9$ + $Ce_{0.86}Mg_{0.14}Co_2$ + $TaCo_2$	$\geq$ 67%
$Ce_{2.50}Mg_{0.5}Co_9$	at 900°C for 7 days) $Ce_{2.66}Mg_{0.34}Co_9$ + $Ce_{0.77}Mg_{0.23}Co_2$	$\geq$ 76%
$Ce_{2.25}Mg_{0.75}Co_9$	$Ce_{2.40}Mg_{0.60}Co_9$ + $Ce_{0.80}Mg_{0.20}Co_2$	$\geq$ 80%
$Ce_2Mg_{1.0}Co_9$	$Ce_{2.18}Mg_{0.82}Co_9$	$\approx$ single phase
$Ce_{1.67}Mg_{1.33}Co_9$	$Ce_{1.89}Mg_{1.11}Co_9$	$\approx$ single phase
$Ce_{1.5}Mg_{1.5}Co_9$	$Ce_{1.77}Mg_{1.23}Co_9$	$\approx$ single phase
$Ce_{1.33}Mg_{1.67}Co_9$	$Ce_{1.65}Mg_{1.35}Co_9$	$\approx$ single phase
$CeMg_2Co_9$	$Ce_{1.42}Mg_{1.58}Co_9$ + $MgCo_2$ + Co	$\geq$ 50%

Panel (a) in FIG. 7.4 shows the mixed phase sample that forms out of a nominal composition $Ce_{2.25}Mg_{0.75}Co_9$ and the panel (b) shows the predominantly single phase sample with EDS composition $Ce_{1.89}Mg_{1.11}Co_9$. In addition TABLE 7.3 summarizes phase analysis based on powder XRD data.

The crystallographic information file obtained from single crystal XRD was used to perform Rietveld refinement of the powder XRD data of polycrystal samples listed in TABLE 7.3. Rietveld refined XRD patterns for a multiple phase polycrystalline samples (Nominal $Ce_{2.75}Mg_{0.25}Co_9$ with $R_p = 0.09$ and $Ce_{2.50}Mg_{0.50}Co_9$ with $R_p = 0.10$) and single phase polycrystalline $Ce_{1.89}Mg_{1.11}Co_9$ (EDS composition) with $R_p = 0.08$ are presented in FIG. 7.5, 7.6 and 7.7 respectively. The melt-annealed nominal $Ce_{2.75}Mg_{0.25}Co_9$ sample contains $\sim$ 67% of $Ce_{2.82}Mg_{0.18}Co_9$ phase, $\sim$ 23% of $Ce_{0.86}Mg_{0.14}Co_2$ and $\sim$ 10% of $TaCo_2$ inferred from Rietveld refinement. The $TaCo_2$ phase is not observed in the nominal $Ce_{2.50}Mg_{0.5}Co_9$ and higher content of Mg as shown in FIG. 7.6 and 7.7. An unidentified XRD peak was observed in nominal $Ce_{2.50}Mg_{0.50}Co_9$ sample as shown in FIG. 7.6 however $TaCo_2$ phase was almost reduced to zero in comparison to nominal composition

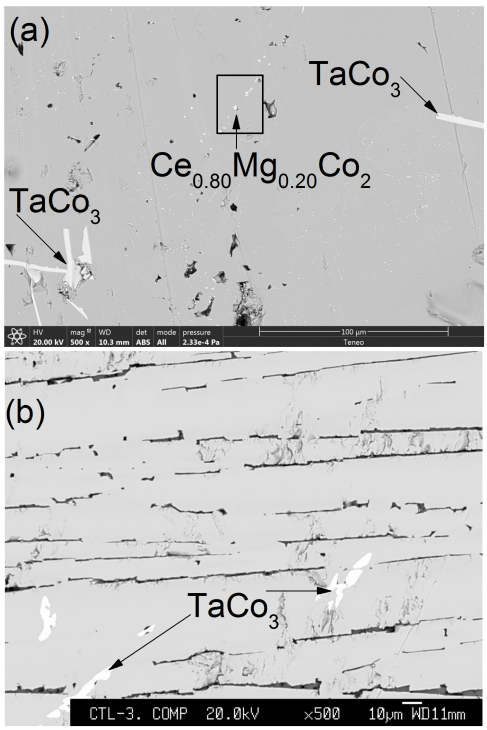

Figure 7.4 SEM images of mixed phase and predominantly single phase $Ce_{3-x}Mg_xCo_9$ samples (a) Nominal $Ce_{2.25}Mg_{0.75}Co_9$ which gave a mixture of $Ce_{2.40}Mg_{0.60}Co_9$ (majority phase) and $Ce_{0.80}Mg_{0.20}Co_2$ (minority phase demonstrated as faint small white spots along the diagonal of the black box in the panel (a)) and large white stripes of $TaCo_3$ impurity phase (b) Predominantly single phase $Ce_{1.89}Mg_{1.11}Co_9$ along with some traces of $TaCo_3$ impurity. The black parallel grooves in the image represent the cracks in the polished sample.

$Ce_{2.75}Mg_{0.25}Co_9$ as shown in FIG. 7.5. But traces of $TaCo_3$ phase was observed in predominantly single phases $Ce_{3-x}Mg_xCo_9$ samples. These results combined with the fact that even pure (Mg = 0) $CeCo_3$ remains mixed phase after 7 days of annealing, suggest that Mg be assisting the annealing of polycrystalline $Ce_{3-x}Mg_xCo_9$ samples.

For nominal $x = 2$ and higher, $Ce_{3-x}Mg_xCo_9$ can no longer be considered a clear majority phase with the presence of the significant amount of $CoMg_2$ and Co. Looking at the composition of the $Ce_{3-x}Mg_xCo_9$ alloys from EDS, it seems that $x \approx 1.4$ is the maximum solid solubility. In the $Nd_{3-x}Mg_xCo_9$ alloys, the structure changes from the trigonal structure for $x \leq 1.5$ to a

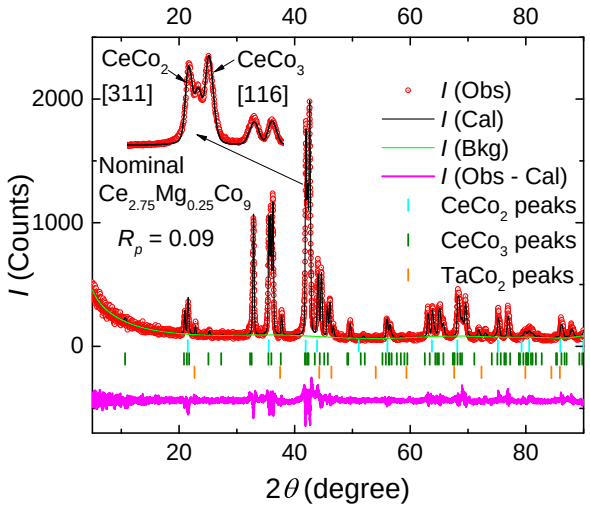

Figure 7.5 A typical example of multiphase polycrystalline XRD pattern for nominal $Ce_{2.75}Mg_{0.25}Co_9$ sample. The enlarged peak on the left top of the graph shows the broadening of the highest intensity peak of $Ce_{3-x}Mg_xCo_9$ around 2θ value of 42° due to presence of Mg doped $CeCo_2$ diffraction peak. I(Obs), I(Cal) and I(Bkg) are experimental, Rietveld refined and instrumental background data respectively. The lower section of the graph shows the Bragg's peaks positions with different coloured vertical lines for phases shown in the graph and the differential X-ray diffractrogram I(Obs-Cal).

tetragonal structure at $x = 2$ (YIn_2Ni_9-type) [6]. The solubility range of Mg in $CeCo_3$ is therefore similar but we do not observe a phase corresponding with the YIn_2Ni_9-type structure for $x \geq 2$. Instead, a three phase region of $MgCo_2$, $Ce_{3-x}Mg_xCo_9$ and Co is observed (see TABLE 7.3). The compositional range of our $Ce_{3-x}Mg_xCo_9$ samples is summarized in FIG. 7.1.

The variation of the polycrystalline lattice parameters and unit cell volume as a function of the Mg content in the $Ce_{3-x}Mg_xCo_9$ phase as determined from EDS is shown in FIG. 7.8. As expected, the substitution of Ce by Mg results in the reduction of the unit cell volume, similar to the case of $Nd_{3-x}Mg_xCo_9$ alloys [6]. Neither the a or c-lattice parameter follows a linear relation with Mg content x. The variation in a lattice parameter shows the slight positive deviation and c lattice parameter shows the slight negative deviation starting in the middle of the single phase region. The negative deviation of lattice parameter c might indicate that the covalent bonding is increased

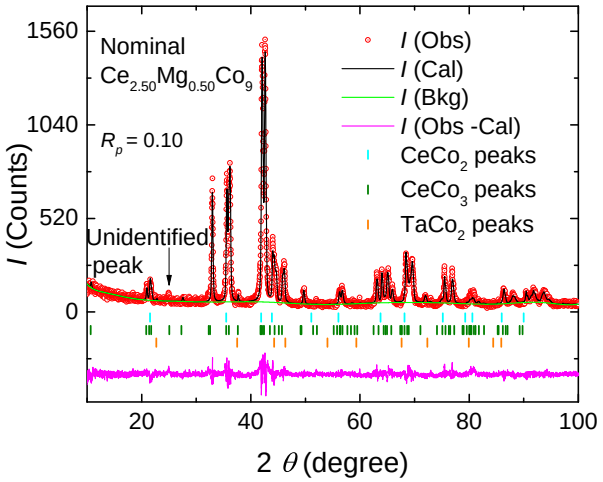

Figure 7.6 Powder XRD pattern for nominal $Ce_{2.50}Mg_{0.50}Co_9$ sample. $TaCo_2$ phase is almost not detectable for XRD however an unidentified XRD peak is observed around 2θ value of 25°. I(Obs), I(Cal) and I(Bkg) are experimental, Rietveld refined and instrumental background data respectively. The lower section of the graph shows the Bragg's peaks positions with different coloured vertical lines for phases shown in the graph and the differential X-ray diffractrogram I(Obs-Cal)

along that direction. It should be noted that the lattice parameters (a, c, v) and composition inferred from the single crystal X-rays (shown as corresponding color $\star$s) agree very well with what we inferred from EDS measurements on the polycrystalline samples.

7.5 Magnetic Properties

Previously reported data do not agree about the magnetic properties of the parent compound, $CeCo_3$. Lemaire reported $CeCo_3$ as a ferromagnetic material with Curie temperature 78 K [15]. Buschow identified it as a Pauli-paramagnetic phase however he left a room for further investigation mentioning $CeCo_3$ could be ferromagnetic below 10 K[16]. To clarify this issue, we measured the temperature dependent magnetization and electric resistivity of our single crystalline samples down to 2 K as shown in FIG. 7.9. The magnetization data shows no signature of a phase transition and is only weakly temperature dependent and is consistent with a Pauli-paramagnet and an impurity

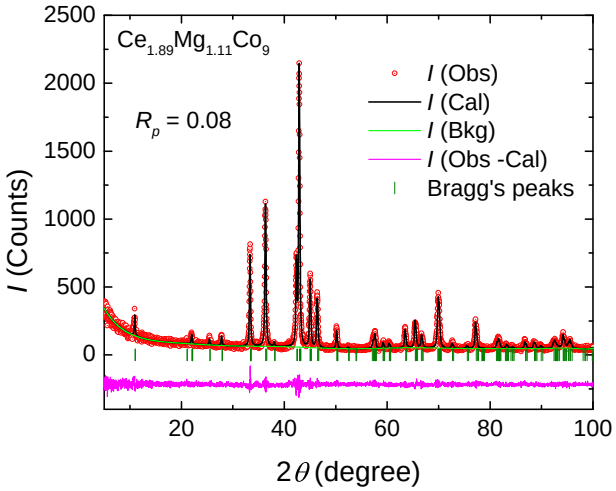

Figure 7.7 A typical example of predominantly single phase polycrystalline XRD pattern for EDS characterized $Ce_{1.89}Mg_{1.11}Co_9$ sample. I(Obs), I(Cal) and I(Bkg) are experimental, Rietveld refined and instrumental background data respectively. The lower section of the graph shows the Bragg's peaks positions with olive vertical lines and the differential X-ray diffractrogram I(Obs-Cal)

tail below 20 K. Assuming Curie tail is because of Ce^{3+} magnetic ions in the single crystalline $CeCo_3$ sample, magnetic susceptibility was fitted to Curie-Weiss law up to 150 K as:

$$\chi(T) = \chi_0 + \frac{C}{T-\theta}$$

where χ_0 is high temperature asymptotic susceptibility, C is Curie constant and θ is Curie-Weiss temperature. The concentration of Ce^{3+} ions was estimated to be $\sim 20\%$ (with $\theta = 3.8$ K) using the spin only moment of $2.54\mu_B$ per Ce^{3+} ion (Equation 1.57 was used to calculate the concentration ie. $\mu_{eff} \propto \sqrt{\text{concentration}}$). The electrical resistivity does not show any signature of a loss of spin disorder scattering that would be anticipated for a magnetic phase transition.

The temperature dependence of the magnetization data of the single phase $Ce_{3-x}Mg_xCo_9$ polycrystalline samples are shown in FIG. 7.10. A rapid increase of the magnetization upon cooling below the Curie temperature is observed for $x = 0.82$ - 1.35 indicating the appearance of ferromagnetism with Mg substitution.

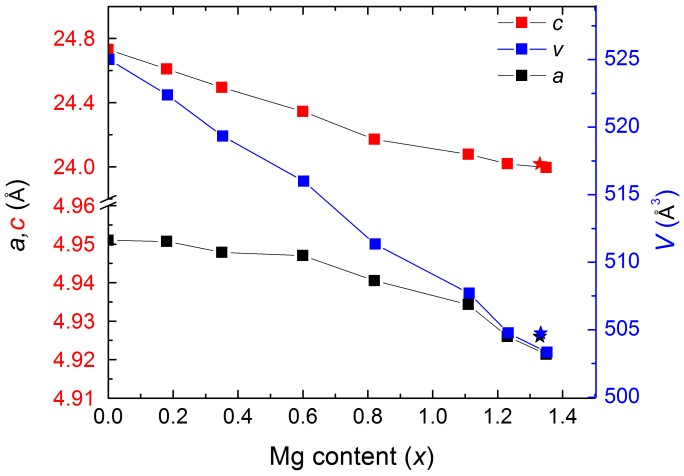

Figure 7.8 Variation of lattice parameters (a,c) and unit cell volume (v) of polycrystalline with Mg content inferred from EDS. Cubic $Ce_{1-x}Mg_xCo_2$ types impurity phases were obtained for $x \leq 0.6$ and predominant single phase $Ce_{3-x}Mg_xCo_9$ is obtained for $0.6 < x \leq 1.4$. The lattice parameters for single crystalline $Ce_{1.66}Mg_{1.34}Co_9$ are presented with corresponding color stars. The uncertainty in the refined lattice parameters is less than 0.01% of the reported lattice parameters and too small to clearly show as an error bar in the diagram.

The Curie temperature T_C is estimated as the cross-point of linear extrapolations of two tangents to magnetization curve around the point of inflection as indicated on the curve $x = 1.11$ and $x = 1.23$ in FIG. 7.10. The variation of T_C with Mg substitution is shown in the inset. The Curie temperature increases with Mg concentration and reaches as high as 450 K for $x = 1.35$.

The substitution of Mg for Ce changes a Pauli-paramagnet ($CeCo_3$) into a ferromagnet that has T_C increase with Mg content. The most likely reason for this is associated with valency and band filling. In $CeCo_3$, the Ce is essentially non-moment bearing; this implies a Ce^{4+} valency. As Mg^{2+} is added, there will be a clear change in band filling that most likely leads to Stoner-type magnetism associated with the Co 3-d bands. Further work, both computational and experimental will be needed to better appreciate the origin of the observed ferromagnetism.

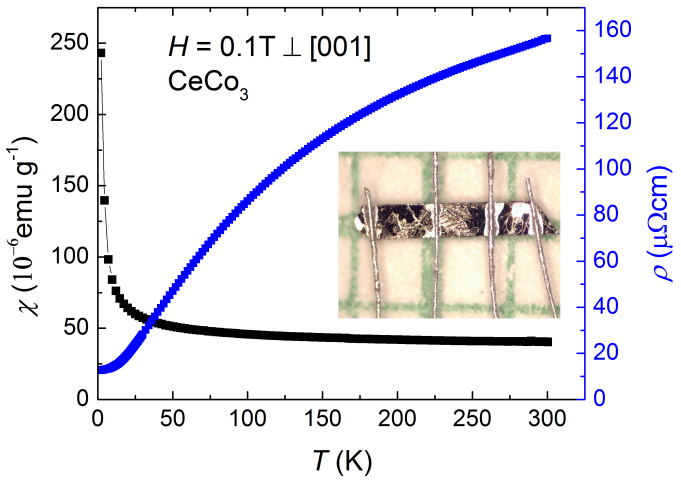

Figure 7.9 Temperature dependent susceptibility (H = 0.1 T $\perp$ [001]) and electrical resistivity (excitation current $\perp$ to [001]) of $CeCo_3$ single crystal. The picture in the inset shows the resistivity bar for four probe measurement. The sample was 60 micrometer thick.

Figure 7.11 shows the magnetic hysteresis curves of various polycrystals along with observed coercivity fields at 50 K (inset). The coercivity field increases with Mg content, becomes maximum ($\sim$ 0.35 T) for x = 0.82 and then decreases. The observation of coercivity is consistent with the axial nature of the magnetic anisotropy as will be detailed below. The abruptly increased coercivity for $x = 0.82$ and spontaneous magnetization for $x = 1.11$ magnesium containing phases were reproduced in multiple samples. It should be noted that differing saturation values for differing x are most likely due to non-random distribution of grains in these as-cast samples. In addition, the non-saturating behaviour of the x = 1.35 sample indicates either the presence of the preferred orientations of the grains with their hard axis along the applied field or presence of some anisotropic magnetic impurity in the sample. The former argument can be easily visualized in $M(T)$ data as x = 1.35 polycrystalline sample and single crystalline $Ce_{1.66}Mg_{1.34}Co_9$ $M(T)$ data along the hard axis are almost identical in nature as shown in FIG. 7.10. The fact that as-cast samples show coercivity is promising for the development of permanent magnets out of this system.

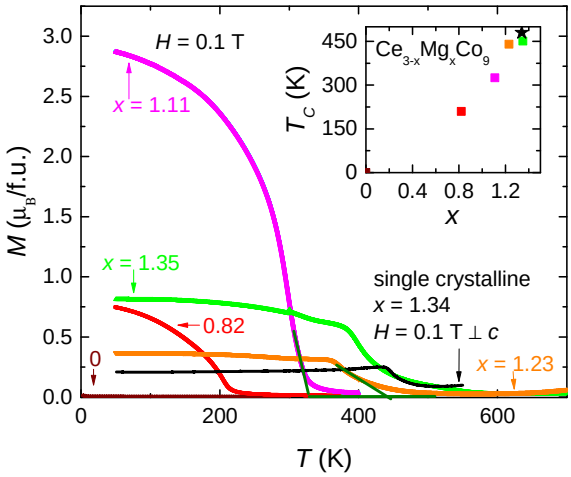

Figure 7.10 Temperature dependent magnetization of single crystalline ($x = 0$ and 1.34) polycrystalline $Ce_{3-x}Mg_xCo_9$ measured under a magnetic field of 0.1 T. The arrow pointed Mg content (x) for each *M(T)* graph are inferred from EDS analysis. The olive coloured straight lines above and below the point of inflection of *M(T)* data for for $x = 1.11$ and $x = 1.23$ shows the scheme for inferring the Curie temperature. Thus obtained Curie temperatures and Mg content phase diagram is presented in the inset. The black $\star$ represents the Curie temperature inferred from the tangents intersection scheme for single crystalline $Ce_{1.66}Mg_{1.34}Co_9$ sample on the *M(T)* data measured along the hard axis of the plate.

Our single crystal sample can provide further insight into this system's promise as a permanent magnet material. FIG. 7.12 shows the temperature dependence of the magnetization parallel and perpendicular to the c-axis of the single crystal of $Ce_{1.66}Mg_{1.34}Co_9$ up to 550 K. The c-axis is the easy axis of magnetization and the saturation magnetization at low temperature is 8 μ_B/f.u. The spontaneous magnetization data points for $Ce_{1.66}Mg_{1.34}Co_9$, represented with red squares, are obtained by the Y-intercept of linear fitting of the high field *M(H)* data (>1.5 T) in the first quadrant. No hysteresis was observed in the *M(H)* loops. The absence of hysteresis in *M(H)* isotherms measured in single crystals is due to absence of grain boundaries, defects and impurity atoms capable of pinning of the ferromagnetic domains. When measurements were performed up to 1000 K, we noticed a non-reproducibility of the results as shown in the inset of FIG. 7.12.

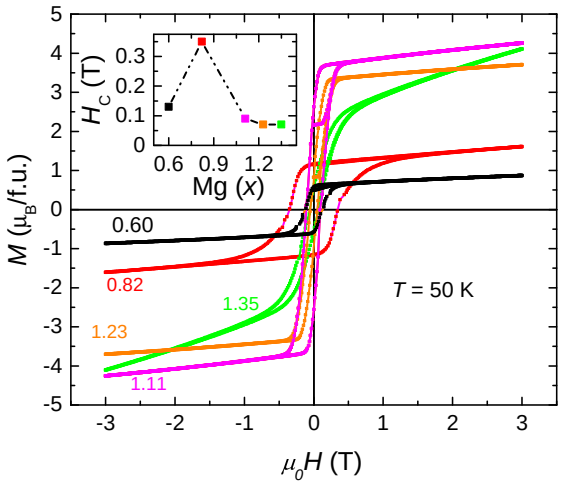

Figure 7.11 Magnetic hysteresis loop of various annealed polycrystalline $Ce_{3-x}Mg_xCo_9$ samples at 50 K. The values of Mg content are from EDS analysis. The inset shows the variation of the observed coercivity fields of the samples as a function of Mg content.

Thermo-gravimetric analysis (not shown here) showed evidence for a decomposition of the samples, this degradation was not observed when limiting the measurements to a maximum temperature of 550 K.

An Arrott plot with several isotherms near the Curie temperature is shown in FIG. 7.13. The internal magnetic field H_{int} was determined using the relation $H_{int} = H_{app} - N * M$, where H_{app} is the applied field, N is the demagnetization factor which is experimentally determined along the easy axis ($N_c = 0.78$) [12, 13] and M is the magnetization. The Arrott curves are not linear indicating $Ce_{1.66}Mg_{1.34}Co_9$ does not follow the mean field theory. The Curie temperature of $Ce_{1.66}Mg_{1.34}Co_9$ is 440 K since Arrott curve corresponding to 440 K passes through the origin. This is comparable with the values of T_C obtained from polycrystals of similar composition (see inset of FIG. 7.10).

The magnetocrystalline anisotropy field was determined to be $\sim$ 10 T (T = 2 K) and $\sim$ 6 T (T = 300 K) for a $Ce_{1.66}Mg_{1.34}Co_9$ single crystalline sample, as shown in FIG. 7.14. The anisotropy field was determined by the linear extrapolation of the observed moment along the plane up to the saturation moment.

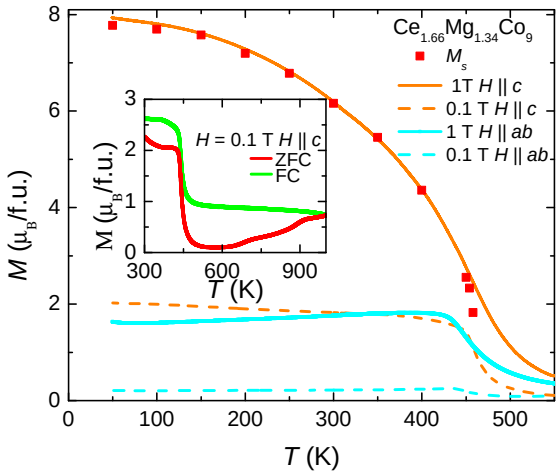

Figure 7.12 Anisotropic temperature dependent magnetization for $Ce_{1.66}Mg_{1.34}Co_9$ at various applied fields and directions. Dashed lines are for $H = 0.1$ T an solid lines are for $H = 1.0$ T. Individual data points (red squares) are spontaneous magnetization, M_S inferred from *M(H)* isotherms. The inset shows the zero field cooled (ZFC) and field cooled (FC) magnetization data along the easy axis of magnetization to temperature above the sample decomposition point.

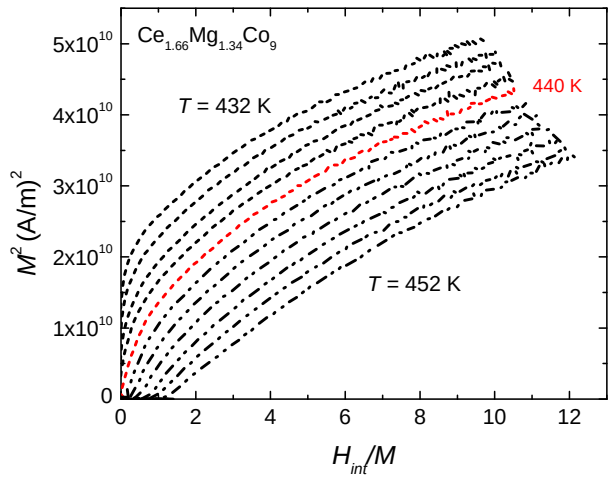

Figure 7.13 Arrott plot for a $Ce_{1.66}Mg_{1.34}Co_9$ single crystal within the temperature range of 432 K to 452 K at a step of 2 K between adjacent curves. The Curie temperature is determined to be 440 K.

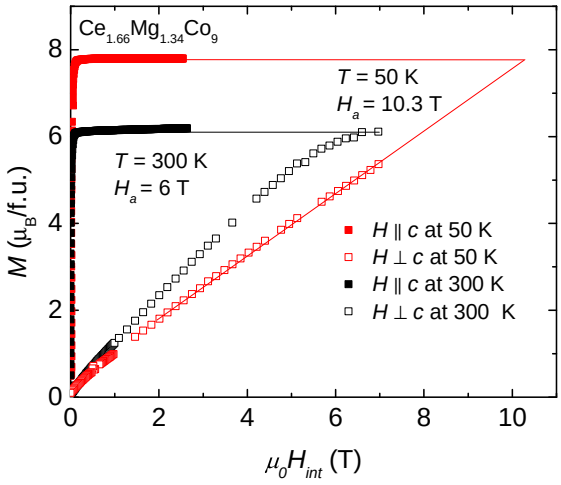

Figure 7.14 Anisotropic field dependent magnetization of $Ce_{1.66}Mg_{1.34}Co_9$ at 50 K ($H_a \approx 10$ T) and 300 K ($H_a \approx 6$ T).

The anisotropy energy was quantified by using the Sucksmith-Thompson plot for field dependent magnetization data along the plane as shown in FIG. 7.15. In the Sucksmith-Thompson plot, the ratio of magnetizing field with hard axis magnetization data is related to the anisotropy constants K_1 and K_2, saturation magnetization M_s and hard axis magnetization ($M_\perp$) as shown in equation (1)[17, 18].

$$\frac{\mu_0 H}{M_\perp} = \frac{2K_1}{M_s^2} + \frac{4K_2}{M_s^4} M_\perp^2 \tag{7.1}$$

The intercept of the Sucksmith-Thompson plot gives the anisotropy constant K_1 and slope gives the anisotropy constant K_2. FIG. 7.16 shows the temperature variation of the measured anisotropy constants. There was a slight mismatch ($< 2\%$) in the anisotropies data above and below the 300 K obtained from VSM and MPMS data. The VSM data were scaled to MPMS data at 300 K since slope of Sucksmith-Thompson plot are better determined with higher applied field. Here the total anisotropy energy of $Ce_{1.66}Mg_{1.34}Co_9$ is determined to be 2.2 MJ/m^3 and $\approx 0.75 MJ/m^3$ at room temperature. Such high anisotropy energy density makes the $Ce_{1.66}Mg_{1.34}Co_9$ as a potential candidate for permanent magnet applications.

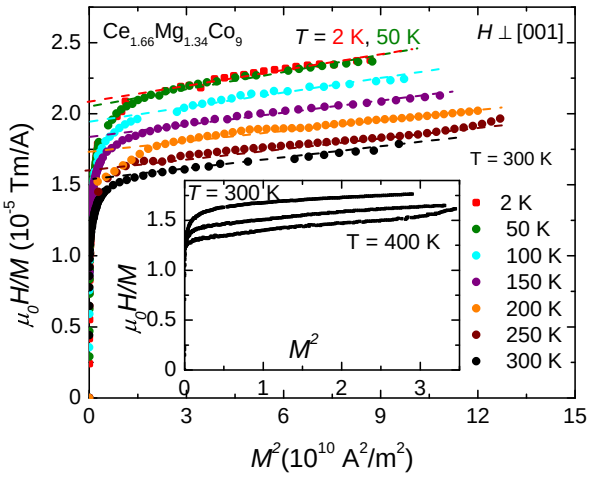

Figure 7.15 Sucksmith-Thompson plot for $Ce_{1.66}Mg_{1.34}Co_9$ to obtain anisotropy constants K_1 and K_2. The field dependent magnetization data were measured up to 7 T along the hard axis of magnetization. The dotted straight lines are the linear fit to $\frac{\mu_0 H}{M}$ at high field magnetization data to obtain the intercepts and slopes of the isotherms. The inset shows the Sucksmith-Thompson plots for VSM data measured along hard axis ($H \perp [001]$) up to 3 T field. K_1 and K_2 obtained by VSM data were matched to MPMS data at 300 K.

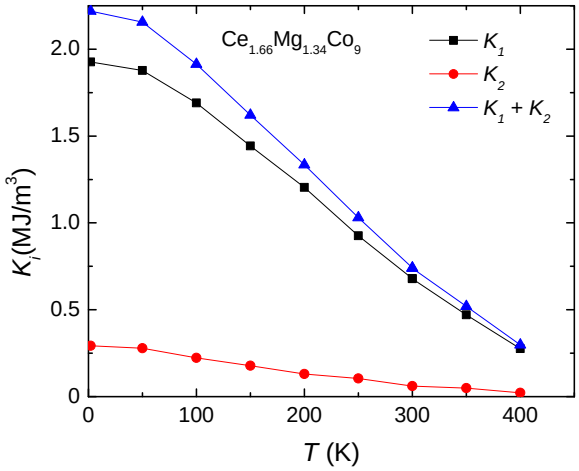

Figure 7.16 Temperature dependent anisotropy energy constants for $Ce_{1.66}Mg_{1.34}Co_9$. The anisotropy constants were determined from the Sucksmith-Thompson plot. The K_1 and K_2 values up to 300 K were measured using MPMS and higher temperature data are measured using VSM.

7.6 Conclusions

We investigated the effect of Mg substitution into the Ce_3Co_9 (e.g. $CeCo_3$) binary phase where Mg partially replaces the Ce atom on the $6c$ crystallographic site giving rise to the $Ce_{3-x}Mg_xCo_9$ solid solution for $0 \leq x \lesssim 1.4$. The substituted Mg induces ferromagnetism; the Curie temperature of the solid solution increases with higher content of Mg and becomes maximum (450 K) for Mg content $x = 1.35$. The magnetic anisotropy was determined for a self-flux grown $Ce_{1.66}Mg_{1.34}Co_9$ single crystal. The uniaxial-anisotropy field was determined to be $\sim$ 10 T at 2 K and $\sim$ 6 T at 300 K. The anisotropy energy density was determined to be 2.2 MJ/m^3 at 2 K. With these observed magnetic properties, $Ce_{3-x}Mg_xCo_9$ solution shows a potential to be used as a permanent magnet.

7.7 Acknowledgements

We would like to thank Dr. T. Kong for useful discussions. Dr. Warren Straszheim is acknowledged for doing SEM on various samples. This research was supported by the Critical Materials Institute, an Energy Innovation Hub funded by the U.S. Department of Energy, Office of Energy Efficiency and Renewable Energy, Advanced Manufacturing Office. Q.L. is supported by the office of Basic Energy Sciences, Materials Sciences Division, U.S. DOE. This work was performed at the Ames Laboratory, operated for DOE by Iowa State University under Contract No. DE-AC02-07CH11358.

7.8 References

[1] G. B. Haxel, J. B. Hedrick, and G. J. Orris. Rare earth elementscritical resources for high technology. *U.S. Geological Survey Fact Sheet 087-02*, 2002.

[2] Pradyot Patnaik. *Handbook of Inorganic Chemicals*. McGraw-Hill, 2003.

[3] Feng Xie, Ting An Zhang, David Dreisinger, and Fiona Doyle. A critical review on solvent extraction of rare earths from aqueous solutions. *Miner. Eng.*, 56:10 – 28, 2014.

[4] Arjun K. Pathak, Mahmud Khan, Karl A. Gschneidner, Ralph W. McCallum, Lin Zhou, Kewei Sun, Kevin W. Dennis, Chen Zhou, Frederick E. Pinkerton, Matthew J. Kramer, and

Vitalij K. Pecharsky. Cerium: An Unlikely Replacement of Dysprosium in High Performance NdFeB Permanent Magnets. *Advanced Materials*, 27(16):2663–2667, 2015.

[5] RV Denys, AB Riabov, R Černỳ, IV Koval'chuk, and I Yu Zavaliy. New $CeMgCo_4$ and Ce_2MgCo_9 compounds: Hydrogenation properties and crystal structure of hydrides. *Journal of Solid State Chemistry*, 187:1–6, 2012.

[6] V.V. Shtender, R.V. Denys, V. Paul-Boncour, I.Yu. Zavaliy, Yu.V. Verbovytskyy, and D.D. Taylor. Crystal structure, hydrogen absorption-desorption behavior and magnetic properties of the $Nd_{3-x}Mg_xCo_9$ alloys. *J. Alloys Compd.*, 695:1426 – 1435, 2017.

[7] M.I. Bartashevich, K. Koui, T. Goto, M. Yamaguchi, I. Yamamoto, and F. Sugaya. Magnetic properties of NdCo3 and its γ-phase hydride NdCo3H4.1. *J. Alloys Compd.*, 202(1):7–12, 1993.

[8] Paul C. Canfield and Ian R. Fisher. High-temperature solution growth of intermetallic single crystals and quasicrystals. *Journal of Crystal Growth*, 225(24):155 – 161, 2001. Proceedings of the 12th American Conference on Crystal Growth and Epitaxy.

[9] Okamoto H. Ce-Co Phase Diagram, ASM Alloy Phase Diagrams Database, P. Villars, editor-in-chief; H. Okamoto and K. Cenzual, section editors. 1990.

[10] A. C. Larson and R. B. Von Dreele. General structure analysis system. *Los Alamos National Laboratory Report No. LAUR 86-748*, 2004.

[11] Brian H. Toby. *EXPGUI*, a graphical user interface for *GSAS*. *Journal of Applied Crystallography*, 34(2):210–213, Apr 2001.

[12] Tej N. Lamichhane, Valentin Taufour, Srinivasa Thimmaiah, David S. Parker, Sergey L. Bud'ko, and Paul C. Canfield. A study of the physical properties of single crystalline Fe_5B_2P. *J. Magn. Magn. Mater.*, 401:525 – 531, 2016.

[13] Tej N. Lamichhane, Valentin Taufour, Morgan W. Masters, David S. Parker, Udhara S. Kaluarachchi, Srinivasa Thimmaiah, Sergey L. Bud'ko, and Paul C. Canfield. Discovery of ferromagnetism with large magnetic anisotropy in ZrMnP and HfMnP. *Appl. Phys. Lett.*, 109(9):092402, 2016.

[14] A. Jesche, M. Fix, A. Kreyssig, W. R. Meier, and P. C. Canfield. X-ray diffraction on large single crystals using a powder diffractometer. *Philos. Mag.*, 96(20):2115–2124, 2016.

[15] R. Lemair. Magnetic properties of the lntermetallic compounds of cobalt with the rare earth metals and yttrium. *Cobalt*, 33:201–211, December 1966.

[16] K.H.J. Buschow. Magnetic properties of $CeCo_3$, Ce_2Co_7 and $CeNi_3$ and their ternary hydrides. *Journal of the Less Common Metals*, 72(2):257 – 263, 1980.

[17] W. Sucksmith and J. E. Thompson. The Magnetic Anisotropy of Cobalt. *Proc. Royal Soc. A*, 225(1162):362–375, 1954.

[18] Valentin Taufour, Srinivasa Thimmaiah, Stephen March, Scott Saunders, Kewei Sun, Tej Nath Lamichhane, Matthew J. Kramer, Sergey L. Bud'ko, and Paul C. Canfield. Structural and Ferromagnetic Properties of an Orthorhombic Phase of MnBi Stabilized with Rh Additions. *Phys. Rev. Applied*, 4:014021, Jul 2015.

CHAPTER 8. Mg ASSISTED FLUX GROWTH AND CHARACTERIZATION OF SINGLE CRYSTALLINE Sm_2Co_{17}

A paper published in *AIP Advances*

Tej N Lamichhane[1,2], Qisheng Lin[2] Valentin Taufour[2,3] ,Andriy Palasyuk[2], Tribhuwan Pandey[4]

David S. Parker[4], Sergey L. Bud'ko[1,2] and Paul C. Canfield[1,2]

1: Department of Physics and Astronomy, Iowa State University, Ames, Iowa 50011, U.S.A.

2: Ames Laboratory, Iowa State University, Ames, Iowa 50011, U.S.A.

3: Department of Physics, University of California Davis, Davis, California 95616, U.S.A.

4: Materials Science and Technology Division, Oak Ridge National Laboratory, Oak Ridge, TN 37831, USA

8.1 Abstract

This paper presents details of Mg-assisted flux growth of Sm_2Co_{17} single crystals in a Ta crucible well below the melting temperature of binary Sm_2Co_{17}. Both the crushed single crystalline powder x-ray diffraction (XRD) and single crystalline XRD data revealed the Th_2Zn_{17} type rhombohedral(R-3m) crystal structure. Ta atom is found to be statistically replacing the Co-Co dumbbell with its position being at the center of the dumbbell. The Curie temperature of our lightly Mg and Ta doped Sm_2Co_{17} sample is determined to be ∼1100 K using method of generalized Bloch law fitting of easy axis spontaneous magnetization data.

8.2 Introduction

Despite of the wide application of Sm_2Co_{17} as a high performance magnet, its basic physical properties are not as extensively studied as other high flux commercial permanent magnets such as $Nd_2Fe_{14}B$, $SmCo_5$, probably due to the lack of easily accessible single crystalline sample. Various

physical properties of single crystalline $Nd_2Fe_{14}B$ sample are studied on self flux grown sample [1, 2, 3]. In case of $SmCo_5$ and other high cobalt content binary R-Co compounds single crystals, the traditional self-flux growth technique out of binary melt is not readily accomplished. Most of the Sm-Co binary compounds are highly reactive with traditional ceramics crucibles and mostly peritectic with very high exposed liquidus temperature ($>$ 1300 °C). Single crystal growth by zone melting, Bridgman and Czochralski technique are also difficult because of high reactivity of Sm-Co compounds and high vapour pressure of Sm. The quality of Bridgman technique grown crystals strongly depend on the quality and type of the crystal growth crucibles and also needs an excess amount of Sm. The Bridgman technique for $SmCo_5$ growth was successful only using the Ta crucible [4]. For Sm_2Co_{17}, the pyrolitic sintered BN-crucible could not assist crystal growth. Aditionally, the BN-coated recrystallized $A1_2O_3$ crucible also produced a reacted complex layer containing Al, B, N and R when reached up to 1400 °C during the Bridgman crystal growth technique [5]. In this work we use Mg-flux to reduce the melting temperature and allow for the use of a sealed Ta crucible to hold the melt to get single crystals. More importantly, this Mg assisted flux growth technique might open a route for the availability of most of R_2T_{17} single crystals which are surprisingly rare so far e.g. Sm_2Fe_{17} [6].

8.3 Experimental results and discussions

8.3.1 Crystal growth and structural characterization

$Sm_9Co_{67}Mg_{24}$ composition was loaded in a 3-capped Ta crucible [7] and growth profile similar to $Ce_{3-x}Mg_xCo_9$ [8] was used for the crystal growth. The single crystals were separated from the flux at 1150°C after cooling the ampoule from 1200 °C over 99 h.

As grown Sm_2Co_{17} single crystals are presented in figure 8.1(a). The plate like Sm_2Co_{17} crystals have [001] axis perpendicular to plate as illustrated by backscattered Laue photograph with a hexagonal pattern as shown in Figure 8.1(b).

Initially, Sm_2Co_{17} single crystals were characterized using crushed single crystal powder x-ray diffraction (XRD) technique. These data were collected using Rigaku Miniflex II diffractormeter

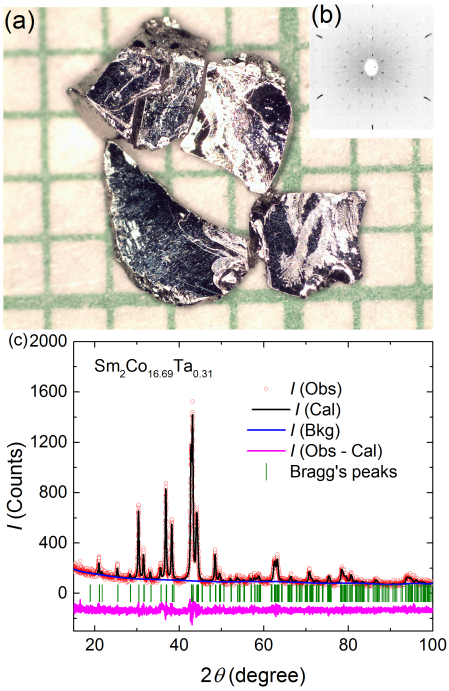

Figure 8.1 (a) $Sm_2Co_{16.69}Ta_{0.31}$ single crystals over the millimeter grid (b) Laue pattern with beam direction [001]. Although the crystals are not looking xexagonal, the back-scattered Laue photograph is hexagonal. (c) Rietveld refined powder XRD for $Sm_2Co_{16.69}Ta_{0.31}$. I(Obs), I(Cal), I(Bkg) and I(Obs - Cal) are experimental, calculated, fitted background and differential diffractrogram data respectively. The vertical lines represents the various diffraction Bragg peaks.

(Cu-K_α radiation). Finely ground Sm_2Co_{17} powder was spread over the silicon wafer sample holder with help of Dow Corning high vacuum grease and diffraction data were collected over 2θ range of 10° to 100° with a scan step of 0.01° with a dwelling time of 5 sec. Powder data were Rietveld refined using EXPGUI and GSAS software package[9]. The Rietveld refined powder XRD pattern using Th_2Zn_{17} type structure with space group R-3m is presented in Figure 8.1(c) with $R_p = 0.08$.

Then the as grown single crystals of Sm_2Co_{17} were characterized using Scanning Electron Microscopy (SEM) technique. As grown crystals were mounted in a SEM sample-mounting-epoxy both parallel and perpendicular to the plate to access both planar and cross sectional area of samples and finely polished to obtain the smooth surfaces as shown in fig. 8.2. Figure 8.2(a) and (b) show

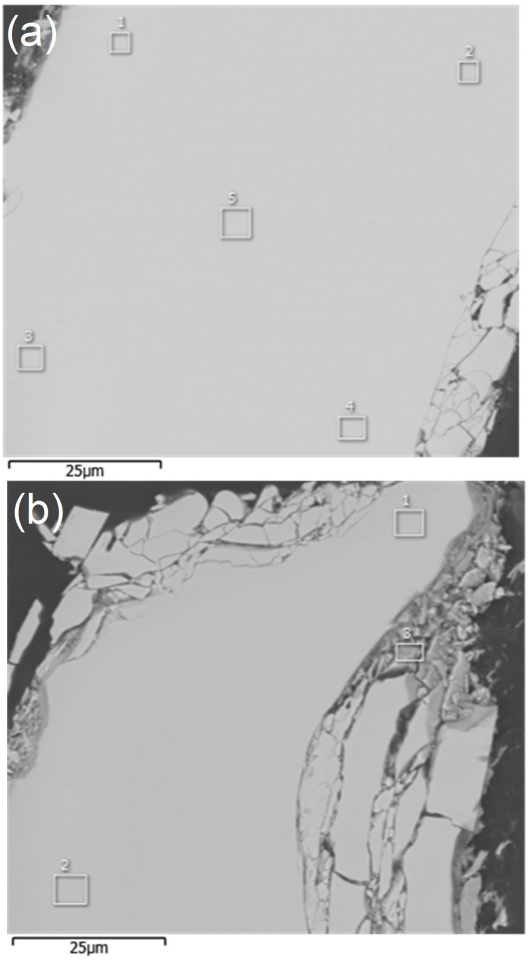

Figure 8.2 (a) SEM image of as grown $Sm_2Co_{16.69}Ta_{0.31}$ single crystal along the planar view (b) along the cross section.

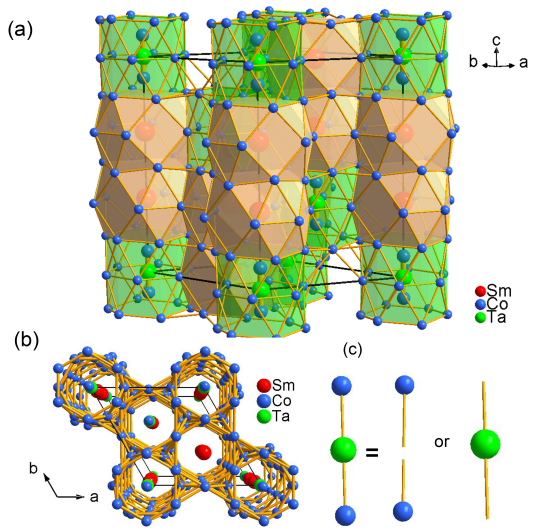

Figure 8.3 (a) Crystal structure of $Sm_2Co_{16.69}Ta_{0.31}$. The Ta atoms are statistically occupying the center of Co-Co dumbbell along the specific veritcal channel. (b) Crystal structure of $Sm_2Co_{16.69}Ta_{0.31}$ viewed along the c-axis to demonstrate the dumbbells and Sm atoms channel. (c) Illustration of statistical replacement of Co-Co dumbbell by Ta atom.

the fine polished more or less homogeneous composition both in planar and cross sectional back scattered SEM images of Sm_2Co_{17} samples. Interestingly, even though the back-scattered images looks uniform, the energy dispersive x-ray spectroscopy (EDS) spectra showed small presence of Mg and Ta in the sample with a average composition of $Sm_2Co_{16.69}Ta_{0.31}$. Then we got motivated to know the specific structural site of Mg and Ta in the structure and employed a single crystalline XRD analysis.

Single crystal XRD intensity data for an as grown single crystal were collected using Bruker smart Apex-II diffractometer (MoK_α $\lambda = 0.71073$ Å) and analysed using SHELXTL structure solution software. In total, 5665 reflections were collected using 0.05° scans in ω. The average exposure time was 10 sec and the crystal to detector distance was 60 mm. In the structure solution, Mg could be included in the specific Co site but the composition is never higher than error bar. Then we dropped Mg in the composition formula. Ta atoms were found to substitute the center

of Co-Co dumbbell as shown in fig. 8.3(a). The structure of $Sm_2Co_{16.69}Ta_{0.31}$ (R-$3m$) features parallel hexagonal tunnels (defined by Co2-Co4 atoms) running along the c axis, cf. figure 8.3 (b). The tunnels are alternately filled by Co1-Co1 dimers and Sm atoms. In the present structure, Ta is statistically substituted for Co-Co dumbbell with Ta position being at the center of Co-Co dumbbell as shown in figure 8.3 (c), consistent with Zr atom position in Zr doped Sm_2Co_{17} magnet alloy predicted via lattice relaxation calculation [10], with a refined occupancy of 2.6(2)%.

Refined crystallographic information data and conditions are presented in Table 8.1 and 8.2 below.

Table 8.1 Crystal data and structure refinement for $Sm_2Co_{16.69}Ta_{0.31}$.

Empirical formula	$Sm_2Co_{16.69}Ta_{0.31}$
Formula weight	1306.99
Temperature	293(2) K
Wavelength	0.71073 Å
Crystal system, space group	Trigonal, R-3m
Unit cell dimensions	a=8.4075(17) Å
	c = 12.241(3) Å
Volume	749.4(3) 10^3 Å^3
Z, Calculated density	3, 8.688 g/cm^3
Absorption coefficient	39.095 mm^{-1}
Reflections collected	5665
Independent reflections	477 [R(int) = 0.0495]
Completeness to $\theta = 25.242°$	100.00%
Absorption correction	multi-scan, empirical
Refinement method	Full-matrix least-squares
	on F^2
Data / restraints / parameters	152 / 0 / 17
Goodness-of-fit on F^2	0.936
Final R indices [I> 2σ(I)]	$R1 = 0.0216$, $wR2 = 0.0466$
R indices (all data)	$R1 = 0.0231$, $wR2 = 0.0299$
Extinction coefficient	0.00188(13)
Largest diff. peak and hole	2.393 and -1.686 e.Å^{-3}

Table 8.2 Atomic coordinates and equivalent isotropic displacement parameters (A^2) for $Sm_2Co_{16.69}Ta_{0.31}$. U(eq) is defined as one third of the trace of the orthogonalized U_{ij} tensor.

atom	Wyck. Occ.	Symm.	x	y	z	U_{eq}
Sm	6c (1)	3m	0.0	0.0	0.3452 (1)	0.005(1)
Co1	6c (0.97)	3m	0.0000	0.0000	0.0969 (1)	0.006(1)
Co2	18f (1)	.2	0.2904 (1)	0.0000	0	0.007(1)
Co3	9d (1)	.2/m	0.5000	0.0000	0.5000	0.006(1)
Co4	18h (1)	.m	0.5015	0.4985	0.1539	0.007(1)
Ta	3a 0.03 (2)	-3m	0	0	0	0.007(2)

8.3.2 Determination of Curie temperature

Temperature and field dependent magnetization data were obtained along easy axis of $Sm_2Co_{16.69}Ta_{0.31}$ single crystals using Quantum Design vibrating sample magnetometer(VSM: 300 K - 1000 K). The Curie temperature of Sm_2Co_{17} single crystalline sample is reported to fall in between 1080 K to 1180 K window [11, 12, 13]. Getting the Curie tail of $Sm_2Co_{16.69}Ta_{0.31}$ to estimate the transition temperature is not possible in commercially available magnetometers like QD VSM with oven option. In order to estimate the Curie temperature we used the method of generalized Bloch fitting of spontaneous magnetization data. Spontaneous magnetization data were obtained via the Y-intercept of linear fit of saturation magnetization part of M(H) data at various temperatures as shown in Fig. 8.4 for 300 K. The two tiny triangular vortexes in the *M(H)* loop might be the signature of ferrimagnetic coupling between Sm and Co demonstrated by domain wall movement at high field [14, 15]. Such spontaneous magnetization data were taken up to 1000 K for each interval of 50 K starting from the room temperature. To reduce the uncertainty,spontaneous magnetization

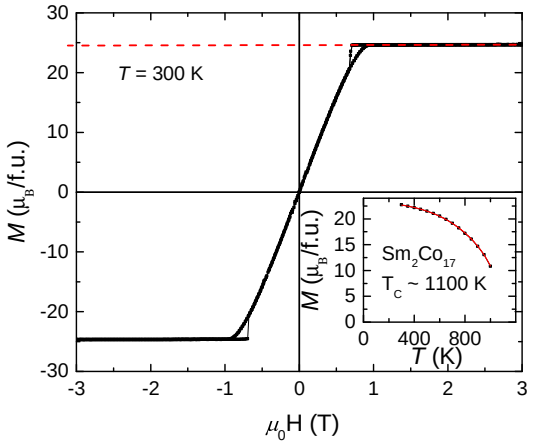

Figure 8.4 Determination of the spontaneous magnetization of $Sm_2Co_{16.99}$ $Mg_{0.01}Ta_{0.35}$ using [001] magnetization data at 300 K. See the text for a possible reason of tiny vortexes in the *M(H)* loop.

data were measured using a well-polished sample which could be better aligned along the easy axis during the measurements. The generalized Bloch Law was fitted as $\frac{M_S(T)}{M_S(2K)} = (1 - (\frac{T}{T_C})^{\alpha})^{\beta}$ shown in the inset of figure 8.4 and the Curie temperature is inferred to be 1100 K[16, 17]. Here $M_S(2K)$ and $M_S(T)$ are the base temperature and high temperature spontaneous magnetization data and T_C is the Curie temperature. The fitted value of the α and β are found to be 2.53 ± 0.07 and 0.49 ± 0.02 respectively.

8.4 Conclusions

Single crystalline Sm_2Co_{17} samples were prepared using Mg assisted self-flux growth technique in a 3-caped Ta crucible. In case of Sm_2Co_{17}, Ta is found to be statistically distributed in the center of Co-Co dumbbell with an empirical formula $Sm_2Co_{16.69}Ta_{0.31}$. The Curie temperature of $Sm_2Co_{16.69}Ta_{0.31}$ is determined to be ~ 1100 K using the generalized Bloch law method.

8.5 Acknowledgements

Dr. Warren Straszheim is acknowledged for doing SEM on various samples. This research was supported by the Critical Materials Institute, an Energy Innovation Hub funded by the U.S. Department of Energy, Office of Energy Efficiency and Renewable Energy, Advanced Manufacturing Office. This work was also supported by the office of Basic Energy Sciences, Materials Sciences Division, U.S. DOE. This work was performed at the Ames Laboratory, operated for DOE by Iowa State University under Contract No. DE-AC02-07CH11358.

8.6 References

[1] J.-Y. Wang, L.H. Lewis, D.O. Welch, and Paul Canfield. Magnetic Domain Imaging of $Nd_2Fe_{14}B$ Single Crystals With Unmodified Scanning Electron Microscopy. *Materials Characterization*, 41(5):201 – 209, 1998.

[2] A. Kreyssig, R. Prozorov, C. D. Dewhurst, P. C. Canfield, R. W. McCallum, and A. I. Goldman. Probing Fractal Magnetic Domains on Multiple Length Scales in $Nd_2Fe_{14}B$. *Phys. Rev. Lett.*, 102:047204, Jan 2009.

[3] Lunan Huang, Valentin Taufour, T. N. Lamichhane, Benjamin Schrunk, Sergei L. Bud'ko, P. C. Canfield, and Adam Kaminski. Imaging the magnetic nanodomains in $Nd_2Fe_{14}B$. *Phys. Rev. B*, 93:094408, Mar 2016.

[4] J.F. Miller and A.E. Austin. The growth of $SmCo_5$ crystals by the bridgman technique. *Journal of Crystal Growth*, 18(1):7 – 12, 1973.

[5] Toshikazu Katayama and Tsugio Shibata. Single crystal preparation of rare earth-cobalt intermetallic compounds by a BN-coated crucible. *Journal of Crystal Growth*, 24-25:396 – 399, 1974.

[6] L. V. B. Diop, M. D. Kuz'min, K. P. Skokov, D. Yu. Karpenkov, and O. Gutfleisch. Magnetic anisotropy of Sm_2Fe_{17} single crystals. *Phys. Rev. B*, 94:144413, Oct 2016.

[7] Paul C. Canfield and Ian R. Fisher. High-temperature solution growth of intermetallic single crystals and quasicrystals. *Journal of Crystal Growth*, 225(24):155 – 161, 2001. Proceedings of the 12th American Conference on Crystal Growth and Epitaxy.

[8] Tej N. Lamichhane, Valentin Taufour, Andriy Palasyuk, Qisheng Lin, Sergey L. Bud'ko, and Paul C. Canfield. $Ce_{3-x}Mg_xCo_9$: transformation of a Pauli paramagnet into a strong permanent magnet. *Phys. Rev. Applied*, 2018.

[9] Brian H. Toby. *EXPGUI*, a graphical user interface for *GSAS*. *Journal of Applied Crystallography*, 34(2):210–213, Apr 2001.

[10] P. Larson and I. I. Mazin. Effect of lattice relaxation on magnetic anisotropy: Zr-doped Sm_2Co_{17}. *Phys. Rev. B*, 69:012404, Jan 2004.

[11] H. Kronmller and D. Goll. Analysis of the temperature dependence of the coercive field of Sm_2Co_{17} based magnets. *Scripta Materialia*, 48(7):833 – 838, 2003. Nanostructured Advanced Magnetic Materials, Based on a workshop held at Irsee, Germany, 9-13 June, 2002.

[12] O. Gutfleisch, K.-H. Mller, K. Khlopkov, M. Wolf, A. Yan, R. Schfer, T. Gemming, and L. Schultz. Evolution of magnetic domain structures and coercivity in high-performance smco 2:17-type permanent magnets. *Acta Materialia*, 54(4):997 – 1008, 2006.

[13] M. V. Satyanarayana, H. Fujii, and W. E. Wallace. Magnetic properties of substituted $Sm_2Co_{17-x}T_x$ compounds (T = V, Ti, Zr, and Hf). *Journal of Applied Physics*, 53(3):2374–2376, 1982.

[14] X. X. Zhang, J. M. Hernàndez, J. Tejada, R. Solé, and X. Ruiz. Magnetic properties and domain-wall motion in single-crystal $BaFe_{10.2}Sn_{0.74}Co_{0.66}O_{19}$. *Phys. Rev. B*, 53:3336–3340, Feb 1996.

[15] Zhaorong Yang, Martin Lange, Alexender Volodin, Ritta Szymczak, and Victor V. Moshchalkov. Domain-wall superconductivity in superconductorferromagnet hybrids. *Nature Materials*, page 793798, Oct 2004.

[16] K. Maaz, M. Usman, S. Karim, A. Mumtaz, S. K. Hasanain, and M. F. Bertino. Magnetic response of core-shell cobalt ferrite nanoparticles at low temperature. *Journal of Applied Physics*, 105(11):113917, 2009.

[17] M. D. Kuz'min. Shape of temperature dependence of spontaneous magnetization of ferromagnets: Quantitative analysis. *Phys. Rev. Lett.*, 94:107204, Mar 2005.

CHAPTER 9. STUDY OF DOPING INDUCED QUANTUM PHASE TRANSITION IN $Ce_{3-x}Mg_xCo_9$

A paper to be submitted to *Philosophical magazine*

Tej N. Lamichhane,[1,2,*] Valentin Taufour,[1,3] Andriy Palasyuk,[1] and Sergey L. Budko,[1,2] and Paul C. Canfield[1,2]

[1]Ames Laboratory, U.S. DOE, Ames, Iowa 50011, USA

[2]Department of Physics and Astronomy, Iowa State University, Ames, Iowa 50011, USA

[3]Department of Physics, University of California Davis, Davis, California 95616, USA

9.1 Abstract

The $Ce_{3-x}Mg_xCo_9$ system evolves from a Pauli paramagnetic ground state for $x = 0$ to a ferromagnetic ground state for $x \approx 0.80$ in single phase, polycrystalline samples [Phys. Rev. Applied 9, 024023 (2018)]. In order to better understand this behavior, single crystalline samples of $Ce_{3-x}Mg_xCo_9$ for $x = 0.01$, 0.16, 0.24, 0.35, 0.43 and 0.50 were grown using the flux growth technique, and electrical transport and magnetic properties were studied. The T_C-x phase diagram we infer shows that the system has a quantum phase transition near $x = 0.35$, transforming to a ferromagnetic ground state.

9.2 Introduction

Fragile magnetic systems [1] tuned via chemical substitution can lead to quantum criticality, or more generally, a quantum phase transition at 0 K. Here we investigate a Pauli paramagnetic to ferromagnetic quantum phase transition in $Ce_{3-x}Mg_xCo_9$ [2, 3].

Despite being 75 % atomic Co, pure $CeCo_3$ has a Pauli paramagnetic, low temperature ground state i.e., the condition for existence for spontaneous magnetization is not achieved. In polycrys-

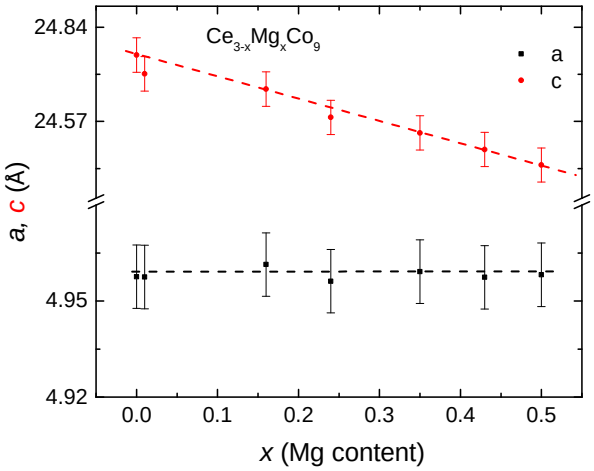

Figure 9.1 Variation of lattice parameters of $Ce_{3-x}Mg_xCo_9$ with Mg content x inferred from EDS. The uncertainty of the lattice parameters values is less than 0.2%. The dashed lines are guides to the eye.

talline $Ce_{3-x}Mg_xCo_9$, transformation of a Pauli paramagnetic $CeCo_3$ into a ferromagnetic phase was studied in our earlier work [2]. For single phase samples, ferromagnetism was observed for $x \geq 0.80$. In mixed phase samples, signs of magnetic order could be found for $x < 0.80$ but in such samples, magnetism could be influenced by several factors such as defects [4], stress [5], impurities [6] etc. To elucidate the phase transformation in a much cleaner way, study of magnetism using single phase, single crystalline samples is always a better idea. We investigated the magnetic properties, electrical transport and specific heat capacity of selected compositions around x∼0.35 of single crystalline $Ce_{3-x}Mg_xCo_9$ samples.

We find a quantum phase transition as $Ce_{3-x}Mg_xCo_9$ changes from a Pauli paramagnetic state for $0 \leq x < 0.35$ to a ferromagnetic state for $0.35 < x < 1.4$. No additional magnetic phases were found in the vicinity of the quantum phase transition composition.

9.3 Experimental details

Single crystalline $Ce_{3-x}Mg_xCo_9$ samples for $x \leq 0.5$ were synthesized in 3-cap Ta crucibles [7] similar to the previous report [2] by maintaining the Ce+Mg to Co ratio as 30:70 i.e. $(Ce_{1-x}Mg_x)_{30}Co_{70}$ with nominal $x = 0.05$, 0.10, 0.15, 0.20, 0.25 and 0.30 as listed in Table 9.1.

Table 9.1 Loaded nominal, EDS and Rietveld refined composition of $Ce_{3-x}Mg_xCo_9$ samples for crystal growth. The uncertainty in Mg content is given in parenthesis which was obtained as a standard deviation of EDS measurement. The average uncertainty in Mg concentration in the Rietveld refinement is $\leq \pm 0.05$.

Loaded nominal composition	EDS composition	Rietveld refined composition
$Ce_{30}Co_{70}$	—	$CeCo_3$
$Ce_{28.5}Mg_{1.5}Co_{70}$	$Ce_{2.99}Mg_{0.01(0.01)}Co_9$	$Ce_{2.95}Mg_{0.05}Co_9$
$Ce_{27}Mg_3Co_{70}$	$Ce_{2.84}Mg_{0.16(0.02)}Co_9$	$Ce_{2.87}Mg_{0.13}Co_9$
$Ce_{25.5}Mg_{4.5}Co_{70}$	$Ce_{2.76}Mg_{0.24(0.02)}Co_9$	$Ce_{2.75}Mg_{0.25}Co_9$
$Ce_{24}Mg_6Co_{70}$	$Ce_{2.65}Mg_{0.35(0.015)}Co_9$	$Ce_{2.68}Mg_{0.32}Co_9$
$Ce_{22.5}Mg_{7.5}Co_{70}$	$Ce_{2.57}Mg_{0.43(0.015)}Co_9$	$Ce_{2.57}Mg_{0.43}Co_9$
$Ce_{21}Mg_9Co_{70}$	$Ce_{2.50}Mg_{0.50(0.02)}Co_9$	$Ce_{2.49}Mg_{0.51}Co_9$

The selected amount of Ce-Co-Mg elements were sealed under almost one atmospheric pressure of Ar at room temperature inside a 3-cap Ta crucible. The Ta crucibles were protected under a partial pressure of Ar inside an amorphous silica jacket with quartz wool buffers on the top and the bottom of the crucible to protect silica ampoule from the consequences of differential thermal expansion during temperature ramping and mechanical shock during the decanting process. The silica ampoule was heated to 900 °C over 3 h and held there for 3 h to allow the initial reaction of elements and potentially avoid the excessive boiling of Mg at higher temperature. Then the growth was heated to 1200 °C over 3 h and held there for 10 h to form a homogeneous liquid. Finally, the growth was slowly cooled down to 1040 °C over ∼100 h for nominal Mg content $x = 0.05$ - 0.15 and centrifuged to separate the crystals from the flux. Similarly, growths with $x = 0.20$ - 0.30 were cooled down to 1070 °C over ∼100 h and crystals were separated. The single crystalline

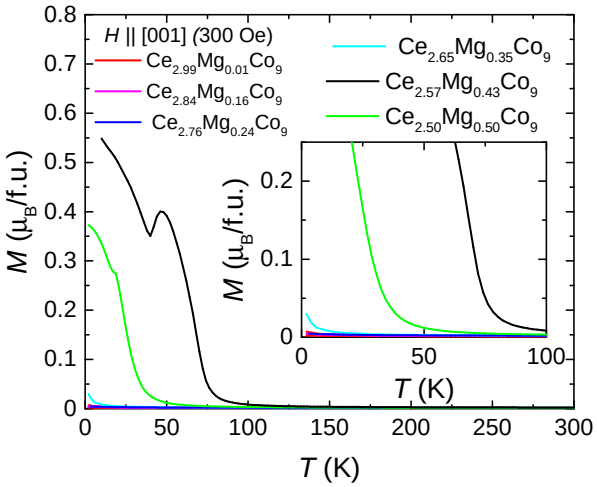

Figure 9.2 ZFC temperature dependent magnetization *M(T)* data of various $Ce_{3-x}Mg_xCo_9$ samples at 300 Oe applied field. The inset shows the enlargement around the upturns to highlight the ferromagnetism development with higher concentrations of Mg.

samples had rhombohedral plate-like morphology with several millimeters in length and width and approximately 1 - 2 mm in thickness. The easy axis of magnetization is perpendicular to the plate ([001] direction) [2].

Crystals from all the batches were characterized using powder X-ray diffraction (XRD) and Scanning Electron Microscopy (SEM). For XRD, a finely ground powder was spread over the zero background silicon wafer and held in place with a thin film of Dow Corning high vacuum grease. Powder XRD data were collected using Rigaku Miniflex II diffractometer within 2θ range of 5 - 100° using a step size of 0.01 degree and a dwell time of 3 seconds. For SEM, single crystalline samples were mounted in epoxy and finely polished perpendicular to the plane of the plate to determine the composition. The nominal composition, average Energy Dispersive Spectroscopy (EDS) composition, and Rietveld refined composition are presented in Table I. For nominal Mg x = 0.05, 0.10 and 0.15 samples, traces of $CeCo_2$ impurities were visible in the cross sectional view of SEM images (not shown here). The EDS and Rietveld refined composition more or less agree each

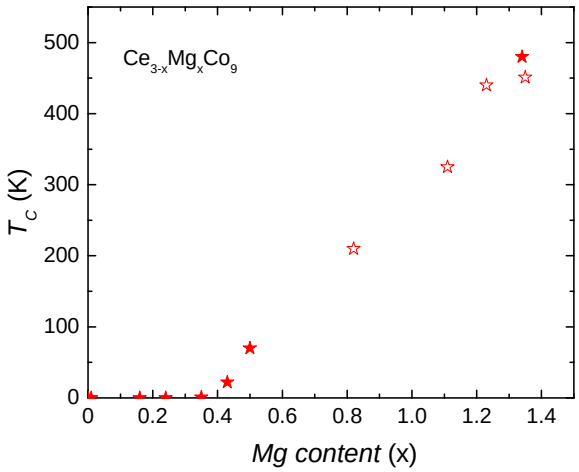

Figure 9.3 T_C - x phase diagram of $Ce_{3-x}Mg_xCo_9$ samples. Above $x \sim 0.35$, the Curie temperature is approximately linearly proportional to Mg content. The solid stars represents the Curie temperatures measured via Arrott plot analysis on single crystalline samples. The hollow stars represents Curie temperatures measured on polycrystalline samples [2].

other except for nominal 5% Mg doped sample. Hereafter, all the compositions are EDS inferred in this paper.

Magnetic properties were measured in a Quantum Design (QD) Magnetic Property Measurement System (MPMS) in between 2 K and 300 K. A QD VersaLab Vibrating Sample Magnetometer (VSM) was used to measure the magnetic properties between 50 K and 400 K. All the magnetization data were measured with magnetic field parallel to [001] direction. The internal magnetization field (H_{int}) was determined as $H_{int} = H_{applied} - N * M$ to determine the Curie temperature using Arrott plots [8]. Here, N is the demagnetization factor related to sample geometry and M is the magnetization. The details of the demagnetization factors determination can be found elsewhere [9, 10, 11]. Electrical transport property was measured using the four probe method with a Linear research Inc. meter bridge LR 700 (1mA; 17 Hz excitation). Thin platinum wires were attached to the resistance bar using DuPont 4929N silver paint to make electrical contacts. A MPMS was used as a temperature controller for the electrical transport measurements. The specific heat capacity was measured in a QD physical property measurement system using the relaxation technique.

9.4 Results and discussion

$Ce_{3-x}Mg_xCo_9$ forms in the rhombohedral structure for all x examined. Fig. 9.1 shows the variation of the lattice parameters a and c with Mg content. The c lattice parameter decreases monotonically whereas the a lattice parameter is more or less constant up to $x \leq 0.50$.

Figure 9.2 shows the zero field cooled (ZFC) temperature dependent magnetization *M(T)* for $x \leq 0.50$. Although $CeCo_3$ was identified as a Pauli paramagnetic compound long ago [12], there has been some room for question because of the presence of a low temperature upturn in temperature dependent magnetization [2]. Moreover recent density functional calculation showed $CeCo_3$ could order ferromagnetically at low temperature [3]. With $x \leq 0.24$ of Mg addition, the low temperature magnetization remains temperature independent and manifests Pauli paramagnetism as shown in the inset of Fig. 9.2. These temperature independent magnetization data for $x = 0.01$, 0.16, and 0.24 confirm that for these x-values, $Ce_{3-x}Mg_xCo_9$ is Pauli paramagnetic system. Since $x = 0.01$ sample is Pauli paramagnetic down to 2 K, this suggests that pure $CeCo_3$ may also be a Pauli paramagnetic. The low temperature upturn [2] is most likely associated with magnetism of impurity ions or traces of extrinsic magnetic impurity.

As we increase the value of x, a low temperature upturn starts to become visible for $x = 0.35$ suggesting it may be close to a critical concentration for achieving the quantum phase transition. For x = 0.43 and 0.50, the upturns in *M(T)* data upon cooling develop large enough magnetization to suggest that they are ferromagnetic samples. The kink only visible on the ZFC *M(T)* data for $x = 0.43$ and 0.50 could be related to reorientation of ferromagnetic domains near the transition temperature.

To better understand the evolution of ferromagnetism with Mg content x, a detailed analysis of easy axis *M(H)* data was performed for all samples. Figure A.1 shows the 2 K *M(H)* data for the non-ferromagnetic samples with EDS inferred Mg concentrations $x = 0.01$, 0.16, 0.24 and 0.35. In Fig. A.2, for the $Ce_{2.65}Mg_{0.35}Co_9$ sample, we can see an increasing low-field induced magnetization upon cooling indicating that it may be getting close to a ferromagnetic transition. The lower right

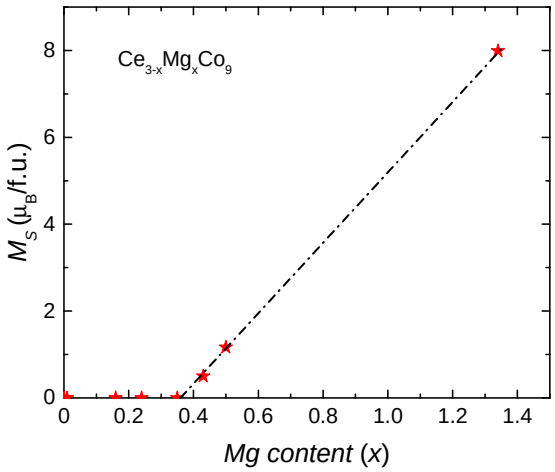

Figure 9.4 M_S - x relation of $Ce_{3-x}Mg_xCo_9$ samples. The graph includes spontaneous magnetization M_S only for single crystalline samples estimated from the Y-intercept of the linear fit of high field 2 K *M(H)* data along the easy axis [001]. The dash-dot line is a guide for the eyes.

inset in Fig. A.2 shows ZFC and field cooled (FC) *M(T)* data at 300 Oe applied field. This reversible nature of the *M(T)* data argues against ferromagnetic transition for $T > 2.0$ K.

In order to study the $x = 0.35$, 0.43 and 0.50 samples in greater detail, *M(H)* loops were performed as shown in Figs. A.2, A.4, and A.6 along with the determination of Curie temperature using Arrott plot method as shown in Figs. A.3, A.5 and A.7. Within the framework of Arrott plot analysis, straight Arrott curves through the origin suggest a mean field interaction in the magnetic system and identify the Curie temperature. The Arrott plot of $x = 0.35$ sample does not manifest straight lines that go through origin (as shown in Fig. A.3). This means that the $Ce_{2.65}Mg_{0.35}Co_9$ is non-ferromagnetic down to 2 K despite the slight upturn in *M(T)* data. On the other hand, the Arrott plot data become straighter for $Ce_{2.57}Mg_{0.43}Co_9$ (Fig. A.5(b)) and almost an ideal mean-field-like for $Ce_{2.50}Mg_{0.50}Co_9$ (Fig. A.7). From these analyses we can infer $T_C \approx 25$ K, 70 K for $x = 0.43$ and 0.50 respectively.

The 2 K *M(H)* data for $x = 0.43$ and 0.50 samples do not saturate up to 7 T applied field in these experiments, as shown in Figs. A.4 and A.6. However, higher magnesium containing samples e.g. x= 1.34 were well saturated with 3 T applied field in our previous work [2]. This could be the

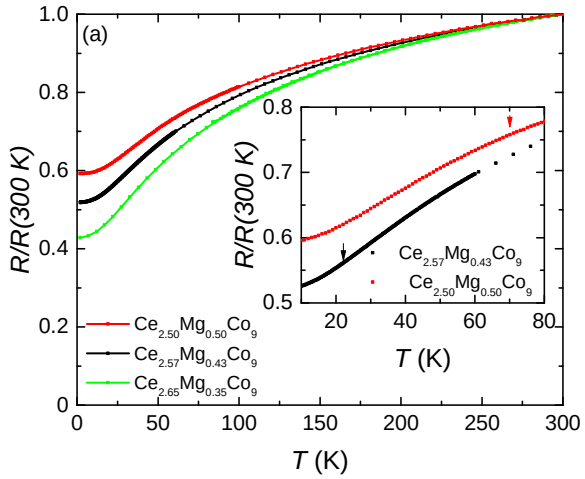

Figure 9.5 Normalised resistance ($\frac{R(T)}{R(300\ \mathrm{K})}$) data for $Ce_{3-x}Mg_xCo_9$ samples near the critical concentration: $x\sim0.35$, 0.43 and 0.50. No anomalies were observed in any of the measured resistances. The inset shows the enlarged high data density $R(T)$ measurements near Curie temperature inferred from Arrott plots indicated with corresponding arrows for $x = 0.43$ and $x = 0.50$ samples.

evidence that the doping induced magnetism is more itinerant for lower Mg content and becomes more local moment-like with higher content of Mg.

Figures 9.3 and 9.4 present the $T_C - x$ and $M_S - x$ phase diagrams for the $Ce_{3-x}Mg_xCo_9$ system. Both figures identify $0.35 < x < 0.40$ as the critical concentration region for the quantum phase transition from a Pauli paramagnet to ferromagnetic state.

To further analyze the nature of the phase diagram and the quantum phase transition region, electrical transport properties of the samples around the critical composition and specific heat capacity of the ferromagnetic, $x = 0.50$ sample, were studied. Figure 9.5 shows the normalized resistance of $Ce_{3-x}Mg_xCo_9$ single crystalline samples for $x = 0.35$, 0.43 and 0.50. Figure 9.6 shows the temperature dependent specific heat data for x= 0.50. Neither resistance nor specific heat data manifest clear signatures of ferromagnetic transitions. In the Stoner model, $\Delta C = \frac{M_0^2}{\chi_0 T_C}$ would give a discontinuity around 2 $\mathrm{Jmol^{-1}K^{-1}}$ at T_C for $x = 0.5$, but if spin fluctuation exist above T_C then discontinuity will be smaller [13]. For the resistance data the anticipated loss of spin disorder

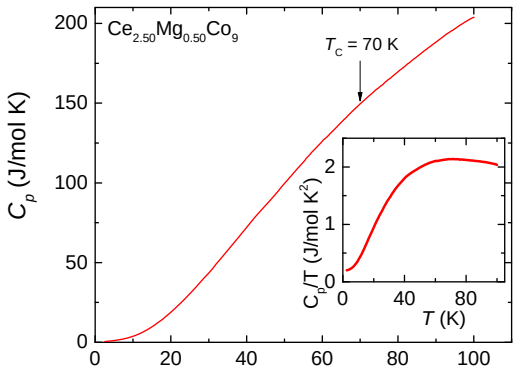

Figure 9.6 Constant pressure specific heat capacity of $Ce_{2.50}Mg_{0.50}Co_9$ sample. The inset shows the $\frac{C_p}{T}$ as a function of temperature. No clear signature of the ferromagnetic phase transition was observed in either C_p or $\frac{C_p}{T}$ around 70 K (pointed with downward arrow).

features may be obscured by the clearly large and increasing disorder scattering. Additionally, doping disorder could have broadened the ferromagnetic transition so that transition feature was undetectable in resistance and specific heat measurements. The lack of a clear feature in specific heat for $x = 0.50$ suggests that there may be relatively little entropy loss associated with the transition. This is consistent with the small spontaneous moment (Fig. 9.4) as well as with this system being a fragile, itinerant moment, ferromagnet.

9.5 Conclusions

The temperature dependent magnetic, electrical transport properties and specific heat capacity of the low Mg content doped $Ce_{3-x}Mg_xCo_9$ samples were studied using flux grown single crystalline samples. From the T_C-x phase diagram, the critical concentration for quantum transition between Pauli paramagnetic and ferromagnetic ground states is determined to be $0.35 \leq x \leq 0.40$.

9.6 Acknowledgements

Dr. Warren Straszheim is acknowledged for doing SEM on various samples. This research was supported by the Critical Materials Institute, an Energy Innovation Hub funded by the U.S. Department of Energy, Office of Energy Efficiency and Renewable Energy, Advanced Manufacturing Office. This work was performed at the Ames Laboratory, operated for DOE by Iowa State University under Contract No. DE-AC02-07CH11358.

9.7 References

[1] Paul C Canfield and Sergey L Bud'ko. Preserved entropy and fragile magnetism. *Reports on Progress in Physics*, 79(8):084506, jul 2016.

[2] Tej N. Lamichhane, Valentin Taufour, Andriy Palasyuk, Qisheng Lin, Sergey L. Bud'ko, and Paul C. Canfield. $Ce_{3-x}Mg_xCo_9$: Transformation of a Pauli Paramagnet into a Strong Permanent Magnet. *Phys. Rev. Applied*, 9:024023, Feb 2018.

[3] Tribhuwan Pandey and David S. Parker. Borderline Magnetism: How Adding Mg to Paramagnetic $CeCo_3$ Makes a 450-K Ferromagnet with Large Magnetic Anisotropy. *Phys. Rev. Applied*, 10:034038, Sep 2018.

[4] G. Z. Xing, Y. H. Lu, Y. F. Tian, J. B. Yi, C. C. Lim, Y. F. Li, G. P. Li, D. D. Wang, B. Yao, J. Ding, Y. P. Feng, and T. Wu. Defect-induced magnetism in undoped wide band gap oxides: Zinc vacancies in zno as an example. *AIP Advances*, 1(2):022152, 2011.

[5] Yusei Shimizu, Bernard Salce, Tristan Combier, Dai Aoki, and Jacques Flouquet. Uniaxial-stress-induced ferromagnetism in the itinerant metamagnetic compound ucoal probed by magnetostriction measurements. *Journal of the Physical Society of Japan*, 84(2):023704, 2015.

[6] Yu-Jun Zhao, S. Picozzi, A. Continenza, W. T. Geng, and A. J. Freeman. Possible impurity-induced ferromagnetism in $II-Ge-V_2$ chalcopyrite semiconductors. *Phys. Rev. B*, 65:094415, Feb 2002.

[7] Paul C. Canfield and Ian R. Fisher. High-temperature solution growth of intermetallic single crystals and quasicrystals. *Journal of Crystal Growth*, 225(24):155 – 161, 2001. Proceedings of the 12th American Conference on Crystal Growth and Epitaxy.

[8] Anthony Arrott and John E. Noakes. Approximate equation of state for nickel near its critical temperature. *Phys. Rev. Lett.*, 19:786–789, Oct 1967.

[9] Amikam Aharoni. Demagnetizing factors for rectangular ferromagnetic prisms. *J. Appl. Phys.*, 83(6):3432–3434, 1998.

[10] Tej N. Lamichhane, Valentin Taufour, Srinivasa Thimmaiah, David S. Parker, Sergey L. Bud'ko, and Paul C. Canfield. A study of the physical properties of single crystalline Fe_5B_2P. *J. Magn. Magn. Mater.*, 401:525 – 531, 2016.

[11] Tej N. Lamichhane, Valentin Taufour, Morgan W. Masters, David S. Parker, Udhara S. Kaluarachchi, Srinivasa Thimmaiah, Sergey L. Bud'ko, and Paul C. Canfield. Discovery of ferromagnetism with large magnetic anisotropy in ZrMnP and HfMnP. *Appl. Phys. Lett.*, 109(9):092402, 2016.

[12] K.H.J. Buschow. Magnetic properties of $CeCo_3$, Ce_2Co_7 and $CeNi_3$ and their ternary hydrides. *Journal of the Less Common Metals*, 72(2):257 – 263, 1980.

[13] P. Mohn and G. Hilscher. Influence of spin fluctuations on the specific heat and entropy of weakly itinerant ferromagnets. *Phys. Rev. B*, 40:9126–9134, Nov 1989.

CHAPTER 10. SINGLE CRYSTALLINE PERMANENT MAGNET: EXTRAORDINARY MAGNETIC BEHAVIOR IN THE SINGLE CRYSTAL Ta, Cu AND Fe SUBSTITUTED $CeCo_5$ SYSTEMS

A paper published in *Physical Review Applied*

Tej N. Lamichhane[1,2], Michael T. Onyszczak[2], Olena Palasyuk[1,3], Saba Sharikadze[2], Tae-Hoon Kim[1], Qisheng Lin[1], Matthew J. Kramer[1,3], R.W. McCallum[1], Aleksander L. Wysocki[1], Manh Cuong Nguyen[1], Vladimir P. Antropov[1], Tribhuwan Pandey[4], David Parker[4], Sergey L. Budko[1,2], Paul C. Canfield[1,2], and Andriy Palasyuk[1]

[1]The Ames Laboratory, U.S. Department of Energy, Iowa State University, Ames, Iowa 50011, USA

[2]Department of Physics and Astronomy, Iowa State University, Ames, Iowa 50011, USA

[3]Department of Material Science and Engineering, Iowa State University, Ames, Iowa 50011, USA

[4]Oak Ridge National Laboratory, Oak Ridge, Tennessee 37831, USA

10.1 Abstract

To reduce material and processing costs of commercial permanent magnets and to attempt to fill the empty niche of energy products, 10 – 20 MGOe, between low-flux (ferrites, alnico) and high-flux ($Nd_2Fe_{14}B$- and $SmCo_5$-type) magnets, we report synthesis, structure, magnetic properties and modeling of Ta, Cu and Fe substituted $CeCo_5$. Using a self-flux technique, we grew single crystals of **I** – $Ce_{15.1}Ta_{1.0}Co_{74.4}Cu_{9.5}$, **II** – $Ce_{16.3}Ta_{0.6}Co_{68.9}Cu_{14.2}$, **III** – $Ce_{15.7}Ta_{0.6}Co_{67.8}Cu_{15.9}$, **IV** – $Ce_{16.3}Ta_{0.3}Co_{61.7}Cu_{21.7}$ and **V** – $Ce_{14.3}Ta_{1.0}Co_{62.0}Fe_{12.3}Cu_{10.4}$. X-ray diffraction analysis (XRD) showed that these materials retain a $CaCu_5$ substructure and incorporate small amounts of Ta in the form of "dumb-bells", filling the $2e$ crystallographic sites within the 1D hexagonal

channel with the $1a$ Ce site, whereas Co, Cu and Fe are statistically distributed among the $2c$ and $3g$ crystallographic sites. Scanning electron microscopy, energy dispersive X-ray spectroscopy (SEM-EDS) and scanning transmission electron microscopy (STEM) examinations provided strong evidence of the single-phase nature of the as-grown crystals, even though they readily exhibited significant magnetic coercivities of ∼1.6 – ∼1.8 kOe caused by Co-enriched, nano-sized, structural defects and faults that can serve as pinning sites. Heat treatments at 1040 °C for 10 h and a hardening at 400 °C for 4 h lead to the formation of a so-called "composite crystal" with a bimodal microstructure that consists of a Ta-poor matrix and Ta-rich laminal precipitates. Formation of the "composite crystal" during the heat treatment creates a 3D array of extended defects within a primarily single grain single crystal, which greatly improves its magnetic characteristics. Possible causes of the formation of the "composite crystal" may be associated with Ta atoms leaving matrix interstices at lower temperatures and/or matrix degradation induced by decreased miscibility at lower temperatures. Fe strongly improves both the Curie temperature and magnetization of the system resulting in $(BH)_{max.}$ ≈13 MGOe at room temperature.

10.2 Introduction

To find new economical alternatives to commercial, high flux, permanent magnets, we focused on the Ta, Cu, and Fe substituted $CeCo_5$ system ($CaCu_5$-type structure) which, unlike typical commercial magnetic grades with critical rare earths (Nd, Sm, Dy, etc.) utilizes widely available and more affordable Ce [1, 2, 3]. The incorporation of Ce into magnets, instead of critical elements, may significantly reduce the price and supply-chain dependence of commercial magnets. Despite the mixed Ce^{3+}/Ce^{4+} valency problem, typically adverse for the magneto-crystalline anisotropy, there are recent experimental efforts on the $Nd_2Fe_{14}B$ (2:14:1) system showing that Ce-substitutes can compete with commercial high-flux grades at lower material costs [4, 5, 6, 7]. Similarly, efforts on the Ce-containing $SmCo_5$ (1:5) and Sm_2Co_{17} (2:17) systems showed that satisfactory cost-to-performance balances suitable for modern rare earth criticalities and market demands are expected [8, 9, 10, 11]. Therefore, we believe that Cu and Fe substituted $CeCo_5$ systems require

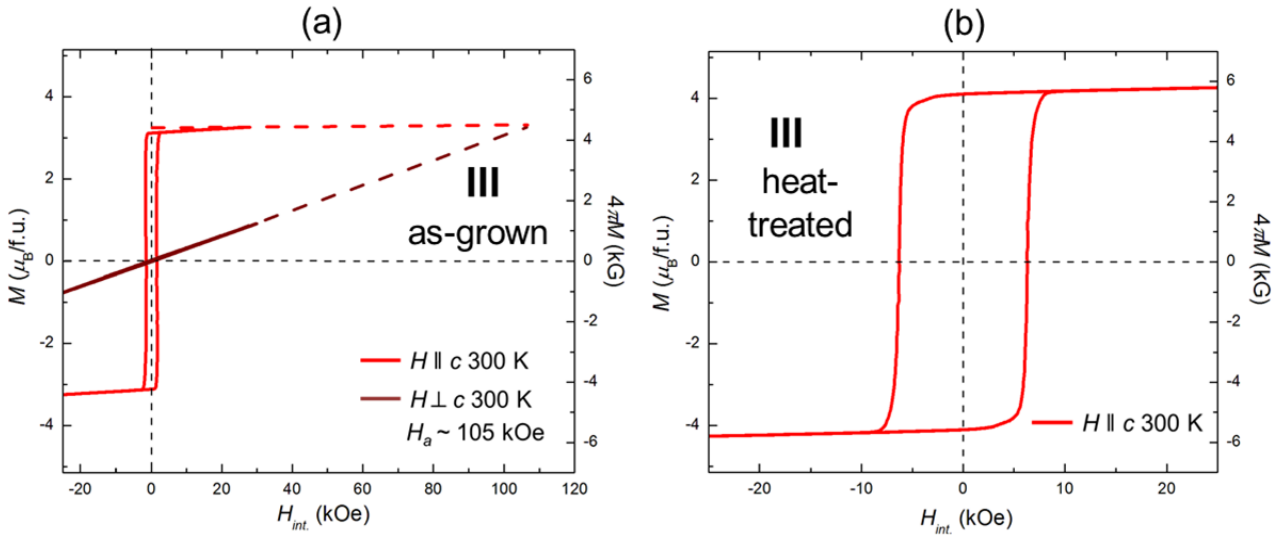

Figure 10.1 (a) – anisotropic field dependent magnetization of the as-grown $Ce_{15.7}Ta_{0.6}Co_{67.8}Cu_{15.9}$ (sample **III**) at 300 K for applied field along and perpendicular to the crystallographic axis. The inferred anisotropy field, H_a, is also shown. (b) – after heat treatment, the magnetic hysteresis loop of the same sample along the easy magnetization axis, i.e., the crystallographic c-axis.

a new and deeper examination [12, 13, 14]. After being understood and optimized these Ce-based systems may compete on both material-processing-cost and properties levels as so-called "gap magnets", performing in the gap of magnetic energies, between 10 – 20 MGOe, which currently exists between the rare-earth-free alnico and ferrite grades and the sintered 1:5 and 2:14:1 magnetic grades which contain critical rare earths [15].

Despite previous extensive explorations, the intrinsic properties of the $CeCo_5$ system has not been fully or systematically established [13, 14, 16, 17, 18, 19, 20, 21, 22, 23, 24, 25, 26, 27, 28, 29, 30, 31, 32, 33, 34, 35, 36] and the metallurgy related to the magnetic pinning/coercivity mechanism is not fully understood. Although anisotropy characterization is best obtained from single crystals,

single crystal growth reports in Cu or Fe substituted $CeCo_5$ systems are scarce and limited to several Bridgman type attempts [21, 22] in the vicinity of the composition $\sim CeCo_{3.5}Fe_{0.5}Cu$ [37].

In this paper we report the successful self-flux growth [38, 39] of five representatives of Ta, Cu and Fe substituted $CeCo_5$ followed by characterization of their structural and magnetic properties. We study the phenomenon of pronounced magnetic coercivity in the "as-grown" crystals and its further development during the heat treatment as illustrated in [Fig. 10.1]. Sub-grain phase segregation creates the necessary conditions for magnetic domain pinning. We also discuss the possible ways to improve, manipulate, and control the system in an attempt to increase its magnetic characteristics in conjunction with first principles DFT calculations and multiscale modeling.

10.3 Experimental

A. Synthesis.

Single crystals were grown via the solution growth method [38, 39]. The reaction metals (Ce (99.99%), Cu (99.95%) from Ames Laboratory MPC and Co (99.95%) from Alfa Aesar) were placed into 3-capped Ta containers [40] welded under an Ar atmosphere, which then were sealed into fused silica tubes and placed into a high-temperature box furnace. The furnace was heated from near room temperature to 900 °C over 3 hours, held at 900 °C for 3 hours, heated to 1200 °C over 3 more hours, and held at 1200 °C for 10 hours. The furnace was then cooled to 1070 °C over 75 hours. At 1070 °C the excess flux was decanted by centrifuging [38, 39]. Decanting took place as the centrifuge accelerated from rest toward a 8.5 krpm set point. The exact temperature profile of the growths and pictures of the typical crystals are presented in Fig. 10.2.

B. Heat Treatment.

After growth, some single crystals underwent identical, two-stage, heat treatments performed in a Dentsply Ceramico (Vulcan 3-Series) multi-stage programmable furnace, which included dwelling at 1040 °C for 10 h, then cooling at a rate of 10 °C/min to 400 °C followed by dwelling at this temperature for the next 8 h with a subsequent furnace cool to room temperature. We based

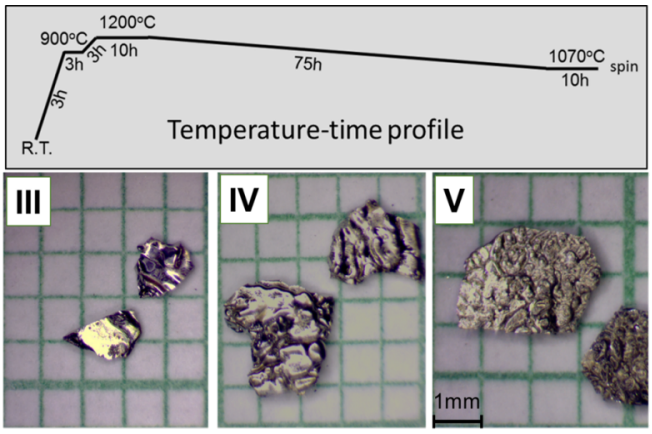

Figure 10.2 Temperature-time profile used for single crystal growths and general look of self-flux grown plate-like crystals of **III** – $Ce_{15.7}Ta_{0.6}Co_{67.8}Cu_{15.9}$, **IV** – $Ce_{16.3}Ta_{0.3}Co_{61.7}Cu_{21.7}$ and **V** – $Ce_{14.3}Ta_{1.0}Co_{62.0}Fe_{12.3}Cu_{10.4}$ (for details see Table I).

this schedule on literature reports [19, 21, 26, 27, 28, 29, 30]. Different Cu contents may require slightly different temperature/time parameters for the best final magnetic characteristics, but the optimization of the heat treatment procedure is a subject of ongoing work.

C. Metallography and SEM/EDS Analysis.

Samples for metallographic examination were placed in ∼1 inch diameter epoxy resin pucks, and polished with various grits of silicon carbide followed by a glycol-based, fine, polycrystalline, diamond suspension. Plate-like single crystals [Fig. 10.2] were mounted with their plates parallel to the polishing surface to allow for characterization along planes perpendicular to the crystals [001] direction. Imaging studies of single crystal samples were performed on an FEI Teneo field emission scanning electron microscope. Their compositions were determined via energy dispersive X-ray spectra obtained using an Oxford EDS/EBSD module averaging over 3-5 regions on their metallographicaly prepared surfaces [see Table 10.1].

Table 10.1 Composition of single crystals (with standard deviation) and their lattice parameters as-grown and after the heat treatment. The lattice parameters and corresponding errors are derived from the Rietveld fits.

3*#	EDS-composition, at. %										Lattice parameters	
	Ce		Ta***		Co		Fe		Cu		*a*, *c*, Å; *V*, Å^3 ****	
	ag*	ht**	ag	ht	ag	ht	ag	ht	ag	ht	ag	ht
I	15.1(1)	16.1(1)	1.0	0.6	74.4(2)	73.6(2)	-	-	9.5(1)	9.8(1)	4.912(1) 4.045(1) 84.52(1)	4.921(1) 4.031(1) 84.58(2)
II	16.3(1)	16.2(1)	0.6	0.4	68.9(2)	69.4(2)	-	-	14.2(1)	14.0(1)	4.933(1) 4.031(1) 84.95(2)	4.933(1) 4.028(1) 84.90(2)
III	15.7(1)	15.8(1)	0.6	0.1	67.8(2)	67.1(2)	-	-	15.9(1)	17.1(1)	4.943(1) 4.032(1) 85.31(1)	4.944(1) 4.028(1) 85.26(1)
IV	16.3(1)	16.5(1)	0.3	0.05	61.7(2)	61.9(2)	-	-	21.7(1)	21.6(1)	4.950(1) 4.033(1) 85.57(2)	4.954(1) 4.028(1) 85.61(2)
V	14.3(1)	13.9(1)	1.0	0.2	62.0(2)	62.7(2)	12.3(1)	13.0(1)	10.4(1)	10.2(1)	4.922(1) 4.075(1) 85.50(2)	4.924(1) 4.071(1) 85.48(2)

* - as grown, ** - heat-treated: 1040 °C (10h) → [10 °C/min] → 400 °C (8h), *** - stardard deviations for Ta vary within 0.02 - 0.05 at. %; **** - space group: $P6/mmm$.

D. TEM Characterization.

Cross sections from single crystal **III** were prepared using a dual-beam focused ion beam system (FEI Helios NanoLab G3 UC) with a lift-out approach. To reduce surface damage sustained during Ga ion milling, the final thinning and cleaning step were conducted using 5 kV and 2 kV for 5 min. The TEM analysis was performed on a Titan Themis (FEI) probe Cs-corrected TEM equipped with a Super-X EDS detector to characterize microstructure and elemental distribution.

E. Powder and single crystal X-ray diffraction

Polycrystalline powders were obtained by crushing the sample with an agate mortar and pestle. X-ray powder diffraction data were collected from the as-grown and heat-treated crystals. The measurements were performed using PANalytical X-Pert Pro (Co K_α - radiation, $\lambda = 1.78897$ Å) and Bruker D8 Advance (Cu K_α - radiation, $\lambda = 1.54056$ Å) diffraction systems. Powdered samples were evenly dispersed on a zero-background Si-holder with the aid of a small quantity of vacuum

grease. Diffraction scans were taken in the $\theta/2\theta$ mode with the following parameters: 2θ region: 20 – 110°, step scan: 0.02°, counting time per step: 60 s. The FullProf Suite program package [41] was used for Rietveld refinement of the crystal structures.

Single-crystal diffraction data were collected at room temperature using a Bruker SMART APEX II diffractometer (Mo K_α - radiation) equipped with a CCD area detector. Four sets of 360 frames with 0.5° scans in ω and exposure times of 10 – 15 s per frame were collected. The reflection intensities were integrated using the SAINT subprogram in the SMART software package [42]. The space group was determined using the XPREP program and the SHELXTL 6.1 software package [43]. Empirical absorption corrections were made using the SADABS program [44]. Finally, each structure was solved by direct methods using SHELXTL 6.1 and refined by full-matrix least-squares on ${F_0}^2$, with anisotropic thermal parameters and a secondary extinction parameter. The error bars for lattice parameters determination by both powder and single crystal XRD methods come from the fits of corresponding data. However, it is anticipated that the instrumental error may be of order 0.005 Å.

F. Magnetic Properties Measurements.

Magnetic properties were obtained using a vibrating sample magnetometer in a cryogen-free VersaLab physical property measurement system (Quantum Design) with magnetic fields up to 3 T and temperatures in the 50 – 350 K range using the standard option and 300 – 1000 K range using the oven option. An alumina cement (Zircar) was used to hold the sample on the heater stick for the high-temperature measurements. The demagnetization factors are determined experimentally using the relation $H_{int.} = H - NM$ [45, 46].

10.4 Structure and Composition Analysis

The $Ce(Co_{1-x-y}Fe_xCu_y)_5$ system favors slightly Ce deficiency [21, 22, 23, 24] and the appearance of transition metal, T, "dumb-bells" may lead to structural transformations towards the 1:7 and 2:17 phases. Therefore, we use ∼1:5 designations for the general description of our reported systems.

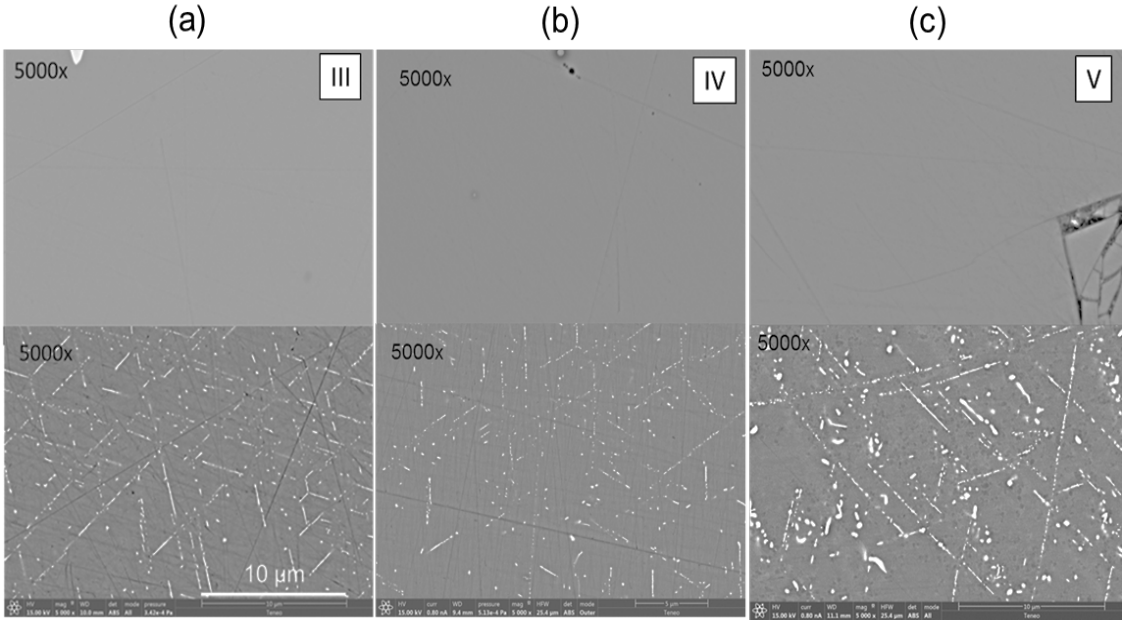

Figure 10.3 SEM backscattered electron images of samples (a) - **III** – $Ce_{15.7}Ta_{0.6}Co_{67.8}Cu_{15.9}$, (b) - **IV** – $Ce_{16.3}Ta_{0.3}Co_{61.7}Cu_{21.7}$ and (c) - **V** – $Ce_{14.3}Ta_{1.0}Co_{62.0}Fe_{12.3}Cu_{10.4}$ before (upper panels) and after (lower panels) heat treatment. All images were taken at a magnification 5000x and 15 kV.

A. SEM/EDS Examinations and Composition Analysis.

The SEM backscattered electron images of the as-grown crystals [Fig. 10.3 (a-c), upper panels] display the uniformity of their ∼(0001) polished surface (even at 30,000× magnification) which suggests a single-phase. Although, the Fig. 10.6 (below) (TEM) does show small ingomogeneities. Elemental EDS analysis [Table 10.1] showed the Ce:Co/Cu ratios are close to the 1:5 stoichiometry with Cu contents increasing from ∼10 to ∼ 22 at. %, corresponding to 12 – 26 % of Co/Cu substitution.

With respect to Ce content, crystal **I** and **III** contain 15 – 15.7 at. %, which is lower than the Ce content in **II** and **IV** and significantly lower than ∼16.7 at. % Ce content required for the exact 1:5 type stoichiometry. Also a minor presence of Ta (0.3 – 1 at.%) was detected in all five samples. The

Ta content appears to be correlated to the Cu content as seen in [Table 10.1]. The presence of Ta is explained by the slight dissolution of the inner walls of the Ta reaction container and diffusion of Ta atoms into the liquid at high temperatures. Since no Ta precipitation or segregation was observed in the SEM/EDS analysis of the as-grown crystals, we believe Ta is either being incorporated into the crystal structure as interstices or as uniformly distributed nano-scale precipitates. However the slight Ce depletion and the presence of Ta suggest the possibility of minor deviations from the classic $CaCu_5$-type crystal structure towards various channel disorders or "dumb-bell" problems characterized elsewhere [47, 48, 49]. These deviations were accounted for in our structural models and refinements [Figs. 10.4, 10.5].

The SEM back scattered electron images taken from the (0001) surface of the heat treated crystals, [Fig. 10.3 (a-c) lower panels], show degradation of the single phase crystal into a bimodal microstructure consisting of a darker matrix and lighter laminas. These laminas follow the hexagonal symmetry of the original crystal crossing each other at 60° or 120° angles. The thickness of the laminar features is ∼0.05 – 0.1 μm, and their lengths vary in the range ∼ 1 – 10 μm. Distances between two laminas are ∼2 – 3 μm. The elemental EDS analysis of the heat treated material [Table 10.1] indicates the segregation of Ta-rich phases into the laminar features, whereas the matrix material becomes practically Ta-free in the Cu-richest crystal **IV**.

B. X-Ray Analysis and Crystal Structure Determination.

Powder and single crystal X-ray analyses were performed to determine the structure of crystals **I** – **V**. Rietveld fitting of the powder X-ray pattern taken from the as-grown, crushed and thoroughly powdered, single crystals of **I** – **V** showed that all Bragg reflections were well indexed within the $CaCu_5$-type structure (*hP6*, $P6/mmm$), providing a strong argument for the single-phase nature of the as-grown crystals in agreement with our SEM observations [Fig. 10.3]. To address the EDS-observed Ta presence and Ce deficiency, especially in the as-grown crystals **I**, **III**, and **V** [see Table 10.1], we considered known structural derivatives of $CaCu_5$ [47]. These derivatives are typically observed in binary and ternary rare-earth – transition metal systems near the ∼1:5 and ∼2:17 stoichiometries and result from the replacement of rare-earth atoms by pairs of transition metal

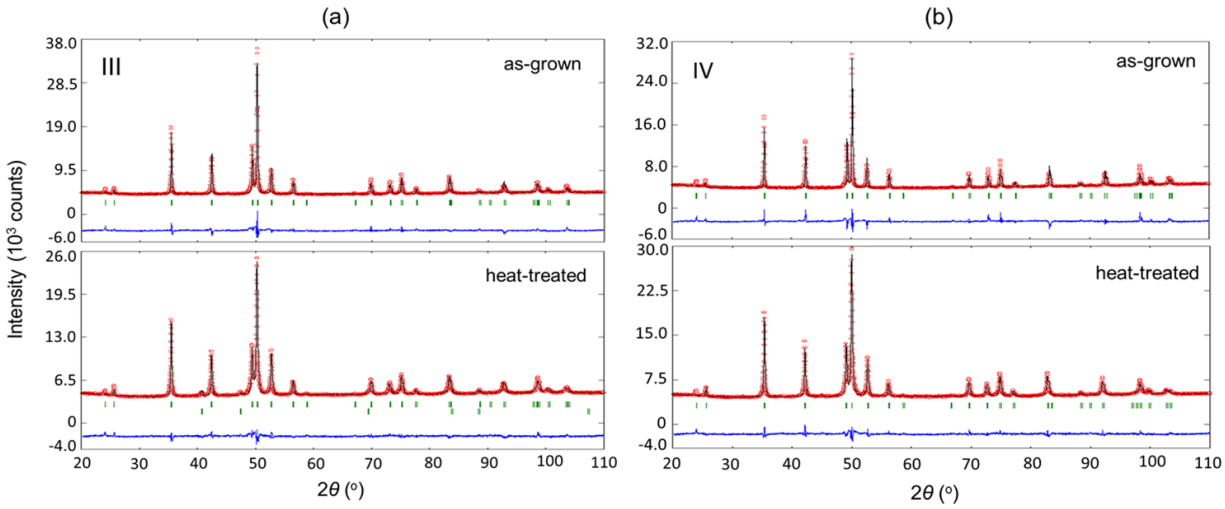

Figure 10.4 Powder X-ray patterns and Rietveld refinement results for (a) - **III** – $Ce_{15.7}Ta_{0.6}Co_{67.8}Cu_{15.9}$, (b) - **IV** – $Ce_{16.3}Ta_{0.3}Co_{61.7}Cu_{21.7}$ before (upper) and after (lower) heat treatment. The observed profile is indicated by circles and the calculated profile by the solid line. Bragg peak positions are indicated by vertical ticks, and the difference is shown at the bottom.

atoms. The $CaCu_5$ substructure can be retained if the replacement is fully random, as in $TbCu_7$ [50], but may be transformed into various superstructures, such as Th_2Zn_{17} [51], Th_2Ni_{17} [52], etc., if the substitution is ordered. A third possibility comes as combination of ordered and disordered rare-earth – "dumb-bell" substitutions which are contained in a superstructure, e.g., $LuFe_{9.5}$ [53] and $PrFe_7$ [54]. We tried Rietveld refinements with structural models allowing the presence of Ta but the clear indexing of Bragg reflections within the parent, $CaCu_5$-type, 1:5 structure [Fig. 10.4] indicates a minor and random distribution of Ta.

We allowed Ce/Ta or T/Ta (T = Co, Cu, Fe) statistical mixings on the $1a$, $2c$, and $3g$ sites with and without an under-occupancy of Ce on the $1a$ site. The substitution of Ce atoms by T – T "dumb-bells" was introduced into the model as an independent crystallographic $2e$ site (0 0 z) with $z = \sim 0.3$. The last model represents a small departure from the $CaCu_5$ structure towards the

Table 10.2 Single crystal and refinement data for **III** – $Ce_{15.7}Ta_{0.6}Co_{67.8}Cu_{15.9}$, **IV** – $Ce_{16.3}Ta_{0.3}Co_{61.7}Cu_{21.7}$ and **V** – $Ce_{14.3}Ta_{1.0}Co_{62.0}Fe_{12.3}Cu_{10.4}$. The errors for the lattice parameters are derived form the crystal structure solution.

crystal	**III**	**IV**	**V**
EDS composition	$Ce_{0.94}Ta_{0.04}Co_{4.06}Cu_{0.94}$	$Ce_{0.99}Ta_{0.00}Co_{3.70}Cu_{1.30}$	$Ce_{0.86}Ta_{0.06}Co_{3.72}Fe_{0.73}Cu_{0.62}$
refined composition	$Ce_{0.98}Ta_{0.04}Co_{4.25}Cu_{0.75}$	$Ce_{0.99}Ta_{0.02}Co_{3.79}Cu_{1.21}$	$Ce_{0.94}Ta_{0.12}Co_{3.68}Fe_{0.72}Cu_{0.60}$
formula mass	442.68	442.57	449.52
Space group, Z	$P6/mmm$; 1	$P6/mmm$; 1	$P6/mmm$; 1
a (Å)	4.946(1)	4.952(1)	4.928(1)
c (Å)	4.038(1)	4.035(1)	4.073(1)
V (Å^3)	85.57(4)	85.70(5)	85.66(2)
d_c (Mg/ m^3)	8.52	8.57	8.69
μ (mm^{-1}; MoK_α) abs. coef.	37.85	37.08	39.78
reflns. collected/ R_{int}	1631/0.025	2002/0.042	1808/0.027
ind. data /restrains/ params.	79/0/12	109/0/13	91/0/11
GoF (F^2)	1.221	1.129	1.172
$R1$/ $wR2$ [I $>2\sigma$(I)]	0.018/ 0.041	0.021/ 0.048	0.030/ 0.063
$R1$ /$wR2$ [all data]	0.021/ 0.041	0.025/ 0.046	0.031/ 0.063
Largest diff peak /hole (e/Å^3)	0.80/ -0.74	1.04/ -0.99	1.91/ -1.53

closely related $TbCu_7$ structure with slight Ce/"dumb-bell" substitution within the hexagonal 1D channel [see Fig. 10.5]. The Ce/Ta and T/Ta mixings did not produce satisfactory fits, significantly increasing the residuals and showing unreasonable isotropic temperature parameters, whereas the "dumb-bell" refinements were insensitive to small amounts of T – T (T = Ta, Co, Cu and/or Fe) pairs and were comparable to those without any Ta, and were proportional to the EDS- determined Co/Cu mixings on the $2c$ and $3g$ sites, suggesting minimal disorder. Although present powder X-ray refinements did not clearly address Ta occupation, they clearly determined lattice parameters as well as demonstrated phase content and purity of the material before and after the heat treatment. Data are presented in [Fig. 10.4 (a, b). upper panels] for the crushed, as-grown, crystals of **III** and **IV**. Phase analysis of powder X-ray patterns taken from crushed heat treated crystals of **III** [Fig. 10.4 (a, b) lower panels] revealed clear presence of Ta-like impurities (Fm-$3m$, $a = 4.446(1)$ Å) confirming the EDS findings [Fig. 10.3], whereas in **IV** Ta was not detected in the X-ray pattern.

Single crystal X-ray diffraction of the as-grown crystals showed poor quality of the crystals suggesting crystal intergrowth, twining, residual stress or stacking fault effects. These defects

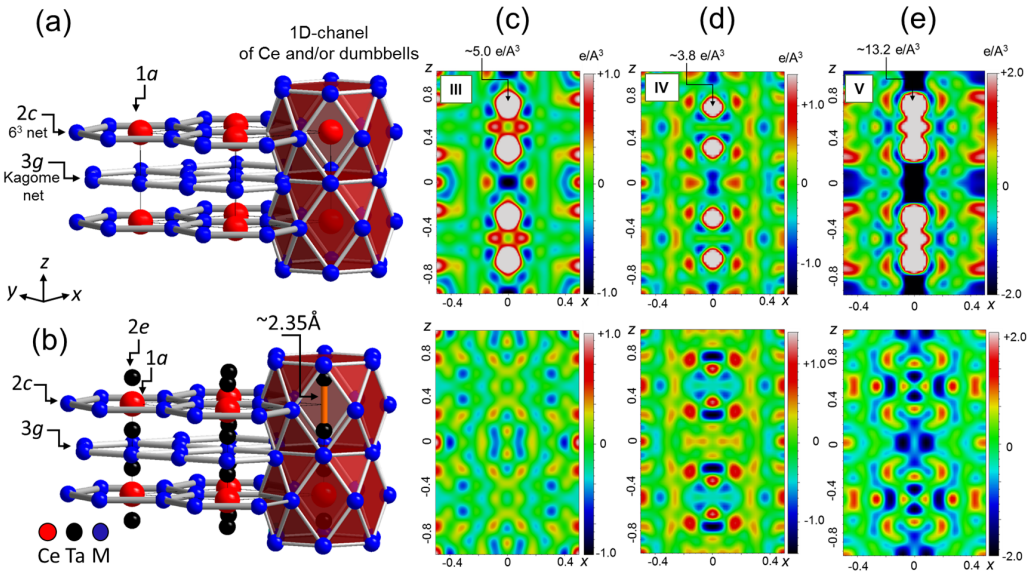

Figure 10.5 Single crystal refinement for **III** – $Ce_{15.7}Ta_{0.6}Co_{67.8}Cu_{15.9}$, **IV** – $Ce_{16.3}Ta_{0.3}Co_{61.7}Cu_{21.7}$ and **V** – $Ce_{14.3}Ta_{1.0}Co_{62.0}Fe_{12.3}Cu_{10.4}$: [110] views of (a) – $CaCu_5$-type and (b) – $TbCu_7$-type structures with and without Ta "dumb-bells", respectively and (c) - (e) – difference electron density maps of structure solutions without "dumb-bells" (upper row) showing significant residual electron density peaks of ∼3.5 – ∼13.5 e/A^3 in 1D structural channels at (0 0 z) with z ≈0.3, and with "dumb-bells" (lower row) with significantly smaller residuals.

were very apparent on Laue frames from numerous (>10) specimens of **I** in form of strong streaking, doubling of the reflections, and sometimes presence of the Debye rings. However, these effects diminished in **II** and were practically absent in **III** and **IV** allowing structural characterization of the as-grown crystals of **III** – **V** [see Table 10.2]. Single crystal structure solutions of **III** – **V** confirmed their $CaCu_5$ substructure [see Table 10.2, 10.3]. However, disorder was detected within the 1D hexagonal channels, as seen in the residual electron density peaks of ∼5.0, ∼3.8 and ∼13.2 e/Å^3 at (0 0 z), z ≈0.295 for **III**, **IV** and **V**, respectively. Only by filling the 2e site with the heaviest and largest available pair, Ta – Ta, we were able to reach satisfactory refinement. The $R1/wR2$ residuals dropped by 50 – 70 % in comparison to the solutions without Ta and showed

Table 10.3 Atomic coordinates, Equivalent Isotropic Displacement Parameters (Å$\times$ 10^3), and Site Occupancy Factors Refined for **III** – $Ce_{15.7}Ta_{0.6}Co_{67.8}Cu_{15.9}$, **IV** – $Ce_{16.3}Ta_{0.3}Co_{61.7}Cu_{21.7}$ and **V** – $Ce_{14.3}Ta_{1.0}Co_{62.0}Fe_{12.3}Cu_{10.4}$.

atom	WP	x	y	z	$U_{eq.}$	SOF	#
Ce	1a	0	0	0	15(1)	0.977(2)	**III**
					16(1)	0.988(1)	**IV**
					19(1)	0.936(3)	**V**
Ta	2e	0	0	0.280(6)	15(1)	0.023(2)	**III**
				0.296(9)	16(1)	0.012(1)	**IV**
				0.292(4)	19(1)	0.064(3)	**V**
M1[a]	2c	2/3	1/3	0	14(1)	1.00 Co	**III**
					15(1)	0.23(7) Cu	**IV**
					23(1)	1.00 Co	**V**
M2	3g	1/2	0	1/2	10(1)	0.25(6) Cu	**III**
					10(1)	0.25(5) Cu	**IV**
					10(1)	0.24 Fe/ 0.20 Cu	**V**

[a]The atomic symbol "M" stands for Co/Cu or Co/Fe/Cu mixed occupancy; 3g occupancy for sample **V** have been fixed.

minimal fluctuations of the rest electron density in the final fits. Fig. 10.5 shows the differential Fourier maps for **III** – **V** with and without the "dumb-bell" disorder. One significant deficiency of the solutions is the interatomic T – T distances of ~2.35 Å, which is typical for Co – Co, Co – Cu and Co – Fe pairs but is extremely short for Ta – Ta.

However, the "dumb-bell" configuration with large and heavy atoms similar to Ta is not unprecedented and was reported for similar structure of $CeFe_{10}Zr_{0.8}$($d_{(Zr\text{ - }Zr)} \approx 2.65$ Å) [55]. However, the stoichiometry of **V** shows significant deviation from the ideal 1:5 stoichiometry. The content of 1D channels (Ce plus the Ta – Ta pairs) does not reach the expected 16.7 at.%, meaning that some of T atoms must participate in the channel disorder.

C. Transmission Electron Microscopy.

Fig. 10.6 (a) is a high-angle-annular-dark-field (HAADF) scanning transmission electron microscope (STEM) image of an as-grown sample **III** showing the overall microstructure. The entire region consists a single crystalline phase. Fig. 10.6 (b) is an enlarged HAADF image which shows a dark-contrast line. It was the only feature that can be found in the entire scan area. Fig. 10.6 (c)

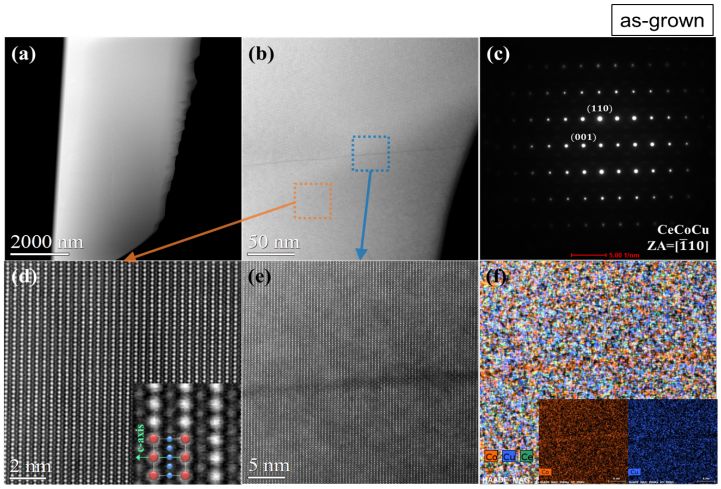

Figure 10.6 (a) - HAADF STEM image of as-grown **III** – $Ce_{15.7}Ta_{0.6}Co_{67.8}Cu_{15.9}$ showing the overall microstructure, (b) - enlarged HAADF image shows a dark-contrast line, (c) - diffraction pattern taken from the region shown in (b) including the matrix and the dark line, (d) - high resolution STEM image taken from orange-boxed area in (b) under [1-10] zone axis. The inset at bottom right is an enlarged atomic image with atomic model of hexagonal 1:5 Ce/Co/Cu phase. The bright dots and dark dots in the images correspond to atomic columns of Ce and (Co, Cu) elements, respectively, (e) - enlarged image of blue-boxed area in (b) and dark line in single crystalline phase is shown clearly, (f) - EDS elemental mapping of (e) clearly showing Co enrichment in the line, the small Co and Cu elemental maps-insets are presented for contrasting observation of Cu depletion in the same line.

is a diffraction pattern taken from the region shown in Fig. 10.6 (b) including the matrix and the dark line. It clearly shows the single crystalline 1:5 phase. It seems that the dark line region has the same crystal structure and it is not a precipitate which would have made additional diffracted spots in Fig. 10.6 (c). Fig. 10.6 (d) is a high resolution STEM image taken from orange-boxed area in Fig. 10.6 (b) under [1-10] zone axis. The inset at bottom right is an enlarged atomic image with an atomic model of hexagonal 1:5 phase. The bright dots and dark dots in the images correspond to atomic columns of Ce and Co/Cu elements, respectively. Fig. 10.6 (e) is an enlarged image of blue-boxed area in Fig. 10.6 (b) and dark line in single crystalline phase is shown clearly. Fig. 10.6

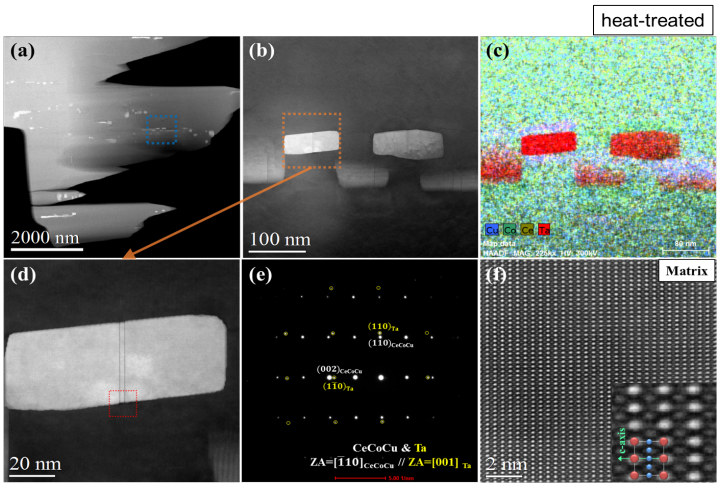

Figure 10.7 (a) - HAADF image of heat treated **III** – $Ce_{15.7}Ta_{0.6}Co_{67.8}Cu_{15.9}$ showing the overall microstructure, (b) - enlarged image of blue-boxed area in (a), (c) - EDS elemental mapping corresponding to (b). The bright regions are Ta-rich and considered as Ta precipitate, (d) - enlarged image of orange-boxed area in (b), (e) - diffraction pattern taken from (d) including the matrix and the Ta precipitate, (f) - high resolution STEM image taken from the matrix in (d) under [1-10] zone axis.

(f) is an EDS elemental mapping of Fig. 10.6 (e). The chemical contrast between the matrix and the dark line is observed. The EDS result shows the dark line is Co-rich and Cu-deficient.

Fig. 10.7 (a) is a HAADF image of an annealed sample showing the overall microstructure. Many bright areas were observed unlike the unannealed sample shown in before in Fig. 10.6. Fig. 10.7 (b) is an enlarged image of the blue-boxed area in Fig. 10.7 (a) and Fig. 10.7 (c) is the EDS elemental mapping corresponding to Fig. 10.7 (b). The bright regions in Fig. 10.7 (b) are Ta-rich and considered as Ta precipitates. Additionally, a few dark lines are observed in the Ta precipitate. The difference in brightness of precipitates is attributed to the difference in the thickness of each precipitate. Fig. 10.7 (d) is an enlarged image of the orange-boxed area in Fig. 10.7 (b) and Fig. 10.7 (e) is a diffraction pattern taken from Fig. 10.7 (d) including the matrix and the Ta precipitates. Fig. 10.7 (d) shows Ta precipitates coherently embedded by epitaxial precipitation and the corresponding diffraction pattern shows the epitaxial relationship between the matrix and

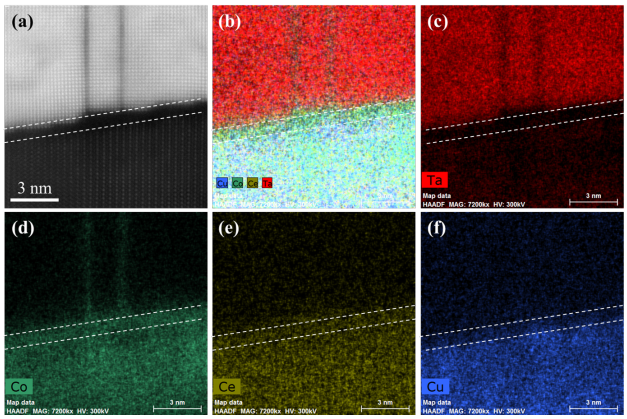

Figure 10.8 (a) - high resolution HAADF image of the interface between the matrix and the Ta precipitate taken from red-boxed area in Fig. 10.7 (d) and (b - f) - corresponding EDS elemental mapping results. The white lines indicate the same position in each image.

Ta precipitate. The orientation relation was observed as follows: (110) CeCoCu // (110) Ta; (002) CeCoCu // (1-10) Ta; and [1-10] CeCoCu // [001] Ta. Fig. 10.7 (f) is a high resolution STEM image taken from the matrix in Fig. 10.7 (d) under [1-10] zone axis. It is the same as that seen in Fig. 10.6 (d). The inset at bottom right is an enlarged atomic image with an atomic model of hexagonal 1:5 Ce/Co/Cu phase. The bright dots and dark dots in the images correspond to atomic columns of Ce and Co/Cu elements, respectively. Fig. 10.8 shows high resolution HAADF images of the interface between the matrix and the Ta precipitate taken from red-boxed area in Fig. 10.7 (d) and corresponding EDS elemental mapping results [Fig. 10.7 (b-f)]. The white dashed lines indicate the same position in each image. Although Cu-rich and Co-deficient region was observed near the precipitate [Fig. 10.7 (c)], there was also Co, Ce-rich and Cu-deficient interface between the matrix and Ta precipitate. The dark lines in the Ta precipitate turned out to be Co-rich. Considering EDS maps at the interface and near the precipitate, it is assumed that Co was infiltrated into the precipitate [Fig. 10.7 (d)], and Co became deficient near the precipitate with relative Cu-rich as a result. As will be discussed below the high resolution TEM results will be returned to, for both

as-grown and heat-treated samples of crystal **III**, to elucidate the pinning mechanism that leads to significant coercivities in the crystals.

10.5 Magnetic Properties

A. As-grown crystals. Curie temperature, magnetocrystalline anisotropy field and energy density.

Fig. 10.9 presents the Curie temperatures for samples **I** – **V** as inferred from the peak in dM/dT shown in the inset. The Curie temperatures T_c estimated by the minimum in the derivative correspond closely to the T_c derived via the more accurate Arrot plot method (see below). The T_c-value decreases rapidly with increasing Cu content for Fe-free samples **I** – **IV**. This is consistent with the early report [36] and indicates weakening in the ferromagnetic exchange interactions within the Co sublattice due to the introduction of nonmagnetic Cu. In contrast, the Fe-doped crystal **V** shows remarkable improvement of T_c, increasing by over 150 K to ~820 K, a value that is significantly higher than the $T_c = 653$ K of the parent $CeCo_5$ [56]. Using band structure analysis, we find that Fe-doping of $CeCo_5$ and $Ce(Co,Cu)_5$ increases the ordering energy $\Delta E = E_{NM} - E_{FM}$ (NM – non-magnetic and FM – ferromagnetic states), as well as the total magnetic moment of the systems (see Section **V** below). This leads to the remarkable increase of the Curie temperature and saturation magnetization.

To more formally determine T_c, we prepared an Arrot plot analysis for **III** using isotherms between 460 K to 500 K [Fig. 10.10]. The Curie temperature for **III** is estimated to be $\sim$ 480 K, since the isotherm at that temperature is closest to a straight line and passes through the origin.

In Fig. 10.5 we show representative $M(H)$ isotherms for sample **V**. In the inset we plot the spontaneous magnetization value for each temperature inferred from the extrapolation of the linear region of the $M(H)$ back to $H = 0$. As can be seen, these data suggest a $T_c \sim 820$ K (estimated by generalized Bloch law fitting of spontaneous magnetization), in good agreement with Fig. 10.9

Fig. 10.12 (a) shows the magnetocrystalline anisotropy field, H_a, at room temperature for all as-grown crystals **I** – **V**; the low temperature estimations of H_a were done for crystals **III**

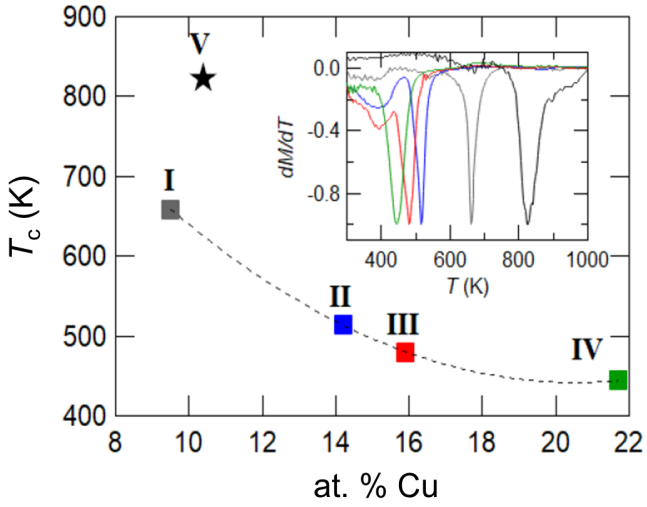

Figure 10.9 Curie temperatures for the as-grown **I** – $Ce_{15.1}Ta_{1.0}Co_{74.4}Cu_{9.5}$, **II** – $Ce_{16.3}Ta_{0.6}Co_{68.9}Cu_{14.2}$, **III** – $Ce_{15.7}Ta_{0.6}Co_{67.8}Cu_{15.9}$, **IV** – $Ce_{16.3}Ta_{0.3}Co_{61.7}Cu_{21.7}$ and **V** – $Ce_{14.3}Ta_{1.0}Co_{62.0}Fe_{12.3}Cu_{10.4}$ inferred from the peaks in derivative of magnetization with respect to temperature, i.e. dM/dT obtained for each crystal (see inset). Magnetization data were obtained under magnetic field of 0.01 T.

and **V** and are presented in Fig. 10.12b. The anisotropy field was estimated by the high-field, linear extrapolation of the field-dependent moment along the easy [001] and hard ($H \perp$ [001]) axes [22, 46]. The room temperature H_a for the Fe-free, as-grown crystals **I** – **IV** exhibit a maximum anisotropy field of ∼118 kOe in crystal **II**. The addition of Fe shows a detrimental influence on the magnetocrystalline anisotropy, (in Fe-doped **V** the anisotropy field drops to ∼65 kOe [see inset in Fig. 10.12a], but the spontaneous magnetization increases by ∼30 % compared to crystals with similar Cu contents). Low temperature measurements estimate the spontaneous magnetization for crystals **III** and **V** to be ∼3.7 and ∼6.8 μ_B/f.u., respectively.

The temperature dependent magnetocrystalline anisotropy energy density was measured using the Sucksmith-Thompson method [57, 58, 46] by using the hard axis magnetization isotherms for crystals **III** and **V** [Fig. 10.13]. In this method, the Y-intercept (I) of $\frac{H_{int}}{M_\perp}$ vs ${M_\perp}^2$ curve is

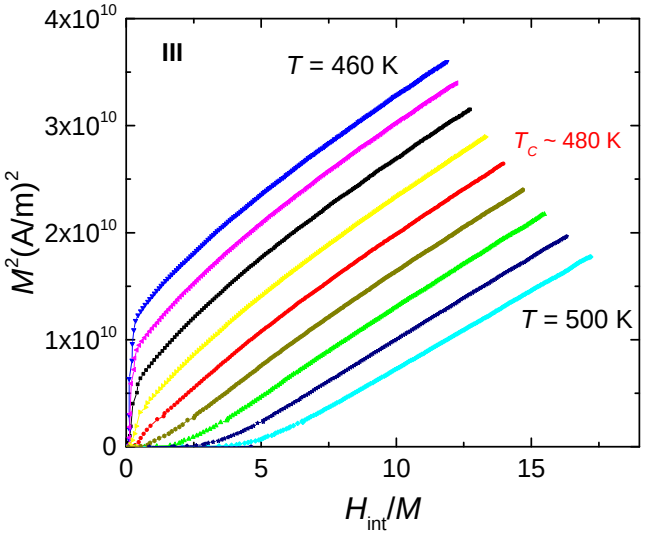

Figure 10.10 Arrott plot for **III** - $Ce_{15.7}Ta_{0.6}Co_{67.8}Cu_{15.9}$ with isotherms taken in 5.0 K intervals as indicated in the graph. The Curie temperature is $\sim$ 480 K as inferred from the plot since the isotherm is closest to linear and passes through origin.

used to determine K_1 as $I = \frac{2*K_1}{{M_S}^2}$ where $M_\perp$ is hard axis magnetization and M_S is the saturation magnetization. The corresponding uncertainty in measurement was determined using the following formula $\Delta K_1 = K_1 * [\frac{\Delta I}{I} + 2 * \frac{\Delta M_S}{M_S}]$ [59]. Here the uncertainty ΔI was determined from the uncertainty of the linear fit. ΔM_S was determined by the difference between maximum possible upper bound of the saturation magnetization (obtained as the Y-intercept intercept of M vs $\frac{1}{H}$) and lower bound (obtained as the linear fit of *M(H)* data as shown in 50 K magnetization data in Fig 11) for each temperature.

Interestingly, the as-grown single crystals showed magnetic hysteresis when measured along the easy axis of magnetization [001]. For example, crystal **III** exhibited a hysteresis (see Fig. 10.1) which reached $H_c \approx 1.6$ kOe and $B_r \approx 4.2$ kG, $M_s \approx 4.2$ kG and $(BH)_{max.} \approx 3.5$ MGOe [Fig. 10.14], which is comparable to most of anisotropic sintered alnico grades [60]. This is remarkable considering the common belief that the appearance of the coercivity is a result of the extrinsic properties, e.g., development of proper microstructure for strong magnetic domain pinning, and this is generally

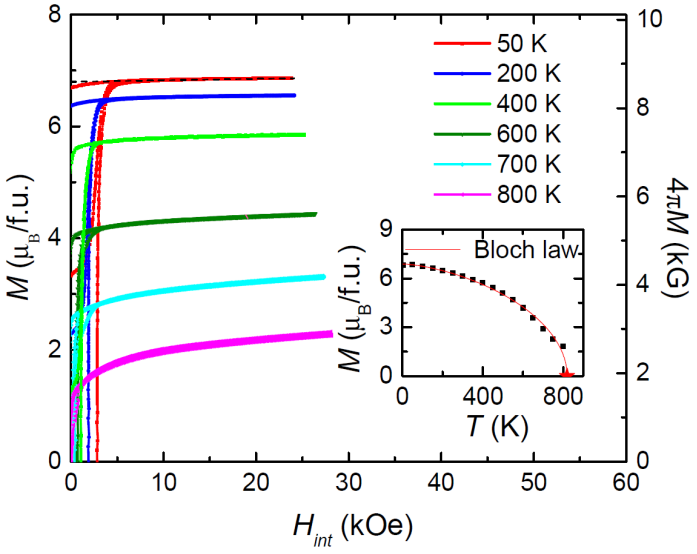

Figure 10.11 Representative of M(H) isotherms for the as-grown crystal **V**– $Ce_{14.3}Ta_{1.0}Co_{62.0}Fe_{12.3}Cu_{10.4}$. In the inset - spontaneous magnetization for each temperature inferred from the extrapolation of the linear regions of the *M(H)* back to $H = 0$. Red star shows extrapolated T_C value following Bloch law $M(T) = M(0)[1 - (T/T_C)]^{3/2}$.

not associated with a single phase single crystal as determined by the SEM and XRD examinations [Figs. 10.3,10.4], which did not reveal any elemental precipitations, segregations, or any microstructure on their corresponding length-scales.

The detailed high resolution STEM examination of the as-grown sample **III** [Fig. 10.6] showed the basic uniformity and integrity with small Co-enriched and Cu depleted regions/stripes coherently dispersed throughout the matrix. Unfortunately, the size of these stripes did not allow for EDS composition determination or structural analysis. However, based on previous reports [21, 22, 23], we assume that these are embryonic structural defects caused by stacking faults compensating for various channel disorders within the material. These may also be the nucleation sites for the decomposition and/or miscibility gap as suggested in previous literature [36].

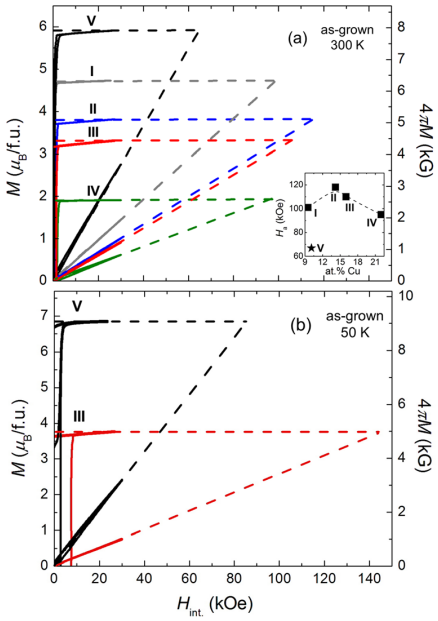

Figure 10.12 (a) - anisotropic field-dependent magnetization along easy and hard axes of the as-grown crystals **I** – $Ce_{15.1}Ta_{1.0}Co_{74.4}Cu_{9.5}$, **II** – $Ce_{16.3}Ta_{0.6}Co_{68.9}Cu_{14.2}$, **III** – $Ce_{15.7}Ta_{0.6}Co_{67.8}Cu_{15.9}$, **IV** – $Ce_{16.3}Ta_{0.3}Co_{61.7}Cu_{21.7}$ and **V** – $Ce_{14.3}Ta_{1.0}Co_{62.0}Fe_{12.3}Cu_{10.4}$ at 300 K. Inset in the lower-right corner - dependence of the anisotropy field H_a *vs.* Cu concentration, (b) - anisotropic field-dependent magnetization along easy and hard axes of the as-grown crystals **III** – $Ce_{15.7}Ta_{0.6}Co_{67.8}Cu_{15.9}$ and **V** – $Ce_{14.3}Ta_{1.0}Co_{62.0}Fe_{12.3}Cu_{10.4}$ at 50 K.

B. Heat-treated crystals. Coercivity, pinning and magnetic energy.

After heat treatment, the crystals **I** – **IV** show significantly increased magnetic hystereses with a monotonic increase of coercivity, H_c, and a linear decrease of spontaneous magnetization M_s with increasing Cu content [Fig. 10.15]. For example, the magnetic characteristics of **III** change as follows: significant increase of H_c from ~1.6 to ~6.3 kOe with an increase of B_r (M_s) from ~4.2 (4.2) to ~5.3 (5.7) kG, resulting in $(BH)_{max.}$ of ~7.8 MGOe [Fig. 10.16]. In addition to the conspicuous increase in magnetic hysteresis, there is a noteworthy increase in saturated magnetization of the heat-treated samples [Fig. 10.1 and Fig. 10.15, upper inset]. This increase in magnetic properties

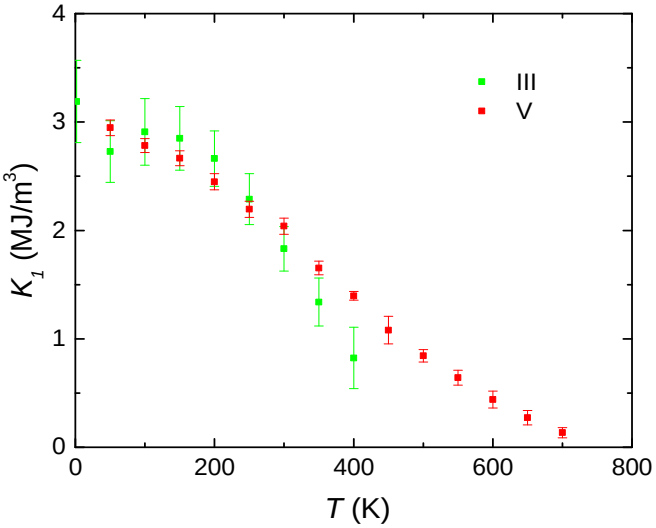

Figure 10.13 Comparison of temperature dependent magnetocrystalline anisotropy energy density of **III** - $Ce_{15.7}Ta_{0.6}Co_{67.8}Cu_{15.9}$ and **V** - $Ce_{14.3}Ta_{1.0}Co_{62.0}Fe_{12.3}Cu_{10.4}$.

correlates with the appearance of the Ta-rich precipitates [see SEM images above, Fig. 10.3]. The STEM analysis confirmed that these are 90 - 95 % pure rectangular blocks of Ta (according to diffraction patterns and elemental analysis), and their interfaces were coherent with the matrix material. However, high magnification TEM EDS maps [Fig. 10.7 (c), Fig. 10.8] observed a Cu-deficient and Co-enriched layer at the interface of the precipitates and the matrix, and Co was detected in precipitates as lines, which somewhat resemble observations of rare Co-enriched and Cu-depleted lines in the as-grown STEM examination [Fig. 10.6].

These results suggest that the high coercivity may be explained by the Ta-rich precipitates serving as pinning sites and can be described using a simple domain pinning model. Typically, the coercive force is inversely proportional to the saturation magnetization for a particular magnetocrystalline energy ($H_c = \sqrt{AK}/M_s l$, where A – exchange constant, K – magnetocrystalline anisotropy, M_s – saturation magnetization and l – the distance between the precipitates) [21, 22, 23]. According to the equation, by increasing the amount of pinning precipitates we decrease the volume fraction of the matrix material and magnetization M_s of the system. Also the distances l between the precipi-

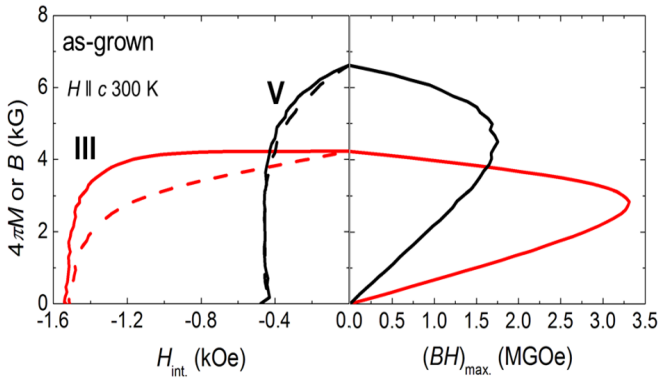

Figure 10.14 Room temperature second quadrant magnetic hysteresis loops for the as–grown crystals **III** – $Ce_{15.7}Ta_{0.6}Co_{67.8}Cu_{15.9}$ and **V** - $Ce_{14.3}Ta_{1.0}Co_{62.0}Fe_{12.3}Cu_{10.4}$, $4\pi M$ indicated as solid line and B as a dashed line (left pannel). Estimation of the energy products $(BH)_{max.}$ (right pannel).

tates become shorter. As a result, the coercivity H_c increases. Thus, the H_c of our crystals should be directly proportional to the Ta content. However we observe the inverse proportionality: total Ta content monotonically decreases in crystals **I** through **IV** [Table 10.1], whereas the coercivity monotonically increases [Fig. 10.15].

In contrast, the H_c increase correlates directly with increasing Cu content [Fig. 10.15, see both insets], also following the proposed precipitation coercivity mechansim (see equation above). Pinning of magnetic domains should occur on the precipitates, the amount of which is regulated by Cu rather than Ta content. However we do not observe precipitates that are clearly associated with Cu, except Cu-depleted regions observed in STEM experiments [Fig. 10.7 (c), Fig. 10.8].

Therefore, we consider the Ta-rich precipitates as a secondary effect, which decorates the extended 3D defects and structural imperfections that originate from Cu depleted and Co enriched lines observed in the as-grown crystals [Fig. 10.6] and consequently develop into the regions between Ta-rich precipitates and matrix in the thermally aged crystals [Fig. 10.7 (c), Fig. 10.8].

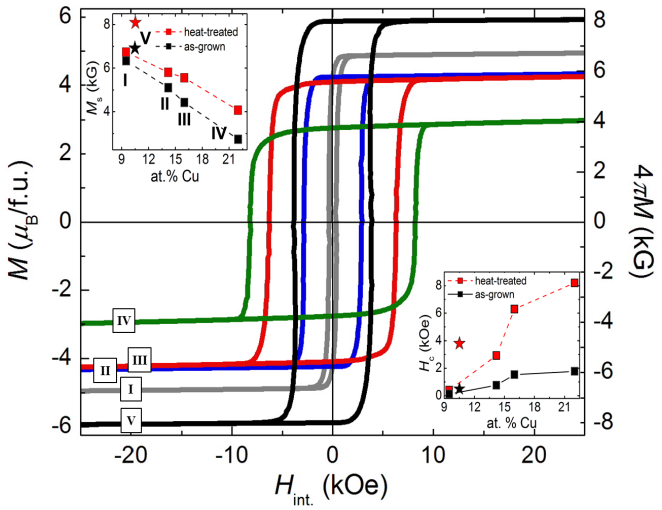

Figure 10.15 Magnetic hysteresis loops of the heat-treated crystals **I** – $Ce_{15.1}Ta_{1.0}Co_{74.4}Cu_{9.5}$, **II** – $Ce_{16.3}Ta_{0.6}Co_{68.9}Cu_{14.2}$, **III** – $Ce_{15.7}Ta_{0.6}Co_{67.8}Cu_{15.9}$, **IV** – $Ce_{16.3}Ta_{0.3}Co_{61.7}Cu_{21.7}$ and **V** – $Ce_{14.3}Ta_{1.0}Co_{62.0}Fe_{12.3}Cu_{10.4}$ at 300 K. Upper-right inset – dependence of the spontaneous magnetization M_s *vs.* Cu concentration for the as-grown and heat treated crystals. Lower-right inset – dependence of the coercivity H_c *vs.* Cu concentration for the as-grown and heat-treated crystals.

The amount of these imperfections must increase with increasing Cu content and lead to increased coercivity.

According to the literature, coercivity in the Cu and Fe substituted $CeCo_5$ is casued by fine precipitates which originate from partial matrix decomposition similar to eutectoidal, observed in pure $CeCo_5$ [21, 22, 23]. Whereas in the Cu substituted $CeCo_5$ the pronounced coercivity is related to a miscibility gap with a critical temperature close to 800 °C [36]. Both observations support the idea of intragranular domain pinning on extended 3D defects created as a result of matrix phase transformations during the heat-treatment (hardening) of the samples. In the first case, the precipitated 2:17 phase serves as a pinning site and contributes slightly to the increase in magnetization. In the second, because of decreased miscibility at lower temperatures, two phases

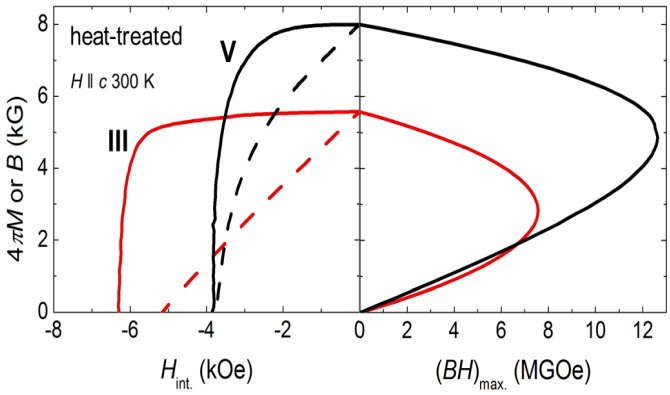

Figure 10.16 Room temperature second quadrant magnetic hysteresis loops for the heat-treated crystals **III** – $Ce_{15.7}Ta_{0.6}Co_{67.8}Cu_{15.9}$ and **V** - $Ce_{14.3}Ta_{1.0}Co_{62.0}Fe_{12.3}Cu_{10.4}$, $4\pi M$ indicated as solid line and B as a dashed line (left pannel). Estimation of the energy products $(BH)_{max.}$ (right pannel).

with similar Cu/Co ratios and different Curie temperatures exist. The Cu-poor phase supposedly serves as a pinning precipitate with increased magnetization, and the Cu-richer phase contributes towards the higher anisotropy matrix. One indirect confirmation of such mechanism is observed in the Fe-free crystals **I** – **IV**, which show atypical and increasing magnetization after the heat treatment [see the left inset in Fig. 10.15]. This suggests a change of the magnetic nature of the matrix. However, this must occur with a minimal composition change as no significant difference in compositions were detected before and after the heat treatment [Table 10.1]. With the addition of Fe, the decomposition process complicates, and besides the miscibility gap, the precipitation of the very stable 2:17 Ce/Co/Fe phase is possible [21, 22, 23]. This however was not clearly confirmed in the Fe-doped crystal **V**. Current SEM/EDS examinations of **V** show a microstructure similar to the Fe-free crystals **III** and **IV** [Fig. 10.3]. After the heat treatment the 2:17 phase was not observed.

Another explanation of pronounced increase in magnetization after the heat treatment may be associated with removal of Ta from the matrix material. Please note that the increase in

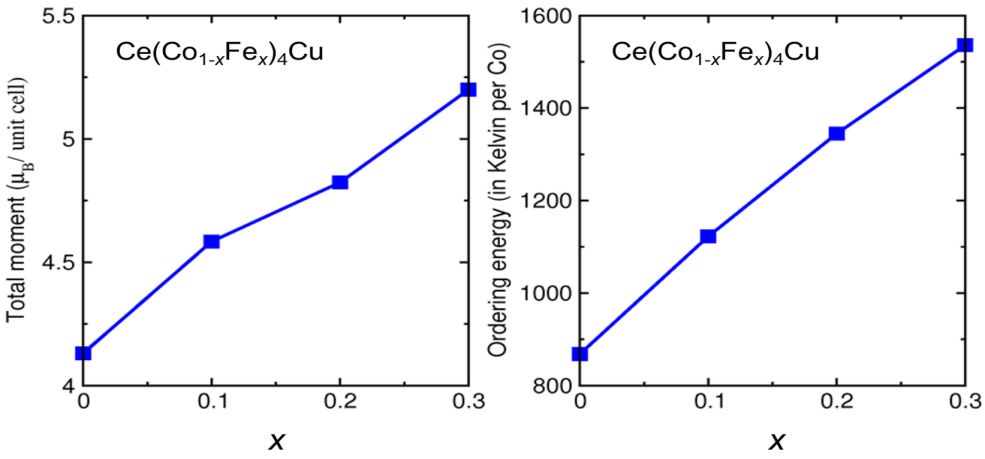

Figure 10.17 (a) - total moment (μ_B/unit cell) as a function of Fe doping; (b) - the energy difference between nonmagnetic state and ground state (ferromagnetic state) in Kelvin on per Co/Fe basis as a function of Fe doping for $Ce(Co_{1-x}Fe_x)_4Cu$.

magnetization is most pronounced in **IV** with most complete removal of Ta after the heat treatment [see Table 10.1]. One possible explanation for the surprisingly large impact of the removal of Ta on magnetic properties of our $CeCo_5$-based material is as follows. Previous theoretical work [61] finds that $CeCo_5$ is surprisingly near to a non-magnetic state, based on Stoner physics, despite its substantial Curie point. We suggest that Ta may locally drive the system toward a non-magnetic or less-magnetic state, so that its removal may restore or enhance magnetic character locally. Further theoretical work would clearly be needed to address this notion, and it may well be difficult to account quantitatively for the observed magnitude of the behavior - ~25 percent increase in magnetization for a removal of 0.3 atomic percent of Ta. Nevertheless, systems near a magnetic instability can exhibit a disproportionate response to small impurity concentrations, as in paramagnetic Fe impurities having huge effective moments in a Pd-Rh matrix [62], and we suggest the possibility of similar behavior here.

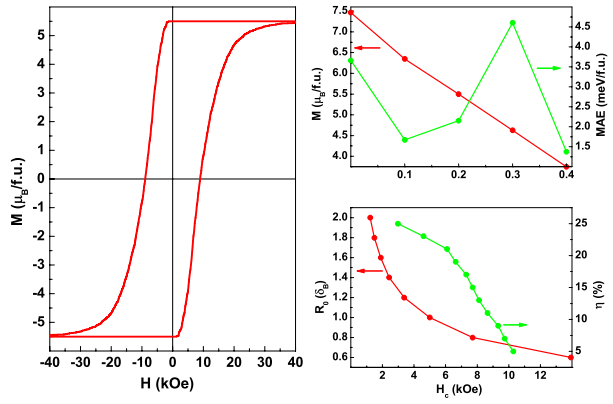

Figure 10.18 (Left) hysteresis loop of $Ce(Co_{0.8}Cu_{0.2})_5$ system (i.e., $Ce_{16.67}Co_{66.67}Cu_{16.67}$) calculated using η=15% and $R_0 = 0.8\delta_B$. The parameter η represents the probability for neighboring blocks to be exchange coupled, while R_0 is the defect size, in units of the Bloch domain wall thickness δ_B, taken here as 4 nm [36]. (Right top) calculated spontaneous magnetization and MAE of $Ce(Co_{1-x}Cu_x)_5$ $Ce_{16.67}Co_{83.33(1-x)}Cu_{83.33x}$) (i.e. as a function of Cu concentration). (Right bottom) coercivity of $Ce(Co_{0.8}Cu_{0.2})_5$ system (i.e., as a function of R_0 and η parameters). η (R_0) dependence was evaluated for fixed R_0=0.8 (η=15%).

10.6 Theoretical calculations

There are two main questions associated with the extraordinary magnetic nature of the Cu and Fe substituted $CeCo_5$: *i* - strong improvement of both Curie temperature and the magnetization by the addition of Fe and *ii* - the high coercivity that is driven primarily by a Cu-regulated intragranular pinning mechanism rather than the more typical strong magnetocrystalline anisotropy. We address these in the next two sections through theoretical calculations and multiscale modeling.

A. Increase of Curie temperature in Fe-doped samples.

To understand the observed magnetic behavior and increase in Curie point with Fe substitution, first principles calculations for $CeCo_5$ and $CeCo_4Cu$ were performed using the density functional theory as implemented in the WIEN2K code [63]. Calculations were performed using the experi-

mental lattice parameters. In this structure all internal coordinates are symmetry-dictated, so no internal coordinate optimization was performed. The LAPW sphere radii were set to 2.4 Bohr for Ce and 2.0 Bohr for Co and Cu. In addition to ensure proper convergence of the basis set Rk_{max} = 9.0, was used. Here R and k_{max} are the smallest LAPW sphere radius and the largest interstitial plane-wave cutoff, respectively. All the calculations are performed by assuming a collinear spin arrangement. The magnetic anisotropy energy (MAE) is obtained by calculating the total energies of the system with spin orbit coupling (SOC) as $K = E_{[100]}$ - $E_{[001]}$, where $E_{[110]}$ and $E_{[001]}$, are the total energies for the magnetization oriented along the a and c directions, respectively. For these MAE calculations the convergence with respect to the number of K-points was carefully checked. All the MAE results reported in this section correspond to 2000 K-points in the full Brillouin zone. To correctly treat the strong interactions between the Ce-f electrons, the Hubbard U correction was applied, with U_{Ce} = 3.0 eV. For the DFT+U calculations, the standard self-interaction correction (SIC) [64, 65] method was used.

For the modeling of $CeCo_4Cu$, Cu was substituted in the Co hexagonal ring (2c Co-site), as our calculations find this location for Cu to be energetically favorable (relative to the 3g site) by some 30 meV/Cu. Fe alloying in $CeCo_4Cu$ was realized within the virtual crystal approximation (VCA). The calculated magnetic behavior for $CeCo_5$ is in good agreement with the experimental measurements with a total magnetization of 6.8 μ_B per unit cell. The calculated spin moment on each 2c-Co atoms was 1.42 μ_B whereas the moment on 3g-Co atoms is 1.5 μ_B. This is accompanied by an orbital moment of $\sim$ 0.13 μ_B. The calculated Ce spin moment is -0.71 μ_B. Upon Cu substitution (for $CeCo_4Cu$) the moment on the Co atoms is reduced to 1.18 and 1.40 μ_B on Co-2c and Co-3g site, respectively. However, upon Fe alloying in $CeCo_4Cu$ ($CeCo_{4-x}Fe_xCu$) the total magnetization in the unit cell increases linearly with Fe doping as shown in Figure 10.17a. The calculated MAE of $\sim$ 3.17 MJ/m^3 without including the Hubbard U parameter ($U = 0$) is rather small when compared to the experimental MAE of 10.5 MJ/m^3 [56]. However a GGA+U calculation with U_{Ce} as 3.0 eV gives an MAE of 9.0 MJ/m^3 in good agreement with the experimental value.

The most remarkable observation of experimental measurements is the increase in Curie temperature of $CeCo_5$ by alloying with Cu and Fe. We explain this observation using two methods, one more roughly qualitative, the other more quantitative. For the first method, we note that for a local moment magnetic material, the Curie point is ultimately controlled by the interatomic exchange interactions, which are often determined by an effective mapping of the first-principles-calculated energies of various magnetic configurations to a Heisenberg-type model. However, the magnetic configurations considered here (using the parameters above) all converged instead to the spin-polarized case with all Co spins aligned in the ferromagnetic fashion. These calculations suggest that the magnetism in this material is of itinerant type.

For such a system the calculation of the Curie point is more involved. For this first qualitative approach we therefore limit ourselves to a simple consideration of the magnetic ordering or formation energy - the energy difference $\Delta E = E_{NM}$-E_{FM} where E_{NM} is the energy of a non-magnetic configuration and E_{FM} is the energy of the ferromagnetic configuration. While this energy contains contributions from both the *intra*-atomic Hund's rule coupling (which does not determine Curie points) and the *inter*-atomic exchange coupling (which does determine Curie points), it is plausible that within a given alloy system, such as $CeCo_{4-x}Fe_xCu$, the *trend* of the Curie point with alloying is generally captured by the *trend* of this energy. For example, the general quenching of $3d$ orbital moments in magnetic systems away from the atomic limit indicates, as expected, that the atomic Hund's rule coupling is not the only relevant interaction here.

In order to get some insight into the Curie temperature, we have therefore calculated this energy ΔE for $Ce(Co_{1-x}Fe_x)_4Cu$ on a per Co/Fe basis. This, along with the associated magnetic moment, is plotted in Figure 10.17 as a function of Fe doping. One observes a substantial ordering energy increase (from $\sim$ 900 K to $\sim$ 1500 K) with increasing Fe doping from $x = 0$ to $x = 0.3$, along with a substantial magnetic moment increase. From a theoretical standpoint, it is noteworthy that ΔE is as high as 1500 K for $x = 0.3$. This large energy does suggest the possibility of some local character of the magnetism on the *3d* (i.e. Co and Fe) atoms with increased Fe content in $Ce(Co_{1-x}Fe_x)_4Cu$. Note that a previous theoretical treatment of $CeCo_5$ [61] found evidence, as we do here, for itinerant

character in $CeCo_5$, so that increased Fe contents in these materials are of both theoretical and experimental interest.

Our second method of calculating the Curie point of this system is more quantitative. While the increase of magnetization and the corresponding magnetic formation energy (Fig. 10.17) with the addition of Fe atoms to $CeCo_5$ is generally expected, the observed increase of Curie temperature T_C requires a more detailed explanation. To describe theoretically the dependence of the T_C on concentration of Fe we employed the traditional mean field approximation (MFA) for systems with non equivalent magnetic atoms in a primitive cell. In this approximation T_C of a system with N nonequivalent magnetic atoms is calculated as the largest solution of the equation

$$\det[T_{nm} - T\delta_{nm}] = 0, \tag{10.1}$$

where n and m are the indices of the non-equivalent magnetic sublattices, $T_{nm} = \frac{2}{3}J^0_{mn}$. Here J^0_{mn} is an effective magnetic exchange interaction of an atom from sublattice n with all other atoms from the sublattice m. The exchange coupling parameters J^0_{mn} have been obtained using the multiple scattering formalism expression obtained in Ref [66] and extensively tested in Ref [67]. The corresponding dependence on content has been described using the coherent potential approximation (see details in Ref.citeCPA).

The calculations for pure $CeCo_5$ revealed that the value of T_C is determined by the strong ferromagnetic nature of the Co-Co interactions. The absolute value of the exchange parameters decays quickly with increasing interatomic distance so that the main contribution to T_C comes from the interaction between atoms lying within a distance of the two first neighboring shells. The average value of the nearest neighbor coupling J_{Co-Co} is approximately 15 meV. The contribution from Ce atoms is weak and negative.

The obtained MFA value of T_C = 790 K in $CeCo_5$ shows the typical overestimation of the experimental T_C in this classical spin approach. The addition of Fe atoms shows an interesting development of exchange coupling. First, we notice the appearance of a strong ferromagnetic Fe-Co coupling J_{Fe-Co}=21 meV. Second, the addition of Fe atoms increases the magnetic moments on Co atoms by approximately 0.1 μ_B with a corresponding increase of Co-Co exchange coupling as

well. Overall this effect leads to nearly 20% increase of T_C with a maximum of 950K at x=0.2-0.23. This qualitatively confirms the experimentally observed trend. We find that further addition of Fe atoms is detrimental for the ferromagnetism in these alloys and T_C starts to decrease. Finally, we also find from theory that a large increase of T_C by nearly 35% can be obtained when replacing Ce by Y atoms in $CeCo_5$ alloys.

B. Multiscale modeling.

In this section we present theoretical studies of the hysteretic behavior of Cu- and Ta-doped $CeCo_5$ crystals in order to better understand the mechanism of coercivity in these systems. The physics of magnetic hysteresis involves multiple length scales and is controlled both by intrinsic and extrinsic properties of magnets. Therefore, our method is based on a multiscale approach that combines first principles electronic structure calculations, micromagnetic models, and statistical macromagnetic simulations.

The electronic structure calculations describe material behavior on atomic length scales and allow us to evaluate intrinsic properties like spontaneous magnetization and MAE. We used density functional theory (DFT) within the rotationally invariant DFT+U method [65] and the PBE approximation to the exchange-correlation functional [68]. We used a Hubbard U=2 eV and J=0.8 eV for Co 3d electrons which were previously demonstrated to provide a good description of magnetic properties for the $LaCo_5$ and YCo_5 materials [69]. The Kohn-Sham equations were solved using the projector-augmented wave method [70] as implemented in the VASP code [71, 72]. We used a 1×1×2 supercell with respect to the primitive unit cell for $CeCo_5$. For the Brillouin zone sampling the Monkhorst-Pack scheme [73] was used with a dense 16×16×10 k-mesh. The energy cutoff for the plane wave expansion was set to 320 eV. The crystal structures were fully relaxed until forces acting on each atom were smaller than 0.01 eV/Å and all stress tensor elements were smaller than 1 kbar. The MAE was evaluated using the force theorem as the total energy difference between states with the magnetization aligned along [100] and [001] directions.

Figure 10.18 (top right) shows the calculated spontaneous magnetization and MAE for $Ce(Co_{1-x}Cu_x)_5$ as a function of Cu content. We assumed that the Cu atoms occupy the 3g atomic sites and we

chose the lowest energy atomic configurations that correspond to the Cu atoms occupying the same atomic layers. As seen, the spontaneous magnetization decreases with Cu content since Cu atoms have negligible moments as expected from their $3d^{10}$ nominal configuration. This is in agreement with the experimental results shown in Fig. 10.15 (inset). Regarding the MAE, our calculations show that it has a complex non-monotonic dependence on Cu content. In particular, whereas small Cu additions decrease the MAE, for larger concentrations the MAE shows a maximum as a function of x. Converting these calculated MAE and magnetization results to anisotropy fields H_A we find the following anisotropy fields (in kOe) for x=0, 0.1, 0.2, 0.3, and 0.4, respectively: 166, 93, 131, 338 and 128. This non-monotonic H_A behavior is qualitatively consistent with the experimental results for the anisotropy field as a function of Cu content shown in Fig. 10.12 except that, experimentally, the H_A maximum is observed at lower Cu content (approximately x= 0.2, vs. x=0.3 for the theory) and the corresponding H_A values differ significantly from the theoretical values. These differences are probably primarily caused by the fact that the configuration of Cu atoms in real samples differs in some respect from the lowest energy configuration used in the calculations.

In order to study the hysteresis process, in addition to the knowledge of the calculated-above, intrinsic parameters (magnetic anisotropy and magnetization), we need to also specify the microstructural features of the system at the nanometer and micron length scales. As discussed in the previous sections, SEM and STEM measurements indicate that a network of planar defects is present in the single crystal samples. For the as-grown crystals these defects form Co-enriched and Cu-depleted laminar regions, which after heat treatment, become nucleation points for Ta-rich planar precipitates. Clearly, these extended defects play a crucial role in establishing coercivity in the system since they can efficiently pin the reversed magnetic domains, thus preventing them from expanding over the entire crystal. In fact, as seen in Fig. 10.3, the crystal can be viewed as a collection of blocks (of the size of several microns) that are, to a large degree, magnetically decoupled by the planar defects. In our model we consider an idealized version of such a microstructure in the form of a simple cubic lattice of identical cubic micron-size $Ce(Co_{1-x}Cu_x)_5$ blocks. While the actual microstructure "blocks" are generally hexagonal (see. Fig. 3), the use of a simple cubic

lattice greatly simplifies the calculation and is not expected to drastically change its qualitative features. We assume periodic boundary conditions in a closed magnetic circuit setup so that there is no demagnetization field. Since the decoupling of blocks by the planar defects is not perfect, we introduce a parameter η which physically represents the probability for neighboring blocks to be exchange coupled.

In addition, the blocks interact via the magnetostatic interaction that is described using the Ewald technique as detailed in Ref. [74]. In a manner similar to the approach in Ref. [75], we assume that each block has a number of magnetically soft defects (e.g. Co precipitates) with exponentially distributed sizes $f(R) = \frac{1}{R_0} e^{-R/R_0}$ where the parameter R_0 is the characteristic defect size. Assuming well-separated spherical defects, the switching field of each block can be determined by micromagnetic calculations using the intrinsic parameters (magnetic anisotropy and magnetization) calculated from the first principles calculations above. The hysteresis loop is then calculated by starting from the saturated state and gradually decreasing the external magnetic field. For each value of the external field the system magnetization is determined as follows. The total magnetic field acting on each block is evaluated as a sum of the external and magnetostatic contributions. When the total field is lower than the negative switching field of the block, the block magnetization is reversed. Subsequently, all blocks that are exchange coupled to the reversed block also have their magnetization reversed. The process is repeated iteratively, until a stable magnetic configuration is achieved.

Figure 10.18 (left) shows the calculated hysteresis loop for a $Ce(Co_{0.8}Cu_{0.2})_5$ system calculated using η=15% and $R_0 = 0.8\delta_B$ where δ_B is the Bloch domain wall thickness of $CeCo_5$ (around 4 nm [36]). As is evident, this choice of parameter results in a rectangular hysteresis loop with a coercivity similar to the measured value for this Cu content [see Fig. 10.15]. Therefore, our model is capable of reproducing the experimental results. Fig. 10.18 (bottom right) shows the dependence of the coercivity on the microstructural parameters: η and R_0. We observe that for $R_0 < \delta_B$, R_0 strongly affects the coercivity while for $R_0 > \delta_B$, the coercivity depends only weakly on R_0. As expected, the coercivity decreases with η. Interestingly, around $\eta = 20\%$ we observe a change of

slope and a much stronger reduction of coercivity is observed for larger η. These results indicate that there are two possible mechanisms by which Cu doping enhances the coercivity. First, Cu doping may increase the number and thickness of planar defects resulting in a decrease of the η parameter. This is consistent with a scenario in which the defects are in fact, precipitates of the Cu-poor 1:5 phase. A second possibility is that the Cu doping reduces the size of the magnetically soft defects in the matrix phase.

10.7 Conclusions

Using a self-flux technique, we synthesized five different single crystals of Ta, Cu and/or Fe substituted $CeCo_5$. They retain a $CaCu_5$ substructure and incorporate small amounts of Ta in the form of "dumb-bells" filling the $2e$ crystallographic sites within the 1D hexagonal channel with the $1a$ Ce site, whereas Co, Cu and Fe are statistically distributed among the $2c$ and $3g$ crystallographic sites. The as-grown crystals appear single phased and homogeneous in composition. Their single crystallinity is confirmed by XRD, SEM and TEM experiments. However they also exhibit significant magnetic coercivities which are comparable to most anisotropic sintered alnico grades. After the heat treatment (hardening), magnetic characteristics significantly improve. Ta atoms leave the matrix interstices of the as-grown crystals and precipitate in form of coherent laminas creating the so-called "composite crystal". The "composite crystal", formed during the heat treatment, contains a 3D array of structural defects within a primarily single grain single crystal. The mechanism of coercivity is regulated by Cu, and pinning occurs on the extended 3D defects and structural imperfections that originate from Cu depleted and Co enriched lines observed in the as-grown crystals and consequently develop into the regions between Ta-rich precipitates and matrix in the thermally aged crystals. The structural defects form as a result of a thermodynamic transformation of the matrix material associated with its partial decomposition and/or decreased miscibility during hardening process. Significant improvement of magnetization in the heat-treated samples may be associated either with the transformation of the matrix phase or with the removal of Ta from the matrix. Fe strongly improves both the Curie temperature and magnetization of

the system, which is associated with a strong increase in the magnetic ordering energy. The peculiar thermodynamic transformations, which lead to intragranular pinning and a unique coercivity mechanism that does not require the typical processing for the development of extrinsic magnetic properties, could be used to create permanent magnets with lowered processing costs. Further composition - temperature - time optimizations may result in a critical material free and cost-efficient gap magnet with energy product 15 – 16.5 MGOe.

10.8 Acknowledgements

This research was supported by the Critical Materials Institute, an Energy Innovation Hub funded by the U.S. Department of Energy, Office of Energy Efficiency and Renewable Energy, Advanced Manufacturing Office. M.C.N. is supported by the office of Basic Energy Sciences, Materials Sciences Division, U.S. DOE. This work was performed at the Ames Laboratory, operated for DOE by Iowa State University under Contract No. DE-AC02-07CH11358.

10.9 References

[1] G. B. Haxel, J. B. Hendrick, and G. J. Orris. Demagnetizing factors for rectangular ferromagnetic prisms. *U.S. Geological Survey Fact Sheet*, (087-02), 2002.

[2] Pradyot Patnaik. *Handbook of Inorganic Chemicals*. McGraw-Hill Professional, 2002.

[3] Feng Xie, Ting An Zhang, David Dreisinger, and Fiona Doyle. A critical review on solvent extraction of rare earths from aqueous solutions. *Minerals Engineering*, 56:10–28, Feb 2014.

[4] J. F. Herbst, J. J. Croat, and W. B. Yelon. Structural and magnetic properties of $Nd_2Fe_{14}B$ (invited). *Journal of Applied Physics*, 57(8):4086–4090, Apr 1985.

[5] Arjun K. Pathak, Mahmud Khan, Karl A. Gschneidner, Ralph W. McCallum, Lin Zhou, Kewei Sun, Kevin W. Dennis, Chen Zhou, Frederick E. Pinkerton, Matthew J. Kramer, and Vitalij K. Pecharsky. Cerium: An unlikely replacement of dysprosium in high performance Nd-Fe-B permanent magnets. *Advanced Materials*, 27(16):2663–2667, 2015.

[6] Arjun K. Pathak, K.A. Gschneidner, M. Khan, R.W. McCallum, and V.K. Pecharsky. High performance Nd-Fe-B permanent magnets without critical elements. *Journal of Alloys and Compounds*, 668:80–86, May 2016.

[7] Michael A. Susner, Benjamin S. Conner, Bayrammurad I. Saparov, Michael A. McGuire, Ethan J. Crumlin, Gabriel M. Veith, Huibo Cao, Kavungal V. Shanavas, David S. Parker, Bryan C. Chakoumakos, and Brian C. Sales. Flux growth and characterization of Ce-substituted $Nd_2Fe_{14}B$ single crystals. *Journal of Magnetism and Magnetic Materials*, 434:1–9, Jul 2017.

[8] Karl J. Strnat and Reinhold M.W. Strnat. Rare earth-cobalt permanent magnets. *Journal of Magnetism and Magnetic Materials*, 100(1-3):38–56, Nov 1991.

[9] H. Senno and Y. Tawara. Permanent-magnet properties of Sm-Ce-Co-Fe-Cu alloys with compositions between 1-5 and 2-17. *IEEE Transactions on Magnetics*, 10(2):313–317, Jun 1974.

[10] M. J. Kramer, R. W. McCallum, I. A. Anderson, and S. Constantinides. Prospects for non-rare earth permanent magnets for traction motors and generators. *JOM*, 64(7):752–763, Jun 2012.

[11] R.W. McCallum, L. Lewis, R. Skomski, M.J. Kramer, and I.E. Anderson. Practical aspects of modern and future permanent magnets. *Annual Review of Materials Research*, 44(1):451–477, Jul 2014.

[12] E. A. Nesbitt. New permanent magnet materials containing rare-earth metals. *Journal of Applied Physics*, 40(3):1259–1265, Mar 1969.

[13] E. A. Nesbitt, R. H. Willens, R. C. Sherwood, E. Buehler, and J. H. Wernick. NEW PERMANENT MAGNET MATERIALS. *Applied Physics Letters*, 12(11):361–362, Jun 1968.

[14] Yoshio Tawara and Harufumi Senno. Cerium, cobalt and copper alloy as a permanent magnet material. *Japanese Journal of Applied Physics*, 7(8):966–967, Aug 1968.

[15] J. M. D. Coey. Permanent magnets: Plugging the gap. *Scripta Materialia*, 67(6):524–529, sep 2012.

[16] Harufumi Senno and Yoshio Tawara. Microstructure of a cerium, cobalt and copper alloy with a high coercivity. *Japanese Journal of Applied Physics*, 8(1):118–118, Jan 1969.

[17] E. A. Nesbitt, G. Y. Chin, R. C. Sherwood, and J. H. Wernick. Effect of processing on permanent magnet materials containing rare-earth metals. *Journal of Applied Physics*, 40(10):4006–4009, Sep 1969.

[18] Thomas J. Cullen. Cast permanent magnets of cobalt, copper, and cerium: Process and performance characteristics. *Journal of Applied Physics*, 42(4):1535–1536, Mar 1971.

[19] R.C. Sherwood, E.A. Nesbitt, G.Y. Chin, and M.L. Green. Preparation and properties of sintered CoCuFeCe permanent magnets. *Materials Research Bulletin*, 7(5):489–493, May 1972.

[20] Y. Tawara and H. Senno. Sintered magnets of copper- and iron-modified cerium cobalt. *IEEE Transactions on Magnetics*, 8(3):560–561, Sep 1972.

[21] G. Chin, M. Green, E. Nesbitt, R. Sherwood, and J. Wernick. Directional solidification of Co-Cu-R permanent-magnet alloys. *IEEE Transactions on Magnetics*, 8(1):29–35, Mar 1972.

[22] E. A. Nesbitt, G. Y. Chin, G. W. Hull, R. C. Sherwood, M. L. Green, J. H. Wernick, Hugh C. Wolfe, C. D. Graham, and J. J. Rhyne. Intrinsic magnetic properties and mechanism of magnetization of Co - Fe - Cu - R permanent magnets. In *AIP Conference Proceedings*. AIP, 1973.

[23] H. Leamy and M. Green. The structure of Co-Cu-Fe-Ce permanent magnets. *IEEE Transactions on Magnetics*, 9(3):205–209, Sep 1973.

[24] E. Nesbitt, G. Chin, R. Sherwood, M. Green, and H. Leamy. Influence of cerium content on the structure and magnetic behavior of Co - Fe - Cu - Ce permanent magnets. *IEEE Transactions on Magnetics*, 9(3):203–205, Fep 1973.

[25] Y. Khan. Intermetallic compounds in the cobalt-rich part of the R-cobalt systems (R = Ce, La, Ce-La). *Journal of the Less Common Metals*, 34(2):191–200, Feb 1974.

[26] M. P. Arbuzov, A. A. Pavlyukov, and A. G. Leskevich. Coercive force of cast and sintered permanent magnets in Co - Cu - Fe - Ce alloys. *Poroshkovaya Metalurgiya*, 9:48, 1974.

[27] M. P. Arbuzov, A. A. Pavlyukov, and A. G. Pogorilyy. X-ray diffraction analysis of the phase composition of the alloy $Co_4CuCe_{1.02}$. *Fiz. Metal. Metalloved.*, 40:848, 1975.

[28] M. P. Arbuzov, A. A. Pavlyukov, A. G. Pogorilyi, and O. S Opanasenko. Crystal structure and coercive force of sintered permanent magnets in alloys of the system Co - Cu - Fe - Ce. *Poroshkovaya Metalurgiya*, 5:97, 1975.

[29] M. P. Arbuzov, A. A. Pavlyukov, E. V. Krakovich, and O. S Opanasenko. Magnetic characteristics of sintered permanent magnets in $(Co, Cu, Fe)_5Ce$ alloys. *Poroshkovaya Metalurgiya*, 7:56, 1977.

[30] M. P. Arbuzov, A. A. Pavlyukov, E. V. Krakovich, and O. S Opanasenko. Magnetic characterisitics of sintered permanent magnets in alloys of the Co-Cu-Fe-Ce system. *Poroshkovaya Metalurgiya*, 8:69, 1977.

[31] M. P. Arbuzov, A. A. Pavlyukov, E. V. Krakovich, and O. S Opanasenko. Magnetic properties of sintered $(Co, Cu, Fe)_5Ce$ alloys. *Poroshkovaya Metalurgiya*, 9:85, 1977.

[32] Koichiro Inomata, Teruo Oshima, Tadashi Ido, and Masakazu Yamada. Sintered Ce-Co-Cu-Fe-Ti magnets. *Applied Physics Letters*, 30(12):669–670, Jun 1977.

[33] Yoshio Tawara, Tetsuichi Chino, and Yukihiro Matsui. Permanent magnets based on (Ce,Sm)(Co,Fe,Cu)$_z$. *Applied Physics Letters*, 33(7):674–675, Oct 1978.

[34] B Labulle and C Petipas. X-ray study of monocrystalline alloys near the composition $CeCo_{3.5}Cu_{1.5}$. *Journal of the Less Common Metals*, 66(2):183–200, Aug 1979.

[35] B Labulle and C Petipas. Oxidation study of monocrystalline $CeCo_{5-x}Cu_x$ by x-ray diffraction methods. *Journal of the Less Common Metals*, 71(2):183–194, Jun 1980.

[36] D. Girodin, C.H. Allibert, F. Givord, and R. Lemaire. Phase equilibria in the $CeCo_5$-$CeCu_5$ system and structural characterization of the $Ce(Co_{1-x}Cu_x)_5$ phases. *Journal of the Less Common Metals*, 110(1-2):149–158, Aug 1985.

[37] H. Okamoto. Ce-Co phase diagram, asm alloy phase diagrams database, p. villars, editor-in-chief; h. okamoto and k. cenzual, section editors. *Ce-Co Phase Diagram, ASM Alloy Phase Diagrams Database, P. Villars, editor-in-chief; H. Okamoto and K. Cenzual, section editors*, 1990.

[38] P. C. Canfield and Z. Fisk. Growth of single crystals from metallic fluxes. *Philos. Mag.*, 65(6):1117–1123, 1992.

[39] P. C. Canfield. *Properties and Applications of Complex Intermetallics, Solution Growth of Intermetallic Single Crystals: A Beginer Guide*. Number Chap. 2. World Scientific, Singapore, 2010.

[40] Paul C. Canfield and Ian R. Fisher. High-temperature solution growth of intermetallic single crystals and quasicrystals. *Journal of Crystal Growth*, 225(24):155 – 161, 2001. Proceedings of the 12th American Conference on Crystal Growth and Epitaxy.

[41] Juan Rodríguez-Carvajal. Recent advances in magnetic structure determination by neutron powder diffraction. *Physica B: Condensed Matter*, 192(1-2):55–69, Oct 1993.

[42] *SMART (Bruker AXS Inc., Madison, Wisconsin, 1996).*

[43] *SHELXTL (Bruker AXS Inc., Madison, Wisconsin, 2000).*

[44] R. H. Blessing. An empirical correction for absorption anisotropy. *Acta Crystallographica Section A Foundations of Crystallography*, 51(1):33–38, Jan 1995.

[45] Tej N. Lamichhane, Valentin Taufour, Srinivasa Thimmaiah, David S. Parker, Sergey L. Bud'ko, and Paul C. Canfield. A study of the physical properties of single crystalline Fe_5B_2P. *J. Magn. Magn. Mater.*, 401:525 – 531, 2016.

[46] Tej N. Lamichhane, Valentin Taufour, Andriy Palasyuk, Qisheng Lin, Sergey L. Bud'ko, and Paul C. Canfield. $Ce_{3-x}Mg_xCo_9$: Transformation of a Pauli Paramagnet into a Strong Permanent Magnet. *Physical Review Applied*, 9(2), Feb 2018.

[47] O. Bodak, Ya. Tokaychuk, M. Manyako, V. Pacheco, R. Černý, and K. Yvon. Structural and magnetic properties of iron-rich compounds in the Yb–Fe–Al system. *Journal of Alloys and Compounds*, 354(1-2):L10–L15, May 2003.

[48] Ya.O. Tokaychuk, O.I. Bodak, Yu.K. Gorelenko, and K. Yvon. Structural and magnetic properties of iron-rich compounds in the Yb–Fe–Ga system. *Journal of Alloys and Compounds*, 415(1-2):8–11, May 2006.

[49] Radovan Černý, Yaroslav Filinchuk, and Stefan Brühne. Local atomic order in the vicinity of Cu_2 dumbbells in $TbCu_7$-type $YCu_{6.576}$ studied by Bragg and total scattering techniques. *Intermetallics*, 17(10):818–825, Oct 2009.

[50] K. H. J. Buschow and A. S. van der Goot. Composition and crystal structure of hexagonal cu-rich rare earth–copper compounds. *Acta Crystallographica Section B Structural Crystallography and Crystal Chemistry*, 27(6):1085–1088, Jun 1971.

[51] I. S. Vinogradova E. S. Makarov. The crystal structure of Th_2Zn_{17} and U_2Zn_{17}. *Kristallografiya*, 1:634, 1956.

[52] J. V. Florio, N. C. Baenziger, and R. E. Rundle. Compounds of thorium with transition metals. II. systems with iron, cobalt and nickel. *Acta Crystallographica*, 9(4):367–372, Apr 1956.

[53] D. Givord, R. Lemaire, J. M. Moreau, and E. Roudaut. X-ray and neutron determination of a so-called 1:7-type structure in the lutetium-iron system. *J. Less-Comm.Met.*, 29:361–369, 1972.

[54] K.H.J. Buschow. The crystal structures of the rare-earth compounds of the form R_2Ni_{17}, R_2Co_{17} and R_2Fe_{17}. *Journal of the Less Common Metals*, 11(3):204 – 208, 1966.

[55] Chen Zhou, Frederick E. Pinkerton, and Jan F. Herbst. Formation of $TbCu_7$-type $CeFe_{10}Zr_{0.8}$ by rapid solidification. *Journal of Alloys and Compounds*, 569:6–8, Aug 2013.

[56] M.I. Bartashevich, T. Goto, R.J. Radwanski, and A.V. Korolyov. Magnetic anisotropy and high-field magnetization process of $CeCo_5$. *Journal of Magnetism and Magnetic Materials*, 131(1):61 – 66, 1994.

[57] W. Sucksmith and J. E. Thompson. The Magnetic Anisotropy of Cobalt. *Proc. Royal Soc. A*, 225(1162):362–375, 1954.

[58] Valentin Taufour, Srinivasa Thimmaiah, Stephen March, Scott Saunders, Kewei Sun, Tej Nath Lamichhane, Matthew J. Kramer, Sergey L. Bud'ko, and Paul C. Canfield. Structural and

Ferromagnetic Properties of an Orthorhombic Phase of MnBi Stabilized with Rh Additions. *Phys. Rev. Applied*, 4:014021, Jul 2015.

[59] P. R. Bevington and D. K. Robinson. *Data reduction and error analysis for the physical sciences.* New York: McGraw-Hill, 2003.

[60] Standard Specifications for Permanent Magnet Materials (MMPA STANDARD N 0100-00).

[61] Lars Nordström, Olle Eriksson, M. S. S. Brooks, and Börje Johansson. Theory of ferromagnetism in CeCo5. *Physical Review B*, 41(13):9111–9120, May 1990.

[62] A. J. Manuel and J. M. P. S. Quinton. The Magnetic Susceptibilities of Palladium and Palladium-Rhodium Alloys from 1.85 to 293 K. *Proceedings of the Royal Society A: Mathematical, Physical and Engineering Sciences*, 273(1354):412–426, May 1963.

[63] P. Blaha, K. Schwarz, G. Madsen, D. Kvasnicka, and J. Luitz. An augmented plane wave+ local orbitals program for calculating crystal properties. 2001.

[64] V. I. Anisimov, I. V. Solovyev, M. A. Korotin, M. T. Czyżyk, and G. A. Sawatzky. Density-functional theory and NiO photoemission spectra. *Physical Review B*, 48(23):16929–16934, Dec 1993.

[65] A. I. Liechtenstein, V. I. Anisimov, and J. Zaanen. Density-functional theory and strong interactions: Orbital ordering in mott-hubbard insulators. *Physical Review B*, 52(8):R5467–R5470, Aug 1995.

[66] A.I. Liechtenstein, M.I. Katsnelson, V.P. Antropov, and V.A. Gubanov. Local spin density functional approach to the theory of exchange interactions in ferromagnetic metals and alloys. *Journal of Magnetism and Magnetic Materials*, 67(1):65–74, May 1987.

[67] V.P Antropov, B.N Harmon, and A.N Smirnov. Aspects of spin dynamics and magnetic interactions. *Journal of Magnetism and Magnetic Materials*, 200(1-3):148–166, Oct 1999.

[68] John P Perdew, Kieron Burke, and Matthias Ernzerhof. Generalized gradient approximation made simple. *Physical Review Letters*, 77(18):3865, 1996.

[69] Manh Cuong Nguyen, Yongxin Yao, Cai-Zhuang Wang, Kai-Ming Ho, and Vladimir P Antropov. Magnetocrystalline anisotropy in cobalt based magnets: a choice of correlation parameters and the relativistic effects. *Journal of Physics: Condensed Matter*, 30(19):195801, Apr 2018.

[70] P. E. Bloechl. Projector augmented-wave method. *Physical Review B*, 50(24):17953–17979, Dec 1994.

[71] G. Kresse and J. Furthmller. Efficient iterative schemes forab initiototal-energy calculations using a plane-wave basis set. *Physical Review B*, 54(16):11169–11186, Oct 1996.

[72] G. Kresse and D. Joubert. From ultrasoft pseudopotentials to the projector augmented-wave method. *Physical Review B*, 59(3):1758–1775, Jan 1999.

[73] Hendrik J. Monkhorst and James D. Pack. Special points for brillouin-zone integrations. *Physical Review B*, 13(12):5188–5192, Jun 1976.

[74] Aleksander L. Wysocki and Vladimir P. Antropov. Micromagnetic simulations with periodic boundary conditions: Hard-soft nanocomposites. *Journal of Magnetism and Magnetic Materials*, 428:274–286, Apr 2017.

[75] R. Blank. What determines the demagnetization in Nd-Fe-B magnets? *Journal of Magnetism and Magnetic Materials*, 101(1-3):317–322, Oct 1991.

CHAPTER 11. SUMMARY AND CONCLUSIONS OF THE THESIS

Clean energy technologies such as high flux permanent magnets, magnetic refrigeration, portable electrolytic batteries and light emitting phosphors need critical elements. High flux permanent magnets namely $Nd_2Fe_{14}B$, $SmCo_5$ and Sm_2Co_{17} need critical rare-earth elements. Finding noncritical, new, high-flux, permanent magnets that can compete with current high flux permanent magnets can not be ruled out, but remains highly elusive in theoretical as well as experimental research. In the meantime, discovery of new gap magnets could greatly reduce the dependency of the permanent magnets industry on rare-earth based, critical, high-flux, permanent magnets. The goal of this thesis was to look for new transition metal and Ce-based ferromagnets with high uniaxial anisotropy ($\geq$5 T), high saturation magnetization ($\geq$0.5 T), and high Curie temperature ($\geq$ 550 K) that could be used for the gap magnets.

An exploratory, high-temperature, solution growth technique was employed in the vicinity of transition metals Fe, Co or Mn rich eutectic points in less studied, volatile/high vapour pressure exhibiting ternary phase diagrams such as Fe-P-B, Hf-Mn-P, Zr-Mn-P, Al-Fe-B and Al-Mn-B. In Fe-P-B system, Fe_5B_2P was studied. The Curie temperature, base temperature saturation magnetization and magnetocrystalline anisotropy energy of Fe_5B_2P is determined to be 655$\pm$2 K, 1.73 μ_B/Fe and $\sim$ 0.5MJ/m^3 respectively. Likewise, both orthorhombic ZrMnP and HfMnP are newly identified ferromagnets with Curie temperature 371 K and 320 K respectively. Corresponding aniostropy fields at 50 K are determined to be $\sim$ 5 T and $\sim$ 10.5 T respectively. Similarly in Al-Fe-B system, re-examination of single crystalline $AlFe_2B2$ was carried out to provide intrinsic magnetic parameters such as 2 K saturation magnetization (1.15 μ_B/Fe), Curie temperature (274 K) and maximum entropy change in phase transition, degree of itinerant nature of magnetism and influence of hydrostatic pressure in its magnetic properties. In the Mn analogue, $AlMn_2B2$,

a near room temperature antiferromagnetic transition temperature (315 K) and low dimensional magnetism ($\beta = 0.21 \pm 0.02$) was observed in single crystalline $AlMn_2B_2$.

Ce is the most abundant and easiest to purify rare-earth element. We investigated the Co rich section of Ce-Co-Mg Ternary phase diagram and discovered ferromagnetism in Mg doped solid solution $Ce_{3-x}Mg_xCo_9$. Mg addition in Pauli paramagnetic $CeCo_3$ introduces the quantum phase transition to ferromagnetic solid solution $Ce_{3-x}Mg_xCo_9$ with the critical concentration $x \sim 0.35$. The solid solution $Ce_{3-x}Mg_xCo_9$ exists as high as $x \leq 1.40$ and Curie temperature raises proportional to Mg content in the solid solution and reaches 450 K for $x \sim 1.40$. The magnetocrystalline anisotropy field and energy density at 300 K are found to be ~6 T and ~0.75 MJ/m^3 respectively which is large enough to qualify this system as a potential gap magnet. During the similar search effort in the Co rich section of the Sm-Co-Mg phase diagram, a relatively simpler method of Mg-flux growth of Sm_2Co_{17} single crystal sample was discovered.

In addition, Several concentrations of Fe, Cu and Ta substituted single crystalline $CeCo_5$ samples (i.e. $Ce(Co_{1-x-y-z}Fe_xCu_yTa_z)_5$) were synthesized and anisotropic intrinsic magnetic parameters were determined. Cu stabilizes the 1:5 phase however magnetization and Curie temperature are proportionally decreased with Cu content. Although Ta was incorporated is the crystal structure inadvertently from the growth crucible, it played a positive role to develop grain boundaries in heat treated single crystalline samples necessary for magnetic domain pinning. The Fe addition significantly increased the Curie temperature and the saturation magnetization, compensating the effect of anisotropy field decrease with Cu and Fe addition. An optimally Fe and Cu doped heat treated sample, $Ce_{14.3}Ta_{1.0}Co_{62.0}Fe_{12.3}Cu_{10.4}$, exhibited approximately 13 MGOe energy product, a value within the existing energy product gap in permanent magnets.

In conclusion, we made several encouraging steps toward our research goals namely two new Mn based ferromagnets with large anisotropy fields, conversion of a Pauli paramagnetic, $CeCo_3$, into a strong uniaxial anisotropic ferromagnet $Ce_{3-x}Mg_xCo_9$ and development of a 13 MGOe energy product in noncritical $Ce_{14.3}Ta_{1.0}Co_{62.0}Fe_{12.3}Cu_{10.4}$ single crystalline permanent magnet were achieved. These results provide proof of principles for the further possibility of developing

new, noncritical, ferromagnets or rehabilitation of weak ferromagnets to be commercially useful gap magnets. It is important to continue such exploratory investigation for novel noncritical elemental phases so as to discover new useful ferromagnets.

APPENDIX A. ADDITIONAL MATERIALS ON "STUDY OF DOPING INDUCED QUANTUM PHASE TRANSITION IN $Ce_{3-x}Mg_xCo_9$"

Field dependent magnetization and the Arrott plots for various samples

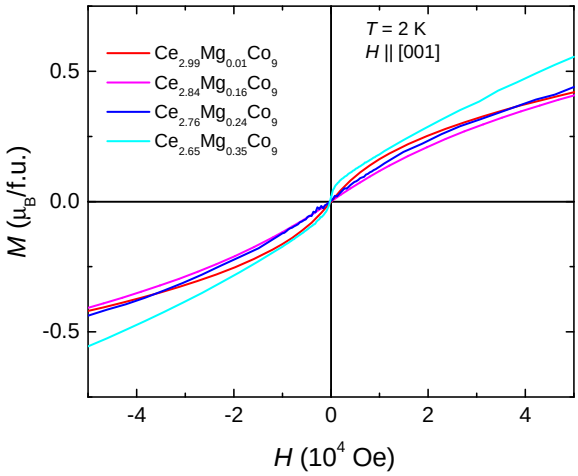

Figure A.1 Field dependent magnetization of various non-ferromagnetic $Ce_{3-x}Mg_xCo_9$ samples at 2 K parallel to c axis.

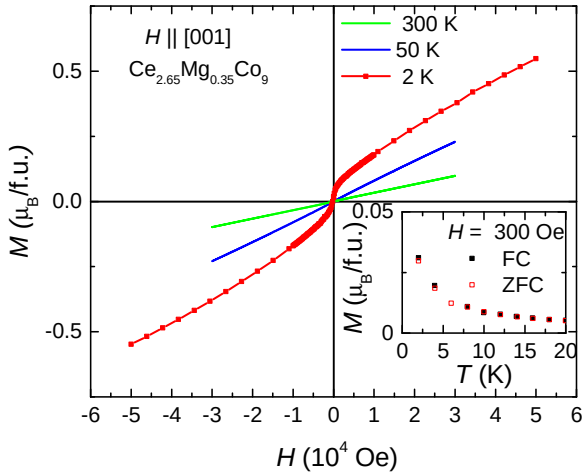

Figure A.2 Field dependent magnetization of $Ce_{2.65}Mg_{0.35}Co_9$ at various temperature to demonstrate only base temperature has some Brillouin type saturation magnetization. The lower inset shows reversible nature of the ZFC and FC *M(T)* data.

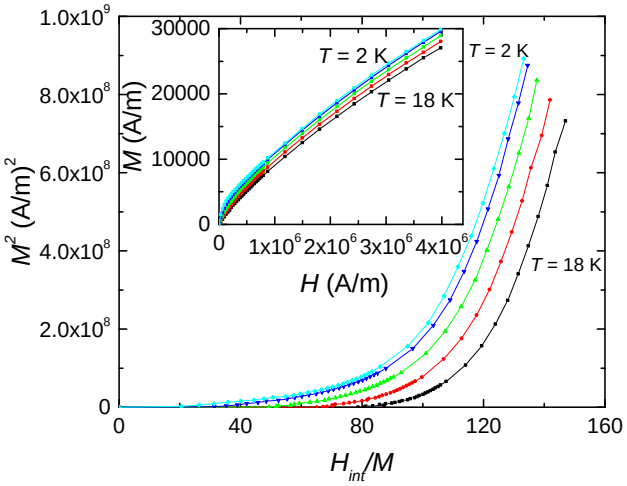

Figure A.3 The Arrott plot of $Ce_{2.65}Mg_{0.35}Co_9$ within 2 K to 18 K at a step of 4 K. The Curie temperature is suggested to be lower than 2 K. The inset shows the corresponding *M(H)* data.

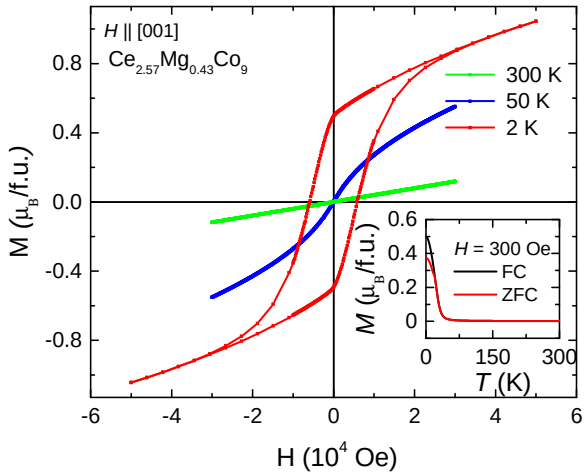

Figure A.4 Field dependent magnetization of $Ce_{2.57}Mg_{0.43}Co_9$ at various temperatures. The hystersis loop observed for 2 K data is a good signature that $Ce_{3-x}Mg_xCo_9$ system could be used for permanent magnet application. The lower inset shows the *M(T)* along with bifurcation of ZFC and FC *M(T)* data consistent with observed low temperature hysteresis loop.

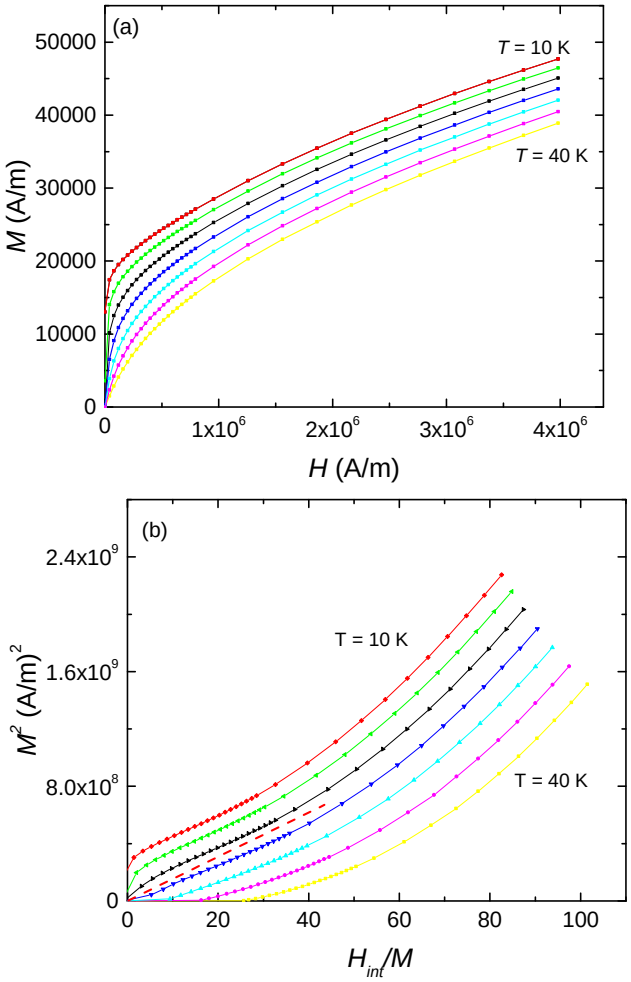

Figure A.5 (a) *M(H)* data for $Ce_{2.57}Mg_{0.43}Co_9$ sample around the Curie temperature within 10 K to 40 K at a step of 5 K. (b) Corresponding Arrott plot to determine the Curie temperature which is found to be around 25 K.

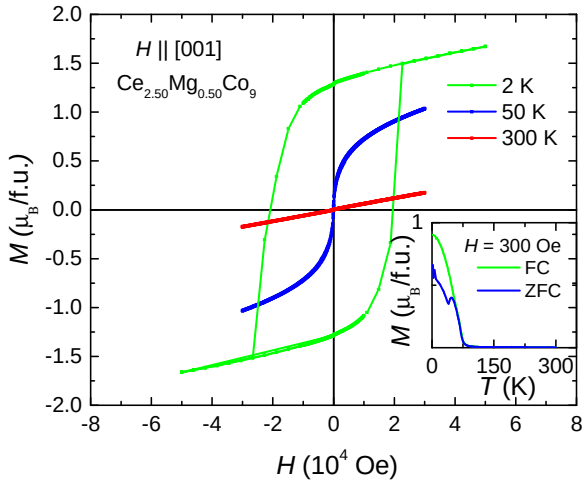

Figure A.6 Field dependent magnetization of $Ce_{2.50}Mg_{0.50}Co_9$ at various temperatures. The hysteresis loop observed for 2 K data (as grown coercivity of 2 T) is a good signature that $Ce_{3-x}Mg_xCo_9$ system could be used for permanent magnet application. The lower inset shows the *M(T)* along with bifurcation of ZFC and FC *M(T)* data consistent with observed low temperature hysteresis loop.

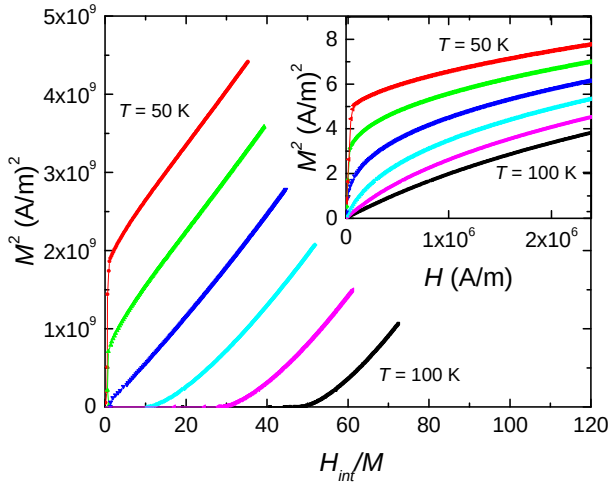

Figure A.7 The Arrott plot of $Ce_{2.50}Mg_{0.50}Co_9$ within 50 K to 100 K at a step of 10 K. The Curie temperature is determined to be around 70 K. The inset shows the corresponding *M(H)* data.

APPENDIX B. MAGNETIC UNIT CONVERSION

Table B.1 Selected magnetic unit conversion table [1, 2]

Quantity	Gaussian	SI
Magnetic field	10,000 Oersted (Oe)	1 Tesla
Magnetic field	1 Oe	$\frac{10^3}{4\pi}$ A/m
Magnetization (Volume)	1 Gauss	$\frac{10^3}{4\pi}$ A/m
Magnetization (mass)	1 emu/g	$4\ \pi \times 10^{-7}$ Tm^3/kg
Energy product	12.57 Mega-Gauss-Oersted (MG Oe)	100 kJ/m^3
Anisotropy energy density	10 $Merg/cm^3$	1 MJ/m^3
μ_0	1	$4\ \pi \times 10^{-7}$ N/A^2
work (energy)	10^7erg	1 J
μ_B (Bohr magneton)	9.274015 $\times 10^{-21}$ erg/G	9.274015 $\times 10^{-24}$ J/T

B.1 References

[1] Lydon J. Swartzendruber. Properties, units and constants in magnetism. *Journal of Magnetism and Magnetic Materials*, 100(1):573 – 575, 1991.

[2] J. M. D. Coey. *Magnetism and Magnetic Materials*. Cambridge University Press, 2010.